Cavity-Optomechanics with Silica Microtoroids: Quantum-Coherent Coupling and Optomechanically Induced Transparency

THÈSE N^{O} 5380 (2012)

PRÉSENTÉE LE 22 JUIN 2012
À LA FACULTÉ DES SCIENCES DE BASE
LABORATOIRE DE PHOTONIQUE ET MESURES QUANTIQUES (SB/STI)
PROGRAMME DOCTORAL EN PHOTONIQUE

ÉCOLE POLYTECHNIQUE FÉDÉRALE DE LAUSANNE

POUR L'OBTENTION DU GRADE DE DOCTEUR ÈS SCIENCES

PAR

Stefan Alexander WEIS

acceptée sur proposition du jury:

Prof. O. Martin, président du jury
Prof. T. Kippenberg, directeur de thèse
Prof. M. Aspelmeyer, rapporteur
Prof. F. Marquardt, rapporteur
Prof. V. Savona, rapporteur

ÉCOLE POLYTECHNIQUE
FÉDÉRALE DE LAUSANNE

Suisse
2012

Meiner Familie gewidmet.

Acknowledgements

Many people have contributed to the success of this thesis, and I owe thanks to all of them.

First, I thank my advisor **Prof. Tobias J. Kippenberg** for giving me the opportunity to be part of his group, for his incredible enthusiasm and never ending optimism, the myriad of ideas he contributed to this work and the outstanding working environment he created.

The first year I worked on a different project together with **Fredrik Hocke**, **Thomas Niemczyk** (both at Walther-Meißner-Institute) and especially **Xiaoqing Zhou**. Thank you very much for the great time inspite of the many setbacks during microfabrication!

Thank you very very much to my colleagues at the helium-3 experiment:

Rémi Rivière brought all the know-how from his preceding experiment and taught me the right working attitude required for successful cryogenic optomechanics experiments... ;) I still do not know how you managed to get a good tapered fiber into the cryostat at 5 a.m.! Thanks for the time we spent in the lab together!

I admire **Olivier Arcizet** for his ability to successfully do complex experiments even under difficult conditions and his close to instant understanding of technical difficulties and physical effects! Thank you also for organizing the ultimate frisbee matches and other sports activities!

I could not have imagined a better colleague to do the move from MPQ to EPFL with than **Samuel Deléglise**, who—being the only native speaker—unselfishly took over so much organizational responsibility. The control software he developed, the much more coherent and automated setup we could realize together and his highly contagious good mood made it extremely nice to do experiments together with him.

Ewold Verhagen lead and put a lot of efforts into the development and fabrication of the new generation of samples, which enabled experiments that had not been imaginable before. I really learned a lot from your way of working! Thank you also for the very careful proof-reading of my thesis and the improvements you suggested!

During all that time **Albert Schliesser** has always been open to theoretical but also technical questions and contributed major parts to the meanwhile routinely used theoretical

model.
I enjoyed very much working with all of you!

I would like to thank **Emanuel Gavartin** for the many hours he spent in the cleanroom fabricating samples for us while we were still at MPQ and - together with **Jens Dobrindt** - for their endless efforts and assistance during the move from Garching to Lausanne, as well as **Ignacio Vasquez Garcia** for launching the development of the spoke-supported microresonators. Also I wish to thank **Pierre Thoumany** for his help regarding the cryogenic setup and the cubic meters of liquid helium that we could borrow on short notice!

I want to thank **Christina Becker**, **Patricia Marti-Rochat** and **Hélène Laurens** for the countless hours of administrative support as well as **Helmut Brückner**, **Charly Linner** und **Wolfgang Simon** at MPQ, and the members of the **PH and BM mechanical workshops** at EPFL for promptly solving so many technical problems. Especially our cryohead fabricated by Charly and Wolfgang is a masterpiece!

Good luck to my successors **Vivishek Sudhir** and **Nicolas Piro Mastracchio** for the future of the experiment!

Many thanks to all other group members, who were not directly involved into the He-3 experiment but nevertheless contributed to making this thesis a successful and very pleasant one, and **Pascal Del'Haye**, who I had the pleasure to share an office with at MPQ!

A special thanks to **Tobias Herr**, who has become a very close friend, for all the time we spent together inside and outside the lab, at and around and especially on the lake!

Last but not least, I would like to thank my entire family, but especially my parents, and Iris for their unconditional support during all these years.

Lausanne, le 14 mai 2012 S. W.

Abstract

Here, I report on a cryogenic cavity optomechanics experiment that has been set up with the goal to cool a mechanical degree of freedom of a fused silica microtoroidal resonator into the quantum regime by means of a combination of cryogenic and laser cooling. Based on the experience with a Helium-4 exchange gas cryostat obtained during a previous cryogenic optomechanics experiment, a novel setup with a Helium-3 cryostat at its heart has been set up. Cooling of a mechanical degree of freedom of a microtoroid close to its motional quantum ground state could be achieved and a regime, where full quantum control becomes possible, has come into reach.

Silica microtoroids sustain at the same time ultra-high finesse optical whispering gallery modes (WGM) as well as radial mechanical modes ("radial breathing modes", RBM). The two degrees of freedom are mutually coupled, since mechanical motion changes the optical resonance frequency, and the mechanical motion is affected by the radiation pressure forces of an optical field contained in the optical mode. As the optical cavity lifetime is finite, the intracavity optical field amplitude is not adjusting instantaneously to the changed boundary conditions as induced by a mechanical displacement, but in a retarded manner, which gives rise to an effect known as dynamical backaction, that for example can be used to laser cool a mechanical mode.

Using a 1550 nm laser important insight has been gained on the dependency of mechanical decay rate and frequency as a function of temperature, which is dominated by two level systems within amorphous fused silica. The different temperature regimes have been explored, including experiments at the lowest accessible temperatures, where evidence of resonant saturable absorption of TLS has been found.

Using 780 nm light instead, cooling below ten quanta could be achieved and "optomechanically induced transparency", the optomechanical equivalent of electromagnetically induced transparency as found in atomic vapors, could be demonstrated, enabling all-optical switching of a laser beam and storage of pulses.

Novel, optimized spokes-supported toroids then enabled us to push up the optomechanical coupling sufficiently, such that cooling to below two thermal quanta could be achieved and—for the first time in the optical domain—the quantum-coherent coupling regime could be accessed. Here, the optomechanical coupling rate exceeds the optical and mechanical decay rates (i.e. "strong coupling"), but also the mechanical decoherence rate, such that quantum-state transfer between optics and mechanics comes into reach.

In addition, this thesis contains the technological steps taken and experimental hurdles

overcome towards these experiments.

Keywords

- cryogenic cavity optomechanics
- helium-3 cryostat
- toroidal silica microresonators
- resolved sideband regime
- laser backaction cooling
- optomechanically induced transparency
- strong coupling
- quantum-coherent coupling

Zusammenfassung

Im Rahmen dieser Arbeit entstand ein neuer experimenteller Aufbau für optomechanische Experimente bei tiefen Temperaturen. Ziel war es dabei, den Schwingungsfreiheitsgrad eines mikroskopischen, aber noch mit bloßem Auge sichtbaren, Glastorus mittels einer Kombination aus herkömmlicher kryogener und Laserkühlung in seinen quantenmechanischen Grundzustand zu überführen. Hierfür wurde, basierend auf den Erfahrungen aus einem Vorgängerexperiment in einem Helium-4 Austauschgaskryostaten, ein Helium-3 Kryostat konfektioniert. Es gelang den mechanischen Freiheitsgrad einer Mikrostruktur in die Nähe des quantenmechanischen Grundzustands zu kühlen und das System soweit zu entwickeln, dass nunmehr eine Kontrolle des mechanischen Quantenzustandes möglich geworden ist.

Mikrotori — kleine Glasringe auf einem Siliziumträger — vereinen optische Flüstergaleriemoden extrem hoher Güte, die entlang der äußeren Oberfläche des Ringes umlaufen, mit mechanischen Radialwellenmoden. Optische und mechanische Moden sind dabei gekoppelt, da mechanische Auslenkungen zu einer Änderung der optischen Weglänge im Resonator führen, d.h. die optische Resonanz verschieben. Gleichzeitig übt aber auch das umlaufende Licht eine Kraft ("Strahlungsdruck") auf den mechanischen Freiheitsgrad aus. Durch die hohe Güte der optischen Mode, kann sich das optische Lichtfeld jedoch nicht instantan an die veränderten Randbedingungen anpassen, was zu Retardierungseffekten führt, die auch als "dynamische Rückwirkung" bezeichnet werden. Diese erlaubt es, ganz analog zur Laserkühlung von Atomen und Ionen, die mechanische thermische Bewegung zu kühlen.

Bei einer Lichtwellenlänge von 1550 nm konnten zahlreiche Erkenntnisse, insbesondere zu Zweiniveausystemen (TLS) in Gläsern, die zu großen Teilen zur mechanischen Dämpfung beitragen, gewonnen werden. Neben der Temperaturabhängigkeit der Dämpfung und mechanischen Resonanzfrequenz, konnten darüber hinaus auch Anzeichen für die resonante Absorption an TLS und deren Sättigung gefunden werden.

Der Wechsel zu einem Titan:Saphir Lasersystem bei 780 nm ermöglichte überdies die Kühlung bis unter zehn Schwingungsquanten. Außerdem konnte erstmals "Optomechanisch Induzierte Transparenz" experimentell nachgewiesen werden. Ganz analog zur "Elektromagnetisch Induzierten Transparenz", erlaubt es dieser Effekt einen Laserstrahl mittels eines zweiten zu schalten, sowie auch Lichtpulse kurzzeitig zu speichern.

Mit der Entwicklung neuer Strukturen — die Ringe sind nunmehr nicht mehr starr mit dem Substrat verbunden, sondern mittels Speichen — konnte die Kopplung zwischen optischer und mechanischer Mode nochmals erheblich gesteigert werden. Dadurch gelang nicht nur das Kühlen der mechanischen Mode bis zu einer Besetzungszahl unter zwei Phononen, sondern es konnte auch erstmalig quantenkohärente Kopplung zwischen optischem und mechanischem Freiheitsgrad nachgewiesen werden. Hierbei erfolgt die Konversion von Schwingungsquanten schneller als der Zerfall eines Quantenzustandes durch Dekohärenz, was den Austausch von Quantenzuständen überhaupt erst ermöglicht.

Diese Arbeit beschreibt darüber hinaus die technischen Schwierigkeiten und gefundenen Lösungen auf dem Weg zu diesen Ergebnissen.

Schlüsselwörter

- Optomechanik bei tiefen Temperaturen
- Helium-3 Kryostat
- Torische Glas-Mikroresonatoren
- Aufgelöstes Seitenband Regime
- Laserkühlung mittels dynamischer Rückwirkung
- Optomechanisch induzierte Transparenz
- Starke Kopplung
- Quantenkoheränte Kopplung

Résumé

Dans le cadre de cette thèse, un dispositif permettant de conduire des expériences optomécaniques en cavité avec des microtores de silice dans un environnement cryogénique a été construit, dans le but de refroidir un degré de liberté mécanique de cet objet dans son état quantique fondamental. Pour cela, un dispositif consistant en un cryostat à hélium-3 a été construit, se basant sur l'expérience acquise dans un cryostat à hélium-4 utilisé dans un montage préalable. Un mode mécanique a été refroidi près de son état quantique fondamentale et un nouveau régime, qui permettra de contrôler son état au niveau quantique a été atteint.

Les microtores de silice abritent en même temps un mode optique de galerie (WGM) de très haute finesse ainsi qu'un mode mécanique de vibration radiale (RBM). Ces deux degrés de liberté sont couplés. En effet, tout mouvement mécanique agit sur la circonférence de la structure, définissant ainsi sa fréquence de résonance optique. D'un autre point de vue, la lumière piégée dans l'anneau influe aussi sur le résonateur mécanique par la force de pression de radiation. La durée de vie finie de la lumière dans le WGM donne naissance à un effet nommé action en retour dynamique, car le champ intracavité ne s'ajuste pas instantanément, ce qui cause un délai de la force de pression de radiation par rapport au mouvement mécanique. Cette dernière donne lieu à un effet nommé “action en retour dynamique”, qui permet de refroidir le mode mécanique.

Avec un laser à 1550 nm, ce montage a permis de comprendre en détail l'influence des systèmes à deux niveaux (TLS) présents dans la silice amorphe qui dominent le facteur de qualité du RBM à basse température et montrent un comportement complexe en fonction de la température. Les expériences réalisées ont permis d'explorer les différents régimes en fonction de la température, et en particulier, des signatures d'un phénomène d'absorption résonante des TLS.

Puis avec un laser à 780 nm, le refroidissement en-dessous de dix quanta a pu être réalisé et, pour la première fois, la "transparence induite optomécaniquement" a été démontrée. Cet effet très similaire à la "transparence induite électromagnétiquement" dans les vapeurs atomiques permet de contrôler un faisceau laser optiquement, ainsi que de stocker des impulsions lumineuses grâce à l'interaction optomécanique.

Le développement de structures où le tore est suspendu à l'aide de fines poutres radiales, a permis d'augmenter nettement le couplage optomécanique, ce qui nous a permis de refroidir en-dessous de deux quanta et—pour la première fois dans le domaine optique—d'atteindre le régime de “couplage quantique cohérent”. Dans ce régime, le taux de couplage optomécanique dépasse non-seulement les taux de dissipation optique et mécanique (i.e. régime de couplage fort), mais également le taux de décohérence mécanique, permettant ainsi le transfert d'états quantiques entre les modes optiques et mécaniques.

Cette thèse présente également les difficultés techniques à dépasser pour atteindre un tel régime.

Mots-Clés

- optomécanique en cavité à basse température
- cryostat à hélium-3
- microtores de silice
- bandes latérales résolues
- action en retour dynamique
- refroidissement par laser
- transparence induite électromagnétiquement
- couplage fort
- couplage cohérent quantique

List of Publications

[1] Stefan Weis*, Rémi Rivière*, Samuel Deléglise*, Emanuel Gavartin, Olivier Arcizet, Albert Schliesser and Tobias J. Kippenberg. "Optomechanically induced transparency.", *Science* **330**, 1520–1523 (2010).

[2] Rémi Rivière, Samuel Deléglise, Stefan Weis, Emanuel Gavartin, Olivier Arcizet, Albert Schliesser and Tobias J. Kippenberg. "Optomechanical sideband cooling of a micromechanical oscillator close to the quantum ground state.", *Physical Review A* **83**, 063835 (2011).

[3] Ewold Verhagen*, Samuel Deléglise*, Stefan Weis*, Albert Schliesser* and Tobias J. Kippenberg. "Quantum-coherent coupling of a mechanical oscillator to an optical cavity mode.", *Nature* **482**, 63–67 (2012).

---

*These authors contributed equally to this work.

List of Presentations

In 2012:

- **DPG Spring Meeting, Stuttgart, Germany, 12 March 2012**
  E. Verhagen, S. Deléglise, S. Weis, A. Schliesser and T.J. Kippenberg,
  “Cavity Optomechanics: Towards Quantum Control of Micromechanical Motion with Light”

In 2011:

- **1st EOS Topical Meeting on Micro- and Nano-Optoelectronic Systems, Bremen, Germany, 8 December 2011**
  E. Verhagen, S. Deléglise, S. Weis, A. Schliesser and T. J. Kippenberg, “Cavity Optomechanics: Towards Quantum Control of Micromechanical Motion with Light”

- **2011 International Conference on Optical MEMS & Nanophotonics, Istanbul, Turkey, 8 August 2011 (invited)**
  E. Verhagen, S. Deléglise, S. Weis, A. Schliesser and T. J. Kippenberg, “Cavity Optomechanics: Towards Quantum Control of Micromechanical Motion with Light”

- **QSIT Lunch Seminar, Zürich, Switzerland, 9 June 2011 (invited)**
  S. Weis, R. Rivière, S. Deléglise, E. Verhagen, E. Gavartin, O. Arcizet, A. Schliesser and T. J. Kippenberg, “Optomechanically Induced Transparency”

- **CLEO/QELS, Baltimore, MD, USA, 6 May 2011**
  S. Weis, R. Rivière, S. Deléglise, E. Verhagen, E. Gavartin, O. Arcizet, A. Schliesser and T.J. Kippenberg, "Cooling of a Micromechanical Oscillator into the Quantum Regime",
  Finalist of the Theodore Maiman Student Paper Competition, prize granted by HRL Laboratories, LLC, IEEE Photonics Society, APS and OSA

- **DPG Spring Meeting, Dresden, Germany, 14 March 2011**
  S. Weis, R. Rivière, S. Deléglise, E. Verhagen, E. Gavartin, O. Arcizet, A. Schliesser and T.J. Kippenberg, "Optomechanically Induced Transparency"

In 2010:

- **NOEKS10, Paderborn, Germany, 19 August 2010 (invited)**
  S. Weis, R. Rivière, S. Deléglise, E. Gavartin, O. Arcizet, A. Schliesser and T.J. Kippenberg, "Cavity Optomechanics with Silica Microresonators at Helium-3 Temperatures"
- **NCCR QP General Assembly 2010, Münchenwiler, Switzerland, 7 July 2010**
  S. Weis, R. Rivière, S. Deléglise, E. Gavartin, O. Arcizet, A. Schliesser and T.J. Kippenberg, "Cavity Optomechanics with Silica Microresonators at Helium-3 Temperatures"
- **CLEO/QELS, San Jose, CA, USA, 17-21 May 2010**
  S. Weis, R. Rivière, S. Deléglise, E. Gavartin, O. Arcizet, A. Schliesser and T.J. Kippenberg, "Cavity Optomechanics with Silica Microresonators at Helium-3 Temperatures"
- **DPG Spring Meeting, Hannover, Germany, 12 March 2010**
  S. Weis, R. Rivière, S. Deléglise, E. Gavartin, O. Arcizet, A. Schliesser and T.J. Kippenberg, "Cavity Optomechanics with Silica Microresonators at Helium-3 Temperatures"

Contents

Acknowledgements **v**

Abstract (English/Deutsch/Français) **vii**

List of Publications **xiii**

List of Presentations **xv**

Table of contents **xix**

List of figures **xxii**

1 Introduction **1**
- 1.1 Cavity Optomechanics 3
  - 1.1.1 Optomechanical Hamiltonian 3
- 1.2 Cavity Optomechanics - Experimental Realizations 5
  - 1.2.1 Overview of existing systems 5
  - 1.2.2 Fused silica microtoroids 6
  - 1.2.3 Optomechanical coupling rate and effective mass 7
- 1.3 High-sensitivity readout of mechanical motion 8
- 1.4 Laser sideband cooling of a mechanical oscillator 12
- 1.5 Optical response of an optomechanical system 13
  - 1.5.1 Optomechanically induced transparency 13
- 1.6 Outline 15

2 Experimental Setup **17**
- 2.1 Spectroscopy of optical modes 17
- 2.2 Detection of mechanical motion 21
  - 2.2.1 Side of the fringe 21
  - 2.2.2 Pound-Drever-Hall detection 22
  - 2.2.3 Balanced Homodyne Detection 23
  - 2.2.4 Other methods 25
- 2.3 Calibration of mechanical spectra 25
  - 2.3.1 Calibration using a phase calibration peak 26

2.4 Sideband Sweeps - measurement of the laser detuning 29
2.5 Cryogenic setup 31
2.5.1 The cryostat 32
2.5.2 The cryohead 34
2.5.3 Additional components 36
2.5.4 Basic operation 37
2.6 Data acquisition and automation 38

3 Challenges 41
3.1 Choice of an appropriate wavelength 41
3.2 Two-level systems 43
3.2.1 Relaxation contribution 45
3.2.2 Resonant processes 48
3.2.3 Fitting the TLS model 48
3.2.4 Resonant saturation phenomena 49
3.3 Sample Design 54
3.3.1 Optimizing conventional toroids 54
3.3.2 Optimized spoke anchored toroidal resonator 56
3.4 Sample degradation and static off-resonant heating 60
3.4.1 Optimized cool-down strategy 62
3.4.2 Pump and probe measurements 62
3.5 Quantum limited measurements - revisited 65
3.5.1 Influence of guided acoustic wave Brillouin scatting 66
3.6 Thermal response measurements and asymmetry in sideband sweeps 68
3.6.1 Thermal response of a toroidal microresonator 68
3.6.2 Asymmetries found in sideband sweeps 70

4 Results 73
4.1 Optomechanically Induced Transparency 73
4.1.1 Introduction 73
4.1.2 Theory 74
4.1.3 Experiment 85
4.1.4 Results 91
4.1.5 Conclusion 93
4.2 Optomechanical Sideband Cooling of a Micromechanical Oscillator Close to the Quantum Ground State 95
4.2.1 Introduction 95
4.2.2 Experiment 97
4.2.3 Results 99
4.2.4 Conclusion 107
4.3 Quantum-Coherent Coupling 108

4.3.1 Introduction 108
4.3.2 Theoretical model 110
4.3.3 Experiment 121

5 Outlook 131
5.1 Locking of the cooling laser 131
5.2 Real-time spectrum analysis 133
5.3 Samples 134
5.4 Experiments 135

Bibliography 150

Press Coverage 152

Curriculum Vitae 153

List of Figures

1.1 The generic optomechanical system. 3
1.2 Zoo of optomechanical systems. 5
1.3 Toroidal microresonators 7
1.4 Resonant readout of mechanical motion. 8
1.5 Mechanical modes found in microtoroids. 10
1.6 Resolved sideband cooling of a mechanical oscillator. 12
1.7 Sideband cooling in a thermal bath picture. 12
1.8 Optical response scheme. 14
1.9 Optomechanically induced transparency. 14

2.1 Optical spectroscopy scheme. 18
2.2 Coupling Series. 19
2.3 Illustration of the thermal effect in toroids. 20
2.4 Side-of-the-fringe detection. 21
2.5 Pound-Drever-Hall scheme. 23
2.6 Balanced homodyne detection. 24
2.7 Calibration of a phase modulator. 28
2.8 Sideband sweeps. 29
2.9 Detailed typical optics setup. 30
2.10 Mechanical quality factor in silica microtoroids vs. temperature. 32
2.11 The Helium-3 cryostat. 33
2.12 The cryohead. 35
2.13 Protecting cup and tapered fiber holders. 37
2.14 Experiment control. 39

3.1 “Cooling” at 1550 nm. 43
3.2 Optical absorption in fused silica fibers. 44
3.3 Schematic of a double well potential with naming of relevant parameters. 45
3.4 TLS effects. 46
3.5 Detailed analysis of different contributions to mechanical damping. . . 49
3.6 Relative mechanical frequency shift vs. temperature. 50
3.7 Pump-probe scheme used to examine saturable absorption. 51

3.8 Saturable absorption for the 76 MHz first order RBM. 52
3.9 Saturation behavior of the second order radial breathing mode. 53
3.10 Engineering clamping losses in conventional microtoroids. 55
3.11 Sample optimization by finite element modelling. 57
3.12 Sample fabrication. 58
3.13 Sample characterization. 59
3.14 Light scattering from tapered fibers. 61
3.15 Example of a successful cooldown. 63
3.16 Measurement of static off-resonant heating. 64
3.17 Shot noise vs. GAWBS 66
3.18 Engineering of the fiber GAWBS noise spectrum. 67
3.19 Setup used for thermal response measurements. 68
3.20 Comparison of thermal responses—large toroid vs. small spokes resonator. 69
3.21 Asymmetry of optical response spectra. 70

4.1 Optomechanically Induced Transparency. 75
4.2 Optomechanical system 85
4.3 The optical setup 86
4.4 Modal splitting 87
4.5 Observation of OMIT. 92
4.6 Controlling optomechanically induced transparency. 93
4.7 Cooling a micromechanical oscillator. 96
4.8 Contribution from TLS. 98
4.9 Detuning series. 102
4.10 Cooling factor and phonon occupancy of the RBM versus laser detuning for (a) different power levels. 104
4.11 Optomechanical microresonators. 110
4.12 Theoretical model used. 111
4.13 Fitting the model to the coherent response. 119
4.14 Influence of the photothermoelastic effect on noise spectra. 120
4.15 Setup. 122
4.16 Optomechanical interaction in the weak coupling regime ($\Omega_c \lesssim \kappa/2$). . 124
4.17 Quantum-coherent coupling. 125
4.18 Coherent exchange between the optical field and the micromechanical oscillator. 129

5.1 Dual tone locking scheme. 132
5.2 Real-time spectrum analyzer. 133
5.3 Future optomechanical systems. 134

1 Introduction

The thought experiment known as Schrödinger's cat, which he first proposed in 1935 [4], has become the quintessential example of how counterintuitive quantum mechanics can be. The—at a first glance—absurd predictions of quantum mechanics do not seem to be compatible with our every-day experience of the macroscopic world around us and one is tempted to restrict quantum behavior to the similarly unfamiliar scale of atoms.

This restriction was justified in the early days of the development of quantum theory, when thought experiments merely stimulated theoretical discussions. Only many years later quantum control of single objects became accessible experimentally with the advent of laser technology [5] and its evolution towards frequency tunable devices with narrow linewidths. These could be used for laser cooling of atoms [6, 7] and ions [8, 9, 10], finally down to their motional ground state in harmonic trapping potentials [11, 12, 13, 14]. By now, almost full control over individual atoms [15], ions [16, 17] but soon after also over dilute ensembles consisting of up to many million atoms, as in Bose Einstein condensates [18, 19] or degenerate Fermi gases [20, 21], has been gained.

A longstanding question has always been whether the motional state of a macroscopic objects, consisting of many trillions of individual atoms, could be controlled on a quantum level and would also obey the same laws. Besides, just to imagine a "quantum system" that is visible to the naked eye is piquing curiosity and motivation, even if it is not directly a cat to start with...

In a process called "decoherence" quantum states of objects are in general almost immediately destroyed by their coupling to the environment. In atom experiments, the interaction of the atoms with their thermal environment is drastically reduced by performing experiments in ultra-high vacuum, where particles are trapped by optical, magnetic or electric means, such that only the coupling to these fields (and potentially particle-particle interaction) is relevant, but no thermal contact to the environment is present. Additionally, due to the extremely low mass of a single atom, laser cooling is very efficient as already an individual optical photon affects its motion significantly. Finally, also their zero point motion in a trap is large as compared to a massive object.

Unless being trapped by optical tweezers, as recently suggested [22], macroscopic objects are in general not very well decoupled from their environment, such that heating from the thermal bath via the support structure is competing with any cooling mechanism acting on the object. The countless number of mechanical degrees of freedom that are in some way all coupled to this environment renders ground state cooling of the whole object a vain endeavor. However, if restricted to a single mechanical mode that is well isolated from the environment and from the other mechanical modes of the structure (i.e. it has a sufficiently high quality factor), cooling into the quantum regime has come into reach in the past years. Obviously, cooling of only one mechanical mode brings the object out of thermal equilibrium and the term “temperature”, which is related to the mean kinetic energy contained in all modes, then needs to be replaced by “effective temperature”, related now to the mean kinetic energy remaining in the very mechanical mode, while the temperature of the sample is mainly unaffected.

Cooling can be achieved in a way very similar to the atomic case by shining in a red-detuned laser into an optical cavity that is coupled to a mechanical mode via the radiation pressure force. Here, the optical cavity takes over the role of the atom’s internal electronic resonance. Progress in micro- and nanofabrication has allowed to create such structures, that are combining high quality factor optical and mechanical degrees of freedom—an overview will be given in section 1.2.1. The whole field of “cavity optomechanics”, which was only named in 2007 [23], emerged. Meanwhile, read-out sensitivities sufficient to monitor the zero-point motion of the mechanics [24, 25] and cooling of a mechanical oscillator [26, 27, 28] close to its quantum ground state [29, 30, 31] have been demonstrated recently, yet, to gain full control over its quantum-state and to be able to manipulate and read-out quantum states of mechanical motion by optical means is still an outstanding goal.

This thesis describes the efforts made to gain a detailed understanding of cavity optomechanics with fused silica microtoroids, involving high-sensitivity read-out, cooling close to their motional ground-state and bringing them into a regime, where quantum-coherent coupling enables to control the quantum-state of a macroscopic mechanical object.

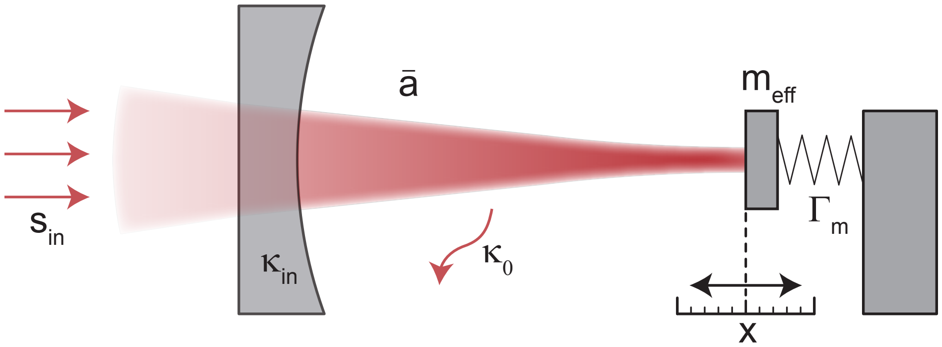

Figure 1.1: **The generic optomechanical system** consists of a Fabry-Pérot cavity, where one endmirror is harmonically suspended and free to move (indicated by the spring), the other one serving as in- and outcoupling mirror. The physics of this system can be characterized by the optical ($\kappa = \kappa_0 + \kappa_{\mathrm{in}}$, including in-/outcoupling and intrinsic) and mechanical (Γ_{m}) loss rates, their respective resonance frequencies ω_{c} and Ω_{m}, the mechanical mass of the moving mirror m_{eff}, as well as an incoming light field of frequency ω_l (corresponding to a detuning $\Delta = \omega_{\mathrm{l}} - \omega_{\mathrm{c}}$) and amplitude s_{in}, which gives rise to an intracavity field $\bar{a}$.

1.1 Cavity Optomechanics

A generic optomechanical system is depicted in Fig. 1.1. It consists of a Fabry-Pérot cavity, with one of the two end-mirrors being suspended by a mechanical spring such that it forms a harmonic oscillator and the other one acting as an in- and outcoupling mirror. Any mechanical displacement of the suspended mirror affects the length of the optical resonator and thus its resonance frequency. If light is coupled into this cavity the optical standing wave is obviously affected by any mechanical motion. At the same time, the radiation pressure force exerted by the circulating light acts on the mechanical oscillator. Due to the finite build-up / decay time of the field inside the cavity the radiation pressure force is not necessarily in phase with the mechanical motion, but can—depending on the laser's detuning and power as well as the optomechanical system's properties—affect the motional state of the mechanical resonator. This is known as "dynamical backaction".

1.1.1 Optomechanical Hamiltonian

An optomechanical system can be characterized by a mechanical (Ω_m) and optical (ω_{c}) angular resonance frequency, a coupling to their respective environment ("energy decay rates" Γ_{m} and $\kappa = \kappa_0 + \kappa_{\mathrm{ex}}$) an effective mechanical mass m_{eff} of the mechanical oscillator and a mutual optomechanical coupling rate G. Here, κ denotes the total optical decay rate that is constituted by a coupling to a waveguide (κ_{ex}) and intrinsic losses of the cavity (κ_0), related to absorption and scattering. G expresses the change of the optical resonance frequency as a function of the mirror displacement x and can thus be written as $G = \mathrm{d}\omega_\mathrm{c}/\mathrm{d}x$.

If the free spectral range of the cavity is much larger than the mechanical oscillation frequency, multimode interaction can be neglected, and the optomechanical Hamiltonian of an ideal optomechanical system ($\kappa_0 = \Gamma_m = 0$) can be written as

$$\hat{H} = \hat{H}_\mathrm{mech} + \hat{H}_\mathrm{opt} + \hat{H}_\mathrm{int} + \hat{H}_\mathrm{drive} \tag{1.1}$$

$$\hat{H}_\mathrm{mech} = \frac{\hat{p}^2}{2m_\mathrm{eff}} + \frac{1}{2}m_\mathrm{eff}\Omega_\mathrm{m}^2\hat{x}^2 \tag{1.2}$$

$$\hat{H}_\mathrm{opt} = \hbar\omega_\mathrm{c}\left(\hat{a}^\dagger\hat{a} + \frac{1}{2}\right) \tag{1.3}$$

$$\hat{H}_\mathrm{int} = \hbar G\hat{x}\,\hat{a}^\dagger\hat{a} \tag{1.4}$$

$$\hat{H}_\mathrm{drive} = i\hbar\,\sqrt{\eta_\mathrm{c}\kappa}\left(\hat{s}_\mathrm{in}(t)\hat{a}^\dagger - \hat{s}_\mathrm{in}^\dagger(t)\hat{a}\right), \tag{1.5}$$

where $\hat{x}$ and $\hat{p}$ are the position and momentum operators of the mechanical degree of freedom and $s_\mathrm{in}(t)$ is the drive amplitude normalized to a photon flux at the input of the cavity. $\hat{a}$ and $\hat{a}^\dagger$ are the annihilation and creation operators of the cavity mode. Furthermore the coupling parameter $\eta_\mathrm{c} \equiv \kappa_\mathrm{ex}/(\kappa_0 + \kappa_\mathrm{ex})$ has been introduced. It will be shown later (cf. section 2.1) that the parameter η_c can be continuously adjusted in our experiment. Based on eq. (1.1) the quantum Langevin equations governing the dynamics of an optomechanical system can be derived [32, 33, 34]. In a frame rotating at the laser frequency ω_l with a laser detuned by $\Delta = \omega_\mathrm{l} - \omega_\mathrm{c}$ relative to the cavity resonance frequency, we obtain:

$$\frac{d}{dt}\hat{a}(t) = \left(+i\Delta - \frac{\kappa}{2}\right)\hat{a}(t) - iG\hat{x}(t)\hat{a}(t) + \sqrt{\eta_\mathrm{c}\kappa}\,\hat{s}_\mathrm{in}(t) + \sqrt{(1-\eta_\mathrm{c})\kappa}\,\delta\hat{s}_\mathrm{vac}(t) \tag{1.6}$$

$$\frac{d}{dt}\hat{x}(t) = \frac{\hat{p}(t)}{m_\mathrm{eff}} \tag{1.7}$$

$$\frac{d}{dt}\hat{p}(t) = -m_\mathrm{eff}\Omega_\mathrm{m}^2\hat{x}(t) - \hbar G\hat{a}^\dagger(t)\hat{a}(t) - \Gamma_\mathrm{m}\hat{p}(t) + \delta\hat{F}_\mathrm{th}(t), \tag{1.8}$$

where $\delta\hat{s}_\mathrm{vac}(t)$ and $\delta\hat{F}_\mathrm{th}(t)$ are the quantum and thermal noise terms [35]. The decay rates for the optical (κ) and mechanical oscillators (Γ_m) have been introduced classically.

While here only some basic conclusions will be presented in a qualitative manner, a detailed derivation can be found together with the corresponding experimental results in sections 4.1, 4.2 and 4.3. This includes appropriate approximations, experimental settings and some more technical details that need to be added before these equations can be applied for interpretation of the obtained results.

1.2 Cavity Optomechanics - Experimental Realizations

1.2.1 Overview of existing systems

During the last few years a vast number of optomechanical systems has been developed in many different groups all over the world. Basically five different types can be identified (refer to Fig. 1.2):

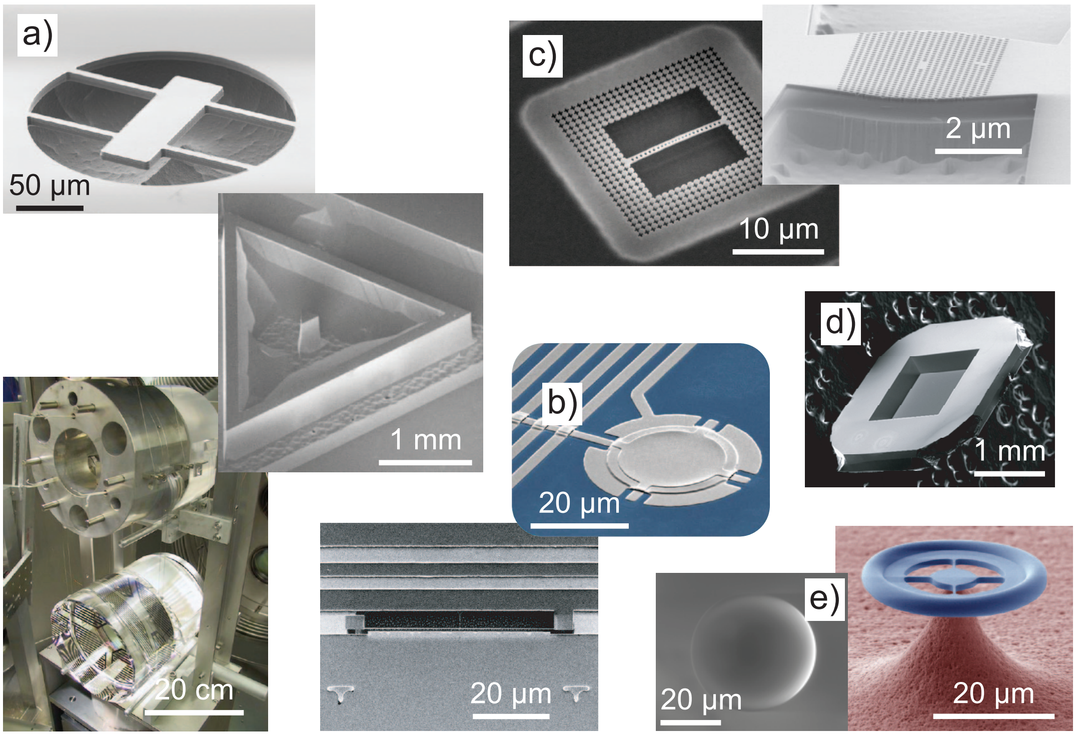

Figure 1.2: **Zoo of optomechanical systems.** a) Fabry-Pérot-type systems with masses from ng to several kg *(top to bottom: [36, 37, 38])* b) Optomechanics in the microwave domain *(top to bottom: [39, 37])* c) 1D and 2D photonic crystal cavities *(left to right: [31, 40])* d) Membrane in the middle *[41, 42]* e) Whispering gallery mode type *(left to right: [43, 3])*

- *Fabry-Pérot type:* Here, very similar to the generic scheme depicted in Fig. 1.1, one endmirror of a Fabry-Pérot cavity is free to move or vibrate. The largest optomechanical systems are gravitational wave detectors, where suspended mirrors weighing up to 10 kg are currently used [36, 37, 38].
- *Superconducting microwave resonators:* A very similar system can be obtained by integrating a mechanical oscillator into a microwave resonator. Here, mechanical motion is changing the (total) capacity of the resonator and, as a consequence, its frequency [39, 37].
- *Photonic crystal cavities:* In suspended photonic crystal cavities, optical modes

can couple to mechanical modes of the entire structure, or to localized modes, that typically show very high optomechanical coupling rates and frequencies in the low GHz range [31, 40].

- *Membrane in the middle:* Here, a dielectric, partly reflective membrane is brought into a Fabry-Pérot cavity. Depending on its exact positioning, a linear (if placed in an antinode of the optical standing wave) or quadratic coupling (if placed in a node, i.e. the cavity frequency is to first order not shifted if the membrane moves) can be obtained [41, 42].

- *Whispering gallery mode cavities:* Optical resonators that have a toroidal or spherical shape, where light is guided by total internal reflections and parametrically coupled to mechanical eigenmodes of the structure, that affect the optical path length [43, 3]. Alternatively, independent mechanical resonators can be coupled to the optical degree of freedom by bringing them into the near-field [44, 45].

In all of these schemes optical and mechanical degrees of freedom are coupled parametrically and the above equation (1.1) applies. A different approach with the goal of controlling the quantum state of a mechanical resonator was pursued in the group of A. Cleland, where a piezoelectrical mechanical resonator with GHz frequencies was resonantly coupled to a microwave resonator [29]. Here, cooling to the mechanical groundstate can be achieved in a conventional cryostat.

1.2.2 Fused silica microtoroids

For this work toroidal silica microresonators as depicted in Fig. 1.3 have been used exclusively. These show ultra-high quality factor optical resonances of the whispering gallery mode type as illustrated in Fig. 1.3d. Quality factors of 10^8 are routinely achieved, corresponding to a finesse of about 10^6. Additionally, the optical mode volumes are small. In principle any mechanical mode that modifies the optical path length (see Fig. 1.5) can be used for optomechanics experiments. However, the so-called radial-breathing modes (Figs. 1.3d and 1.5) at several tens of MHz are the most suitable. The reason is that this mode, which shows mostly radial displacement of the structure, can in principle be well decoupled from the substrate, thus yielding high mechanical quality factors in excess of 10000. Additionally, this mechanical mode maximally affects the optical pathlength leading to a large optomechanical coupling rate.

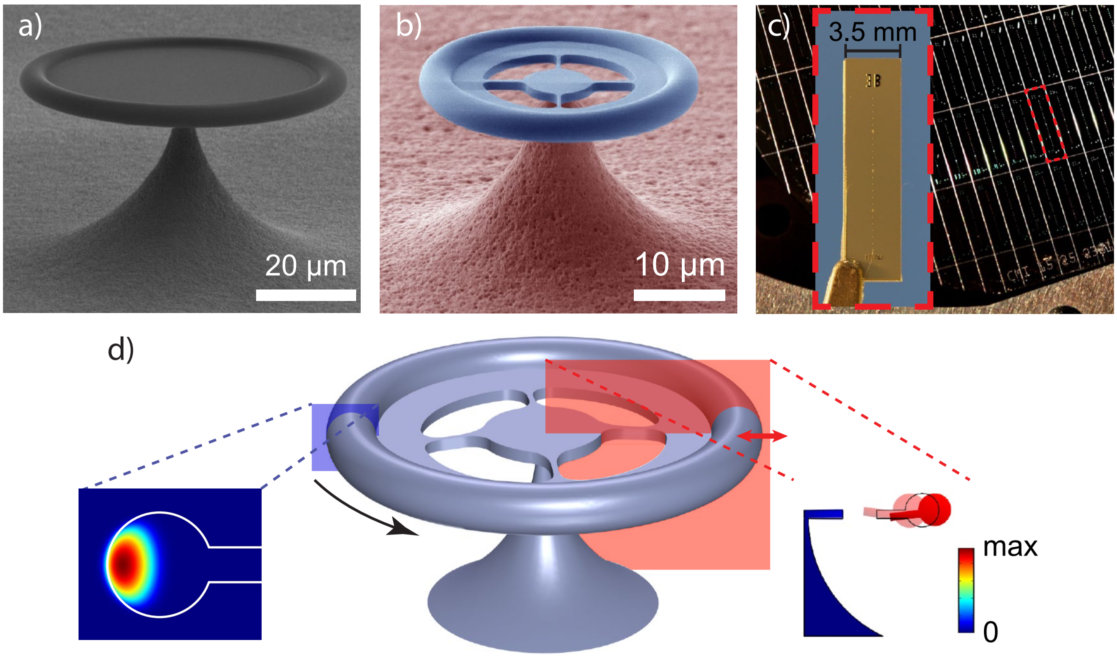

Figure 1.3: **Toroidal microresonators.** *a)* shows a conventional silica microtoroid residing on a silicon substrate, *b)* shows a spokes supported microtoroid as used towards the end of this thesis. Note the large difference in dimensions. *c)* shows a part of a 4” silicon wafer carrying many individual chips (red dashed line), every chip contains typically 20 resonators aligned in a row in the center of the chip. *d)* On the *left* a mode profile of an optical whispering gallery mode obtained by finite element analysis is shown. The *right* illustrates the mechanical radial breathing mode in a spoke-supported toroid.

Modal splitting of optical resonances

In ideal WGM resonators, two degenerate counterpropagating optical modes exist. If light is coupled to one of the two, it will circulate in only one direction and no standing wave is formed (in contrast to Fabry-Pérot cavities). In real resonators, however, already minor defects can lead to scattering to the counterpropagating mode, which lifts the degeneracy and leads to a modal splitting. This splitting appears as two distinct absorption dips in a spectroscopy experiment. As will be detailed in section 3.4, especially particles bound to the surface of a WGM resonator induce such a modal splitting [46, 47]. This effect has been taken into account and mathematically modeled in sections 4.1 and 4.2.

1.2.3 Optomechanical coupling rate and effective mass

While there is a straightforward way of defining the mechanical mass and its displacement for the generic optomechanical scheme as depicted in Fig. 1.1, this is no longer the case for many of the systems shown in section 1.2.1, e.g. for localized modes in photonic crystal cavities. For microtoroids, we choose to define the optomechanical coupling rate in eq. (1.4) by $G = \frac{d\omega_\mathrm{c}}{dx}|_{x=r}$, describing the optical resonance frequency shift for a small displacement x in radial direction. It is evaluated at the outermost rim (r is the radius of the structure), i.e. the point of maximum displacement for a RBM. As the radial displacement is varying in radial direction, this choice is somewhat arbitrary. The choice fixes the definition of the “effective mass” of the particular mechanical mode, as the mean energy $\bar{E}$ stored within this mechanical mode must still be given by $\bar{E} = \frac{1}{2} m_\mathrm{eff} \Omega_\mathrm{m}^2 \langle x^2 \rangle$. As shown in [48], such ambiguities in the definition of G and m_eff can be avoided by considering the vacuum optomechanical coupling rate $g_0 = G x_\mathrm{ZPM}$ (with the zero point motion $x_\mathrm{ZPM} = \sqrt{\hbar/2 m_\mathrm{eff} \Omega_\mathrm{m}}$), that does no longer depend on the concrete choice of x. Additionally, Gorodetsky *et al.* [48] present a scheme that allows to accurately determine g_0 of an optomechanical system by applying a phase-modulation of well-known absolute modulation depth. This scheme has been used for all characterization measurements performed at EPFL.

1.3 High-sensitivity readout of mechanical motion

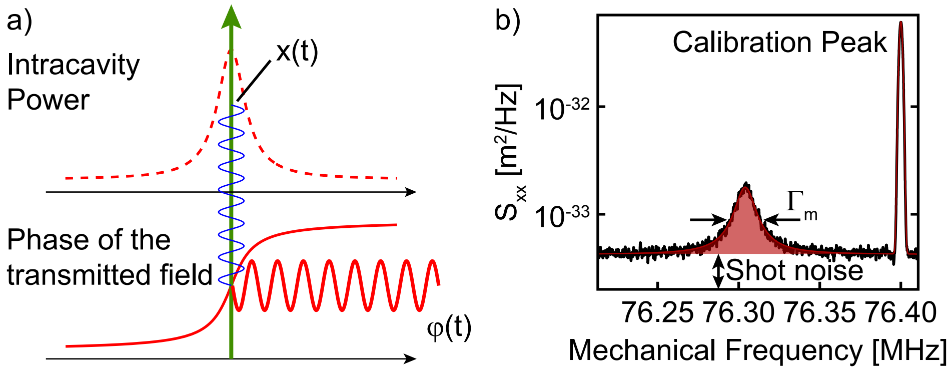

Figure 1.4: **Resonant Readout of mechanical motion.** *a)* Here, the Lorentzian lineshape *(top)* and the phase response *(bottom)* as a function of the laser detuning are depicted. The amplitude of the transmission of a resonant laser is to first order not affected by mechanical motion. However, it is transduced into a phase modulation imprinted onto the laser used for probing the mechanics. If the output signal is directed onto a phase sensitive detection scheme, a mechanical spectrum as shown in *b)* is obtained. Mechanical resonance frequency and linewidth are easily determined. Adding an additional phase calibration tone (here: at 76.40 MHz) of known modulation depth, the vertical axis can be recalibrated as a noise spectral density S_xx. The area under the curve (red filling) is proportional to the effective temperature of the mode and the background is (in this measurement) dominated by shot noise.

A mechanical displacement x of the mechanical degree of freedom in an optomechanical system changes the optical resonance frequency by $\Delta\omega_\mathrm{c} = Gx$. Thermal Brownian motion of a mechanical mode thus causes fluctuations of the optical resonance frequency ω_c (see Fig. 1.4a for illustration).

A laser coupled to the resonator experiences a phase modulation and one can recover a mechanical noise spectrum using a phase sensitive measurement setup and an electronic spectrum analyzer (ESA). Fig. 1.4b shows such a spectrum for a microtoroid. The mechanical resonance frequency Ω_m and linewidth Γ_m are easily extracted from the graph. An additional feature is the so-called "calibration peak" that will be introduced in the following.

The displacement fluctuations of the mechanical mode can be described as a noise spectral density [49, 50, 51, 48]:

$$S_{xx}(\Omega) \approx \frac{1}{m_\mathrm{eff}} \frac{2\Gamma_\mathrm{m} k_\mathrm{B} T}{(\Omega^2 - \Omega_\mathrm{m}^2)^2 + \Gamma_\mathrm{m}^2 \Omega^2} \tag{1.9}$$

with the temperature of the bath T and Boltzmann's constant k_B. The fluctuations of the cavity resonance frequency are then linked via:

$$S_{\omega\omega}(\Omega) = G^2 S_{xx}(\Omega) \approx g_0^2 \frac{2\Omega_\mathrm{m}}{\hbar} \frac{2\Gamma_\mathrm{m} k_\mathrm{B} T}{(\Omega^2 - \Omega_\mathrm{m}^2)^2 + \Gamma_\mathrm{m}^2 \Omega^2}. \tag{1.10}$$

Integrating this relation yields:

$$\left\langle \delta\omega_\mathrm{c}^2 \right\rangle = \int_{-\infty}^{+\infty} S_{\omega\omega}(\Omega) \frac{\mathrm{d}\Omega}{2\pi} = 2 \left\langle n_\mathrm{m} \right\rangle g_0^2, \tag{1.11}$$

with the mean phonon occupancy of the mechanical mode $\langle n_\mathrm{m} \rangle$. As a consequence, the integrated spectral density gives access to the mechanical mode's (effective) temperature.

If light is coupled to the cavity, the intra-cavity field experiences a phase modulation. The corresponding spectral density is related to eq. (1.10) via $S_{\Phi\Phi}(\Omega) = S_{\omega\omega}(\Omega)/\Omega^2$. The absolute intra-cavity phase modulation depth is in general difficult to measure with high accuracy as its transduction onto the transmitted laser depends on the exact coupling conditions between optical mode and tapered fiber (e.g. detuning, optical linewidth and coupling coefficient, input power,...). Instead, it can be proven mathematically [52], that the transduction of a classical coherent phase modulation added to the probe laser in the vicinity of the mechanical resonance frequency ("calibration peak") is equal to the transduction of mechanical motion, as long as the optomechanical coupling is weak [53, 3].

This allows first to compare spectra obtained under varying experimental conditions if divided by the area under the calibration peak[1]. Second, spectra obtained on a

---

[1] If normalized to the amplitude of the calibration peak, the resolution bandwidth (RBW) of the spectrum analyzer, which is chosen to be narrow as compared to the mechanical linewidth, needs to be taken into account additionally. The maximum value of the coherent calibration peak is constant independently of the chosen RBW, whereas the incoherent signal amplitude scales proportionally to the RBW and so does the calibration peak's width,

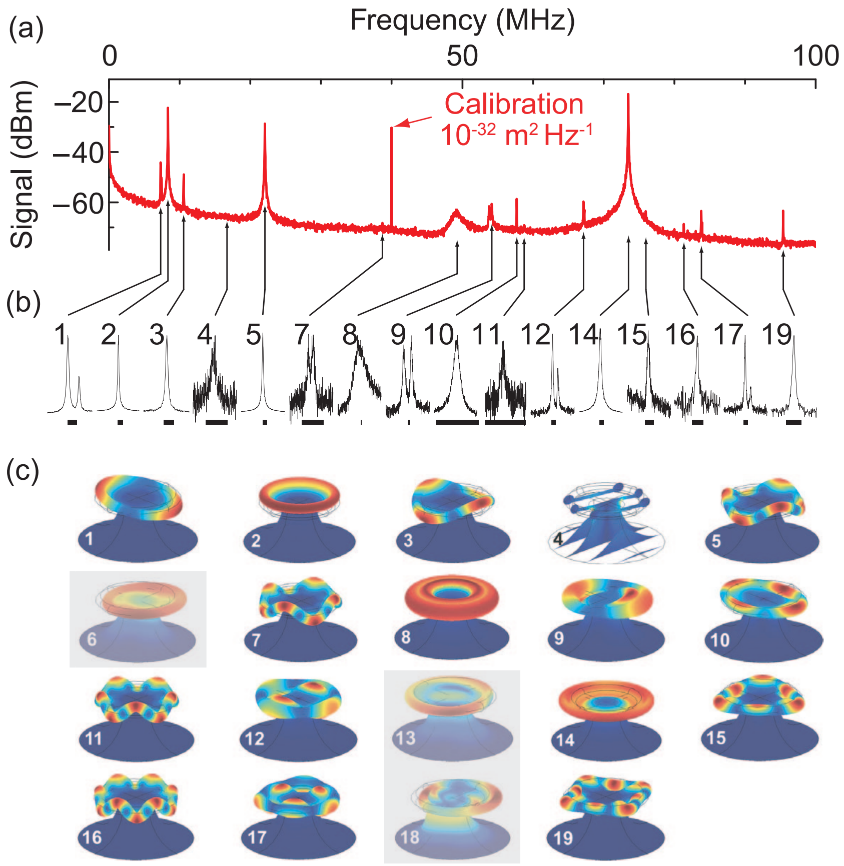

Figure 1.5: **Mechanical modes found in microtoroids.** As mentioned earlier, the RBM *#14* is only one out of many mechanical modes present in toroids. All others, though, show a much weaker optomechanical coupling (i.e. inferior signal-to-noise). The different peaks in *a)* are magnified in *b)* and can be identified using finite-element-simulation to the mechanical modes depicted in *c)*. # 6, 13 and 18 are coupled to the light too weakly to be seen. The bar below each spectrum in *b)* indicates a 100 kHz frequency span *(adapted from [54])*

spectrum analyzer can be converted between the different noise spectral densities mentioned before[2]. Fig. 1.4b has been recalibrated in this way using the displacement spectral density S_{xx}.

Finally, from eq. (1.11) one can also determine g_0 if the mechanical resonance frequency, $\langle n_\mathrm{m} \rangle$ (which can be derived from the ambient temperature, assuming good thermalization) and the absolute phase modulation depth of the calibration sideband are known. Here, these measurements are done at room temperature with an overcoupled resonance at very low input power levels in order to minimally affect the mode's effective temperature.

---

i.e. area.

[2] Conversion to the displacement spectral density requires the radius of the structure, that is most easily obtained using a calibrated microscope.

Using an appropriate measurement scheme (see section 2.2), very large sensitivities can be achieved, that are only limited by the laws of quantum mechanics. Two effects limit the best possible sensitivity for a resonant measurement: On the one hand laser shot-noise, whose equivalent displacement noise spectral density scales inversely to the injected power, such that increasing the laser power also increases the signal to noise. On the other hand, quantum fluctuations of the light used to measure the mechanical motion drive the oscillator—an effect known as "measurement backaction". The equivalent displacement spectral density of this effect scales linearly with the probing power. The sum of these two contributions constitutes the background in an ideal experiment and optimal sensitivity is reached at its minimum, which is also referred to as the "standard quantum-limit" (SQL). The corresponding background at the mechanical frequency expressed as a displacement spectral density is given by [52]

$$S_{xx}^{\mathrm{SQL}}(\Omega_{\mathrm{m}}) = \frac{1}{\sqrt{\eta_{\mathrm{c}}}} \frac{\hbar}{m_{\mathrm{eff}}\Gamma_{\mathrm{m}}\Omega_{\mathrm{m}}}, \tag{1.12}$$

For a resonant quantum-limited measurement the expected signal-to-noise ratio for a mechanical oscillator in its ground-state is unity.

In practice, with a laser tuned to the red mechanical sideband, we are always limited by the shot noise background that can be expressed in the limit of resolved sidebands ($\Omega_{\mathrm{m}} \gg \kappa$) as an equivalent displacement spectral density:

$$S_{xx}(\Omega_{\mathrm{m}}) = \frac{\Omega_{\mathrm{m}}^2}{4\eta_{\mathrm{c}}^2 G^2} \frac{\hbar\omega_{\mathrm{l}}}{P_{\mathrm{in}}}. \tag{1.13}$$

Here, the shot noise background is a factor of four larger than for resonant probing. For parameters $[\Omega_{\mathrm{m}}/2\pi,\ \omega_{\mathrm{l}}/2\pi,\ G/2\pi] = [78.2\,\mathrm{MHz},\ 385\,\mathrm{THz},\ 25\,\mathrm{GHz/nm}]$ as achieved in [3], assuming critical coupling ($\eta_{\mathrm{c}} = 1/2$) and an input power of $P_{\mathrm{in}} = 1\,\mathrm{mW}$ a shot noise level of $\sqrt{S_{xx}(\Omega_{\mathrm{m}})} = 5 \times 10^{-20}\,\mathrm{m\,Hz^{-\frac{1}{2}}}$ is expected and a sensitivity $\sqrt{S_{xx}^{\mathrm{exp}}(\Omega_{\mathrm{m}})} < 10^{-19}\,\mathrm{m\,Hz^{-\frac{1}{2}}}$ is shown.

Obviously, any classical laser noise at the Fourier frequencies of interest is added to the background and reduces sensitivity. As a consequence shot-noise limited laser sources at the frequencies and power level of interest and an appropriate detection scheme are required for ultimate sensitivities.

Finally, a high-resolution wide-band mechanical noise spectrum of a conventional toroid is depicted in Fig. 1.5. The RBM is clearly visible, as well as a vast number of other mechanical modes, that can be identified with the help of finite-element simulation.

1.4 Laser sideband cooling of a mechanical oscillator

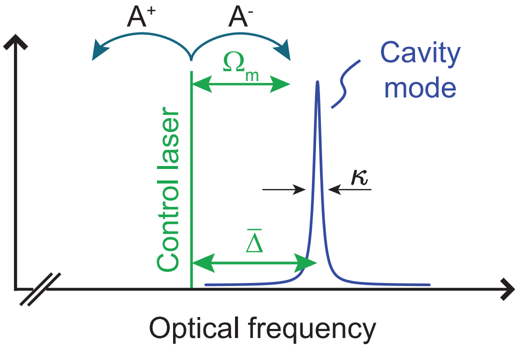
A+
A-
Ω_m
Cavity mode
Control laser
κ
$\bar{\Delta}$
Optical frequency

Figure 1.6: **Resolved sideband cooling of a mechanical oscillator.** Refer to text for details.

Similar to laser cooling of atoms or ions, mechanical modes in optomechanical systems can be cooled by red-detuning the laser from the cavity resonance frequency. One can distinguish two regimes. In the so-called bad-cavity limit, the optical linewidth exceeds the mechanical frequency. It can be shown that ground-state cooling is not possible in this regime [55, 56, 57], as the fluctuations of the cooling field provide a significant driving of the mechanical motion, as compared to the cooling effect. However, once Ω_{m} exceeds κ—a limit referred to as the resolved-sideband regime—ground-state cooling becomes (theoretically) possible; this situation is depicted in Fig. 1.6. If the laser's detuning $\bar{\Delta} = \omega_{\mathrm{l}} - \omega_{\mathrm{c}}$ is equal to $-\Omega_{\mathrm{m}}$ (i.e., the laser resides on the red "mechanical sideband" of the cavity), Stokes scattering processes occurring at a rate A^{-} are resonantly enhanced as compared to Anti-Stokes processes (A^{+}). As a result, phonons are removed from the mechanical resonator and lost into the optical field, leading to a net cooling of the mechanics.

In an alternative picture one can also think of the process as an optical and mechanical degree of freedom, that are exchanging quanta at a rate $\Omega_{\mathrm{c}} = 2\sqrt{\bar{n}_{\mathrm{c}}}g_0$, where

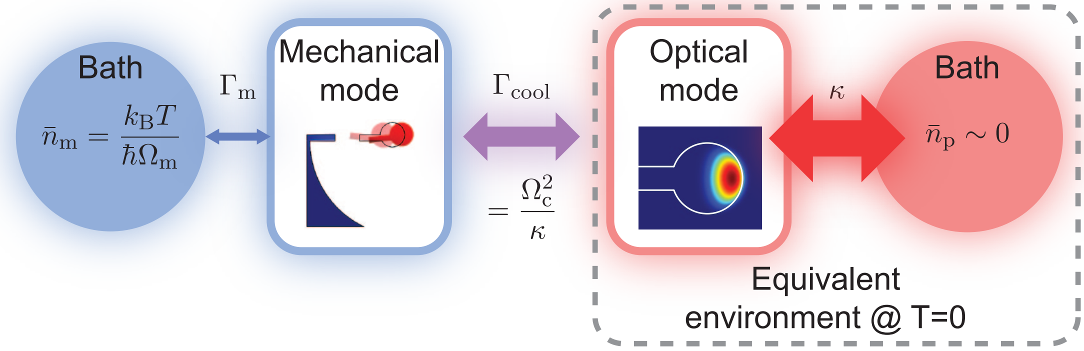
Bath
$\bar{n}_{\mathrm{m}} = \frac{k_{\mathrm{B}}T}{\hbar\Omega_{\mathrm{m}}}$
Γ_{m}
Mechanical mode
Γ_{cool}
$= \frac{\Omega_{\mathrm{c}}^2}{\kappa}$
Optical mode
κ
Bath
$\bar{n}_{\mathrm{p}} \sim 0$
Equivalent environment @ T=0

Figure 1.7: **Sideband cooling in a thermal bath picture.** Refer to text for details

$\bar{n}_\mathrm{c}$ is the mean number of photons in the cavity. While the environment has a mean occupancy $\bar{n}_\mathrm{m} \gg 0$, the environment that the displaced optical field is coupled to is, due to the high optical frequencies in its groundstate. Obviously, a shot noise limited laser source is required to fulfill this, as any classical noise would correspond to a non-zero occupancy, and thus prevent ground-state cooling. For a more detailed analysis, refer to [58]. The mechanical mode exchanges energy at the same time with its environment at a rate Γ_m and with the optical mode at rate Γ_cool. This in turn dissipates any excitation into its cold environment at a rate of κ. If $\Gamma_\mathrm{cool} \ll \kappa$, this means that any excitation transferred into the optical mode is lost leading to an effective cooling of the mechanical degree of freedom. Once the optomechanical coupling rate becomes similar to the optical decay rate, excitations are rather written back into the mechanical domain than dissipated and one enters the regime of strong coupling, which will be discussed in detail in section 4.3.

1.5 Optical response of an optomechanical system

One major experimental advance was the implementation of what we call a “sideband sweep”. The idea is to do optical spectroscopy of the optical resonance with a weak laser (“probe”), while simultaneously performing a cooling experiment with a stronger laser (“pump”). Therefore, a second laser line needs to be swept across the optical mode as depicted in Fig. 1.8. Instead of using a second laser source, that would need to be phase locked to the pump laser, a phase modulator is used to generate symmetric sidebands. The second sideband (far detuned from the optical cavity) does not interact with the cavity, and can thus be neglected. Spectroscopy is performed by sweeping the RF frequency sent to the phase modulator. On resonance, the signal is lost into the cavity and thus an absorption signal can be recovered in transmission. Demodulation of the transmitted signal is readily done with a network analyzer.

This technique allowed for the first time to accurately determine the laser’s detuning during our experiments. Moreover, the beating signal of pump and probe also gives rise to a further phenomenon named optomechanically induced transparency (OMIT) - the optomechanical analog of electromagnetically induced transparency (EIT).

1.5.1 Optomechanically induced transparency

While a full theoretical model will be developed in section 4.1, here an intuitive picture of the phenomenon is presented. A weak probe, that is scanned across the optical mode of a toroid experiences absorption when hitting the resonance. Now, a strong pump is added and tuned to the red mechanical sideband (cf. Figs. 1.8 and 1.9). While

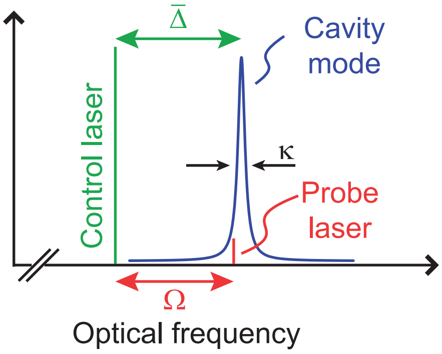
$\bar{\Delta}$
Cavity mode
Control laser
κ
Probe laser
Ω
Optical frequency

Figure 1.8: **Optical response scheme.** A strong pump residing in the vicinity of the red mechanical sideband cools the mechanical resonator, while a second swept laser beam probes the optical response. This allows to determine the pump laser's exact detuning. In practice, the second laser beam is generated using a phase modulator that adds a weak sideband to the pump.

the probe's transmission is still mostly unchanged off resonance, there is an important difference exactly on resonance. Here, the beating signal frequency of pump and probe coincides with the mechanical resonance frequency Ω_m. The corresponding modulation of the intra-cavity radiation pressure force drives the mechanical mode. The resulting mechanical motion in turn modulates the pump, creating a sideband, that is degenerate with the probe beam, but phase shifted by π leading to destructive interference. As a consequence, a transparency window opens, that depends on the pump's power, where unity transmission can be achieved.

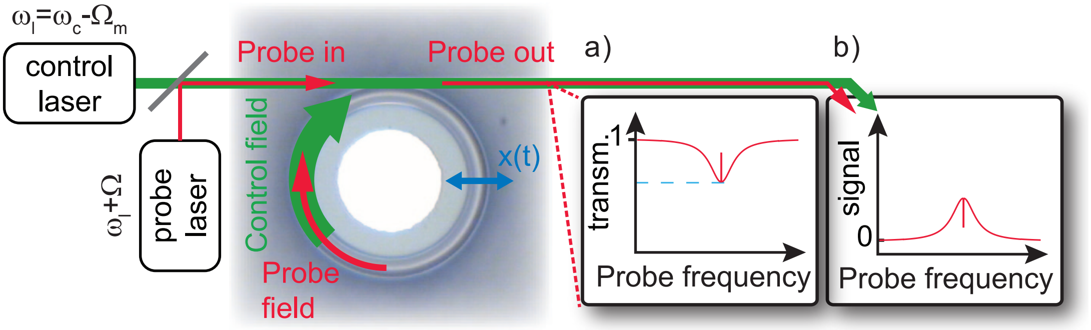
ω_l=ω_c-Ω_m
control laser
ω_l+Ω
probe laser
Probe in
Probe out
Control field
Probe field
x(t)
a)
b)
transm.
1
Probe frequency
signal
0
Probe frequency

Figure 1.9: **Optomechanically induced transparency.** A laser beam tuned to the red mechanical sideband (i.e. $\omega_l = \omega_c - \Omega_m$), while a weak probe sweeps across the optical resonance ($\omega_l + \Omega$, where Ω is varied). Optomechanically induced transparency gives rise to a transparency window on resonance shown in *a). b)* Due to the homodyne measurement scheme, rather a signal corresponding to the absorption is probed.

It will also be shown in section 4.1, that this phenomenon obeys equivalent equations of motion as compared to the effect of EIT found in atomic vapors.

1.6 Outline

In chapter 2 basic experimental techniques are introduced and the optical and cryogenic setup are described. In particular, different schemes that allow to read-out mechanical motion, to calibrate mechanical spectra and to accurately determine the detuning of the laser are shown. Chapter 3 contains particularities encountered when performing cryogenic experiments with silica microtoroids. It is shown, that it is of great importance to choose the right wavelength for cooling experiments and highlights the major influence of two level fluctuators onto the mechanical properties of the resonators. The latter, in combination with spurious heating of the samples, also limits the maximum achievable cooling, which triggered the development of novel spokes-supported structures. In addition, it is shown that mechanical modes of optical fibers can affect the cooling and measurement process. Finally, chapter 4 summarizes the three major results obtained during this thesis. Still at the Max Planck Institute of Quantum Optics, the first demonstration of optomechanically induced transparency [1] and cooling of a mechanical mode of a conventional toroid to around nine phonons [2] could be achieved. Drastic advances in sample design and experimental control after moving to the Ecole Polytechnique Fédérale de Lausanne allowed to push up the optomechanical coupling rate, now exceeding mechanical and optical dissipation (and decoherence!) rates. This regime of “quantum-coherent coupling” between optical and mechanical mode, was demonstrated for the first time in the optical domain and enables conversion of quantum states of light into the mechanical domain and back [3].

2 Experimental Setup

2.1 Spectroscopy of optical modes

An important step in the characterization of microresonators is to determine its optical properties, i.e. resonance frequencies (ω_c), corresponding optical line widths (κ_0) and potential modal splitting (cf. 1.2.2). Therefore, a fiber-coupled scanning external cavity diode laser (ECDL, New Focus Velocity models 6312 and 6330) is used that is coupled to the microtoroid using a tapered fiber [59, 60, 61, 52, 62]. Then, the transmitted absorption signal is captured by a photodiode. This setup is sketched in Fig. 2.1. The diode laser is used for its superior scanning speed and tuning range as compared to other laser systems, which provides a fast visual feedback on the oscilloscope.

Following the formalism introduced by Haus [63], the expected transmitted field amplitude $s_{\text{out}}(t)$ is related to the injected field amplitude $s_{\text{in}}(t)$ via

$$s_{\text{out}}(t) = s_{\text{in}}(t) - \sqrt{\eta_c \kappa}\, a(t) \tag{2.1}$$

with the intracavity field amplitude $a(t)$. For a constant driving, $s_{\text{in}}(t) = \bar{s}_{\text{in}}$ one can deduce a steady-state intracavity field amplitude[1] $a(t) = \bar{a} = \frac{1}{-i\Delta+\kappa/2}\sqrt{\eta_c\kappa}\,\bar{s}_{\text{in}}$. Thus, one expects an amplitude transmission of:

$$\frac{\bar{s}_{\text{out}}}{\bar{s}_{\text{in}}} = 1 - \frac{\eta_c \kappa}{-i\Delta + \kappa/2} \tag{2.2}$$

or a transmitted normalized power:

$$\frac{P_{\text{out}}}{P_{\text{in}}} = \left|\frac{\bar{s}_{\text{out}}}{\bar{s}_{\text{in}}}\right|^2 = 1 - \frac{\eta_c \kappa^2 (1-\eta_c)}{\Delta^2 + (\kappa/2)^2} \tag{2.3}$$

---

[1] Coupling to mechanical modes is omitted in this consideration.

This formula describes a Lorentzian dip of width κ with a transmission on resonance of $1-\frac{1}{4}\eta_c(1-\eta_c)$. For $\eta_c=\frac{1}{2}$, a minimum with a transmission of zero is reached. This coupling condition, where $\kappa_0=\kappa_{ex}$, is called “critical coupling”. A resonance is “undercoupled” (“overcoupled”) if $\kappa_0>\kappa_{ex}$, i.e. $\eta_c<\frac{1}{2}$ (if $\kappa_0<\kappa_{ex}$, i.e. $\eta_c>\frac{1}{2}$).

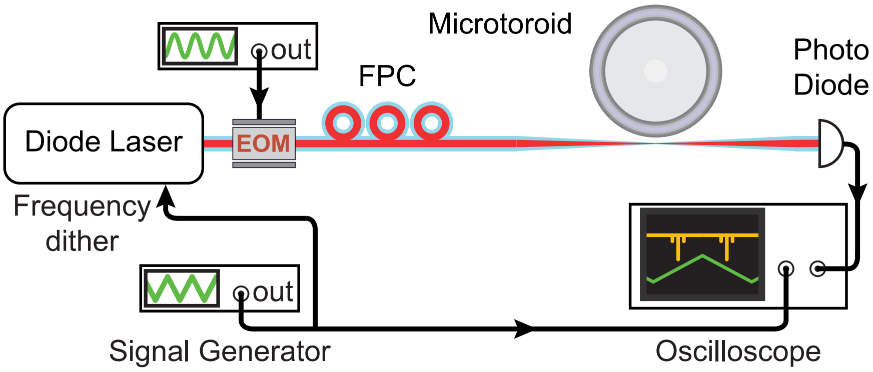

Figure 2.1: **Optical spectroscopy scheme.** This graph shows a basic setup permitting to search and analyze optical modes in toroids. An ECDL is dithered at typically 100 Hz with an amplitude corresponding to a few GHz. The laser light passes a fiber coupled phase modulator (“EOM”) that adds optical sidebands to the light. A fiber polarization controller (FPC) is used to match the polarization in the fiber to the optical mode’s. The transmitted light is captured by a photodiode and displayed on an oscilloscope. If a resonance is hit and the modulation frequency exceeds the optical linewidth, three absorption dips (originating from the center frequency and the two sidebands) are found. The toroid (or fiber) is aligned using piezo positioners.

Tapered fibers are fabricated by stripping off the buffer of a normal optical fiber (types 780HP at 780 nm and SMF28 at 1550 nm are used) and by pulling it above a hydrogen flame. Once the center of the pulled region is thin enough, the fiber becomes single mode (which was not the case during the pulling process) and a significant fraction of the light is guided in the evanescent field, while transmission can still exceed 99 %. Approaching a tapered fiber to a toroid, one can achieve overlapping of the evanescent field of the taper and the cavity mode. κ_{ex} depends on this overlap and can easily be tuned by changing the distance between toroid and fiber.

Fig. 2.2 shows spectra obtained in this way. The small dips on either side of the resonance are sidebands added (see Fig. 2.1) to the laser light (here: at $\omega_l/(2\pi)\pm$ 100 MHz) that serve as a calibration marker for the horizontal (“time”) axis. In order to obtain comparable results in general the unloaded (intrinsic) linewidth κ_0 is measured. This can be achieved in the limit where the coupling to the waveguide is very weak ($\eta_c\to 0$) and consequently $\kappa\to\kappa_0$. While instead for $\eta_c=1/2$ (“critical coupling”) one would expect a drop to zero transmission, this can only be achieved if polarization and propagation constants of the incident light is matched to that of the mode (“phase matching”). Close to perfect phase matching can be easily achieved by varying the

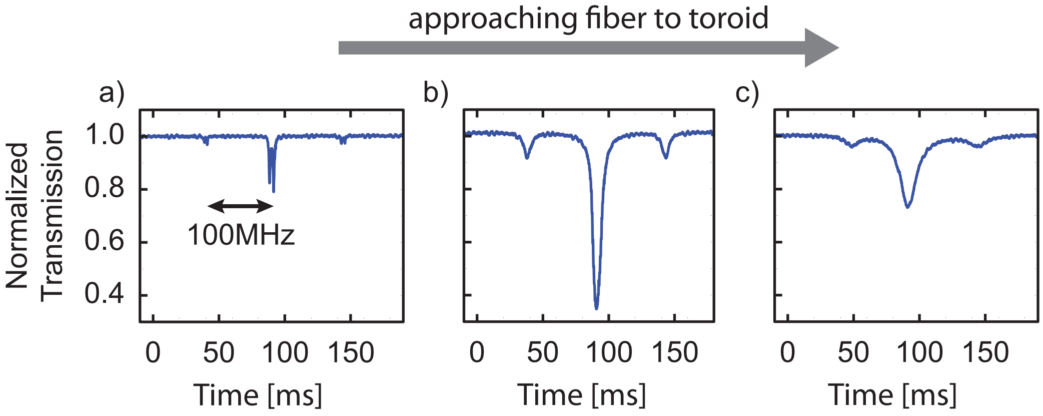

Figure 2.2: **Coupling Series.** Here, optical spectra, as obtained in a setup like depicted in Fig. 2.1, are shown. Optical sidebands have been added at $\omega_l \pm 100\,\text{MHz}$. From left to right the coupling is increased from *a)* "undercoupling" ($\kappa_{\text{ex}} < \kappa_0$) via *b)* "critical coupling" ($\kappa_{\text{ex}} = \kappa_0$) to *c)* "overcoupling" ($\kappa_{\text{ex}} > \kappa_0$). Using *a)*, an intrinsic linewidth of 2 MHz and a modal splitting of 6 MHz can be extracted for this particular resonance.

diameter of the tapered fiber, which is possible by moving the toroid along the fiber, as long as it is thin enough in the middle [64].

One obstacle in the accurate measurement of optical linewidths in this setup is the thermal bistabiliy [65] due to laser absorption in the material. Here, the resonators resonance frequency ω_c is no longer fixed, but needs to be expressed (to first order) as a function of its temperature:

$$\omega_c(T+\delta T) \approx \omega_c\left(1-\left(\alpha+\frac{1}{n}\frac{dn}{dT}\right)\delta T\right), \tag{2.4}$$

with the thermal expansion coefficient α and the refractive index n, where the change in temperature δT is proportional to the intracavity power. As a consequence, the resonance frequency reacts differently on a laser tuned to frequencies higher ("blue") or lower ("red") than ω_c. Depending on the sign of the coefficient $\alpha + \frac{1}{n}\frac{dn}{dT}$, a laser tuned to the red is shifting the resonance frequency away (if negative) or attracting the resonance frequency (if positive). In the first case, the red flank of the resonance is said to be "thermally stable", as a scanning laser (with increasing frequency) is pushing along the resonance leading to a thermal triangle (Fig. 2.3 shows an extreme version of this effect), and consequently thermal self-locking (locking of the toroid resonance frequency to the laser frequency) becomes possible (more details are contained in [52]). While at room temperature the blue side is stable, which makes cooling a very difficult thing to achieve, the effect changes sign at around 13 K [66], and thus facilitates cryogenic optomechanics experiments.

Consequently, accurate measurements can only be achieved in a limit of very low intracavity power, where the thermal effect can be neglected. At room temperature and room pressure, where thermalization to the environment is efficient, this is not really a limiting factor. In a cryostat at low pressure it is, however, close to impossible to measure linewidths accurately. Here, sideband sweeps as introduced in section 1.5 (see also section 2.4) can be used allowing to achieve very high signal-to-noise levels, while sending only tiny optical power levels to the cavity.

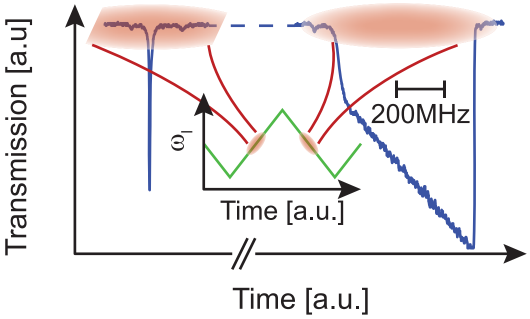

Figure 2.3: **Illustration of the thermal effect in toroids.** This graph shows the optical spectra of a toroid with an intrinsic linewidth of about 8 MHz and no significant modal splitting. For an unknown reason it showed particularly strong absorption losses (instead of scattering losses), leading to a huge thermal effect. The spectra were taken at room temperature and pressure at only around 5 μW of optical power. The left (right) dip appears when scanning from red to blue (blue to red) detuning, clearly demonstrating the significance of the thermally stable (self-locking) side (right) and the thermally instable side (left). The inset shows the lasers frequency versus time.

For most of the experiments shown in this thesis a Ti:Sapphire laser was used. Here the aforementioned scheme is also used for alignment of the fiber and determination of the resonance frequency. The wavelength of the Ti:Sapph laser is subsequently adjusted with the help of a Coherent WaveMaster wavelength meter. For fine-tuning, the two lasers are coinjected producing a beating signal which is well visible on the oscilloscope together with the optical resonance resulting from the (swept) diode laser.

As the tuning range of a Ti:Sapph laser is much larger that the free spectral range of microtoroids, the only criterion on the resonance frequency is to be as close as possible to 780 nm, the design wavelength of the optics setup (relevant especially for the employed waveplates). At an early stage of the experiment, however, when Koheras fiber lasers at around 1550 nm with their very limited tuning range (about 1 nm, to be compared to a free spectral range of about 10 nm) were used, the number of suitable resonances was strongly reduced and careful preselection was required. Besides such considerations, it is desirable to work with optical resonances that can be operated deeply in the resolved-sideband regime. Assuming mechanical resonance frequencies of about 80 MHz, a typical criterion is to only work with resonances of

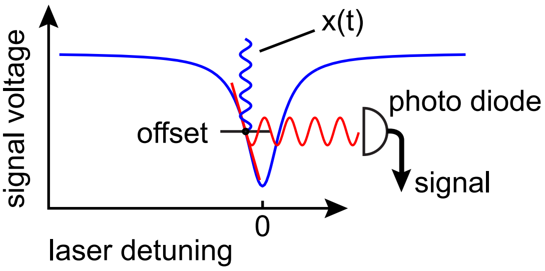

Figure 2.4: **Side-of-the-fringe detection.** Placing a laser on the flank of an optical resonance, a small mechanical vibration shifting the optical resonance is transduced into an amplitude modulation of the transmitted light that can be captured on a photo diode and analyzed on an electronic spectrum analyzer. Locking of a laser to this point is easily achieved by adding an offset as indicated to the signal and feeding back onto the laser's frequency modulation input.

linewidths (FWHM) that were significantly below 10 MHz; the same holds for modal splitting.

2.2 Detection of mechanical motion

Besides the previously presented coupling of a laser into the optical resonator, detection of mechanical motion is a key technology required to determine mechanical properties of microtoroids but also to determine the motional state of the mechanical resonator close to its quantum ground state. While the theoretical detection limits are discussed elsewhere (e.g. [67, 68, 69]), the focus will be put on the technical implementation and challenges in the following.

During this thesis several detection schemes of different complexity but also sensitivity have been implemented and used on a regular basis, depending on experimental requirements. These are quickly explained in the following together with their advantages and disadvantages.

2.2.1 Side of the fringe

A basic but very useful scheme is "side of the fringe" detection as sketched in Fig. 2.4. Here, the laser is detuned slightly off resonance. Mechanical motion is (partly) transduced into an amplitude modulation signal that can directly be observed in the photodiode current using a spectrum analyzer.

Locking the laser to resonance

The transmission signal can also directly be used to lock close to a resonance by applying an offset to the photodiode signal as sketched in Fig. 2.4. Obviously, the best error signal is obtained detuned by half the optical linewidth, whereas locking further off is getting more complicated. By definition, locking to a mechanical sideband in the deeply resolved sideband regime is not feasible.

Applications

This scheme is used routinely in the characterization of mechanical modes (their linewidths and vacuum optomechanical coupling rates) in a test setup in a vacuum chamber. Care has to be taken to make sure that the detuned laser is weak enough in order not to cause significant optical damping or driving, which typically requires power levels below 1μW. In order to still be able to see mechanical motion, one needs to surpass the electronic noise of the detection scheme, which for the required detection bandwidth of about 80 MHz is not feasible at these low optical powers. Therefore a low noise optical amplifier (erbium doped fiber amplifier, EDFA) in combination with a narrow-bandwidth optical filter is routinely used[2].

2.2.2 Pound-Drever-Hall detection

Fig. 2.5 shows the schematic of a Pound-Drever-Hall (PDH) detection scheme [70, 71]. Here the laser sent to the resonator is passing through a phase modulator driven at a radio frequency Ω_{mod} which is larger than the optical linewidth. The photodetector signal is demodulated using a frequency mixer with an in-phase local oscillator and low-pass filtered, giving rise to a DC error signal as depicted in Fig. 2.5. The non-zero slope on resonance, but also at $\omega_c \pm \Omega_{\mathrm{mod}}$ allows to detect a phase modulation imprinted onto the transmission signal. This detection scheme allows close to shot noise limited performance if the input laser power is sufficiently high (several mW) to surpass the electronic detector noise or if a low noise optical amplifier is used.

Locking the laser

Locking on resonance or slightly detuned (by adding an offset to the error signal) can be easily achieved. In principle also locking to the mechanical sideband can be done, if the modulation frequency is chosen to be close to the mechanical resonance frequency and by using the slope on the sideband for locking. However, as will be discussed at length in 4.1, the beating signal between carrier and sideband also

---

[2] Note that low noise optical amplifiers do not exist at 780nm, such that one is restricted to 1550nm laser light.

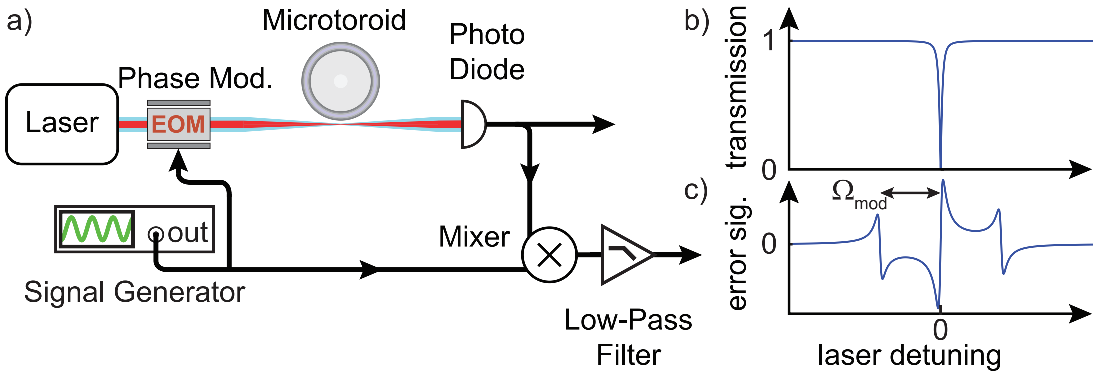

Figure 2.5: **Pound-Drever-Hall scheme.** *a)* shows the optical scheme, where sidebands at (typically) some frequency exceeding the optical linewidth is applied. The DC transmission signal of a scanning laser is depicted in *b)*. Demodulating the photo diode signal with a local oscillator of the same frequency and a phase shift of a multiple of 2π gives rise to an error signal as shown in *c)*. The signal is centered around zero and can be easily used for locking to any zero crossing that is then insensitive to changes of the laser power or coupling changes. The phase of the LO is in general adjusted by a phase shifter. As in our setup there is a large imbalance of the two RF paths' lengths, it is sufficient to change the modulation frequency by a few MHz.

drives the mechanical oscillator, and this method is therefore not suitable for cooling experiments.

Applications

The PDH scheme provides a particularly stable lock that is especially independent of the laser power (and its drifts) and the taper-toroid coupling, such that this kind of detection can be nicely used for tracking mechanical and optical resonance frequencies and mechanical linewidths for example as a function of temperature (see section 3.2). PDH locking has also been used for pump-probe experiments (as in sections 3.2.2 or 3.6), where one laser was used to read out the coherent thermal response imprinted onto the system by a second amplitude-modulated laser locked to a different optical mode.

2.2.3 Balanced Homodyne Detection

This is the standard scheme used for all experiments aiming at cooling of a mechanical oscillator during this thesis (see Fig. 2.6). Here, the phase fluctuations of the weak probe beam are amplified by a local oscillator, which allows to surpass the electronic noise present in the detection circuit. The two beams are split in front of the experiment and recombined behind it, giving rise to interference fringes. Using a balanced

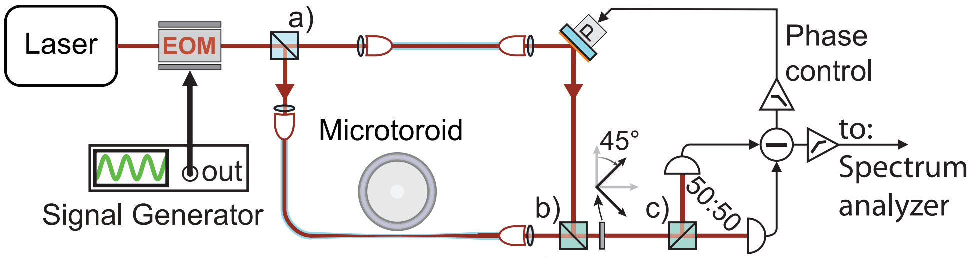

Figure 2.6: **Balanced homodyne detection.** *a)* The laser light is split into a local oscillator and a signal beam. The latter passes the toroid and the two beams are recombined (with orthogonal polarizations) on a polarizing beamsplitter *b)*. A subsequent waveplate rotates the polarizations by 45° such that LO and signal are mixed and the total power is split into two beams of identical power that are projected onto a balanced photoreceiver. Probing the phase quadrature is achieved by locking the DC component of the voltage signal to a zero using a piezo mirror as an actuator on the LO path length. The AC component contains the relevant signal. Waveplates and polarizers used for adjustment and purification of the polarizations have been omitted for clarity.

photo detector, the large DC component of the signal can be removed by locking the differential signal to a zero using feedback control of the optical path length of the local oscillator. The remainder contains the radio frequency phase noise induced by the optomechanical system. If the lengths of the two paths are equal, classical noise on the incoming laser beam is entirely canceled in the balanced photo-detectors.

While it is tedious to implement the homodyne detection and to balance the armlengths, this setup is the only scheme presented so far that allows shot noise limited detection of even weak optical signals.

Locking the laser on resonance

As the DC (low frequency) signal is locked to a zero of an interference fringe, there is no direct access to an error signal that can be used to lock a laser to the cavity. A straightforward way to implement locking would be to split off some probe light, however, since any loss in the detection path deteriorates the sensitivity this has never been implemented. One can imagine schemes similar to PDH locking, but as one cannot send any modulation signal too close to the mechanical resonance frequency this does not allow to easily lock on the mechanical sideband. So far, all realized experiments using homodyne detection have been relying on the passive mutual stability of optical resonance and laser frequency.

Balancing

A priori, the Ti:Sapph laser used for our experiments shows quantum-limited noise performance at the relevant Fourier frequencies, such that balancing of the arm lengths is not mandatory for the readout of mechanical motion. However, at several points we introduce a classical modulation (“calibration peak” or “sideband sweep”, see sections 1.5 and 2.4) that is transduced into an amplitude modulation. In order to avoid any transduction by the homodyne setup itself, the armlengths need to be balanced in order to suppress any background signal in the absence of a cavity. It is found experimentally that the small phase shift induced by a path length difference of about one millimeter is still measurable and affecting the measurement. Thus the challenge is to match two approximately 8 m long fibers to that length difference. This is routinely achieved by injecting a diode laser into the (non-locked) homodyne setup. Dithering of the laser frequency by a few GHz is translated into $n_\text{cycle} = (\Delta l \Delta f)/c'$ (with path length difference Δl, frequency dithering amplitude Δf and c' the speed of light in fibers) interference cycles. By shortening one of the fibers[3] by a certain length and recounting cycles the total length difference can be estimated. Using linear stages mounted below fiber couplers fine adjustments can be done. In order to balance on the sub-millimeter level a strong phase modulation is added to the laser, the homodyne interferometer is locked and the transmitted signal is monitored on a spectrum analyzer. Minimizing this signal concludes the procedure.

2.2.4 Other methods

Another method that allows quantum-limited detection while not requiring the balancing step has been developed by Hänsch and Couillaud [72]. Here LO and signal having orthogonal polarizations are both passing through the same fiber, where the polarization is adjusted such that only the signal is coupled to the resonator. Especially if a weak signal beam is required this scheme is not appropriate in our (cryogenic) setup for two reasons. Polarizations within the fibers are not perfectly stable, as they are affected by air turbulences shaking the (partly) free-hanging fibers. More importantly, there are scattering losses inside the cryostat, which heat the environment of the toroid (see section 3.4).

2.3 Calibration of mechanical spectra

Having read out a mechanical spectrum, as for example depicted in Fig. 1.4b, it is a straightforward task to extract mechanical frequency and linewidth. In addition, the area under the curve is proportional to the effective temperature of the corresponding mechanical mode. It is however also proportional to the transduction of mechanical motion into a voltage signal on the ESA. Since this transduction depends on the coupling rate to the tapered fiber κ_{in}, the laser's detuning, power and polarization (and all these parameters are affecting each other and depend on the cryostat temperature), one needs to account for a possible variation of the transduction during up to tens of minutes.

---

[3] The fiber is cleaved, then the two fiber ends are brought close to each other using a commercial fusion splicer. The actual splicing is performed only in the very end once the lengths are matched to a few millimeters.

2.3.1 Calibration using a phase calibration peak

Therefore, a weak modulation sideband is coinjected, which adds a sharp peak close to the mechanical noise spectrum. It can be proven that this artificial coherent modulation and the phase modulation of mechanical origin are transduced identically (see Appendix A of [48]), as long as the optomechanical coupling is small as compared to the optical linewidth and mechanical spectrum and calibration peak do not overlap [73, 3]. This means that several measurements can be easily compared by comparing the corresponding areas that have been normalized by the area under the calibration peak.

In practice, one spectrum taken at low laser power and high ambient pressure, where thermalization to the ambient temperature can be assumed, can serve as a reference, allowing to extract effective temperatures for all other measurements. Note however, that indeed the only information contained in such a measurement is the effective mode temperature. If effects such as spurious heating of the environment are to be estimated, other methods have to be used (cf. sections 4.2 or 4.3).

Additionally, knowing the exact modulation depth of the phase calibration and assuming perfect thermalization and negligible optical backaction the vacuum optomechanical coupling rate g_0 can be extracted (and subsequently the coupling rate G by estimating r) [48].

Calibration of the phase modulator

An accurate measurement of g_0 is only possible, if the power in the calibration peak is known precisely. Therefore, measurements of g_0 are always performed in the same setup using a dedicated Rohde & Schwarz SMY01 signal generator in conjunction with a fiber phase modulator (General Photonics, model LPM-001-15-PP-FC/APC) and a fixed cable in between. This assembly has been characterized as detailed in the following.

Phase modulators as used in our setup are based on the linear electro-optic effect.

Here, the refractive index change Δn of the material depends linearly on the applied electric field E:

$$\Delta n = \frac{1}{2} n^3 r E \tag{2.5}$$

with the unperturbed index of refraction n and the appropriated component of the electro-optic tensor r. The total acquired phase shift $\Delta\Phi$ of an optical beam of free-space wavelength λ passing through a crystal of length l and height h with an applied transverse, homogeneous electric field $E = V/d$ (V is the applied voltage) is then:

$$\Delta\Phi = \frac{2\pi}{\lambda}\left(\frac{1}{2}n^3 r\right)\frac{l}{d}V \tag{2.6}$$

$$= \pi\frac{V}{V_\pi} \text{ with } V_\pi = \frac{\lambda d}{n^3 r l}. \tag{2.7}$$

All material and device properties have been subsumed into only one wavelength dependent parameter V_π with the dimension of a voltage. If a voltage $V = \pm V_\pi$ is applied, the passing beam is delayed or advanced by a π phase shift as compared to an unperturbed beam.

If a sinusoidal voltage is applied to the phase modulator, each of two added sidebands contains a fraction $P_1/P_{\mathrm{in}} = (J_1(\Delta\Phi_{\mathrm{max}}))^2$ of the incident power, the fraction remaining in the carrier is $P_0/P_{\mathrm{in}} = (J_0(\Delta\Phi_{\mathrm{max}}))^2$, where J_1 (J_0) is the first (zero) order Bessel function and Φ_{max} the phase shift corresponding to the peak voltage of the driving signal.

A simple spectroscopic measurement as shown for example in Fig. 2.2 gives direct access to V_π. Therefore, only the ratio of the depths of the dips caused by first sideband and carrier needs to be compared to the ratio P_1/P_0. Here, however, a slightly different approach was chosen, as the coupling setup is unfortunately not stable enough to obtain accurate results.

Instead, a 1550 nm diode laser was scanned across an imbalanced fiber Mach-Zehnder interferometer (cf. Fig. 2.7a), with the fiber phase modulator contained in one of the arms. Scanning of the diode laser frequency results in sinusoidal fringes in the transmitted signal that are monitored on an oscilloscope. Simultaneously, a radio frequency tone is applied to the phase modulator "shaking" the sinusoidal fringes back and forth. The expected Voltage signal can be expressed as (see 2.7b) for parameter definitions):

$$V(t) = V_0 + \Delta V_2 \sin\left(\frac{2\pi}{\Delta t_2}t + \phi_2 + \Delta\phi_{\mathrm{max}}\sin\left(\frac{2\pi}{\Delta t_1}t + \phi_1\right)\right) \tag{2.8}$$

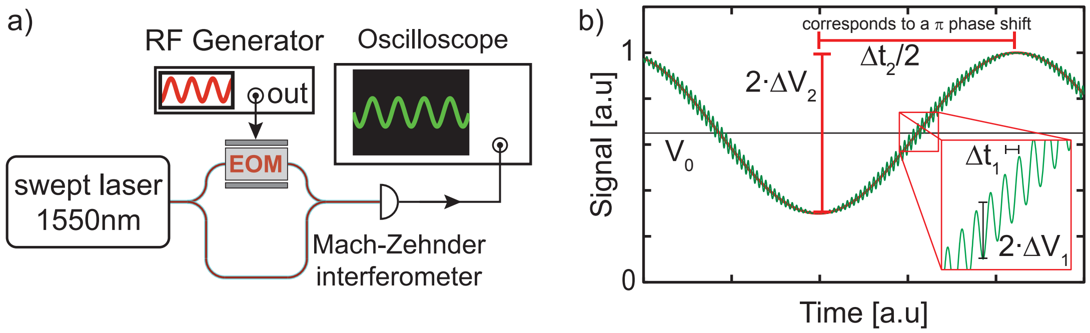

Figure 2.7: **Calibration of a phase modulator.** *a)* shows the setup used to accurately calibrate a fiber coupled phase modulator (EOM) used to determine the vacuum optomechanical coupling rate g_0 . A swept diode laser is injected into an imbalanced fiber Mach-Zehnder interferometer, with the EOM in one of the two arms. The interference fringes and the RF phase modulation is monitored with a fast photo diode and an oscilloscope. *b)* shows the expected behavior: The scanning laser causes the slow fringe pattern, while the phase modulator "shakes" in x-direction. Obviously, the phase modulation is only converted into an amplitude signal on a zero-crossing (here: at V_0) of the fringe. Measurement of the two characteristic amplitudes is sufficient to extract V_π. See text for details.

Here, $\phi_{1,2}$ are two arbitrary phase constants, where $\phi_2 = 0$ without any loss of generality. Δt_2 is the time between two consecutive interference fringes and depends on the scanning speed and the interferometer's imbalance. It is chosen such that it is significantly longer than $\Delta t_1 = 2\pi/\Omega_{\mathrm{mod}}$, the inverse of the RF modulation frequency, however not too long, in order to be able to acquire a few fringes with a temporal resolution that is sufficient to still see the RF modulation. $\Delta\phi_{\max} = \pi V/V_\pi$ links the voltage applied to the phase modulator and V_π that is to be determined. This function can be directly used for fitting, however, it is easier to develop (2.8) around a "zero"-crossing (here: positive slope) of the slow signal, assuming $\Delta\phi_{\max}$ to be small:

$$V(t) \approx V_0 + \Delta V_2 \left(\frac{2\pi}{\Delta t_2} t + \Delta\phi_{\max} \sin\left(\frac{2\pi}{\Delta t_1} t + \phi_1 \right) \right) \tag{2.9}$$

$$= V_0 + \Delta V_2 \frac{2\pi}{\Delta t_2} t + \Delta V_2 \Delta\phi_{\max} \sin\left(\frac{2\pi}{\Delta t_1} t + \phi_1 \right) \tag{2.10}$$

One can easily see that it is sufficient to find the amplitude of the RF signal ($\Delta V_1 = \Delta V_2 \Delta\phi_{\max}$), which together with ΔV_2 gives direct access to $\Delta\phi_{\max}$, and finally with the input signal amplitude to V_π.

This routine was automated and the whole experimental range from 50 MHz to 100 MHz was covered and values of $V_\pi = 6.8...8.3V$ were found. It is unclear what causes the variation.

Hereby, the only source of a potential error is the detector response. A different responsitivity at $2\pi/\Delta t_2$ and Ω_{mod} leads to a systematic error. Therefore, a detector with a 1 GHz bandwidth (much larger than the frequencies involved, New Focus model 1811-FC) was used. According to the data sheet, the responsitivity in the range 0-100 MHz is constant within a ±5% margin.

2.4 Sideband Sweeps - measurement of the laser detuning

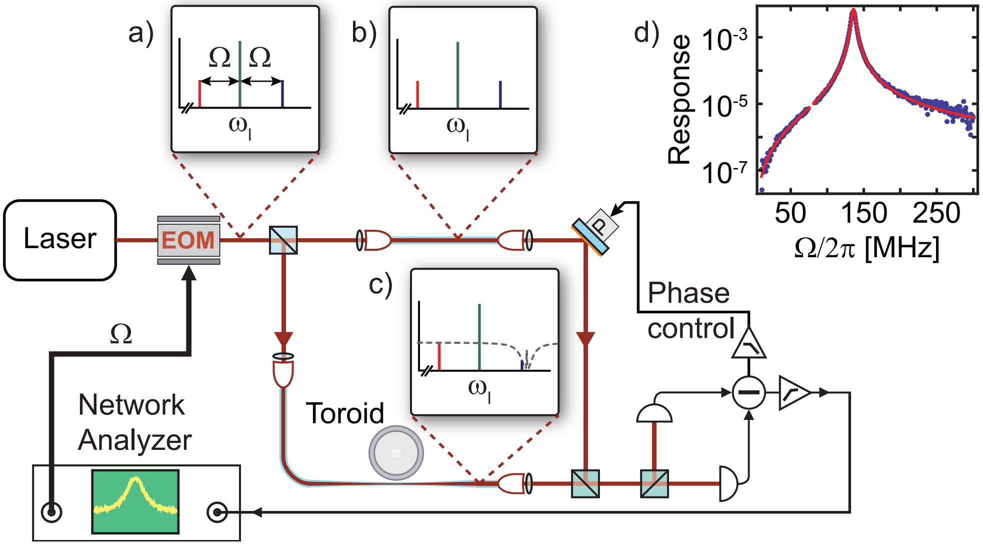

Figure 2.8: **Sideband sweeps.** Adding a network analyzer driving the phase modulator to the homodyne setup described in Fig. 2.6 allows to create sidebands to the laser frequency ω_l *(a)*. While they are not affected in the LO path (*b)*) the blue sideband is absorbed into the cavity, if a resonance is hit *(c)*. Within the balanced detector, the non-affected sidebands will just cancel, however, due to the amplitude imbalance between blue sideband in LO and signal path, an amplitude modulation will remain that can be related to the intracavity power. Sweeping the sideband across an optical mode yields traces as shown in *(d)*. Here, it is straight forward to fit (red line) the laser detuning as well as the optical linewidth. The OMIT feature (see 4.1) has been removed in this figure.

In order to be able to fit the results to a theoretical model, it is important to have accurate knowledge of the laser detuning. For this reason, we have developed a technique that we call a “sideband sweep” which yields an optical coherent response.

This is implemented experimentally by frequency sweeping a sideband that is added to the cooling laser by means of a phase modulator across the optical resonance. A network analyzer provides the frequency sweep and also demodulates the signal captured on the photo detector (cf. Fig. 2.8). Neglecting any optomechanical coupling this acts in the first place just like a second laser beam sweeping across the optical resonance[4]. This scheme - taking into account the optomechanical coupling - is also

---

[4] The second far-detuned sideband does not interact with the cavity and is transmitted unchanged and cancelled

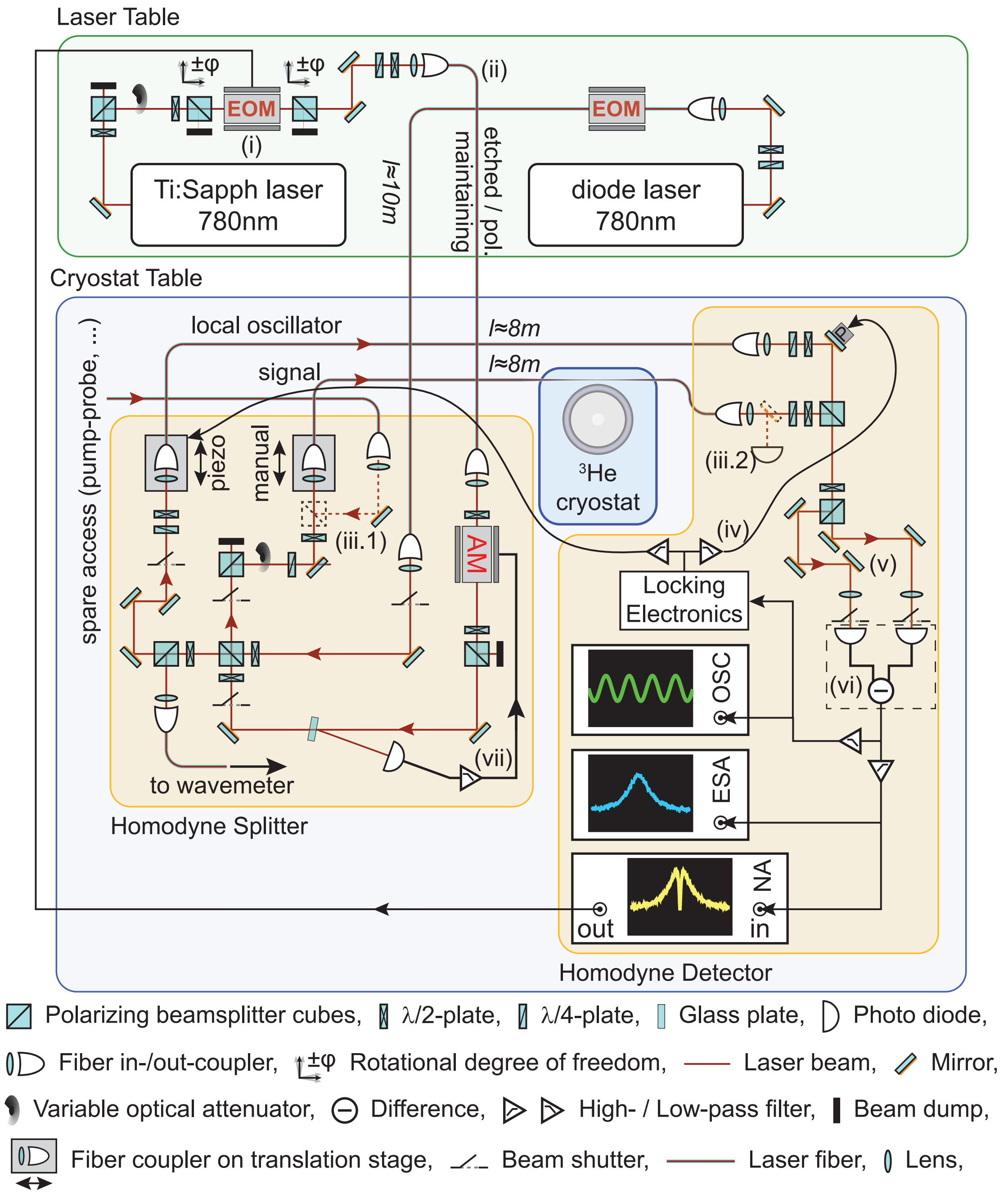
Laser Table
±φ
±φ
EOM
(i)
(ii)
Ti:Sapph laser
780nm
l≈10m
etched / pol. maintaining
EOM
diode laser
780nm
Cryostat Table
spare access (pump-probe, ...)
local oscillator
signal
l≈8m
l≈8m
piezo
manual
(iii.1)
AM
³He cryostat
(iii.2)
P
(iv)
(v)
Locking Electronics
OSC
ESA
(vi)
NA
out
in
(vii)
to wavemeter
Homodyne Splitter
Homodyne Detector
Polarizing beamsplitter cubes,
λ/2-plate,
λ/4-plate,
Glass plate,
Photo diode,
Fiber in-/out-coupler,
±φ Rotational degree of freedom,
Laser beam,
Mirror,
Variable optical attenuator,
Difference,
High- / Low-pass filter,
Beam dump,
Fiber coupler on translation stage,
Beam shutter,
Laser fiber,
Lens,

Figure 2.9: **Detailed typical optics setup.** *(i)* In order to avoid spurious amplitude-modulation, it has proven crucial to have a maximally pure polarization, well aligned with the crystal axis. Instead of waveplates, we turn the cubes. *(ii)*: Both, etched (cf. 3.5) and polarization maintaining fibers are used. *(iii.1+2)* serve as additional access + pick-up, e.g. for pump-probe experiments. *(iv)*: Fast (slow) fluctuations of the relative path lengths of the interferometer are compensated by a fast piezo mirror (long travel range piezo stage). High-voltage (HV) amplifiers driving the piezos have been omitted. *(v)*: Also this part needs to be balanced to suppress classical noise! *(vi)*: Meanwhile an AC-coupled detector with a DC monitor is used. *(vii)*: Laser power stabilization. HV amplifier and locking electronics have been omitted.

used to measure the effect of optomechanically induced transparency, as described in section 4.1. Finally, this coherent optical response measurement (i.e. all incoherent noise can be suppressed by averaging or the choice of a narrow detection bandwidth) can replace the calibration peak, which becomes obsolete once strong optomechanical coupling is achieved. Additionally, such a trace also contains information on dynamic parameters governing the optomechanical coupling, like optical linewidth, mechanical frequency and optical detuning, but especially the optomechanical coupling that allows to deduce the intracavity photon number as will be shown in section 4.3.

In order to obtain clean sideband sweeps with lowest possible background all effects leading to coherent amplitude modulation (AM) at the same (driving) frequency need to be minimized. As we found out an important contribution was generated directly in the New Focus Model 4002 phase modulator. The birefringence of the crystal used in this device leads to a modulation of the polarization, if the incident polarization is not precisely matched to one of the optical axes, which is converted into an AM at the first subsequent polarizing beam splitter (PBS). Therefore PBS used in transmission[5] were placed before and behind the EOM with the only goal to maximally purify the polarization. Additionally all optical elements behaving like Fabry-Pérot etalons were removed, replaced or turned away from normal incidence. Here mostly beam splitters caused problems.

2.5 Cryogenic setup

In a preceding experiment taking place in a He-4 cryostat [62] a lot of insight has been gained. From a technological point of view, the main developments involve the preparation of a cryohead on a routine basis permitting to cooldown a tapered fiber as well as a sample to 1.6 K without degradation and the ability to couple them at low temperatures. Beyond, it was confirmed that for temperatures below around 13 K the thermal effect $\frac{d\omega_\mathrm{c}}{dT}$ (compare to eq. (2.4)) changes sign such that there is no more fast laser lock required for laser cooling on the—now thermally stable—red sideband. From a physical point of view these experiments have enabled cooling the mechanical radial-breathing mode of a toroidal microcavity from 1.65 K (corresponding to around 500 Phonons) to an occupancy as low as 60 Phonons [74] and high sensitivity monitoring of the residual mechanical motion. In addition a lot of insight on two level systems and thin layers of superfluid helium films condensing on the toroids has been gained [62, 66].

A major inconvenience of working at low temperatures is, that the mechanical

---

in a homodyne setup by the corresponding sideband in the local oscillator

[5] Polarization purity of transmitted light in standard PBS is significantly better than in reflection

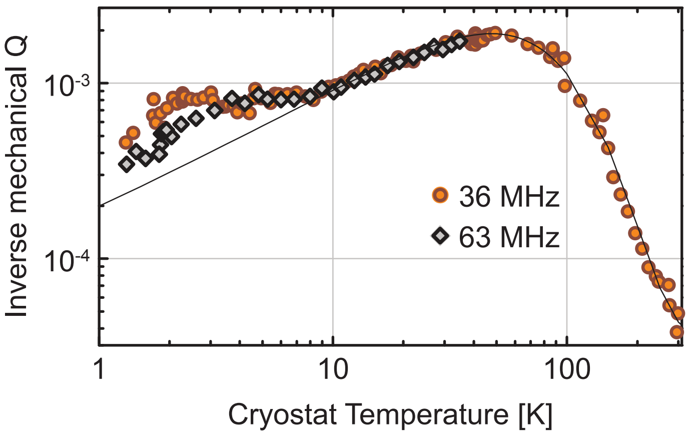

Figure 2.10: **Mechanical quality factor in silica microtoroids vs. temperature.** As found in a previous experiment, mechanical quality factors obtained in silica microtoroids show a complex temperature dependency that can be explained by intrinsic phonon scattering due to two level systems. One motivation to move experiments into a helium-3 cryostat was the drastic increase in mechanical quality factors for temperatures below 2K, as also suggested by the roll-off seen in this graph. *Adapted from [62].*

quality factors found at room temperature are not conserved down to low temperatures but degrade severely at low temperatures (Fig. 2.10). This can be attributed to the intrinsic material absorption in silica due to two level systems in the amorphous structure. The motivation to move experiments to a He-3 cryostat was twofold; on the one hand one gains a factor of around two in the initial temperature (while maintaining a comparable vapor pressure), and on the other hand one could hope to find a significant drop of the intrinsic absorption of phonons as suggested in literature [75] and by the onset of a roll off as seen for the lowest temperatures in Fig. 2.10. A third important advantage as found during the first measurements within the helium-3 cryostat is its superior temperature stability as well as its mechanical stability, which allows data averaging under stable experimental conditions for about a minute, limited only by the relative drift of laser and optical cavity.

2.5.1 The cryostat

For all cryogenic experiments described in this thesis, a commercial toploading He-3 cryostat (Heliox TL, Oxford Instruments, see Fig. 2.11) was used. The design allows exchanging samples while keeping the cryostat cold. This does (in principle) reduce turnover time significantly. However, due to the special needs of our very sensitive samples, the basic cool down strategy needed to be refined as will be described in section 3.4.

The basic operation principle is as follows: Helium-3 occupies the entire innermost

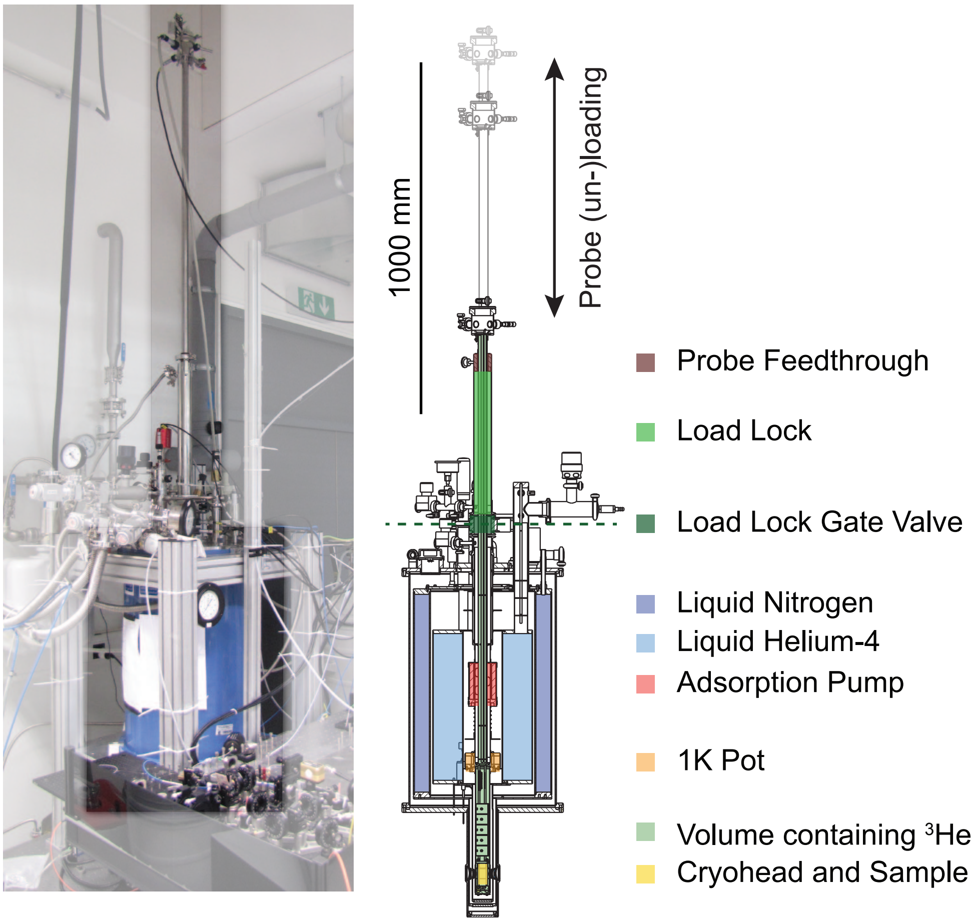

Figure 2.11: **The Helium-3 cryostat.** Shown in this figure are a technical drawing of the cryostat and a photo of its natural environment. Embedded into a large vacuum vessel (“outer vacuum chamber”, “OVC”) are—surrounding everything—superinsulation foil and concentric reservoirs for liquid nitrogen and helium. The nitrogen shield’s only purpose is to lower the thermal load via thermal radiation onto the helium and thus reduces its consumption. The helium bath itself lowers the thermal load onto the probe space. Both are extended down into the sample space by metallic cylinders. The whole inner part is a priori filled with helium-3 that is kept in a closed volume consisting of the cryostat, an external sorption pump (“sorb”) and expansion chamber (both not shown in the schematic) and tubings connecting them. While the sorb acts as a temperature-variable pump for gaseous helium-3, the 1K Pot provides the low temperatures required to condense helium-3 into the helium-3 tail (bottom of the helium-3 chamber). Both are cooled by needle valve controlled tubes that are fed by the helium bath. Additionally, the sorb can be heated via an electric heater. The probe can be lowered into the system while it is cold. Therefore, a load lock is implemented that consists of a larger tube that is fixed to the probe via a feed-through consisting of two O-rings in a row. The other end can be flanged to the top part of the cryostat. The load lock can be evacuated and, after cutting the pump, the load lock gate valve linking probe and helium-3 chamber can be opened and the probe is pushed in. In order not to lose helium-3, it is pumped into the sorb before closing the gate valve when the probe is removed. In the bottom of the cryostat a window gives optical access to the cryohead, helping to align fiber and sample.

chamber (which contains the coupling setup and sample) as well as an external reservoir which serves as an expansion chamber to avoid overpressures within the system. Thermally connected to the helium-3 chamber is a 1K-pot that can be filled with liquid helium-4 through a motorized needle valve and be cooled to about 1.2 K by pumping it with an external roughing pump.

Another central component is an adsorption pump or "sorb", which is basically a piece of charcoal with a very large surface, that is inside the helium-3 chamber. It is thermally connected to a capillary that guides helium from the bath. The cooling power is regulated by a needle valve in front of the sorb and a roughing pump pulling out the helium vapor on the other end of the capillary. Heating is achieved by an electric resistive heater that is coupled to the sorb. Since the adsorption of helium-3 is strongly temperature dependent it serves as a very efficient pump with a temperature controlled pumping speed. Cooling the sorb to low temperature (below 10 K) leads to adsorption of essentially all of the helium-3. Increasing the sorb temperature to around 50 K releases most of the helium-3 and cooling of the 1K-pot leads to condensation of helium-3 on its surface, which forms small droplets gathering in the bottom of the helium-3 chamber ("helium-3 tail"). Once the condensation has reached a steady state the sorb temperature is reduced, leading to a reduction of the vapor pressure and thus of the temperature, until—after several hours—the liquid helium-3 is evaporated and needs to be recondensed.

2.5.2 The cryohead

Fig. 2.12 shows a photograph and rendering of the coupling setup or "cryohead". It needs to provide support for the tapered optical fiber and sample, as well as all degrees of freedom required for efficient coupling of the tapered fiber to a toroid. A protecting cup (shown in Fig. 2.13) ensures maximal mechanical stability during the insertion / cooldown and carries a resistive heater that allows heating the sample and stabilizing its temperature beyond 1.3 K. Additionally, there is a temperature sensor close to the sample, as well as two others on the protecting cup.

Inserting the probe including a prepared cryohead into the cryostat is a severe test for sample and fiber, due to mechanical forces (scratching of the cryohead along the inner surfaces of tubes / sliding baffles causing vibrations) and thermal gradients. Temperature drops by $> 200\,\mathrm{K}$ in a few minutes lead to distortions of the setup, due to the different thermal expansion coefficients of the materials in use. Consequently, coupling of the taper to the toroid needs to be done afterwards, once the cryohead is cold and in its final place in the helium-3 tail. Experience shows that two degrees of freedom—"z": approaching the chip to the fiber and "x": moving the chip along the axis of the toroids—are sufficient. Thus, phase matching is done at room temperature

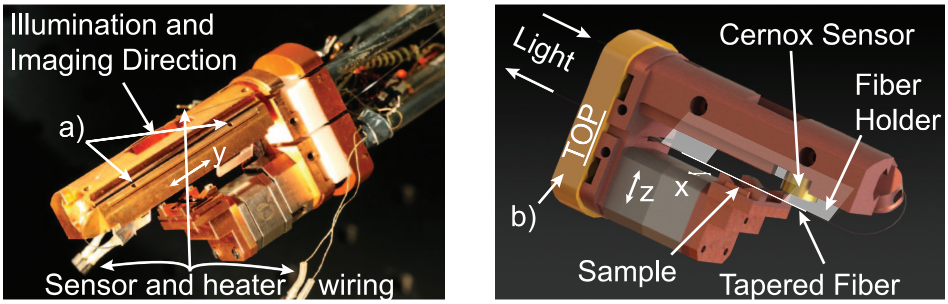

Figure 2.12: **The cryohead.** This figure shows a photograph (*left*) and a drawing (*right*) of the cryohead used to couple a toroidal silica microresonator to a tapered fiber. Three translational degrees of freedom ("z": approaching the chip to the fiber, "x": selecting a resonator and coupling, "y": phase matching by moving the fiber along its axis) as well as one rotational degree of freedom to ensure parallelism of chip and fiber are required. "x" and "z" are realized by attocubes that can be operated in vacuum and at cryogenic temperatures, while "y" needs to be adjusted at room temperature by moving the slide that holds the fiber holder up or down. Parallelism is adjusted using the two (threaded) holes (*a)*) by inserting a screw or screwdriver to push the fiber holder out of its support on either side. Thermal contact to the rest of the probe is reduced by a plastic spacer (*b)*). Additionally, a custom calibrated cernox temperature sensor is included close to the sample. The assembly is protected against mechanical external loads by a protecting cup (*not shown here, cf. Fig. 2.13*) that carries two more temperature sensors used to stabilize the cryostat temperature as well as a resistive heater.

by sliding the fiber holder in the trench that holds it along "y" (see Fig. 2.12). One critical parameter is the parallelism of tapered fiber and substrate. Coupling to a toroid can only be done if the taper reaches the toroid before touching the substrate at the edge of the chip. Especially for the latest experiments done with very small samples, adjusting fiber and chip to be parallel was a major challenge. For a chip width of 4 mm and a distance of 10 μm between toroid and substrate the acceptance angle is below 1°. As the XeF_2 etching releasing the structure (cf. section 3.3.2) is stronger at the edges of the chip, leading to a convex shape of the chip surface this condition is alleviated a bit. Parallelism is achieved by pushing the fiber holding glass plate in or out of its clamp using a thin screw driver or screws pushing the glass plate at either of its ends.

Assembly

Assembling of the cryohead involves the following relevant steps:

- *Preparation of a tapered fiber and gluing onto a glass holder:* This very critical process is described in great detail in section 3.4.2 of [62].
- *Insertion of the fiber taper into the cryohead:* Here, the glass holder is fixed in its holder that is subsequently sled onto the cryohead. Afterwards, the fiber is

pushed through a thin tube made of PTFE all the way to the top of the probe. Once all other steps are done, a vacuum tight feed through is achieved using the method described in [76] aided by Varian TorrSeal vacuum proof two component glue.

- *Insertion of the sample:* The sample is clamped to a copper holder that is fixed to the top of the stack consisting of the two piezo positioners.
- *Checking the parallelism of chip and toroid:* Imaging the assembly from the side and bringing the fiber close to the chip surface, one monitors the fiber and its reflection from the chip surface. If they are not parallel, adjustments are done as described earlier. Otherwise, coupling to the toroid serves as final proof for the correct adjustment.
- *Adjusting the x-position of the chip:* The positioners can be moved by ±1.5mm, such that six to seven out of typically twenty toroids are accessible. Consequently, the sample needs to be placed in its holder such that all relevant toroids can be accessed.
- *Phase matching:* In order to be able to couple critically, the fiber needs to be moved in y-direction until extinction on resonance approaches 100%. This is done by moving the fiber together with its holder.
- *Closing the cryohead:* Finally, the protecting cup is inserted and screwed to the top of the cryohead and the heater and temperature sensors attached to it are connected to the wires running down the probe. In order to avoid any damage during the cooldown, all external wires need to be contained in a circle of 38 mm diameter. Therefore, they are taped to the the outer (flat) surfaces of the cryohead.

2.5.3 Additional components

Operation of the cryostat requires additional hardware that will be explained in the following. In order to independently control the sorb and 1K-pot temperatures two roughing pumps and pressure gauges are connected to the sorb and 1K-pot. The latter (being more powerful) is also used to evacuate the helium bath, which is necessary in order to remove any gas other than helium that could potentially freeze the needle valves, before filling in the helium for the first time. When inserting the probe, O-rings are sliding along its outer surface, which is a not entirely leak-tight process. Therefore an assembly of two consecutive O-rings is used and the space in between is pumped with an additional small roughing pump. In this way, any contamination of the helium-3 is avoided, while small losses may occur. Load-lock and the isolating

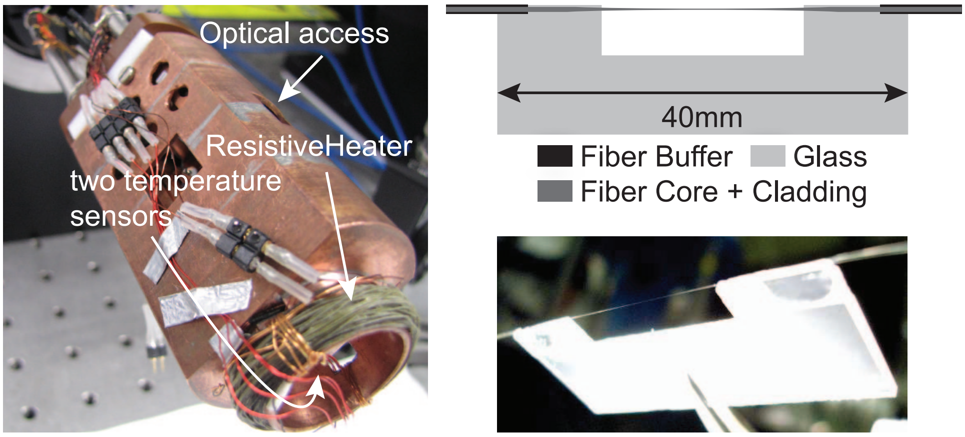

Figure 2.13: **Protecting cup and tapered fiber holders.** The *left* picture shows the cryohead that is entirely prepared for cooldown, with temperature sensors and heater wires being connected. All wires are taped to the outer surface using adhesive aluminum tape in order to reduce the risk of breaking them during the insertion process. On the *right* a schematic drawing and a photo of a tapered fiber holder can be found. The taper holder consists of an object holder glass plate that is cut into a shape as shown. The fiber is glued onto this holder using UV-curing optical adhesive (NOA61). Care is taken to prepare the fiber sufficiently short, such that the fiber buffer can still be glued to the glass plate, which largely reduces the risk of breaking the fiber during the cryohead assembly; especially in the bottom, where it is bent with a bending radius smaller than 10 mm.

outer vacuum chamber (OVC) of the cryostat are evacuated with a dry (= oil-free) high-vacuum pumping stage consisting of a diaphragm and turbo pump and pressure is monitored with a full-range gauge. While the OVC only needs to be pumped before the initial cooldown of the cryostat, the load-lock is evacuated whenever a new sample is to be put in.

Needle valve openings and heaters are operated by Oxford Instruments temperature controllers. Additionally, a level meter for helium and nitrogen is used. All controllers are interfaced to a computer, which allows to remote control, read and archive all cryogenic settings and parameters. A capacitance pressure gauge with very high absolute accuracy connected to the probe allows to monitor the pressure of helium-3 during the experiments. As the helium-3 circuit is entirely closed, a second external sorb that is connected in permanence is the tool allowing to remove the helium-3 from the cryostat if needed. Therefore, it is inserted into a dewar containing liquid helium.

2.5.4 Basic operation

Once the cryohead is prepared and made leak-tight it is put on top of the (here: cold) cryostat, connected to the load lock gate valve and load lock pumping line and evacuated. Once a pressure in the low 10^{-4} mbar range is reached, the sorb temperature is reduced[6], the pumping valve is closed and the gate valve can be opened.

Inserting the probe is straightforward and the sample temperature will drop rapidly when approaching the sorb. Efficient cooling is achieved by cooling the sorb itself, which has a strong thermal link to the probe.

In this way, the sample is cooled to around 4 K. Cooling below this temperature is achieved by heating the sorb (such that it releases helium-3 gas) and opening the 1K-pot needle valve. Once the 1K-pot is filled entirely, its needle valve is closed completely. This ensures it is strongly isolated from the helium bath and pumping the 1K-pot allows achieving temperatures below 1.2 K. This temperature is sufficient to condense helium-3 that is raining down into the helium-3 tail. Once a steady state is reached (to be seen in a pT-diagram plotting the cryostat temperature and vapor pressure), the sorb temperature is slowly reduced, which also reduces the thermal load on the 1K-pot and allows to reach lower temperatures, corresponding to more efficient cooling. At sorb temperatures below around 27 K the condensation process stops and the sorb starts to pump and cool the helium-3. Any temperature between 500mK and 1.3 K can now be achieved by choosing the correct sorb temperature. Therefore, a digital PID-locking scheme is implemented in the temperature controller, where the difference between measured sample temperature and set point is fed back onto the sorb temperature. Temperatures above 1.3 K are set using the heater connected to the cryohead.

Depending on the desired working temperature, thermal load and condensation efficiency the liquid helium-3 lasts for several hours.

2.6 Data acquisition and automation

All experiments involving 780 nm lasers realized until now rely on the passive stability of the laser's frequency relative to the toroid's resonance. Additionally, measurement time is limited by the finite amount of liquid helium-3 in each cooldown run. As a consequence, an efficient data acquisition and semi-automated control of experimental parameters is required. For most of the experiments realized during this thesis the laser's frequency was swept in a stepwise manner from a large red-detuning towards the optical resonance. A computer controlled analog voltage output is used to step the laser's frequency, followed by consecutive acquisition of a mechanical noise spectrum and a sideband sweep. During the early phase of the experiment,

---

[6] In this way, there is no significant pressure difference between He-3 bath and the load-lock; otherwise the flow of helium-3 when opening the gate valve could damage the tapered fiber.

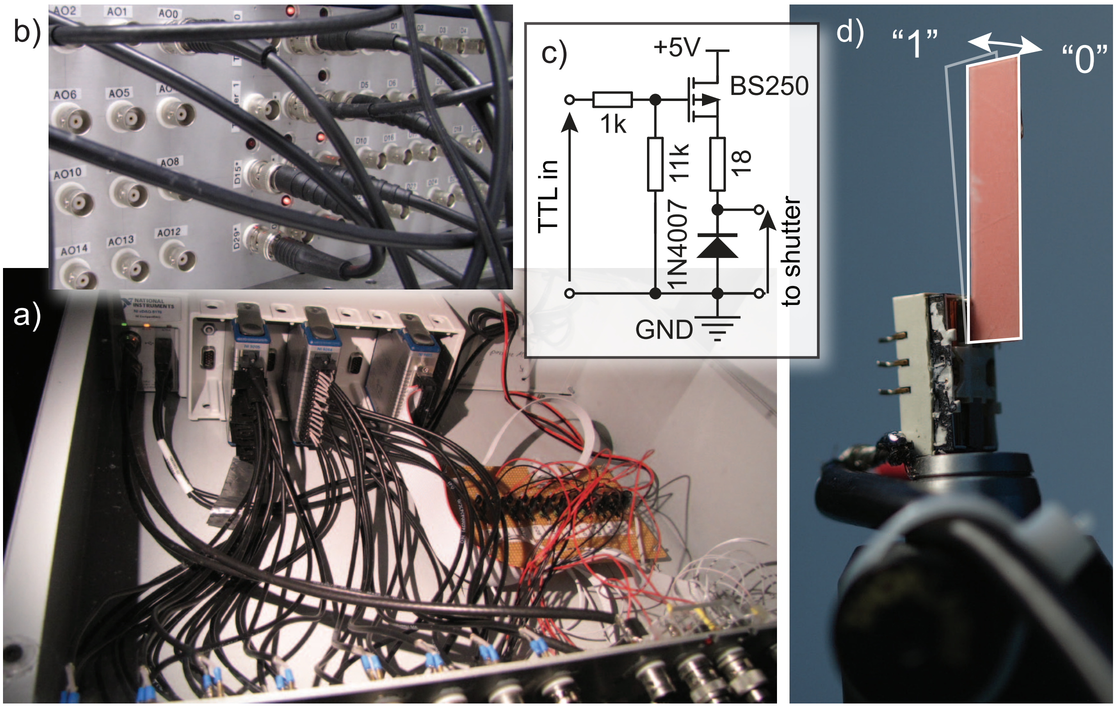

Figure 2.14: **Experiment control.** *a)* shows the box housing the National Instruments data acquisition device (top left), the wiring of the different inputs/outputs to the frontpanel (depicted in *b)*). Ten digital outputs are fed into simple transistor driver circuits (right and *c)*), able to drive home-made, relay based shutters (*d)*. LEDs put in parallel with these outputs indicate the current status. The shutters are glued on standard pillar posts, such that they can easily be put in between optical components, requiring a minimum of space.

National Instruments LabView was used to control and initiate the data taking. After the move to EPFL, effort has been put into further automatization. Python[7] based control software has been initiated and pushed forward by Samuel Deléglise that is not only more flexible when it comes to implementing a novel experimental sequence, but also allows to roughly analyze data online. As a consequence, trouble shooting is simplified and less useless data is recorded.

In a typical experiment several configurations that require blocking and opening of optical paths, are routinely performed. For example, tapered fiber coupling using a scanning diode laser requires the local oscillator of the homodyne setup and the Ti:Sapph input to be blocked, whereas homodyne measurements require signal and local oscillator arm to be opened, but the diode laser needs to be blocked.

For efficient switching between these configurations, laser shutters have been included into the setup. Because of the very limited space available for the optics setup, these have been homemade (see Fig. 2.14d). Therefore, the top of the housing of a small electronic print relay (model OMRON G6S-2F) has been cut open and removed, such that the mechanical rocker switch (or “Bifurcated Crossbar”), that is normally opening and closing the electrical contact, could be accessed. A piece cut out of an IR viewer card and glued onto the rocker perpendicularly serves as a (moving) beam dump. The driving range has been found to be just sufficient to entirely shut the collimated laser beams in our setup without requiring focusing.

---

[7] Python is an open source high-level programming language operating mostly on scripts. It is widely spread in science and research, such that numerous libraries already exist that contain routines for data acquisition, data processing and curve fitting, as well as for device control. Refer to http://www.python.org/ for more information.

Additionally, a National Instruments CompactDAQ system (model NI cDAQ-9178) with three different modules, providing analog input (model NI 9205), analog output (model NI 9264) and digital in- and output ports (model NI 9403) was implemented. It controls the laser’s frequency, reads out slow signals from the detectors and controls the homemade shutters. Therefore, a few digital output ports, that cannot provide sufficient power to drive the relays, are fed into simple transistor driving circuits that are able to switch the relays. All ports are wired to the front panel of a homemade box (see Fig. 2.14).

In combination, simple and fast routines used for alignment purposes or allowing to measure the overlap of the homodyne detection are easily implemented using Python and the automatic shutters.

3 Challenges

3.1 Choice of an appropriate wavelength

A crucial component in the whole setup is the laser source used for the experiments. While for precharacterization and alignment diode lasers are the best choice due to their wide mode-hop free tuning range, fast dithering capabilities and ease of use, they are no longer suited when it comes to ground-state cooling and shot-noise limited read-out of mechanical motion [58], due to their poor noise performance.

Here, the criteria are discussed that lead to an appropriate choice of the laser source. The ideal laser source should:

1. show quantum limited noise performance at Fourier frequencies around 80 MHz at a power of a few mW. Any classical noise would lead to a driving (heating) of the mechanics and manifests itself in squashing in the measured mechanical spectra [30].
2. allow significant tuning on a scale defined by the free spectral range of the examined toroids, which is of the order of 1 THz. Importantly, a resonance frequency shift of about 1‰ occurs when cooling from room temperature to 1 K.
3. be easy to use, allow fast sweeping, but still be intrinsically stable.
4. operate at a wavelength for which components are easily available (filters, phase modulators, amplitude modulators, low-noise amplifiers)
5. operate at a wavelength that is compatible with silica microtoroids

The following table reviews briefly the different laser sources available in our lab that are shot noise limited at the Fourier frequencies and power levels of interest and could be of potential interest for cryogenic cavity-optomechanics experiments. A 780 nm Ti:Sapphire laser that had already previously been used for the preceding experiment operating in a helium-4 cryostat [74], a neodymium-YAG (at 1064 nm) laser used for previous optomechanics experiments ([26, 54]) and Koheras fiber lasers available in the frequency range defined by the gain region of erbium-doped fiber around 1550 nm.

	Ti:Sapph	Nd:YAG	Koheras
Operating Wavelength	780 nm	1064 nm	1550 nm
Tuning range approx.	100 nm / 50 THz	30 GHz	1 nm / 125 GHz
Wavelength stability	fine (locked to reference cavity)	fine (passive)	fine (passive)
Ease of use	no continuous tuning, wavemeter required	fine	fine
Low noise optical amplifiers	none	available	available ("EDFA")
	all fall into the transparency window of SiO_2 and similar quality factors have been measured in the past		

While the very limited tuning range of Nd:YAG lasers is fine for large toroids with their small free spectral range and dense spectrum of transverse modes, the goal was to use light and small toroids (number of transverse modes is reduced and the free spectral range is increased) being incompatible with its use for this project. Identifying the difference between a Ti:Sapph laser and a Koheras laser is more difficult. The first is widely tunable but rather complicated to operate and to tune to a resonance, while the second requires a preselection of suitable toroids with resonance frequencies matching the tuning range, but offers the option of using evolved telecommunication components, especially low-noise optical amplifiers permitting close to shot-noise limited readout of mechanical motion in a simple PDH scheme that additionally allows to lock a laser on resonance. The decision was made to operate at 1550 nm, and all early experiments, especially on two-level systems in silica, were obtained at this wavelength.

However, we found that even though optical linewidths were comparable to the ones obtained at 780 nm, absorption losses (in contrast to scattering losses) within the toroids are much stronger at 1550 nm than at 780 nm, rendering cooling experiments impossible (see Fig. 3.1). In experiments using 1550 nm laser light it was found, that independent of the exact experimental conditions (cryostat temperature, detuning, coupling and input power), no significant cooling could be achieved. Instead, only a mechanical damping that was overcompensated by absorption heating was seen. The substantially higher absorption at 1550 nm is attributed to water ab- and adsorbed by

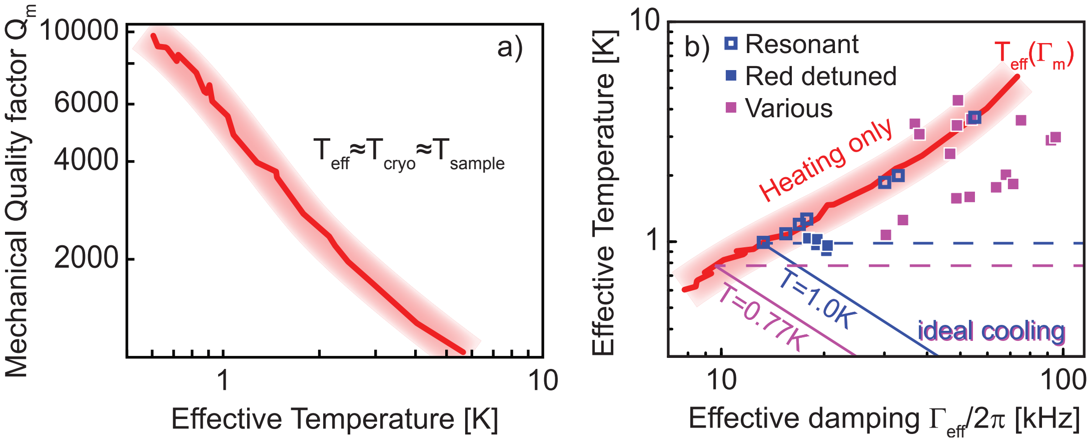

Figure 3.1: **"Cooling" at** 1550 nm. These data illustrate the cooling performance achieved using a $\lambda = 1550\,\mathrm{nm}$ Koheras fiber laser. *a)* shows the mechanical quality factor Q_m as a function of the temperature. Care has been taken to reduce the optical input power to a minimum, such that the effective mode temperature is equal to the environmental temperature. *b)* shows the effective mode temperature T_eff as a function of the effective damping $\Gamma_\mathrm{eff} = \Gamma_\mathrm{m} + \Gamma_\mathrm{cool}$, being composed of the (temperature dependent) intrinsic mechanical damping and the contribution caused by dynamical backaction cooling. Ideal sideband cooling increases the effective damping, but reduces the effective temperature. For reference, the trace from *a)* is inverted and also included into this graph. In an experiment, the cryostat temperature has been fixed to $T_\mathrm{cryo,1} = 1.0\,\mathrm{K}$ ($T_\mathrm{cryo,2} = 0.77\,\mathrm{K}$), indicated by the blue (violet) color. At $T_\mathrm{cryo,1}$, a resonant probing ($P_\mathrm{in} = 0.2$ to $90\,\mu\mathrm{W}$) clearly shows heating only (open squares), whereas detuning to the mechanical sideband ($P_\mathrm{in} = 50$ to $70\,\mu\mathrm{W}$) leads to a deviation from the red trace (filled squares). However, the effective temperature drops only by a tiny amount below the cryostat temperature (blue dashed line), and is far from the ideal behavior (blue solid line). At $T_\mathrm{cryo,2}$, all experimental parameters (detuning, laser power $P_\mathrm{in} = 200$ to $600\,\mu\mathrm{W}$, coupling condition) have been widely varied, but are obviously largely dominated by heating.

the silica during the fabrication process, as already observed by Gorodetsky *et al.* [77] and [78]. Diffusion into silica then takes place on a minute time scale [79] and clear absorption peaks, especially in the telecom band can be found (see Fig. 3.2 and [80]). As a consequence, further experiments were performed using a Ti:Sapph laser, which gave much more favorable results.

3.2 Two-level systems

Tunneling systems in amorphous SiO_2 play an important role in cryogenic operation of silica mechanical oscillators. They lead to a temperature-dependent frequency shift of mechanical modes via a change in the speed of sound and a temperature-dependent mean free path of phonons (i.e. mechanical quality factor), due to phonon scattering. These effects are discussed in the following. Only the essential results are

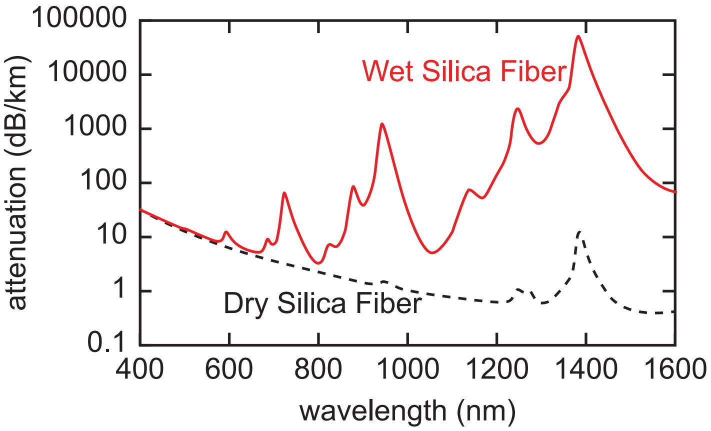

Figure 3.2: **Optical absorption in fused silica fibers.** Water within the optical mode profile of silica microtoroids causes significant absorption. The above spectrum shows a comparison of the attenuation spectrum of dry (0.2 ppm OH content) and wet (700 ppm OH content) silica fiber, and clearly shows the dramatic difference between 780 nm and 1550 nm, where we have to assume our toroids to be "wet". *Figure taken from Humbach et al. [80] and vectorized; for illustration purposes only.*

summarized, while an extensive study of TLS effects can be found in [81, 82]

As first considered by L. Pauling in 1930 [83], tunneling of atoms occurs in solids with a certain degree of disorder, where in the local environment of an atomic site, several potential minima exist. This can be the case in the vicinity of defects in crystals or, more frequently, in amorphous materials. For amorphous solids at low temperatures, the tunneling dynamics can be well captured in a simple model consisting of an ensemble of two level systems (TLS) each of which is described by a generic double-well potential (Fig. 3.3). This potential is parameterized only by the barrier height V, the initial energy asymmetry Δ_0 and the spatial separation between the two potential minima d. A tunneling coupling strength

$$\Delta_1 = \hbar\Omega_1 e^{-\lambda} \tag{3.1}$$

with the intrinsic oscillation angular frequency of the individual atomic sites Ω_1 can then be deduced, where the tunneling parameter is given by

$$\lambda \approx \sqrt{\frac{2mV}{\hbar^2}}\frac{d}{2}. \tag{3.2}$$

Here, m is the atomic mass. Due to this tunnel coupling, the new eigenmodes of the coupled system exhibit an energy splitting of

$$E = \sqrt{\Delta_0^2 + \Delta_1^2}. \tag{3.3}$$

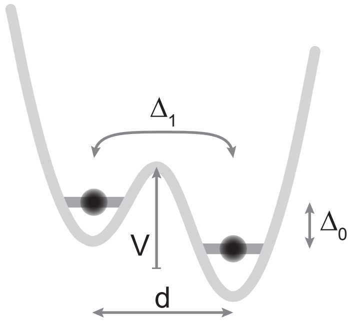

Figure 3.3: **Schematic of a double well potential with naming of relevant parameters.** The shown energy levels correspond to the unperturbed levels of the individual harmonic potentials.

Phonons parametrically couple to TLS via their strain field that leads to a deformation of the TLS potential. As a consequence, the TLS are driven out of thermal equilibrium and relaxation processes exchange energy with the thermal environment. Transitions between the two energy levels are induced by several distinct processes that become dominant in different temperature regimes. Mechanical quality factors are affected by three qualitatively different effects

- For very low temperatures, the density of thermal phonons is low, such that relaxation processes only play a minor role. Here, a significant population imbalance between lower and excited states exists for the relevant phonon frequencies and the most important loss mechanism is resonant absorption of phonons.
- At higher temperatures (here: above $\approx 0.5\,\mathrm{K}$) relaxation processes start to dominate. Phonons in the resonator mode deform the double-well potentials of the TLS that they are coupled to, which drives the TLS occupancy out of equilibrium. If a relaxation process happens, the deformation energy is lost into the bath of thermal phonons. First, one phonon processes dominate which involves one thermal phonon that picks up energy and a tunneling through the barrier. It is mainly this temperature range that will be relevant for the description of phenomena seen during cooling experiments.
- Later, at even higher temperatures ($> 10\,\mathrm{K}$), multi-phonon processes involving an excitation across the barrier dominate.

3.2.1 Relaxation contribution

If relaxation is the dominant process, the general expression for the mean free path of a phonon of frequency Ω_m is given by [81, 82]

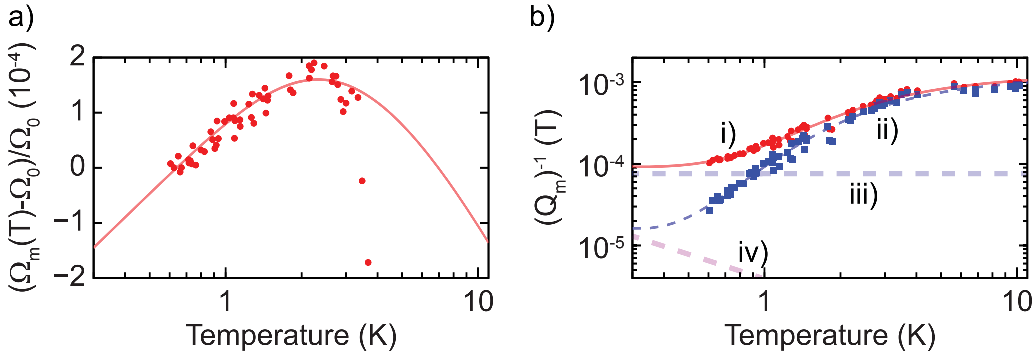

Figure 3.4: **TLS effects.** TLS-induced change of the resonance frequency $\Omega_m(T)$ (a) and inverse mechanical quality factor $Q_m^{-1}(T)$ (b) of the radial breathing mode. Measured data (points) agree well with the model. Subtraction of the temperature-independent clamping damping (line iii) from the raw data (line i and red points) yields the theoretically possible material-limited damping values (squares and line ii). At very low temperatures, damping by resonant interaction with TLS (line iv) would be dominant. Ω_0 is the mechanical angular frequency $\Omega_m(T)$ measured at the (arbitrarily chosen) temperature $T = 620\,\text{mK}$. The model parameters are given in section 3.2.3.

$$l^{-1}(T) = \frac{1}{\rho c_s^3}\iint\left(-\frac{\partial n_0}{\partial E}\right)4B^2\frac{\Delta_0^2}{E^2}\frac{\Omega_m^2\tau}{1+\Omega_m^2\tau^2}\bar{P}(\Delta_0,\lambda)\,\mathrm{d}\Delta_0\,\mathrm{d}\lambda. \tag{3.4}$$

The integration is performed on all TLS that can interact with the phonon. Here, $\bar{P}(\Delta_0,\lambda)$ is the number density of TLS with energy asymmetry between Δ_0 and $\Delta_0+\mathrm{d}\Delta_0$ and tunnel parameter between λ and $\lambda+\mathrm{d}\lambda$,

$$n_0 = \frac{1}{e^{E/k_BT}+1} \tag{3.5}$$

is the thermal equilibrium Boltzmann repartition function, c_s the speed of sound, ρ the mass density of the solid, τ the relaxation time of the individual TLS and B the coefficient linking a deformation δe to a change of E via $\delta E = 2B(\Delta_0/E)\delta e$. A mechanical quality factor of

$$Q_m^{-1}(T) = \frac{c_s l^{-1}(T)}{\Omega_m} \tag{3.6}$$

can then be deduced. For the corresponding relative change in the speed of sound (i.e. frequency shift of a mechanical resonance) one obtains from the Kramers-Kronig relations

$$\delta\Omega_m(T) = -\frac{\Omega_m}{2\rho c_s^2}\iint\left(-\frac{\partial n_0}{\partial E}\right)4B^2\frac{\Delta_0^2}{E^2}\frac{1}{1+\Omega_m^2\tau^2}\bar{P}(\Delta_0,\lambda)\,\mathrm{d}\Delta_0\,\mathrm{d}\lambda. \tag{3.7}$$

Tunneling-assisted relaxation

Within the framework of the so-called tunneling model [81, 82] the relaxation time is given by

$$\tau = \tau_{\mathrm{m}} \frac{E^2}{\Delta_1^2}, \quad \text{with} \quad \tau_{\mathrm{m}}^{-1} = \frac{3}{c_{\mathrm{s}}^5} \frac{B^2}{2\pi\rho\hbar^4} E^3 \coth\left(\frac{E}{2k_{\mathrm{B}}T}\right), \tag{3.8}$$

where τ_{m} is the maximum relaxation rate. Parameterizing the integrals in terms of the energy splitting E and the parameter $u = \tau^{-1}/\tau_{\mathrm{m}}^{-1}$ yields [81, 82]

$$Q_{\mathrm{tun}}^{-1}(T) = \frac{2\bar{P}B^2}{\rho c_{\mathrm{s}}^2} \int_0^\infty \left(-\frac{\partial n_0}{\partial E}\right) \Omega_{\mathrm{m}} \tau_{\mathrm{m}} \int_0^1 \frac{\sqrt{1-u}}{u^2 + \Omega_{\mathrm{m}}^2 \tau_{\mathrm{m}}^2} \, \mathrm{d}u \, \mathrm{d}E \tag{3.9}$$

and

$$\delta\Omega_{\mathrm{tun}}(T) = -\frac{\Omega_{\mathrm{m}} \bar{P} B^2}{\rho c_{\mathrm{s}}^2} \int_0^\infty \left(-\frac{\partial n_0}{\partial E}\right) \int_0^1 \frac{u\sqrt{1-u}}{u^2 + \Omega_{\mathrm{m}}^2 \tau_{\mathrm{m}}^2} \, \mathrm{d}u \, \mathrm{d}E, \tag{3.10}$$

where it is assumed that the density $\bar{P}(E,\lambda) = \bar{P}$ is constant, which is justified by comparison to solid-state experiments [81]. A prominent feature in this regime is a plateau of the quality factors for temperatures of a few Kelvins with Q values of

$$Q_{\mathrm{plateau}}^{-1} = \frac{\pi}{2} \frac{\bar{P}B^2}{\rho c_{\mathrm{s}}^2}. \tag{3.11}$$

Thermally activated relaxation

At higher temperature the rate is given by the Arrhenius law and only depends on the energy barrier height,

$$\tau_{\mathrm{th}}^{-1} = \tau_0^{-1} e^{-V/k_{\mathrm{B}}T}, \tag{3.12}$$

where τ_0 represents the period of oscillation in individual wells [84, 81]. Figure 3.4 (2.10) illustrates the low (high) temperature behavior of the mechanical quality factors as a function of temperature, where resonant and tunneling contribution (thermally activated relaxation) are taken into account to fit the data. In both cases a weak probe laser beam was locked to an optical resonance while the temperature of the cryostat was varied.

3.2.2 Resonant processes

For resonant interaction between phonons and TLS, it can be shown that [81, 82]

$$Q_{\mathrm{res}}^{-1}(T) = \frac{\pi \bar{P} B^2}{\rho c_{\mathrm{s}}^2} \tanh\left(\frac{\hbar \Omega_{\mathrm{m}}}{2 k_B T}\right) \tag{3.13}$$

$$\delta\Omega_{\mathrm{res}}(T) = \frac{\Omega_{\mathrm{m}} \bar{P} B^2}{\rho c_{\mathrm{s}}^2} \ln\left(\frac{T}{T_0}\right), \tag{3.14}$$

where T_0 is an arbitrarily chosen reference temperature. While resonant processes do not significantly contribute to the mechanical quality factors in our experiment, the frequency shift is dominated by resonant processes (cf. Fig. 3.4).

3.2.3 Fitting the TLS model

The curves shown in Fig. 3.4 have been fitted with the equations given in the previous sections. For the frequency shift the sum of the tunneling relaxation and the resonant contribution has been taken into account. The latter dominates this effect up to about $T = 2$ K. The contribution of thermally activated relaxation has been omitted since it doesn't contribute significantly in the considered temperature range. Fitting of the Q-dependency has been done using the sum of tunneling relaxation, resonant contribution and a constant offset accounting for the clamping losses (Q_{cla}^{-1}), i.e. loss of acoustic energy due to leaking into the substrate for this particular toroid. Here the resonant contribution plays a minor role. For the curves shown in Fig. 3.4, we used the material parameters

$$c_{\mathrm{s}} = 5800\ \mathrm{m/s}, \quad \rho = 2330\ \mathrm{kg/m^3},$$

the measured resonance frequency

$$\Omega_{\mathrm{m}} = 2\pi \times 76.3\ \mathrm{MHz},$$

as well as the adjusted parameters

$$B = 1.1 \times 10^{-19}\ \mathrm{J}, \quad \bar{P}_{Q_{\mathrm{m}}} = 2.5 \times 10^{45}\ \mathrm{m^{-3}}, \quad \bar{P}_{\Omega_{\mathrm{m}}} = 4.6 \times 10^{45}\ \mathrm{m^{-3}}.$$

For the fitting of the two curves (mechanical quality factor, resonance frequency shift) two different values for $\bar{P}$ had to be used. Given that the two traces are governed by two different regimes, small differences in the density of contributing TLS to the two effects seem to be justified. The literature [75] value of the dimensionless parameter $C = \bar{P} B^2/(\rho c_s^2) = 3.0 \times 10^{-4}$ shows a reasonable agreement with the parameters of the resonance frequency ($C_{\Omega_{\mathrm{m}}} = 7.1 \times 10^{-4}$) and damping ($C_{Q_{\mathrm{m}}} = 3.9 \times 10^{-4}$) fits. These

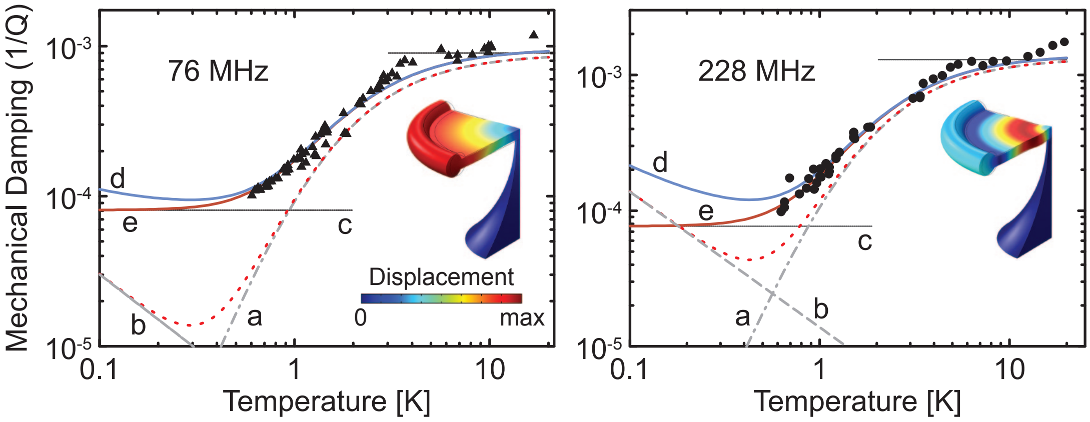

Figure 3.5: **Detailed analysis of different contributions to mechanical damping.** This graph shows measured (black triangles and dots) and fitted (d+e) quality factors as a function of temperature for two mechanical modes at 76 MHz and 228 MHz. Herein, (a) is the contribution from relaxational damping and (c) corresponds to the estimated clamping losses of the mechanical modes. Finally, (b) corresponds to the contribution from non-saturated TLS. (d) and (e) correspond to the traces expected for perfectly thermalized and completely saturated TLS, respectively. The insets show FEM simulations of the mechanical modes, where colors indicate displacement.

fits will also be used in section 4.2, where the TLS properties help to independently calibrate the temperature of the toroids.

3.2.4 Resonant saturation phenomena

In an early experiment in Munich, just before switching laser systems from 1550 nm to 780 nm the effect of saturable absorption was examined. Many physical systems exist that can be modeled or approximated as two-level systems—(some) electronic transitions in atoms, spins in a magnetic field or the manifold of experimental qubit implementations. They can, as previously introduced, also be used as model for defect states in solid material [85]. An excited and a ground state, as well as a coupling rate for resonant absorption or stimulated emission (that depends on the incoupled power of a resonant oscillation) and a spontaneous emission rate (resonant and off-resonant) is required to describe their dynamics. A weak resonant beam is attenuated, as part of its energy is used to excite TLS which is subsequently lost into the thermal environment of the TLS. Once the external driving is strong enough to compete with or even overcome spontaneous emission, the mean occupation is no longer described by Boltzmann's law, but the occupancy difference decreases. Simultaneously, the attenuation of the driving is decreased as the maximum power that can be dissipated into the TLS is limited—a process called saturable absorption.

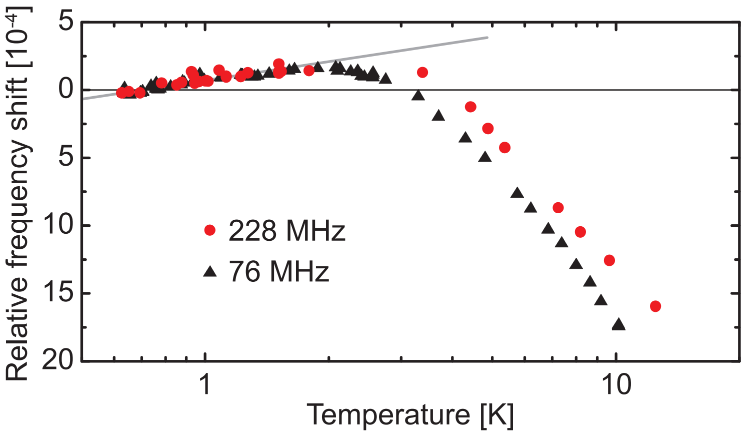

Figure 3.6: **Relative mechanical frequency shift vs. temperature.** This graph shows the relative mechanical frequency shift for the first and second order radial breathing mode, as well as a fit in the relevant temperature range. Fitting yields the functional description: $\frac{\Delta\Omega_\mathrm{m}}{\Omega_\mathrm{m}} = 2.0\times10^{-4}\ln T/T_\mathrm{ref}$, where $T_\mathrm{ref} = 0.7\,\mathrm{K}$ is an arbitrarily chosen reference temperature. Scatter is due to uncertainties in the effective temperature measurement.

The TLS under consideration here can be driven by mechanical phonons or also electric fields and one expects a change of the mechanical quality factor as a function of this driving. Here, a two laser pump-probe scheme was used, where a driving (pump) laser is amplitude modulated and drives the mechanical mode while a second one is used to probe its mechanical quality factor. Therefore, the two lasers are both locked to well-separated ($\gg 1\,\mathrm{nm}$) optical modes of the microtoroid.

As the contribution of saturable absorption to the quality factor is very small for a resonator with a resonance frequency below 100 MHz and the accessible temperature range in our setup, this experiment was not only performed using the fundamental radial breathing mode at (here:) $\Omega_\mathrm{m}/2\pi = 76\,\mathrm{MHz}$, but also using the second order mode at about three times higher frequency (here: $\Omega_\mathrm{m}/2\pi = 228\,\mathrm{MHz}$). As can be found in Fig. 3.5, the expected resonant contribution is significantly higher. At a later point, also the third order mode could be detected, which was found to be at $\Omega_\mathrm{m}/2\pi = 375\,\mathrm{MHz}$. Obviously, the small expected changes at around 750 mK of $\Delta Q_\mathrm{m}/Q_\mathrm{m} \approx 3(15)\%$[1] for the first (second) order mode require an enormous stability of the experiment, as already a small change of the toroid's temperature (via the cryostat temperature, or induced by a change in coupling, polarization, input power or detuning) leads to comparable effects. Validation of the toroid's temperature can be accomplished by noise thermometry of a non-driven mechanical mode, however, in order to avoid any static heating, very low optical power levels were used, rendering this kind of thermometry very inaccurate. Instead, the mechanical frequency of

---

[1] Note, that the corresponding population imbalance of a thermalized, resonant TLS is only of the order 2.5‰(7.5‰)!

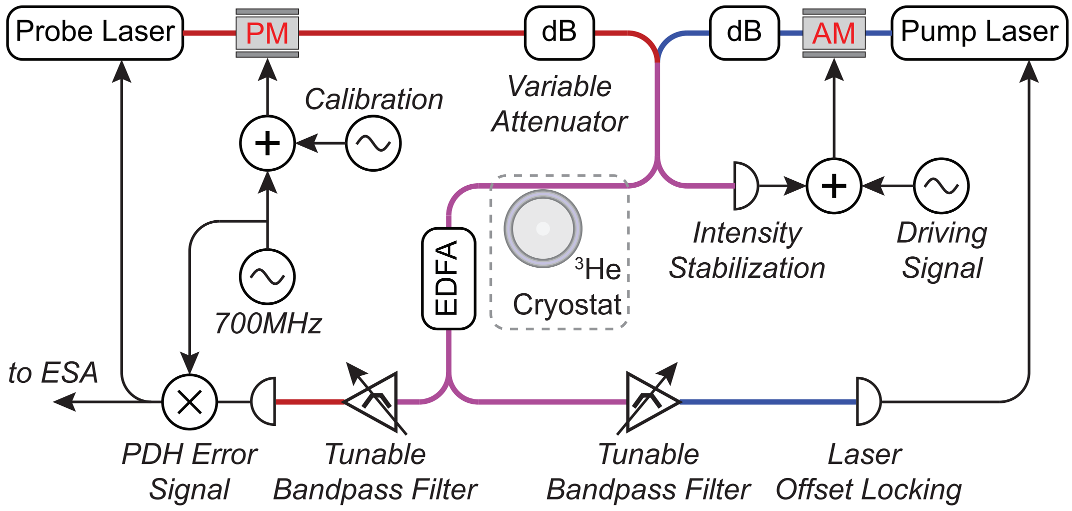
Probe Laser
PM
dB
Variable Attenuator
dB
AM
Pump Laser
Calibration
700MHz
EDFA
^{3}He Cryostat
Intensity Stabilization
Driving Signal
to ESA
PDH Error Signal
Tunable Bandpass Filter
Tunable Bandpass Filter
Laser Offset Locking

Figure 3.7: **Pump-probe scheme used to examine saturable absorption.** Refer to text for details.

the considered mechanical mode itself was used as a thermometer (cf. Fig. 3.6c)), which can easily be extracted from a fit and compared to an independent calibration measurement as shown in Fig. 3.6. The employed setup is depicted in Fig. 3.7. The two lasers—a Koheras fiber laser and a diode laser, serving as probe and pump, respectively—are superimposed on a 2-by-2 fiber splitter, where one of the two output ports is passing the cryostat and coupled to the toroid. The other port is sent to a photo diode whose output signal is used to feed back onto an amplitude modulator in the pump beam path in order to stabilize the total injected power. Additionally a signal used to drive the mechanical mode is added. The transmitted signal is amplified by a low-noise EDFA and the two lasers are separated using tunable optical bandpass filters with a 1nm-transmission window. Both laser beams are sent onto photo diodes, where the pump signal is used to lock the pump to a cavity mode by a simple offset lock. A phase modulator in the probe beam, driven by a 700 MHz signal generator, is used for PDH locking the probe laser to another cavity mode and for detection of mechanical motion on an electronic spectrum analyzer. Additionally, a phase calibration peak can be added. The low power levels used are adjusted using variable optical attenuators. As no network analyzer with sufficient sensitivity and bandwidth was available for these experiments, the mechanical response was reconstructed by stepping the driving signal frequency across the mechanical resonance and by demodulating the signal on an ESA in zero span mode.

Fig. 3.8 shows the data obtained for the first order RBM. While care has been taken to minimize all effects masking or mimicking saturable absorption, the scatter of the mechanical quality factor is still too large to allow conclusive results. The very same experiments have been done for the second order RBM. Fig. 3.9 shows the

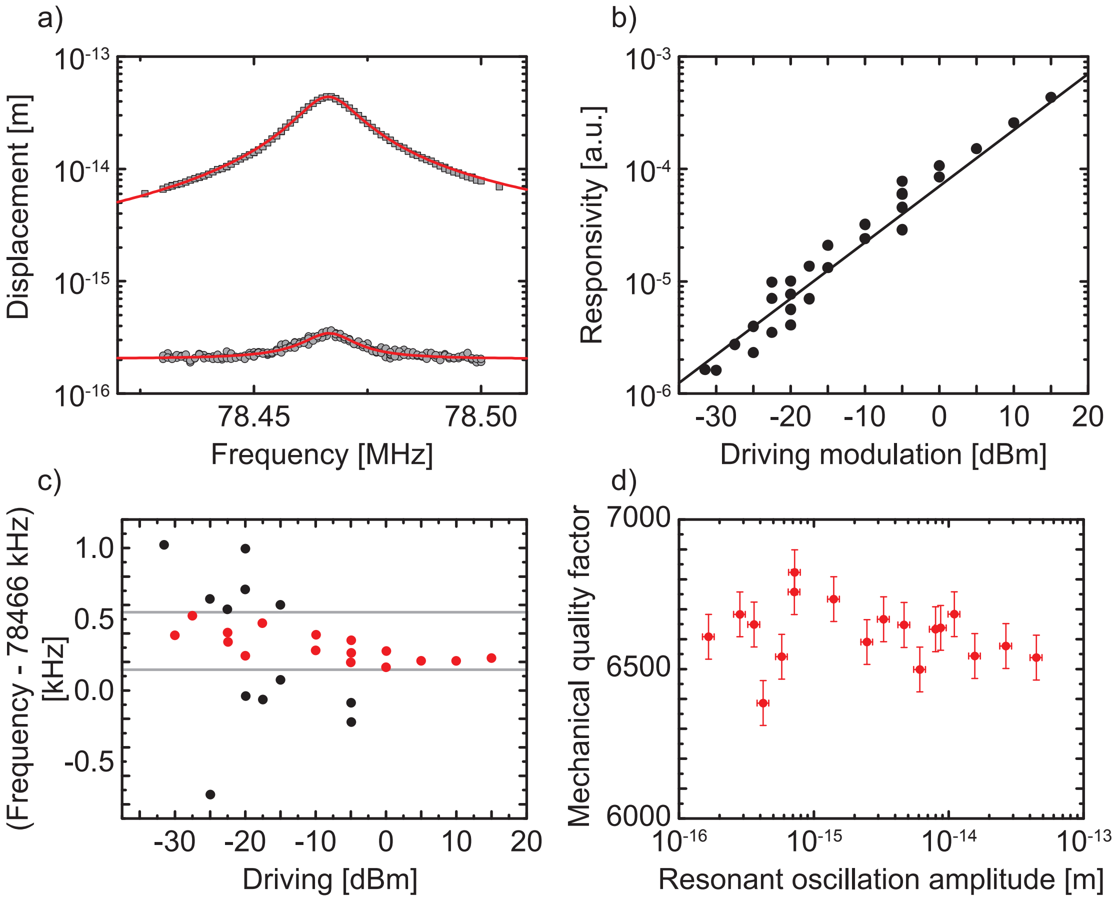

Figure 3.8: **Saturable absorption for the 76 MHz first order RBM.** *a)* Displayed are the traces obtained at the highest and lowest driving power. Data are obtained by stepping the amplitude-modulation frequency across the resonance and by demodulating the transmission with an electronic spectrum analyzer. *b)* Plot of the signal height vs. the power sent to the amplitude modulator. The black line corresponds to a linear fit to the data, confirming the linearity of the driving. *c)* While one does not expect any frequency shift of the mechanical mode for resonant and weak laser beams, some scatter is observed, indicating optical effects or—more likely—small deviations of the toroid's temperature or the power in the two laser beams. This is why, a tolerance interval of 400 Hz was chosen, corresponding to a temperature uncertainty of 18 mK (cf. Fig. 3.6) and all out-lying points were cut off. *d)* Plotted is the mechanical Q vs. the oscillation amplitude on resonance for the remaining points. Due to the large scatter, the expected saturable absorption effect (with a change in Q of less than 200) is not visible.

graph equivalent to Fig. 3.8d. Several similar experimental runs suggest that indeed the saturation behavior can be seen. The data indicate that saturation occurs at an oscillation amplitude of around 0.5×10^{-15} m. According to Jaeckle [82] the acoustic

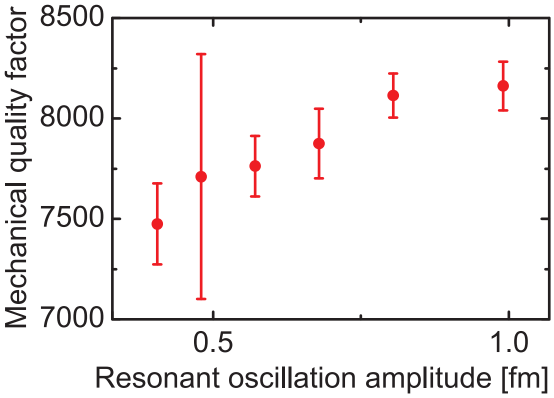

Figure 3.9: **Saturation behavior of the second order radial breathing mode.** This graph shows data obtained as in Fig. 3.8 but monitoring the second order mode of resonance frequency $\Omega_\mathrm{m}/2\pi \approx 230\,\mathrm{MHz}$. While one expects an increase of the mechanical quality factor by $\Delta Q \approx 1000$, one indeed finds a change approaching this value. Only the most trustworthy data points are shown in this plot. Therefore a selection has including some "soft" criteria, like for example the stability of the laser locking during the acquisition. Consequently, even if we believe that we could see saturable absorption (assured by similar trends in different experimental runs and the compatibility of theory and experiment), further (refined) experiments need to be done in order to proof these claims.

power required to begin to saturate the TLS is given by

$$J_\mathrm{a}^\mathrm{sat} = \left(\frac{1}{c_\mathrm{l}^5} + \frac{2}{c_\mathrm{t}^5}\right) \frac{\Gamma c_\mathrm{l}^3 \Omega_\mathrm{m}^3}{2\pi^2} \coth \frac{\hbar \Omega_\mathrm{m}}{2 k_B T} \tag{3.15}$$

with longitudinal $c_\mathrm{l} = 5800\,\mathrm{m/s}$ and transverse $c_\mathrm{l} = 3750\,\mathrm{m/s}$ speed of sound in silica, linewidth of the TLS frequency (according to [82]: $\Gamma/\Omega_\mathrm{m} \approx 2 \times 10^{-3}$). For a toroid of mechanical frequency $\Omega_\mathrm{m}/2\pi = 228\,\mathrm{MHz}$, in an environment at a temperature of $0.7\,\mathrm{K}$ one finds for a RBM (=longitudinal) a value of $J_\mathrm{a}^\mathrm{sat} \approx 2 \times 10^{-6}\,\mathrm{W/m^2}$. One can then estimate the corresponding mechanical displacement of the RBM required to achieve this level of saturation. In a simplified picture (corresponding to a disc with a perfectly radial mechanical mode), the flux of mechanical energy within the structure can be expressed as:

$$J_\mathrm{a} = \frac{1}{2} \rho_{\mathrm{SiO_2}} c_\mathrm{l} \Omega_\mathrm{m}^2 \Delta x^2 \tag{3.16}$$

assuming the acoustic energy density to be homogeneously distributed across the structure, propagating at the speed of longitudinal sound waves in bulk silica. Here, $\rho_{\mathrm{SiO_2}} = 2330\,\mathrm{kg/m^3}$ is the mass density of silica. Equating the two previous formulae, the rms displacement of the toroid (Δx) required for saturation can be estimated to be:

$$\Delta x^{\mathrm{sat}} = \sqrt{\frac{2 J_{\mathrm{a}}^{\mathrm{sat}}}{\rho_{\mathrm{SiO}_2} c_{\mathrm{l}} \Omega_{\mathrm{m}}^2}} \approx 4 \times 10^{-16}\,\mathrm{m}. \tag{3.17}$$

This corresponds well to the behavior observed in Fig. 3.9. It is interesting to note, that in general TLS also have an electric dipole momentum, such that they do also couple to electromagnetic (em) fields. As Laermans *et al.* [86] showed for the first time, the TLS coupling to em fields and those coupling to acoustics are mostly the same, enabling RF to mechanical / optical coupling. An envisioned, yet never performed experiment, is to use a laser to read out the mechanical quality factor (i.e. saturation), while changing the amount of em RF power shone onto the sample in some capacitive arrangement. The obtained experimental values in [86] suggest, that the intensity levels required for saturation of the second order RBM should be in the range of $1-10\,\mathrm{mW/cm^2}$, which is experimentally feasible.

The tunneling model describing TLS in amorphous materials is very old and most of its results have been carefully verified. In general, though, only parameters on averaged ensembles have been studied in great detail, the reason being that conventional measurements are not sensitive enough so address individual TLS in solids and to read out mechanical motion at a single phonon level. Since optomechanical schemes are available that are able to monitor these tiny effects, and as they can have a major influence on cavity optomechanical experiments, a lot of interest in TLS has arisen [66, 87, 88]. It has only recently been shown [89], that TLS embedded into the isolating barrier of a Josephson junction could be individually examined and frequency-tuned by applying external strain to the sample, such that a direct access to structural parameters of individual TLS became available. A detailed understanding of TLS is also of great relevance for superconducting resonators, circuits or qubit, as they constitute a major source of noise and decoherence.

3.3 Sample Design

3.3.1 Optimizing conventional toroids

A crucial prerequisite for achieving cooling of a mechanical oscillator to low phonon occupancy is the choice of an appropriate optomechanical system. As already described earlier various systems have been developed and examined in the past years. We have chosen toroidal silica microcavities for their extraordinary optical quality factors, and the high optomechanical coupling rates that can be achieved. Furthermore, they have proven in a ^{4}He-cryostat to be compatible with cryogenic environments, and all required technologies had already been developed. In this section, the design criteria for toroidal microresonators will be quickly reviewed.

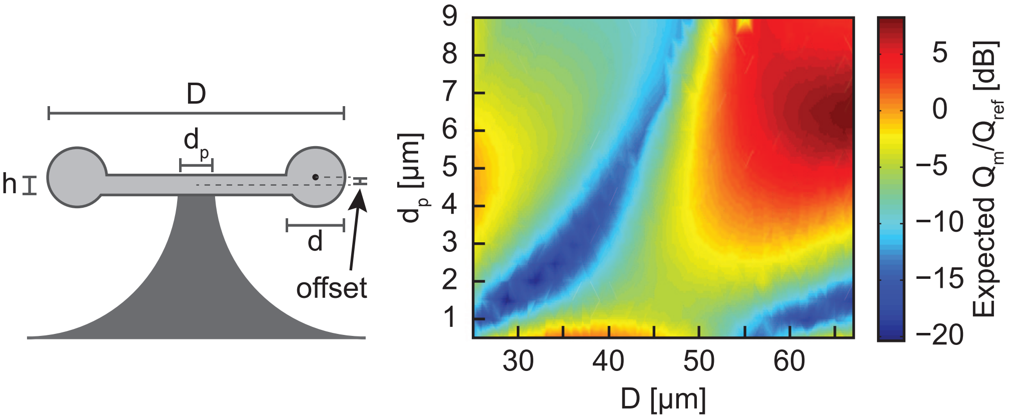

Figure 3.10: **Engineering clamping losses in conventional microtoroids.** The color plot shows the clamping quality factors simulated using finite-element modelling as a function of the toroid's diameter D and pillar diameter d_p, for the parameters $\{h, d, \mathrm{offset}\} = \{2, 5.5, 0.5\}\,\mu$m. The color code indicates the expected quality factor change in a dB scale with respect to parameters of an average (good) toroid (see section 3.3.2 for a clean definition). While this simulation has not been compared to the experiment in a strict manner, it has been found to be qualitatively correct. While toroids of diameter around $40\,\mu$m require needle pillars, diameters around $55\,\mu$m come along with good Q only for much larger pillar diameters. Also diameters below $35\,\mu$m never gave good quality factors.

For several reasons it is desirable to achieve ground state cooling at the lowest possible laser powers. Besides the obvious reason, that the available laser power in our setup is limited, at a certain threshold value also non-linear optical effects start to play a significant role [46, 90, 91]. Most importantly, however, the cooling power achieved in a cryogenic environment is very low, causing static (due to stray light, see section 3.4) or resonant (via absorbed power within the toroid) heating. Both effects do not only lead to an increased temperature of the environment, but also to a reduced mechanical quality factor as discussed in section 3.2, thus reducing the achievable occupation. In the deeply resolved sideband regime, assuming $\Gamma_\mathrm{cool} \gg \Gamma_\mathrm{m}$ the final occupancy one can hope to achieve is given by:

$$n_\mathrm{f} \approx \frac{\Gamma_\mathrm{m}}{\Gamma_\mathrm{cool}} n_\mathrm{i}. \tag{3.18}$$

With $n_\mathrm{i} = \frac{4k_B T}{\hbar\Omega_\mathrm{m}}$, $\Gamma_\mathrm{cool} = \frac{\bar{n} g_0^2}{\kappa}$, and $g_0 = x_\mathrm{zpf}\frac{\omega_\mathrm{c}}{R}$, where $x_\mathrm{zpf} = \sqrt{\frac{\hbar}{2m_\mathrm{eff}\Omega_\mathrm{m}}}$ and $\bar{n} \propto P_\mathrm{in}\kappa$ one obtains:

$$n_\mathrm{f} \propto \frac{\Gamma_\mathrm{m}}{g_0^2 P_\mathrm{in}\Omega_\mathrm{m}} T \propto \frac{\Gamma_\mathrm{m} m_\mathrm{eff} R^2}{\omega_\mathrm{c}^2 P_\mathrm{in}\Omega_\mathrm{m}} T \tag{3.19}$$

Assuming a fixed input power P_in, laser wavelength (tuned to the lower motional sideband) and environmental temperature, the only remaining parameter is $g_0^2\Omega_\mathrm{m}$, as the mechanical damping is limited by intrinsic material losses (3.2). For a simple toroid as depicted in Fig. 1.3a, there are further restrictions: to a good approximation Ω_m is inversely proportional to the toroid's radius R and the effective mass scales—if coupling to other modes is negligible—as $R^{(1...2)}$. Consequently $n_\mathrm{f} \propto R^{(4...5)}$. Thus, the strategy is to reduce the radius of the toroids to the minimum. Unfortunately, at diameters around 40 μm a natural boundary is hit, as for smaller toroids coupling to flexural (out of plane) modes becomes strong, which results in high clamping losses (see Fig. 3.10). Already in the range between $35-45\,\mu$m, the only viable way is to reduce the pillar diameter to a minimum ("needle pillar"). This does not only strongly reduce its mechanical stability but also increases the fabricational overhead, as an individual toroid, tested to have good optical properties and optionally an optical mode falling into the laser's tuning range, needs to be chosen in advance. This is because typically only one or two toroids can be fabricated to show a needle pillar, while all others remain too large, or are destroyed, due to inhomogeneities in the etching process.

3.3.2 Optimized spoke anchored toroidal resonator

One way to gain more design freedom is to use spoke anchored toroidal resonators as depicted in Fig. 1.3b. They have first been developed in our group by Anetsberger and Rivière [92], who used isotropic wet etching to transfer the spokes into the structures. This, however, prevented further miniaturization which is required to push up frequencies sufficiently.

As can be seen in eq. (3.19) it is obviously beneficial to reduce the sample dimensions to decrease R and m_eff. While this miniaturization is accompanied by an increase of the mechanical frequency Ω_m, as well as an increase of Γ_m due to enhanced clamping losses for normal toroids, here, these adverse effects are counteracted by designing the position and size of the spokes holding the toroidal resonator (see Fig. 3.11a).

The introduction of spokes serves three purposes. First, they isolate the mechanical motion of the toroidal RBM from the pillar support, which strongly reduces clamping losses [92]. Second, they reduce the mechanical mode volume and thereby the effective mass. Third, the effective spring constant is reduced, which lowers the mechanical resonance frequency. In practice, one needs to carefully consider the precise dimensions and positioning of the spokes, as these strongly affect both clamping losses Γ_clamp and g_0. Figure 3.11b shows the displacement profile of the RBM of a spoke-supported toroid of radius $R = 15\ \mu$m for various combinations of spoke length and position, as simulated with a finite element method. The $\mathrm{SiO_2}$ thickness is 1 μm,

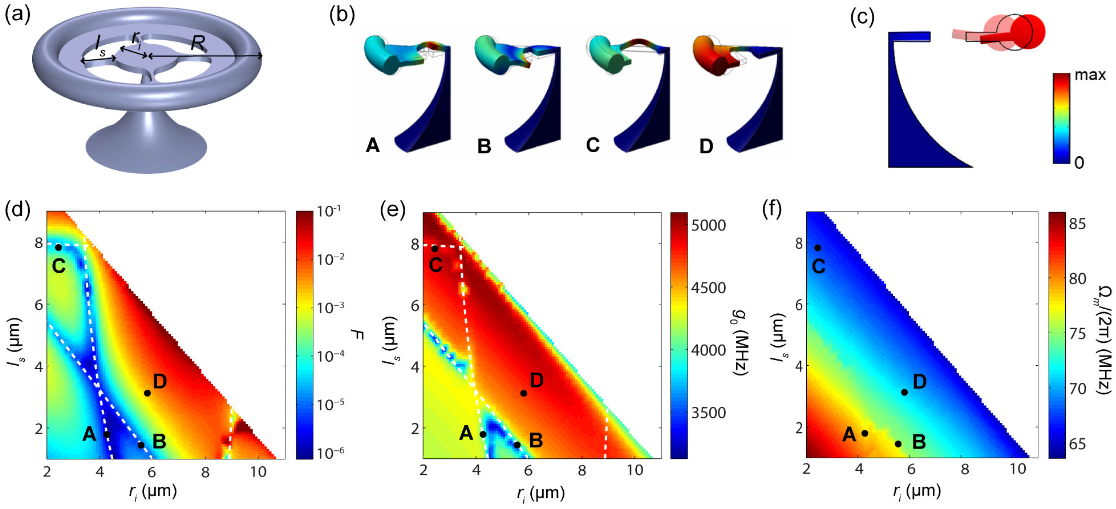

Figure 3.11: **Sample optimization by finite element modelling.** See text for details.

the minor toroid radius is 2 μm, the spoke width is 500 nm, the pillar diameter is 1 μm, and the toroid is vertically offset from the middle SiO_2 disk by 400 nm. Since we are interested in the RBM only, it suffices to simulate 1/8 portion of the microresonator while assuming symmetric boundary conditions on both of the two 'cut' planes. As can be seen from these examples, the mechanical mode profiles can change drastically depending on the spoke dimensions. Of the examples in Fig. 3.11b, only 'D' depicts a mode that is purely localized to the outer toroid, with purely radial displacement, as illustrated in the cross-section in Fig. 3.11c.

The origin of this wildly varying nature of the RBM is revealed in Fig. 3.11d, where the radius r_i of the inner disk (defining the spoke placement) and the spoke length l_s are varied systematically. The color scale depicts the parameter F, defined as

$$F = \frac{2\pi E_\mathrm{mech}}{c\rho\Omega_\mathrm{m}^2 \int_{A_\mathrm{p}} |\Delta z(\mathbf{x})|^2 \, dA}. \tag{3.20}$$

Here, E_mech is the total mechanical energy in the mode, c the speed of sound in silica, ρ the density of silica, and $\Delta z(\mathbf{x})$ the out-of-plane displacement amplitude, with the integration extending over the area A_p of the interface between the pillar and the silica disk. F is proportional to the expected value of $\Gamma_\mathrm{clamp}^{-1}$, when the clamping area A_p is considered as a membrane radiating energy with a power $P = c\rho\Omega_\mathrm{m}^2 \int_{A_\mathrm{p}} |\Delta z(\mathbf{x})|^2 \, dA$ [92]. A previous study has experimentally found a correspondence of $F \approx \left(3\Gamma_\mathrm{clamp}/(2\pi)\right)^{-1}$ for larger toroids. As can be seen from the figure, the expected clamping losses vary strongly with spoke dimensions, ranging from 10^1 to 10^6 Hz. Most notably, several lines can be identified in this parameter space where clamping losses are large (indicated by the dashed lines). For parameter combinations along each of these lines, the

RBM frequency approaches that of another mechanical mode of the structure. As a result, the two modes exhibit an anticrossing, with the hybridized modes showing a character of both uncoupled modes. This is the case for examples 'A', 'B', and 'C' in Fig. 3.11b, which show the RBM hybridized with a flexural mode of the inner SiO_2 disk, the outermost SiO_2 membrane, and the spoke itself, respectively. In the vicinity of these anticrossings, the vertical displacement at the pillar, and as such the radiation into the substrate F^{-1}, are strongly enhanced. To achieve a design that exhibits small clamping losses, it is therefore crucial to avoid these parameter regions, as is the case for mode 'D' in Fig. 3.11b. The aforementioned anticrossings affect the coupling rate g_0 as well, albeit to a lesser degree. Fig. 3.11e shows g_0, calculated as in [93], assuming the optical mode is localized at the edge of the toroid with negligible transverse size. At the anticrossings, g_0 is reduced (i.e., the effective mass is increased), as a significant part of the mode's energy is in that case associated with displacements that do not modulate the cavity length. Away from the anticrossings, however, the RBM mode is localized exclusively in the toroid and outermost part of the membrane, well isolated from the inner disk and pillar support. As a result, m_{eff} is nearly identical to the physical mass of this volume. It is therefore important to minimize the volume of the outermost membrane, i.e., the distance between the spokes and the toroid. As can be seen in Fig. 3.11f, this simultaneously allows to reach the smallest possible resonance frequency. In practice, the laser reflow process used to form the toroid poses a lower limit on the remaining distance between spokes and toroid.

Sample fabrication

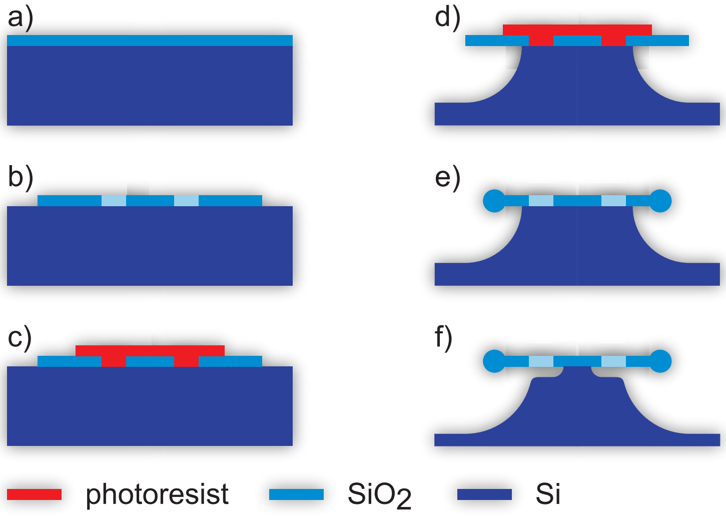

Figure 3.12: **Sample fabrication.** See text for details.

To fabricate the spoke-anchored microresonators, a combination of optical lithography and dry etching techniques outlined in Fig. 3.12 is used. In a first step *(b)*, a disk including the spokes is transferred into a 1 μm thick film of thermal oxide on a Si wafer *(a)*, through optical lithography followed by reactive ion etching of the SiO_2. In a second photolithography step *(c)*, smaller disks of photoresist are defined that cover the center of the SiO_2 disks, including the spokes. These serve to protect the exposed Si surface between the spokes during the subsequent isotropic XeF_2 etch *(d)* of the Si substrate. Care is taken to stop the etch shortly before it reaches the apertures in the SiO_2 disk. After removing the protective photoresist disks, a laser reflow of the underetched disk is performed *(e)*, forming the silica toroid. Finally *(f)*, a second XeF_2 etch releases the toroid and reduces the pillar diameter, typically to a value smaller than 1 μm. The fabrication process with XeF_2 strongly depends on the sample's surface. This is why wafer scale processing of the samples is not feasible, as it would take way too long.

An alternative process to replace the first XeF_2 etching step has been developed, based on reactive ion etching with SF_6/O_2 as process gases and is successfully used in other experiments [94]. Very smooth surfaces and good optical quality factors could be obtained in this way. However, for an unknown reason, this process is not compatible with an additional, second XeF_2 etching step. It has been found, that optical quality factors are degraded severely.

Sample characterization

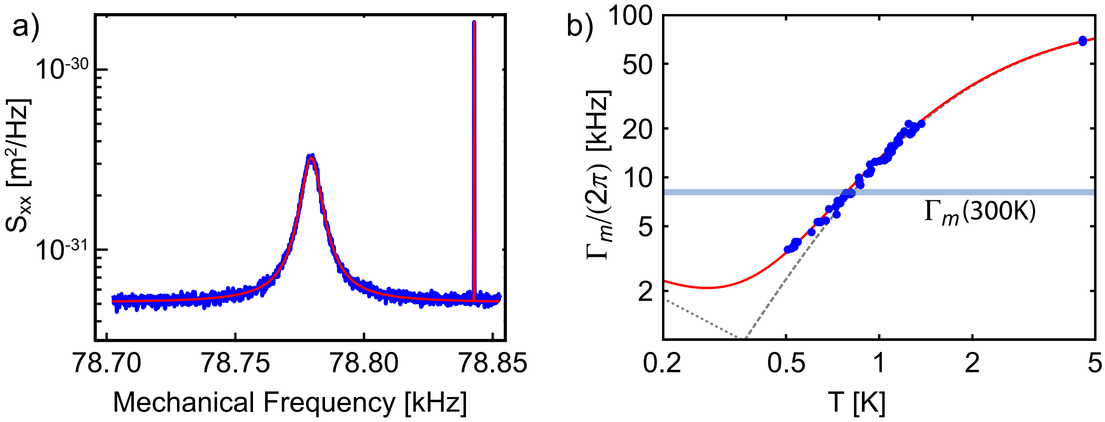

Figure 3.13: **Sample characterization.** a) shows a calibrated mechanical noise spectrum for the resonator described here and used throughout 3.2, which was measured at room temperature in vacuum. The fit (red line) was used to extract a vacuum optomechanical coupling rate of 3.4 kHz at 780 nm. b) mechanical damping of this toroid vs. cryostat temperature. The red line is a fit according to the TLS model presented in 3.2, the grey lines represent the contributions from resonant (dotted) and relaxational (dashed) processes. The fit yields a negligible contribution of clamping losses. The blue solid line indicates the mechanical linewidth measured at room temperature.

The vacuum optomechanical coupling rate g_0 is measured at room temperature in a vacuum chamber. Therefore, the mechanical motion is read out using an external cavity tunable diode laser at 1550 nm that is locked to a cavity resonance. In order to avoid any radiation pressure effects these measurements are done at very low laser power (typically around 100 nW). The transmitted light is amplified by a low noise erbium-doped fiber amplifier and sent onto a photodector. For absolute calibration of the mechanical spectrum registered by an electronic spectrum analyzer, a phase-modulation technique is used ([48] and section 3.3.2). Vacuum optomechanical coupling rates in excess of $g_0/2\pi = 2.0\,\text{kHz}$ for a wavelength of 1550 nm (i.e. $g_0/2\pi = 4.0\,\text{kHz}$ at $\lambda = 780\,\text{nm}$) have been found in this way, which corresponds to a more than threefold improvement over conventional toroids ($g_0/2\pi = 1.2\,\text{kHz}$ at $\lambda = 780\,\text{nm}$ has been measured for the sample used in section 3.2) The measured mechanical linewidth for small spokes-supported structure has been found to be generally higher (for the sample used in section 4.3: $\Gamma_\text{m}(300\,\text{K})/2\pi = 8.1\,\text{kHz}$) than expected from the calculated F-parameter. However, performing the same measurements in the cryostat, lower linewidths (as low as $\Gamma_\text{m}/2\pi = 3.6\,\text{kHz}$ for the sample used for section 4.3, cf. Fig. 3.13b) are found on the same microresonators, indicating that a loss mechanism other than clamping losses must dominate at room temperature. Since their losses due to two level fluctuators (TLS, [81, 66]) have been found to be significantly lower (linewidths below 4 kHz have been measured at room temperature for conventional toroids of similar frequency), we believe that the dominating loss mechanism is thermo-elastic damping (TED) [95]. At low temperatures, where TED is strongly reduced, the main loss mechanism is coupling to TLS. Figure 3.13b shows the measured temperature dependence of the mechanical linewidth at low temperature, obtained with a very low-power laser (with 100 nW power) resonant with a strongly overcoupled optical resonance to avoid dynamical backaction. The variation of Γ_m with temperature is fitted using a model for the TLS losses (compare 3.2). It is found that this mechanism dominates the total losses for all reachable cryogenic temperatures. This means that it is not possible to retrieve an accurate estimation of the temperature-independent contribution Γ_clamp. We can however conclude that it must be at least smaller than 2 kHz for this sample. This shows that in our optimized spoke-supported design, we have successfully mitigated the clamping losses to the level where they are insignificant compared to intrinsic dissipation.

3.4 Sample degradation and static off-resonant heating

The first cooling experiments, where the effective temperature of the mechanical mode was measured as a function of the laser detuning, revealed that off-resonant heating plays an important role. With a laser detuned far beyond the cooling sideband (such that any resonant heating or optical effects could be neglected), but close enough to an optical resonance to still see a mechanical spectrum, an increase of the mechanical mode's effective temperature, as well as an increase of the mechanical linewidth and frequency (both consistent with the TLS effects for increased temperatures) was found. This was also confirmed in an experiment involving a weak resonant read-out laser and a separate off-resonant laser of varying power that is shown later (cf. section 3.4.2). Indeed, when observing the optical fiber in a microscope while 780 nm light was passing through, which is still visible to the silicon CMOS camera in use, the fiber was shining, due to many small scattering centers as depicted in Fig. 3.14a, suggesting that scattered light from the tapered fiber is absorbed in the silicon substrate giving rise to a local increase of the environmental temperature.

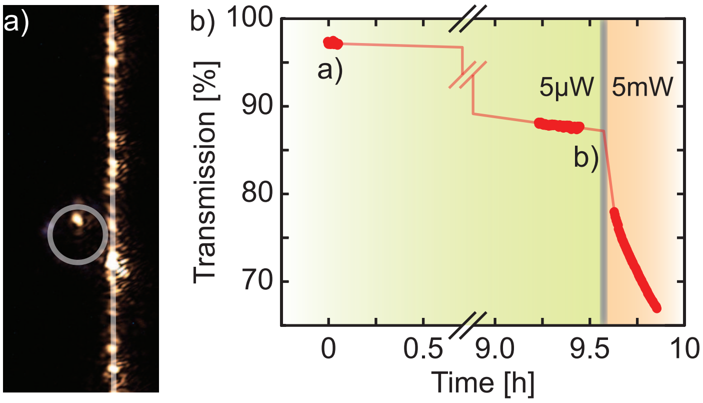

Figure 3.14: **Light scattering from tapered fibers.** *a)* shows a camera image of a tapered fiber coupled to a toroid in the cryostat. The injected laser light is resonant with cavity mode. Individual scattering centers are clearly visible. It could be proven, that scattering is partly due to dust particles. *b)* shows the temporal evolution of a tapered fiber, fabricated at $t = 0$ with an injected light power of $5\,\mu$W. During almost 10 h the transmission drops by only about 10%, whereas after increasing the light power to 5 mW, it rapidly decays on a timescale of 15min.

It was found, that partly scattering arose from dust particles (that could be identified in an SEM) sticking to the tapered fiber. Also it was observed, that sometimes scattering centers were transferred to the toroid surface when touching, leading to modal splitting, and in general samples degraded within days. One reason for the contamination was—besides the fact, that fibers were fabricated and handled in a non-cleanroom environment at MPQ, which is no longer the case now at EPFL—that the amount of light injected into the fiber during the tapering process was generally rather high (on the order of 1 mW). The strong field gradients in the evanescent field in the vicinity of the tapered region gives rise to dipole forces attracting dielectric media such as dust particles. This effect could be proven by fabricating a tapered fiber at very low transmitted laser power and by monitoring transmission . During almost 10 hours, only a 5% change of the transmission was observed. Increasing the injected laser power to 5 mW, however, led to an instantaneous and rapid decay of transmission (cf. Fig. 3.14b).

Unfortunately, solving the dust contamination problem did not solve the entire problem. As we found out, a small contamination of the helium-3 gas by nitrogen causes the formation of nitrogen crystals on the sample and taper leading to similar effect, especially also modal splitting of the resonances, which does explain the degradation inside the cryostat.

3.4.1 Optimized cool-down strategy

Heating the sample to the boiling point of nitrogen does allow to recover small or even negligible modal splitting. Partly, the toroids could be unfrozen by simply heating the sample to around 90 K within the cryostat, or by shining a 10 W Coherent Verdi laser through the optical window onto the sample. However, the best results were achieved by avoiding any freezing to the sample and taper by optimizing the cool-down process. Therefore, during the insertion of the probe, special care has to be taken to make sure, that other parts of the cryostat are significantly colder than the cryohead at any time. In our case, the easiest approach is to insert the probe rather fast, while maximally cooling the sorb. Since in general it holds the entire volume of helium-3 when being cold, heating of the sorb leads to outgassing of He-3 and consequently an increased thermal contact, which can lead to a thermal runaway process. Therefore, before inserting the probe, the He-3 is entirely removed from the inner part of the cryostat and stored in the external reservoir and only slowly admitted after the probe is inserted. Fig. 3.15 shows an example of a very successful cool-down where the sorb temperature could be kept much below the sample temperature at any time.

Degradation of samples inside the cryostat, which was a severe problem in the early phase of the experiment, can be entirely avoided in this way and samples can now be used for months. However, even though the scattering of light can be almost completely avoided, the off-resonant static heating seems not largely affected.

3.4.2 Pump and probe measurements

A pump and probe experiment done at EPFL was set up in order to quantify the off-resonant heating with two lasers as depicted in Fig. 3.16a. Therefore, a very weak probe at $\lambda \approx 780\,\mathrm{nm}$ with an optical power of $P_{\mathrm{in}} \approx 100\,\mathrm{nW}$ is tuned to a resonance of a strongly overcoupled toroid. The transmitted probe signal is used to acquire a mechanical noise spectrum in a homodyne setup permitting to extract mechanical resonance frequency and linewidth, as well as the mechanical mode's effective temperature. The power is chosen such that the toroid's temperature and motional state is unaffected.

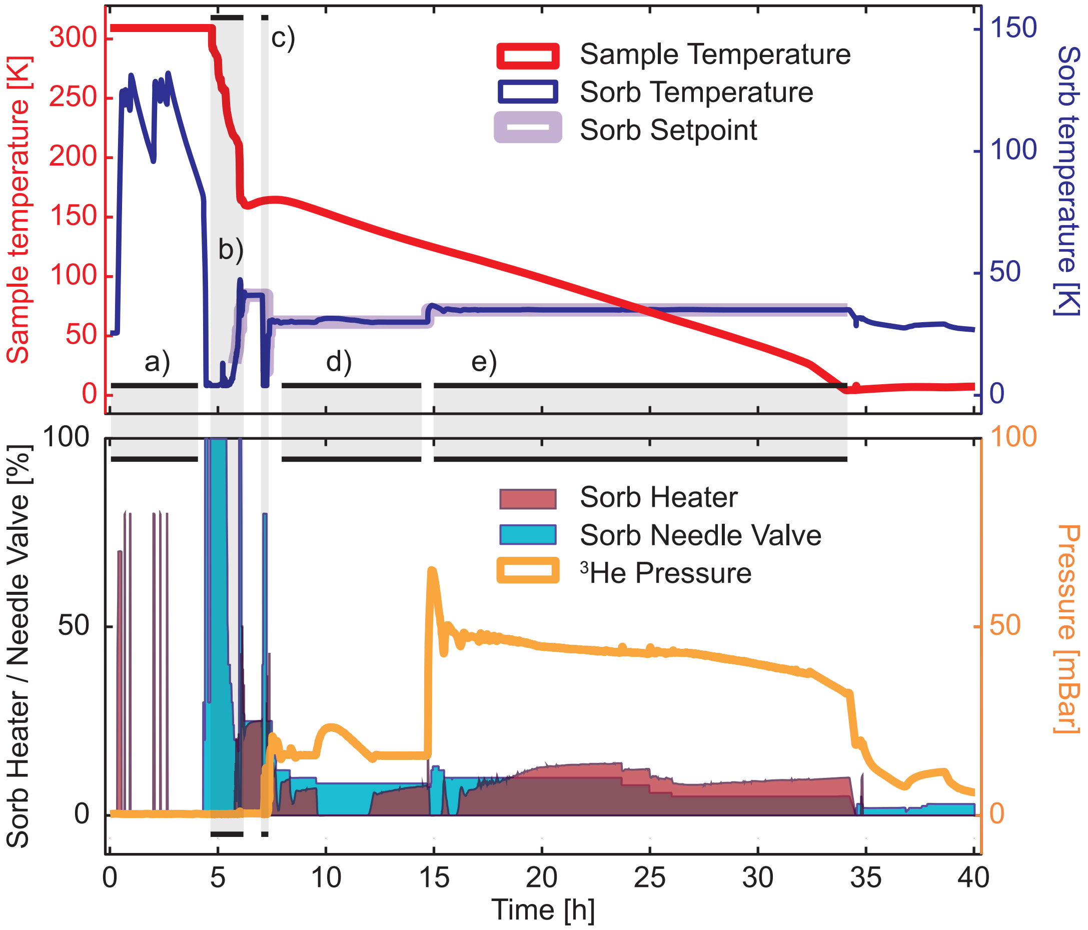

Figure 3.15: **Example of a successful cooldown.** Shown here is an example of a successful cool-down, in a sense that the sample's temperature stayed at any time largely above the sorb's (note the different y-scales). The two graphs include, with a common time axis, the sample's and sorb's temperature *(top)* as well as *(bottom)* the sorb heater power and needle valve opening in relative units and the background pressure of the helium-3. In phase *(a)* the load lock, housing the prepared probe, is evacuated and simultaneously the helium-3 is removed from the inner vacuum chamber. Therefore, the sorb's temperature is heated to 120 K, in order to release much of the adsorbed helium-3 that can then be efficiently pumped into the external sorb. Before opening the load lock, the evacuation is stopped and the sorb is maximally cooled. Insertion of the probe is done in a steady way, such that the sorb's temperature does not increase too much (here: not above 50 K). Note that there is no significant background pressure of helium-3 or any contaminant in this phase. Once the probe is entirely inserted and some time has passed, the sorb is once again maximally cooled *(c)* and the helium-3 gas is admitted very slowly into the cryostat and immediately bound inside the sorb. Afterwards, the sorb's temperature is slightly increased *(d+e)* increasing the gas pressure inside the cryostat to speed up the cooling of the probe. Care needs to be taken to avoid the thermal run-away process described earlier, so the background pressure is increased further only after a while *(e)*. Once the sample is cooled to around 4 K, the sorb is kept below 30K and is only temporarily heated further during the condensation of helium-3, as it has been found, that no degradation of the cold sample is seen for sorb temperatures below 35 K.

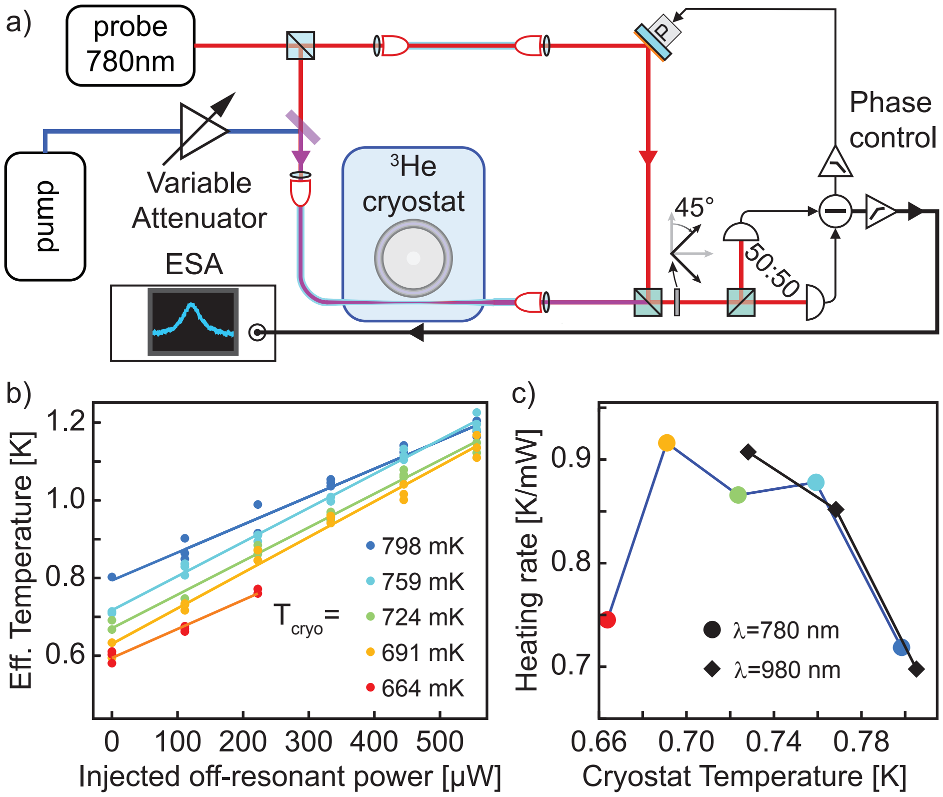
a)
probe 780nm
pump
Variable Attenuator
ESA
^{3}He cryostat
Phase control
45°
50:50
b)
Eff. Temperature [K]
1.2
1.0
0.8
0.6
0
100
200
300
400
500
Injected off-resonant power [μW]
T_{cryo}=
798 mK
759 mK
724 mK
691 mK
664 mK
c)
Heating rate [K/mW]
0.9
0.8
0.7
0.66
0.70
0.74
0.78
Cryostat Temperature [K]
λ=780 nm
λ=980 nm

Figure 3.16: **Measurement of static off-resonant heating.** See text for details.

Coinjection of a second off-resonant laser beam into the signal arm of the balanced homodyne setup then allows tracking the change in effective temperature as a function of the off-resonant power. In this case, as one can safely neglect optical backaction, the effective temperature is assumed to be equal to the temperature of the local environment of the toroid. Fig. 3.16b shows the results obtained for several cryostat setpoints and an off-resonant pump wavelength of about $\lambda \approx 780\,\text{nm}$. The slopes of the linear fits (solid lines) are then plotted as a function of the cryostat setpoint in Fig. 3.16c (circles). Additionally, the very same experiment has been done with a pump laser at $\lambda \approx 980\,\text{nm}$ (black squares). The two traces are coinciding nicely, which indicates that the heating mechanism has most probably nothing to do with an absorption in fused silica, as the absorption coefficients at $\lambda \approx 780\,\text{nm}$ and $\lambda \approx 980\,\text{nm}$ are small (cf. 3.2).

The heating rate of around 0.8 K/mW can be compared to the off-resonant heating rate of 0.1 K/mW estimated for [2][2]. There, the cryostat setpoint of $T_{\text{cryo}} = 850\,\text{mK}$ was slightly higher, but still this number suggests, that the main contribution to static heating is indeed not due to the scattering centers.

---

[2] cf. section 4.2, the frozen nitrogen issue has not yet been solved at that time

The current working hypothesis is, that the heating is caused by non-adiabaticities of the fiber (i.e. a too rapid change of the fiber's diameter) itself, leading to a forward scattering of light, which is not captured by the camera but still absorbed on the silicon chip. This explanation would be compatible also with the fact, that off-resonant heating at $\lambda = 780\,\mathrm{nm}$ and $\lambda = 980\,\mathrm{nm}$ is similarly strong, as reflectivities (33% vs. 32%) and absorption depths ($10\,\mu$m vs. $100\,\mu$m, i.e. very small) are comparable [96, 97].

To circumvent this problem, it is envisaged to work with slightly longer tapered fibers. An alternative approach might be to put a reflective layer onto the silicon close to the toroid, such that the optical power is dissipated elsewhere, far away from the sample. The cernox temperature sensor, which is only a few millimeters away, does essentially not show an increase in temperature for these moderate optical power levels, which indicates, that the cooling power of the cryostat itself is not yet the limiting factor.

3.5 Quantum limited measurements - revisited

A crucial prerequisite for optomechanical measurements in the quantum regime is the use of a quantum limited light source. From the point of view of quantum manipulations, added noise in the coupling beam corresponds to an improper state preparation, the optical beam being in a statistical mixture of pure quantum states. In the weak coupling limit $\Omega_c \ll \kappa$, where the optical field acts as an effective bath, these extra fluctuations correspond to an increased temperature of the bath and prevents cooling close to the quantum ground state [74, 98, 99, 100]. In addition, classical laser noise driving the optomechanical system can lead to ambiguous signatures such as squashing in the noise spectra, as reported previously [101]. During the first experiments conducted at EPFL it became apparent that the laser light that was sent to the resonator was not completely quantum limited in its phase quadrature, but single classical peaks could be found in the measured spectra (see Fig. 3.18b, blue trace). In order to enhance the responsitivity to classical phase noise the homodyne detection was artificially imbalanced. Fig. 3.17 shows spectra obtained in this configuration, where a strong local oscillator power P_{LO} and different signal power levels P_{sig} were injected.

In the ideal situation of a quantum-limited light source, with $P_{\mathrm{sig}} \ll P_{\mathrm{LO}}$ one does expect the traces measured on a spectrum analyzer to scale with the total injected power $P_{\mathrm{sig}} + P_{\mathrm{LO}}$[3]. The laser source itself could be ruled out as the origin of the peaks, as the employed Ti:Sapph is known to exhibit only quantum fluctuations at the Fourier frequencies of interest. Besides the laser source also the optical fibers used to guide the light to the microresonator can affect the noise properties of the laser light.

---

[3] The optical power spectral density on the receiver scales like the square root of the total power but is converted into a voltage.

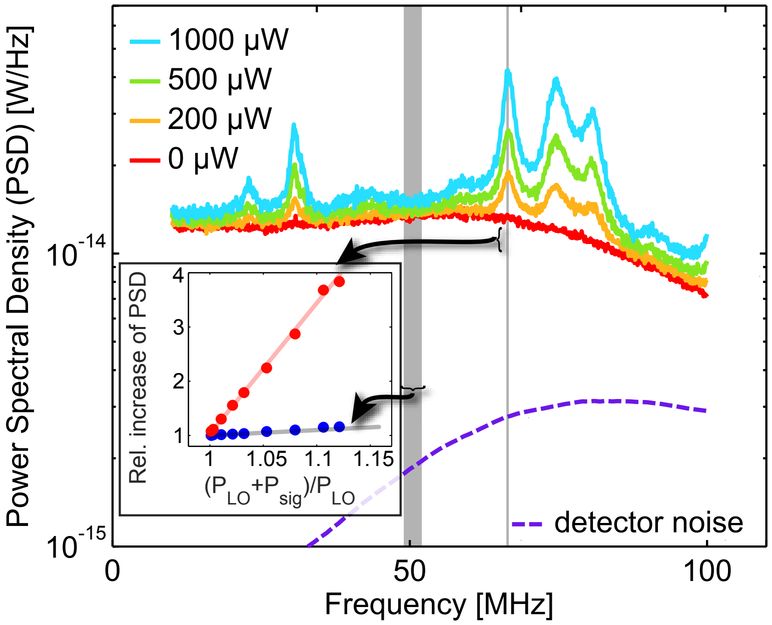

Figure 3.17: **Shot noise vs. GAWBS.** Noise spectra in this graph have been obtained in an imbalanced homodyne detection with unetched fiber (Nufern 780HP), where a strong local oscillator (9.5 mW) and varying probe powers of 0 to 1000 μW were used. The inset shows the relative increase of the power spectral density for a GAWBS peak (red) and for the background (blue). Refer to text for more details.

3.5.1 Influence of guided acoustic wave Brillouin scattering

As is well known from fiber-based quantum optics experiments [102], optical fibers can give rise to classical phase noise, in the form of guided acoustic wave Brillouin scattering (GAWBS). This process involves thermally driven radial mechanical modes of the fiber that also modulate the optical path length. The consequences are two-fold: As already discussed, classical phase noise can drive the mechanics and lead to squashing in the obtained spectra. In addition classical noise generated in one of the two arms (here: 8m each) is not canceled by the balanced detection. So there is a GAWBS signal added to the obtained spectrum which is not desirable for aesthetic reasons.

To investigate the presence of GAWBS noise spectra from the homodyne detector have been recorded when the fiber is retracted away from the optomechanical cavity in an imbalanced Mach-Zehnder interferometer. Several classical peaks are observed on top of the shot-noise background (see Fig. 3.18a, not corrected for the detector response). The width (i.e. damping) of the noise peaks was observed to

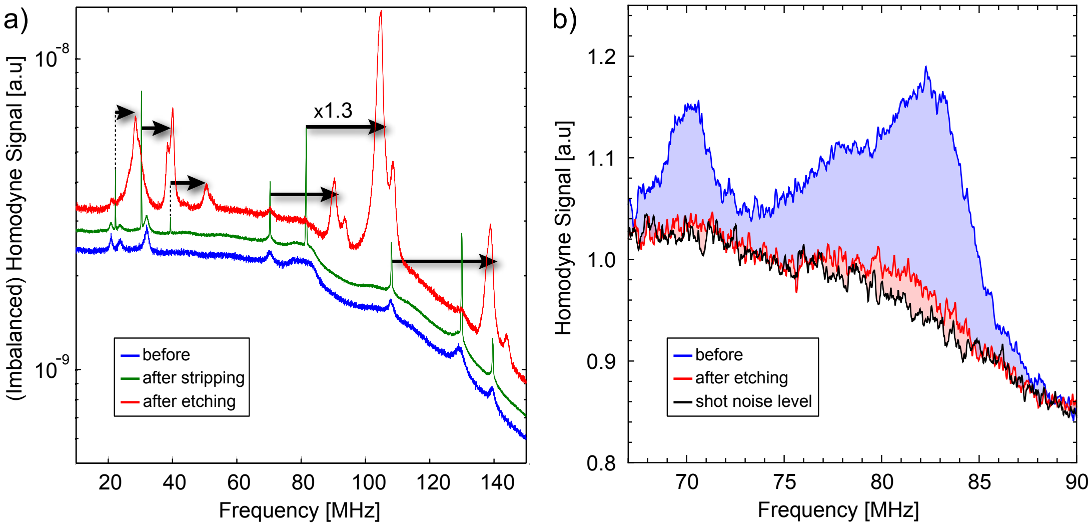

Figure 3.18: **Engineering of the fiber GAWBS noise spectrum.** **a**) shows a broadband background spectrum of the imbalanced homodyne signal where the GAWBS modes are visible. Blue, green and red traces are taken with unmodified, partly stripped buffer and (almost entirely) etched fiber respectively. As expected for guided dilatational acoustic waves of the optical fiber the frequencies are increased by a factor of about 1.3 for a thinned fiber of around 95 μm diameter (as compared to 125 μm before). Doublets in the red trace are due to slightly different final etching radii (difference is about 3 μm) of the different fibers in our setup (i.e., local oscillator fiber and the signal fiber). The difference in relative heights of the peaks is attributed to varying readout conditions, and as such only the peak's frequencies are of interest. **b**) shows a zoom of the background for the final setup (i.e., etching reduced diameter fibers, balanced homodyne arm lengths) and illustrates the achieved improvements, i.e., the reduced contribution of GAWBS to the background at the mechanical resonance frequency.

narrow dramatically when the buffer was partly stripped off the fiber, clearly demonstrating the mechanical nature of the peaks. One of the peaks coincided with the mechanical resonance frequency of 78 MHz used for the first experiments conducted at EPFL—including the published data described in section 4.3.

However, the frequency of the radial, dilatational fiber modes is proportional to the inverse fiber radius and can therefore be shifted by etching the fiber cladding in an HF solution. First tries have shown, that handling of a 10 m long etched fiber without acrylate buffer is hardly possible without breaking it. Inspired by [103], immersing the fibers directly without removing the acrylate buffer, which is permeable to HF, has been tried, which works surprisingly well. It has been found, that 50 minutes in a 40 % HF solution reduces the cladding diameter from 125 μm to 95 μm. This increased the GAWBS mode frequencies of all fibers in the setup by ≈ 30 %, shifting them away from the mechanical resonance frequency of the toroid. A comparison of the background in the final setup before and after etching as well as the corresponding shot noise level can be found in Fig. 3.18b. Splicing of etched fiber ends using a fusion splicer

(Ericsson FSU 925) turned out to be a lengthy task, as the transmission through the splices was in general bad. As a consequence, care has been taken to not etch the fiber ends, that still needed to be spliced to connectors, but to keep the non-etched parts as short as possible (below 15 cm).

3.6 Thermal response measurements and asymmetry in sideband sweeps

Measurement of the thermal response of microtoroids is a powerful tool permitting to better understand thermalization processes [52] or properties of layers, such as superfluid helium-4 films, forming on its surface [62]. Therefore, two laser beams tuned to different optical resonances of the resonators are coupled into the tapered fiber (cf. Fig. 3.19), one of which ("pump") is amplitude modulated. The second laser ("probe") is directed onto a phase sensitive detection demodulated at the frequency of the amplitude modulation. Hooking up the amplitude modulator and output signal to a network analyzer allows to quickly probe the response over a wide frequency range.

3.6.1 Thermal response of a toroidal microresonator

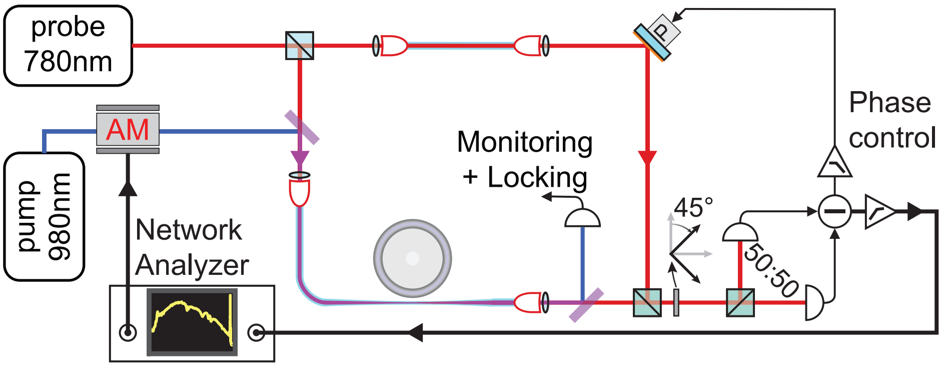

Figure 3.19: **Setup used for thermal response measurements.** Within the balanced homodyne setup used to read out mechanical motion with at 780 nm probe laser, a second "pump " laser operating at 980 nm is coupled to the toroid in the signal beam path using a short-pass filter. The two wavelengths are separated again by a short-pass filter, where an additional photo-diode is then used to monitor the pump laser and to keep it on a resonance. A network analyzer is used to probe the response to a coherent driving brought into the system by the pump. Care has been taken to minimize direct transmission, i.e. background.

Every effect that affects the toroid's optical resonance frequency is adding to the measured signal. Here, three sources can be distinguished: resonant absorption heating leads to thermal expansion and a change of the refractive index, radiation pressure can drive mechanical modes (compare to section 3.2.4) and the optical Kerr effect causes a power dependent optical refractive index. While the first was found to dominate up to about 1 MHz for rather large toroids at room temperature, the mechanical response of the radial breathing mode was found to reside in a frequency region, where the Kerr response dominates, which is in the relevant frequency range flat and instantaneous (compare Fig. 3.20a).

Once the frequency of the driving exceeds the time needed for thermalization of the structure, a thermal cutoff frequency is reached. In other words, the sample dimensions as a function of the heat wave's wavelength are probed.

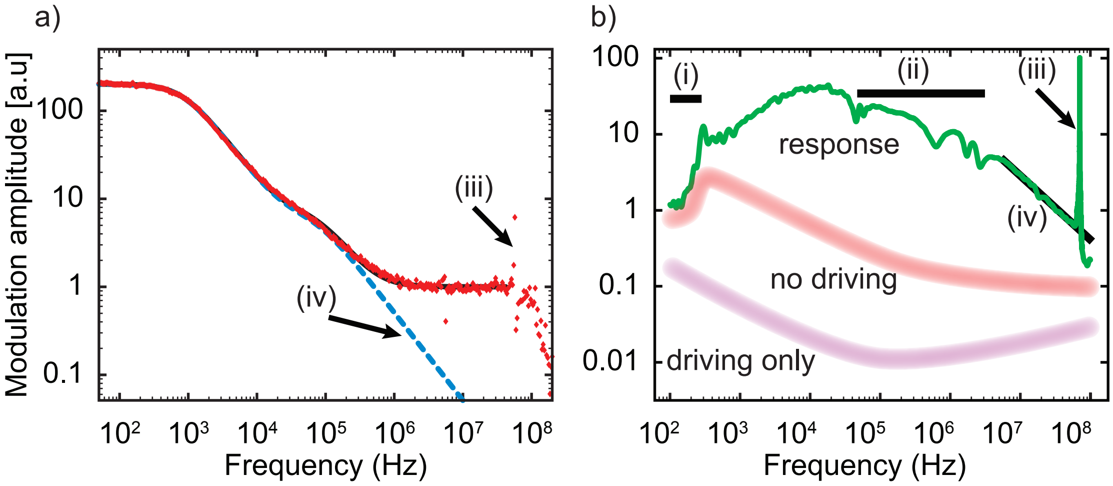

Figure 3.20: **Comparison of thermal responses—large toroid vs. small spokes resonator.** *(a)* is taken from [52] and shows a thermal response measurement of a 58 μm-diameter toroid. Two thermal cutoff frequencies can be clearly seen and fitting with a two-poles low pass filter response *(iv)* works well up to about 1 MHz. For higher frequencies a constant Kerr background, the mechanical response of the RBM *(iii)* as well as a detector cutoff at around 100 MHz are visible. *(b))* shows a response measurement performed with a spokes resonator in a homodyne configuration. Modulation frequencies up to several 100 Hz are suppressed by the homodyne lock *(i)*. Due to technical constraints, filters causing artifacts *(ii)* needed to be used. *(iii)* response of the RBM. *(iv)* contribution from thermal response. The red curve indicates the measurement background with the RF-driving of the amplitude modulator being switched off. The violet curve indicates the background induced by the amplitude modulated driving laser only, while the probe is switched off. Both are of illustrative character only and have been smoothed largely. In *(b)*, the detector cutoff has been corrected.

This experiment is straight-forward to implement, if performed at room temperature, where thermalization is not a problem, or at $\lambda = 1550$ nm, where low-noise amplifiers can be used to reduce the required probe laser powers. Some more care needs to be taken, when operating at low temperatures and using a $\lambda = 1550$ nm laser is not an option. We chose a 980 nm laser as a pump[4] and the 780 nm Ti:Sapph laser as a probe. Contrary to the previous experiment, where an offset and PDH locking scheme could be used, allowing to measure down to very low frequencies, here balanced homodyne detection - permitting to achieve the required sensitivity at power levels in the tens of μW range - was used. This scheme, however, does severely alter the response at frequencies below 1 kHz, as the homodyne phase lock does not distinguish phase fluctuations from the interferometer arms and the actual phase response from the toroid imprinted onto the probe (Fig. 3.20b). Additionally, filters in the RF circuitry required to avoid impedance mismatch above 10 MHz add additional spurious features. Even though, the data obtained are not as conclusive as in Fig. 3.20a, they still show a very important difference: At the RBM frequency, the background is by no means given by the Kerr effect, but still mainly by a thermal frequency dependent response. Additionally, this response is not instantaneous and therefore slightly out of phase with the drive. As a consequence, one expects also to find an influence on the coherent optical response measurements as introduced in 1.5.

---

[4] Note that $\lambda = 980$ nm light is still reasonably well transmitted through 780 nm fiber and tapers

3.6.2 Asymmetries found in sideband sweeps

Indeed, the previous measurement was motivated by the fact that the sideband sweeps showed an asymmetry that could not be explained during a while. Figure 3.21 illustrates this finding. The top graphs show two theoretical spectra for two different detunings of the laser. Here, optical and mechanical properties as well as the optomechanical coupling are included into the model. One finds, that the maximum signal

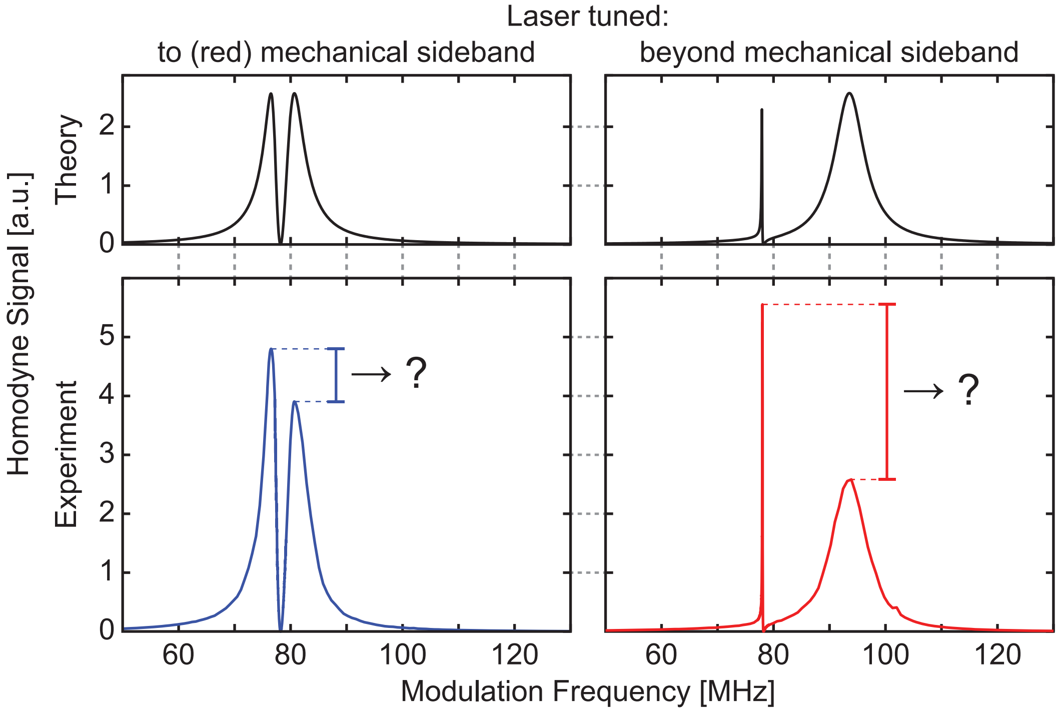

Figure 3.21: **Asymmetry of optical response spectra.** See text for details.

amplitude should be constant for all frequencies, if the swept sideband is assumed to have constant power. In an experiment, it has to be taken into account, that both the phase modulator creating this sideband and the detector show a cut-off at frequencies around 100 MHz.

For the experimental traces plotted in the bottom of Fig. 3.21, however, this has been taken into account and compensated for. Still, a strong asymmetry can be seen. The reason being, that a sideband sweep can be seen as a thermal response measurement, with the driving being induced by the beating signal between pump and probe. Obviously, this is only efficient, if the (very weak) probe laser is coupled into the resonator which happens only for frequencies corresponding to the pump laser's detuning within the cavity bandwidth.

In section 4.3.2 a refined theoretical model taking into account this thermal contribution to the measured response is presented that allows to accurately fit even the asymmetric traces and to assess the governing numerical parameters.

4 Results

In this chapter the published results obtained during this thesis are presented. Sections 4.1 and 4.2 are based on measurements obtained before our move to EPFL on conventional toroids and show the concept of optomechanically induced transparency (OMIT) and cooling of a mechanical mode to the low phonon occupancy of nine phonons. The last section combines these first results and demonstrates the major improvements both in sample design and experimental procedures but also in theoretical understanding of the measurement results after having moved to Lausanne, which allowed us to access the regime of quantum-coherent coupling.

4.1 Optomechanically Induced Transparency

This section is based on Weis *et al.* [1] published in the journal *Science* in December 2011 reporting the first experimental demonstration of optomechanically induced transparency.

4.1.1 Introduction

Coherent interaction of laser radiation with multilevel atoms and molecules can lead to quantum interference in the electronic excitation pathways [104]. A prominent example observed in atomic three-level-systems is the phenomenon of Electromagnetically Induced Transparency (EIT), in which a control laser induces a narrow spectral transparency window for a weak probe laser beam. When this generic EIT effect had first been observed in an atomic gas [105], its relevance in non-linear optics and optical (quantum) information processing was quickly recognized. In particular, the rapid variation of the refractive index concomitant with the opening of the transparency window gives rise to a dramatic reduction of the group velocity of a propagating optical pulse [106, 107]. Dynamic control of EIT via the control laser enables even a complete stop, that is, storage, of the pulse in an atomic medium [108, 109]. The experimental demonstration of slowing and stopping light [106, 107, 108, 109] has attracted strong attention, as it provides a route to implement a photonic quantum memory [110] or a classical optical buffer. EIT has subsequently been studied in a wide variety of atomic media, but also in several solid-state systems [111, 112] with a well-suited level structure.

Recent experiments with optomechanical systems have demonstrated that the mechanical response to thermal forces can be controlled by an optical field. This effect has been exploited, for example, to implement optomechanical laser cooling and amplification [113, 26, 27, 28] as well as normal mode splitting [114]. In other work, the mechanical response was optically tailored to exhibit destructive interference between different mechanical excitation pathways [115]. Whereas in these studies, the mechanical response to thermal Langevin force was modified, we demonstrate here, as recently suggested [52, 93], that the system's optical response to a weak 'probe' laser can be controlled by a second, 'control' laser driving the lower motional sideband. A window of transparency arises from the destructive interference of excitation pathways for the intracavity probe field when a two-photon resonance condition is met.

As pointed out independently, this effect can be considered a strict optomechanical analog of EIT [116], originating from a similar effective interaction Hamiltonian [117]. Advantageously, this form of induced transparency does not rely on naturally occurring resonances and could therefore also be applied to previously inaccessible wavelength regions such as the technologically important near-infrared. Furthermore, already a single optomechanical element can achieve unity contrast, which in the atomic case is only possible within the setting of cavity QED [118].

4.1.2 Theory

Our experiment (Fig. 4.1) consists of an optomechanical system featuring linear optomechanical coupling G in the sense that the cavity resonance frequency is given by $\omega'_{\mathrm{c}}(x) = \omega_{\mathrm{c}} + Gx$, where ω_{c} is the unperturbed resonance frequency. A control laser (frequency ω_{l}) maintains a control field $\bar{a}e^{-i\omega_{\mathrm{l}}t}$, containing $|\bar{a}|^2$ photons, in the cavity. The static radiation pressure originating from this field displaces the mechanical mode by $\bar{x}$, leading to an effective detuning from the cavity resonance $\bar{\Delta} = \omega_{\mathrm{l}} - (\omega_{\mathrm{c}} + G\bar{x})$. We consider the situation where the control laser is tuned close to the lower motional sideband, i.e. $\bar{\Delta} \approx -\Omega_{\mathrm{m}}$. A second, weak laser oscillating at $\omega_{\mathrm{p}} = \omega_{\mathrm{l}} + \Omega$, is subsequently used to probe the (modified) cavity resonance by driving an intracavity probe field contained in a perturbation term $\delta a(t)$.

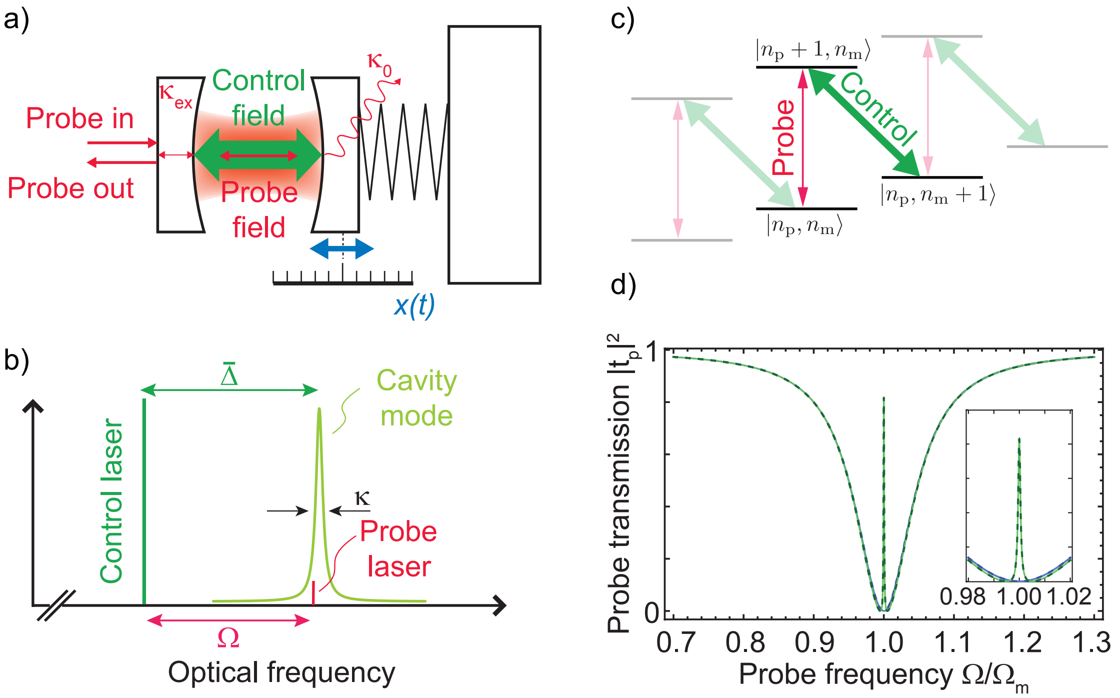
a)
Probe in
Probe out
κ_{ex}
Control field
Probe field
κ_0
x(t)
b)
$\bar{\Delta}$
Cavity mode
Control laser
κ
Probe laser
Ω
Optical frequency
c)
$|n_p+1, n_m\rangle$
Probe
Control
$|n_p, n_m\rangle$
$|n_p, n_m+1\rangle$
d)
Probe transmission $|t_p|^2$
1
0
0.7 0.8 0.9 1.0 1.1 1.2 1.3
Probe frequency Ω/Ω_m
0.98 1.00 1.02

Figure 4.1: **Optomechanically Induced Transparency.** (A) A generic optomechanical system consists of an optical cavity with a movable boundary, illustrated here as a Fabry-Pérot-type resonator in which one mirror acts like a mass-on-a-spring movable along x. The cavity has an intrinsic photon loss rate κ_0 and is coupled to an external propagating mode at the rate κ_{ex}. Through the external mode, the resonator is populated with a control field (only intracavity field is shown). The response of this driven optomechanical system is probed by a weak probe field sent towards the cavity, the transmission of which (i.e. the returned field "Probe out") is analyzed here. (B) The frequency of the control field is detuned by $\bar{\Delta}$ from the cavity resonance frequency, where a detuning close to the lower mechanical sideband, $\bar{\Delta} \approx -\Omega_{\mathrm{m}}$, is chosen. The probe laser's frequency is offset by the tunable radio frequency Ω from the control laser. The dynamics of interest occur when the probe laser is tuned over the optical resonance of the cavity, which has a linewidth of $\kappa = \kappa_0 + \kappa_{\mathrm{ex}}$. (C) Level scheme of the optomechanical system. The control field is tuned close to red-sideband transitions, in which a quantum of mechanical energy is annihilated (mechanical occupation $n_{\mathrm{m}} \rightarrow n_{\mathrm{m}} - 1$) when a photon is added to the cavity (optical occupation $n_{\mathrm{p}} \rightarrow n_{\mathrm{p}} + 1$), therefore coupling the corresponding energy eigenstates. The probe field probes transitions in which the mechanical oscillator occupation is unchanged. (D) Transmission of the probe laser power through the optomechanical system in the case of a critically coupled cavity $\kappa_0 = \kappa_{\mathrm{ex}}$ as a function of normalized probe frequency offset, when the control field is off (blue lines) and on (green lines). Dashed and full lines correspond to the models based on the full (Eq. (1)) and approximative (Eq. (3)) calculations, respectively.

In the case of a weak probe field (compared to the control field), one can linearize the optomechanical dynamics [32] for the mechanical displacement $x(t) = \bar{x} + \delta x(t)$ and the intracavity field $a(t) = (\bar{a} + \delta a(t))e^{-i\omega_l t}$ around the steady state values $(\bar{x}, \bar{a})$. For the probe power transmission—that is, the ratio of the probe power returned from the system divided by the input probe power—the general expression

$$|t_\mathrm{p}|^2 = \left|1 - \frac{1 + i f(\Omega)}{-i(\bar{\Delta} + \Omega) + \kappa/2 + 2\bar{\Delta} f(\Omega)} \eta_\mathrm{c} \kappa \right|^2 \tag{4.1}$$

with

$$f(\Omega) = \hbar G^2 \bar{a}^2 \frac{\chi(\Omega)}{i(\bar{\Delta} - \Omega) + \kappa/2}. \tag{4.2}$$

can be derived (see refs. [52, 93, 116] and the following paragraphs). Here, $\chi(\Omega) = (m_\mathrm{eff}(\Omega_\mathrm{m}^2 - \Omega^2 - i\Gamma_\mathrm{m}\Omega))^{-1}$ is the susceptibility of the mechanical oscillator of effective mass m_eff, resonance frequency Ω_m and damping rate Γ_m. The optical mode is characterized by a total loss rate $\kappa = \kappa_0 + \kappa_\mathrm{ex}$ and the cavity coupling parameter $\eta_\mathrm{c} = \kappa_\mathrm{ex}/(\kappa_0 + \kappa_\mathrm{ex})$. The presence of a control field $\bar{a}$ induces a transmission window for the probe beam when the resonance condition $\Omega \approx \Omega_\mathrm{m}$ is met (Fig. 4.1). The depth and the width of this transmission window are tunable by the power of the control beam as in the case of atomic EIT, with the best contrast achieved in the case of critical coupling $\eta_\mathrm{c} = 1/2$.

The previous expressions describing the optomechanical equivalent of Electromagnetically Induced Transparency (EIT) will be derived and discussed in the following. The starting point of the following analysis is the Hamiltonian formulation of a generic optomechanical system put forward by Law [119].

Hamiltonian

If the free spectral range of the cavity is much larger than the mechanical oscillation frequency, such that only one optical mode is coupled to the mechanical mode, the optomechanical Hamiltonian can be written as:

$$\hat{H} = \hat{H}_{\mathrm{mech}} + \hat{H}_{\mathrm{opt}} + \hat{H}_{\mathrm{int}} + \hat{H}_{\mathrm{drive}} \tag{4.3}$$

$$\hat{H}_{\mathrm{mech}} = \frac{\hat{p}^2}{2m_{\mathrm{eff}}} + \frac{1}{2} m_{\mathrm{eff}} \Omega_{\mathrm{m}}^2 \hat{x}^2 \tag{4.4}$$

$$\hat{H}_{\mathrm{opt}} = \hbar\omega_{\mathrm{c}} \left(\hat{a}^\dagger \hat{a} + \frac{1}{2} \right) \tag{4.5}$$

$$\hat{H}_{\mathrm{int}} = \hbar G \hat{x}\, \hat{a}^\dagger \hat{a} \tag{4.6}$$

$$\hat{H}_{\mathrm{drive}} = i\hbar \sqrt{\eta_{\mathrm{c}}\kappa} \left(\hat{s}_{\mathrm{in}}(t) \hat{a}^\dagger - \hat{s}_{\mathrm{in}}^\dagger(t) \hat{a} \right), \tag{4.7}$$

where $\hat{x}$ and $\hat{p}$ are the position and momentum operators of the mechanical degree of freedom having effective mass m_{eff} and angular frequency Ω_m, and $s_{\mathrm{in}}(t)$ is the drive amplitude normalized to a photon flux at the input of the cavity. $\hat{a}$ and $\hat{a}^\dagger$ are the annihilation and creation operators of the cavity mode. We have furthermore used the coupling parameter $\eta_{\mathrm{c}} \equiv \kappa_{\mathrm{ex}}/\kappa_0 + \kappa_{\mathrm{ex}}$, where κ_0 denotes the intrinsic loss rate and κ_{ex} the external loss rate (i.e. wave guide coupling). Experimentally, the parameter η_{c} can be continuously adjusted by tuning the taper-resonator gap [60, 64].

We will solve this problem for a driving field $s_{\mathrm{in}}(t) = (\bar{s}_{\mathrm{in}} + \delta s_{\mathrm{in}}(t))\, e^{-i\omega_{\mathrm{l}} t}$, where ω_{l} is the driving laser frequency, and we deliberately identify $\bar{s}_{\mathrm{in}} = s_{\mathrm{l}}$. We will then first derive the linearized Langevin equations [32] for a generic perturbation term $\delta s_{\mathrm{in}}(t)$ before identifying it with the probe field $\delta s_{\mathrm{in}}(t) = s_{\mathrm{p}} e^{-i(\omega_{\mathrm{p}} - \omega_{\mathrm{l}})t}$.

Langevin equations

In a frame rotating at ω_{l} with $\Delta = \omega_{\mathrm{l}} - \omega_{\mathrm{c}}$, we obtain:

$$\frac{d}{dt}\hat{a}(t) = \left(+i\Delta - \frac{\kappa}{2} \right) \hat{a}(t) - iG\hat{x}(t)\hat{a}(t) + \sqrt{\eta_{\mathrm{c}}\kappa}\, s_{\mathrm{in}}(t) + \sqrt{(1-\eta_{\mathrm{c}})\kappa}\, \delta\hat{s}_{\mathrm{vac}}(t) \tag{4.8}$$

$$\frac{d}{dt}\hat{x}(t) = \frac{\hat{p}(t)}{m_{\mathrm{eff}}} \tag{4.9}$$

$$\frac{d}{dt}\hat{p}(t) = -m_{\mathrm{eff}}\Omega_{\mathrm{m}}^2 \hat{x}(t) - \hbar G \hat{a}^\dagger(t)\hat{a}(t) - \Gamma_{\mathrm{m}}\hat{p}(t) + \delta\hat{F}_{\mathrm{th}}(t), \tag{4.10}$$

where the decay rates for the optical (κ) and mechanical oscillators (Γ_m) have been introduced classically, and $\delta\hat{s}_{\mathrm{vac}}(t)$ and $\delta\hat{F}_{\mathrm{th}}(t)$ are the quantum and thermal noise terms [35]. We first denote $\bar{a}$ and $\bar{x}$ the intracavity field and mechanical displacement for the static solution, in which all time derivatives vanish and $s_{\mathrm{p}} \to 0$. From eqs. (4.8) and (4.10), it follows immediately that $\bar{a}$ and $\bar{x}$ must fulfill the self consistent equations:

$$\bar{a} = \frac{\sqrt{\eta_c \kappa}}{-i(\Delta - G\bar{x}) + \kappa/2} \bar{s}_{\text{in}} \tag{4.11}$$

$$\bar{x} = \frac{-\hbar G \bar{a}^2}{m_{\text{eff}} \Omega_m^2}, \tag{4.12}$$

where we have assumed a to be real and positive. This system can give rise to bistability for sufficiently strong control fields [120, 32]. However, for weak and detuned control fields, only one solution exists and $|\bar{a}|^2 \propto \eta_c \bar{s}_{\text{in}}^2$. We then linearize the problem for $\delta\hat{a} \ll |\bar{a}|$, plugging the ansatz $\hat{a}(t) = \bar{a} + \delta\hat{a}(t)$ and $\hat{x}(t) = \bar{x} + \delta\hat{x}(t)$ into equations (4.8), (4.9) and (4.10) and retain only first order terms in the small quantities $\delta\hat{a}$, $\delta\hat{a}^\dagger$ and $\delta\hat{x}$. We then obtain

$$\frac{d}{dt}\delta\hat{a}(t) = \left(+i\bar{\Delta} - \frac{\kappa}{2}\right)\delta\hat{a}(t) - iG\bar{a}\delta\hat{x}(t) + \sqrt{\eta_c\kappa}\delta s_{\text{in}}(t) + \sqrt{(1-\eta_c)\kappa}\delta\hat{s}_{\text{vac}}(t) \tag{4.13}$$

$$\frac{d^2}{dt^2}\delta\hat{x}(t) + \Gamma_{\text{m}}\frac{d}{dt}\delta\hat{x}(t) + \Omega_{\text{m}}^2\delta\hat{x}(t) = -\frac{\hbar G}{m_{\text{eff}}}\bar{a}\left(\delta\hat{a}(t) + \delta\hat{a}^\dagger(t)\right) + \delta\hat{F}_{\text{th}}(t), \tag{4.14}$$

where we used the Hermitian property $\delta\hat{x}(t) = \delta\hat{x}^\dagger(t)$ in equation (4.13), and introduced the corrected detuning $\bar{\Delta} = \Delta - G\bar{x}$. Since the drives are weak, but classical coherent fields, we will identify all operators with their expectation values $y(t) \equiv \langle\hat{y}(t)\rangle$, and drop the quantum and thermal noise terms, which average to 0.

Solution

General solution We now have to solve the equations of the expectation values for the drive (in the rotating frame) $\delta s_{\text{in}}(t) = s_{\text{p}} e^{-i(\omega_{\text{p}} - \omega_{\text{l}})t}$. For a given $\Omega = \omega_{\text{p}} - \omega_{\text{l}}$ we use the ansatz

$$\delta a(t) = A^- \, e^{-i\Omega t} + A^+ \, e^{+i\Omega t} \tag{4.15}$$

$$\delta a^*(t) = (A^+)^* \, e^{-i\Omega t} + (A^-)^* \, e^{+i\Omega t} \tag{4.16}$$

$$\delta x(t) = X \, e^{-i\Omega t} + X^* \, e^{+i\Omega t}. \tag{4.17}$$

If sorted by rotation terms, this yields six equations. However, the probe field's transmission at frequency $\omega_l + \Omega$ only depends on A^-. In this sense, the three equations of interest are:

$$\left(-i(\bar{\Delta}+\Omega)+\kappa/2\right)A^{-} = -iG\bar{a}X + \sqrt{\eta_{\mathrm{c}}\kappa}s_{p} \tag{4.18}$$
$$\left(+i(\bar{\Delta}-\Omega)+\kappa/2\right)(A^{+})^{*} = +iG\bar{a}X \tag{4.19}$$
$$m_{\mathrm{eff}}\left(\Omega_{\mathrm{m}}^{2}-\Omega^{2}-i\Gamma_{\mathrm{m}}\Omega\right)X = -\hbar G\bar{a}\left(A^{-}+(A^{+})^{*}\right). \tag{4.20}$$

The solution of interest is

$$A^{-} = \frac{1+if(\Omega)}{-i(\bar{\Delta}+\Omega)+\kappa/2+2\bar{\Delta}f(\Omega)}\sqrt{\eta_{\mathrm{c}}\kappa}s_{p}, \tag{4.21}$$

with

$$f(\Omega) = \hbar G^{2}\bar{a}^{2}\frac{\chi(\Omega)}{i(\bar{\Delta}-\Omega)+\kappa/2} \tag{4.22}$$

and the mechanical susceptibility

$$\chi(\Omega) = \frac{1}{m_{\mathrm{eff}}}\frac{1}{\Omega_{\mathrm{m}}^{2}-\Omega^{2}-i\Omega\Gamma_{\mathrm{m}}}. \tag{4.23}$$

Spectrum of the transmitted light Using the input-output relation [34], one obtains:

$$s_{\mathrm{out}}(t) = s_{\mathrm{in}}(t) - \sqrt{\eta_{\mathrm{c}}\kappa}\,a(t) \tag{4.24}$$
$$= (s_{\mathrm{c}}-\sqrt{\eta_{\mathrm{c}}\kappa}\bar{a})e^{-i\omega_{c}t} + (s_{\mathrm{p}}-\sqrt{\eta_{\mathrm{c}}\kappa}A^{-})e^{-i(\omega_{c}+\Omega)t} - \sqrt{\eta_{\mathrm{c}}\kappa}A^{+}e^{-i(\omega_{c}-\Omega)t}. \tag{4.25}$$

The transmission of the probe beam is then given by:

$$t_{p} = \frac{s_{\mathrm{p}}-\sqrt{\eta_{\mathrm{c}}\kappa}A^{-}}{s_{\mathrm{p}}} \tag{4.26}$$
$$= 1-\frac{1+if(\Omega)}{-i(\bar{\Delta}+\Omega)+\kappa/2+2\bar{\Delta}f(\Omega)}\eta_{\mathrm{c}}\kappa. \tag{4.27}$$

Here, we refer to the probe transmission in the general sense of the ratio of the probe field returned from the system divided by the sent probe field. In this work, the returned probe field corresponds to the field transmitted through the fiber taper that is used for evanescent coupling of an ideal WGM resonator. In Fabry-Pérot-type resonators it would correspond to the field that is reflected from the input coupler.

Resolved-sideband limit In the resolved sideband regime [55] ($\kappa \ll \Omega_m$), the lower sideband, being far off-resonant, can be neglected:

$$A^+ \approx 0.$$

In addition, we can linearize the mechanical susceptibility for small values of the parameter $\Delta' = \Omega - \Omega_m$:

$$(\Omega_m^2 - \Omega^2 - i\Gamma_m\Omega) \approx \Omega_m(2\Delta' - i\Gamma_m).$$

The system (4.18)(4.19)(4.20) then simplifies to:

$$\left(-i(\bar{\Delta} + \Omega_m + \Delta') + \kappa/2\right) A^- = -iG\bar{a}X + \sqrt{\eta_c\kappa}s_p \tag{4.28}$$
$$m_{\text{eff}}\Omega_m(2\Delta' + i\Gamma_m)X = \hbar G\bar{a}A^-. \tag{4.29}$$

The solution for the intracavity field is:

$$A^- = \frac{\sqrt{\eta_c\kappa}s_p}{-i(\bar{\Delta} + \Omega_m + \Delta') + \kappa/2 + \frac{\Omega_c^2/4}{(-i\Delta' + \Gamma_m/2)}}, \tag{4.30}$$

where we have introduced the coupling between the mechanical and optical resonators:

$$\Omega_c = 2G\bar{a}x_{\text{zpf}},$$

with

$$x_{\text{zpf}} = \sqrt{\frac{\hbar}{2m_{\text{eff}}\Omega_m}},$$

the zero point fluctuations amplitude of the mechanical oscillator. This formula becomes

$$A^- = \frac{\sqrt{\eta_c\kappa}s_p}{-i\Delta' + \kappa/2 + \frac{\Omega_c^2/4}{(-i\Delta' + \Gamma_m/2)}} \tag{4.31}$$

for a control laser tuned to the lower motional sideband ($\bar{\Delta} = -\Omega_\text{m}$).

The achievable coupling rate is only limited by the appearance of radiation pressure bistability for high control power. In the resolved sideband regime, the upper limit for the coupling rate is found to be $\Omega_\text{c} < \Omega_\text{m}$ [56, 121].

Simplified expressions in the weak coupling case

In addition to the resolved sideband approximation, we will consider the case where the optomechanical coupling is weak compared to the optical losses ($\Omega_c, \Gamma_m \ll \kappa$). We also assume that the control laser is tuned on the lower sideband ($\bar{\Delta} = -\Omega_m$). Then, the EIT feature is very well described by a Lorentzian transmission window in the optical transmission spectrum. This can be seen by applying the simplification $-i\Delta' + \kappa/2 \approx \kappa/2$ in equation (4.31):

$$A^- \approx \frac{4\sqrt{\eta_c \kappa}(-i\Delta' + \Gamma_m/2)}{2\kappa(\Gamma_m/2 - i\Delta') + \Omega_c^2} s_p. \tag{4.32}$$

Plugging the corresponding value of A^- in (4.26), one obtains:

$$t_p = 1 - 2\eta_c + \frac{2\eta_c \Omega_c^2}{\Omega_c^2 + \Gamma_m \kappa - 2i\Delta'\kappa}. \tag{4.33}$$

In order to isolate the interesting physics of OMIT from the well-understood waveguide-cavity coupling effects, we introduce the normalized transmission:

$$t'_p = \frac{t_p - t_r}{1 - t_r}, \tag{4.34}$$

where t_r is the residual on resonance transmission in the absence of a coupling laser:

$$\begin{aligned} t_r &= t_p(\Delta' = 0, \Omega_c = 0) \qquad (4.35) \\ &= 1 - 2\eta_c. \qquad (4.36) \end{aligned}$$

The normalized transmission is then independent of η_c:

$$t'_p = \frac{\Omega_c^2}{\Omega_c^2 + \Gamma_m \kappa - 2i\Delta'\kappa}. \tag{4.37}$$

This corresponds to the transmission in the case of critical coupling $\eta_c = 1/2$. The optomechanically induced transparency window is hence given by:

$$|t'_p|^2 = \frac{\Omega_c^4/\kappa^2}{\left(\Omega_c^2/\kappa + \Gamma_m\right)^2 + (2\Delta')^2}. \tag{4.38}$$

A Lorentzian of width

$$\begin{aligned} \Gamma_{\mathrm{OMIT}} &= \Gamma_m + \Omega_c^2/\kappa \qquad (4.39) \\ & \qquad (4.40) \end{aligned}$$

and peak value

$$|t'_p(\Delta' = 0)|^2 = \left(\frac{\Omega_c^2/\kappa}{\Gamma_m + \Omega_c^2/\kappa} \right)^2 . \tag{4.41}$$

These two quantities can be expressed very simply by introducing the cooperativity of the coupled systems $C = \Omega_c^2/(\Gamma_m \kappa)$ [122]:

$$\Gamma_{\mathrm{OMIT}} = \Gamma_m (1 + C) \tag{4.42}$$

$$|t'_p(\Delta' = 0)|^2 = \left(\frac{C}{1 + C} \right)^2 . \tag{4.43}$$

Additional Remarks

In order to gain more physical insight into this phenomenon, it is instructive to consider this effect in a sideband picture. The simultaneous presence of control and probe fields generates a radiation-pressure force oscillating at the frequency difference Ω. If this driving force oscillates close to the mechanical resonance frequency Ω_{m}, the mechanical mode starts to oscillate coherently, $\delta x(t) = 2\mathrm{Re}[X\, e^{-i\Omega t}]$. This in turn gives rise to Stokes- and anti-Stokes scattering of light from the strong intracavity control field. If the system resides deep enough in the resolved-sideband (RSB) regime with $\kappa \ll \Omega_{\mathrm{m}}$, Stokes scattering (to the optical frequency $\omega_{\mathrm{l}} - \Omega$) is strongly suppressed as it is highly off-resonant with the optical cavity. We can therefore assume that only an anti-Stokes field builds up inside the cavity, $\delta a(t) \approx A^- e^{-i\Omega t}$. However, this field of frequency $\omega_{\mathrm{p}} = \omega_{\mathrm{l}} + \Omega$ is degenerate with the near-resonant probe field sent to the cavity. Destructive interference of these two driving waves can suppress the build-up of an intracavity probe field.

Equation (4.31):

$$A^- = \frac{\sqrt{\eta_{\mathrm{c}} \kappa}\, s_p}{-i\Delta' + \kappa/2 + \frac{\Omega_c^2/4}{(-i\Delta' + \Gamma_m/2)}} \tag{4.44}$$

governing the intracavity probe field, has a form well-known from the response of an EIT medium to a probe field [104]. The coherence between the two ground states of an atomic Λ system, and the coherence between the levels probed by the probe laser undergo the very same evolution as do the mechanical oscillation amplitude and the intracavity probe field in the case of OMIT. The role of the control laser's Rabi frequency in an atomic system is taken by the optomechanical coupling rate $\Omega_{\mathrm{c}} = 2\bar{a} G x_{\mathrm{zpf}}$.

We will now briefly review the formalism used to describe EIT in the context of atomic physics to emphasize this analogy between the two phenomena.

Atomic EIT

For atomic EIT, we essentially revisit the well-known derivation developed in [123], which will assist in identifying the close resemblance between OMIT and atomic EIT. We consider a Λ-system, consisting of a common upper state $|3\rangle$ and two (long-lived) ground states $|1\rangle$ and $|2\rangle$. In a semiclassical treatment [124], the relevant Hamiltonian is given by:

$$\hat{H} = \sum_j \hbar\omega_j \hat{\sigma}_{jj} - (\mu_{23}\hat{\sigma}_{23} + \mu_{23}^*\hat{\sigma}_{32})E(t) - (\mu_{13}\hat{\sigma}_{13} + \mu_{13}^*\hat{\sigma}_{31})E(t), \tag{4.45}$$

where $\hat{\sigma}_{ij} = |i\rangle\langle j|$ are the atomic projection operators and $i, j \in \{1,2,3\}$ label the three involved levels. ω_{ij} and μ_{ij} are the frequency and dipole moment along the electric field's direction for the $i \to j$ transition. The (classical) field contains the two (coupling and probe) components

$$E(t) = \frac{1}{2}\mathscr{E}_{\mathrm{c}}\left(e^{-i\omega_{\mathrm{c}}t} + e^{+i\omega_{\mathrm{c}}t}\right) + \frac{1}{2}\mathscr{E}_{\mathrm{p}}\left(e^{-i\omega_{\mathrm{p}}t} + e^{+i\omega_{\mathrm{p}}t}\right), \tag{4.46}$$

where ω_{c} is tuned close to ω_{32} and ω_{p} close to ω_{31}. The usual Heisenberg equations of motion for the operators $\hat{\sigma}_{ij}$ can then be derived using $i\hbar\frac{d\hat{\sigma}_{ij}}{dt} = [\hat{\sigma}_{ij}, \hat{H}]$. Retaining only near-resonant terms, the equations of motion can be written as

$$\dot{\hat{\sigma}}_{12} = -i\omega_{21}\hat{\sigma}_{12} + \frac{i}{2\hbar}\mu_{23}\mathscr{E}_{\mathrm{c}}\hat{\sigma}_{13}e^{+i\omega_{\mathrm{c}}t} - \frac{i}{2\hbar}\mu_{13}^*\mathscr{E}_{\mathrm{p}}\hat{\sigma}_{32}e^{-i\omega_{\mathrm{p}}t} \tag{4.47}$$

$$\dot{\hat{\sigma}}_{23} = -i\omega_{32}\hat{\sigma}_{23} + \frac{i}{2\hbar}\mu_{23}^*\mathscr{E}_{\mathrm{c}}(\hat{\sigma}_{22} - \hat{\sigma}_{33})e^{-i\omega_{\mathrm{c}}t} + \frac{i}{2\hbar}\mu_{13}^*\mathscr{E}_{\mathrm{p}}\hat{\sigma}_{21}e^{-i\omega_{\mathrm{p}}t} \tag{4.48}$$

$$\dot{\hat{\sigma}}_{13} = -i\omega_{31}\hat{\sigma}_{13} + \frac{i}{2\hbar}\mu_{23}^*\mathscr{E}_{\mathrm{c}}\hat{\sigma}_{12}e^{-i\omega_{\mathrm{c}}t} + \frac{i}{2\hbar}\mu_{13}^*\mathscr{E}_{\mathrm{p}}(\hat{\sigma}_{11} - \hat{\sigma}_{33})e^{-i\omega_{\mathrm{p}}t}. \tag{4.49}$$

We emphasize that the rotating wave approximation (neglecting all non-resonant contributions) is analogous to the resolved sideband approximation presented in the context of OMIT. For a sufficiently weak probe field, the expectation values $\sigma_{ij} = \langle\hat{\sigma}_{ij}\rangle$ can further be approximated to obey $\sigma_{11} \approx 1$ and $\sigma_{22} \approx \sigma_{33} \approx \sigma_{23} \approx \sigma_{32} \approx 0$ at all times, while the remaining expectation values obey

$$\dot{\sigma}_{12} = -i(\omega_{21} - i\gamma_{12}/2)\sigma_{12} + \frac{i}{2\hbar}\mu_{23}\mathscr{E}_{\mathrm{c}}\sigma_{13}e^{+i\omega_{\mathrm{c}}t} \tag{4.50}$$

$$\dot{\sigma}_{13} = -i(\omega_{31} - i\gamma_{13}/2)\sigma_{13} + \frac{i}{2\hbar}\mu_{23}^*\mathscr{E}_{\mathrm{c}}\sigma_{12}e^{-i\omega_{\mathrm{c}}t} + \frac{i}{2\hbar}\mu_{13}^*\mathscr{E}_{\mathrm{p}}e^{-i\omega_{\mathrm{p}}t}, \tag{4.51}$$

where damping rates γ_{12} and γ_{13} were introduced classically. Changing to a rotating frame $\sigma_{12} = S_{12}e^{-i\Omega t}$, $\sigma_{13} = S_{13}e^{-i(\omega_{\mathrm{c}}+\Omega)t}$ and $\mathscr{E}_{\mathrm{p}}e^{-i\omega_{\mathrm{p}}t} = \mathscr{E}_{\mathrm{p}}e^{-i(\omega_{\mathrm{c}}+\Omega)t}$ with $\omega_{\mathrm{p}} = \omega_{\mathrm{c}} +$

Ω, we obtain in the steady state

$$(-i(\Omega-\omega_{21})+\gamma_{12}/2)S_{12} = +\frac{i}{2\hbar}\mu_{23}\mathscr{E}_{\mathrm{c}}S_{13} \tag{4.52}$$

$$(-i(\Omega+\omega_c-\omega_{31})+\gamma_{13}/2)S_{13} = +\frac{i}{2\hbar}\mu_{23}^{*}\mathscr{E}_{\mathrm{c}}S_{12}+\frac{i}{2\hbar}\mu_{13}^{*}\mathscr{E}_{\mathrm{p}}, \tag{4.53}$$

which is solved by

$$S_{13} = \frac{i\mu_{13}^{*}\mathscr{E}_{\mathrm{p}}/2\hbar}{-i(\Delta'+\omega_c-\omega_{32})+\gamma_{13}/2+\frac{\Omega_{\mathrm{R}}^2/4}{-i\Delta'+\gamma_{12}/2}}, \tag{4.54}$$

where we now abbreviate $\Delta' = \Omega-\omega_{21} = \omega_{\mathrm{p}}-\omega_{31}$ and the Rabi frequency is defined as $\Omega_{\mathrm{R}} = |\mu_{23}|\mathscr{E}_{\mathrm{c}}/\hbar$. We note as an aside that an equivalent calculation can be made for the atomic coherences ρ_{12} and ρ_{13}, yielding essentially the same result [124]. This result simplifies for a control field on resonance ($\omega_c = \omega_{32}$):

$$S_{13} = \frac{i\mu_{13}^{*}\mathscr{E}_{\mathrm{p}}/2\hbar}{-i\Delta'+\gamma_{13}/2+\frac{\Omega_{\mathrm{R}}^2/4}{-i\Delta'+\gamma_{12}/2}}. \tag{4.55}$$

The induced dipole moment along the electric field's direction is given by $p = 2\mu_{13}S_{13}$ so that the polarizibility $\alpha = p/\mathscr{E}_{\mathrm{p}}$ of the medium at the probe frequency in the presence of the coupling beam can be directly given by

$$\alpha = \frac{2\mu_{13}S_{13}}{\mathscr{E}_{\mathrm{p}}} = \frac{i|\mu_{13}|^2/\hbar}{-i\Delta'+\gamma_{13}/2+\frac{\Omega_{\mathrm{R}}^2/4}{-i\Delta'+\gamma_{12}/2}}. \tag{4.56}$$

Evidently one can identify a formal correspondence between the physical entities involved in EIT in atomic physics and OMIT in optomechanical systems. Equations (4.52) - (4.55) are perfectly equivalent to (4.28) - (4.31) by applying the identifications listed in the following table.

Table 4.1: **Comparison of physical entities relevant for EIT and OMIT.**

EIT	OMIT
projection operator σ_{13} (coherence ρ_{13})	intracavity field amplitude A^{-}
projection operator σ_{12} (coherence ρ_{12})	mechanical displacement amplitude X
energy difference between ground states $\hbar\omega_{21}$	phonon energy $\hbar\Omega_{\mathrm{m}}$
Rabi frequency $\Omega_{\mathrm{R}} = |\mu_{23}|\mathscr{E}_{\mathrm{c}}/\hbar$	optomech. coupling rate $\Omega_{\mathrm{c}} = 2g_0\bar{a}$

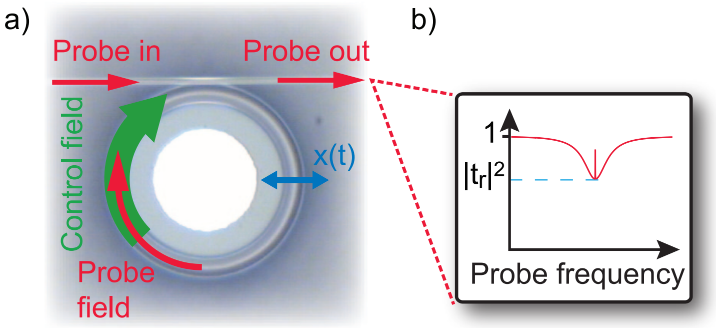

Figure 4.2: **Optomechanical system.** A) A toroidal microcavity is used to demonstrate OMIT: the resonator is coupled to the control and probe fields using a tapered fiber. The optical mode couples via radiation pressure force to the radial breathing mode of the structure. In this ring geometry, the cavity transmission, defined by the ratio of the returned probe field amplitude divided by the incoming probe field is simply given by the transmission through the tapered fibered. B) Under the chosen waveguide-toroid coupling conditions, there is a non-zero probe power transmission $|t_\mathrm{r}|^2$ at resonance. The control field induces an additional transparency window with a contrast up to $1-|t_\mathrm{r}|^2$.

4.1.3 Experiment

Optomechanically Induced Transparency is realized in this work using toroidal whispering-gallery-mode microresonators (Fig. 4.2A [113, 93].

As shown in Figure 4.3, the experiment was carried out at cryogenic temperatures using a Helium-3 buffer gas cryostat. In addition to reducing the thermal Brownian motion of the mechanical oscillator this also circumvents the problem of thermo-optical nonlinearities [66] which can impede driving the lower motional sideband with a strong control laser. Also, the optical thermal effect changes sign, such that the red sideband becomes stable. The sample is mounted on a cryogenic head, which allows approaching a tapered fiber for near field evanescent coupling using piezoelectric positioners. While an external-cavity diode laser was used for initial characterization, a low-noise, continuous-wave Titanium Sapphire laser operating at a wavelength of $\lambda \approx 775\,\mathrm{nm}$ is employed for the actual OMIT experiments. The Ti:sapphire laser's linewidth is reduced below 30 kHz by stabilization to a temperature-controlled reference cavity using the Pound-Drever-Hall technique [70, 71]. This approach furthermore proved to provide sufficient mutual frequency stability of the cryogenic microresonator and the cavity-stabilized laser on the relevant scale of the cavity linewidth κ.

In order to detect the optical response of the optomechanical system with a high sensitivity, we use a homodyne detection scheme: The RF beat of the beam transmitted through the optomechanical system with a strong local oscillator is detected using fast balanced photodiodes. This allows extracting the parameters of the device used

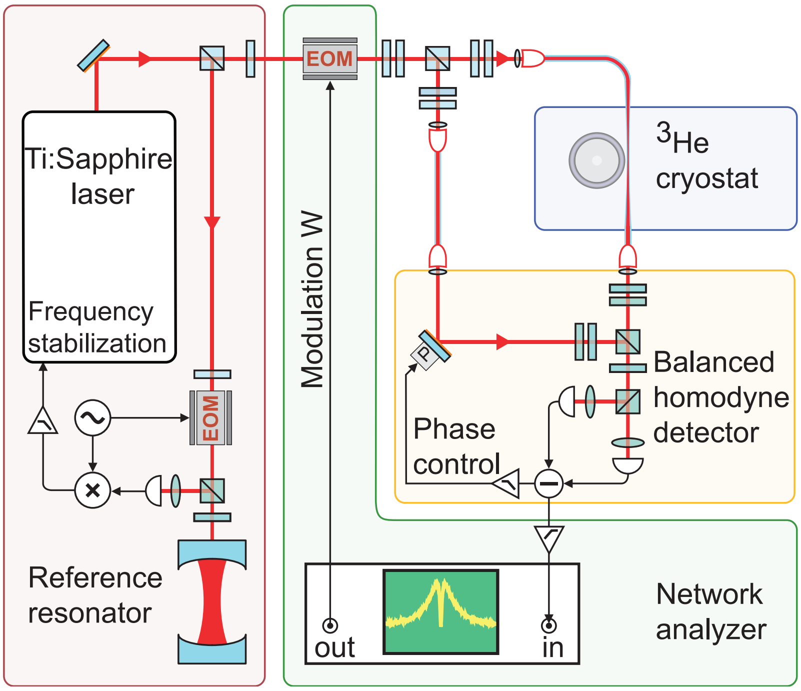
EOM
Ti:Sapphire laser
Frequency stabilization
EOM
Reference resonator
Modulation W
^{3}He cryostat
Balanced homodyne detector
Phase control
out
in
Network analyzer

Figure 4.3: **The optical setup.** The laser is phase modulated, creating two sidebands at frequency $\omega_l \pm \Omega$. The local oscillator field is transmitted unchanged whereas the field in the signal arm is affected by the cavity transmission. In the RSB regime, lower sideband and carrier, off resonant by approximately $2\Omega_m$ and Ω_m are not affected.

in these experiments, which are given by $(m_{\mathrm{eff}}, G/2\pi, \Gamma_{\mathrm{m}}/2\pi, \Omega_{\mathrm{m}}/2\pi, \kappa/2\pi) \approx (20\,\mathrm{ng}, -12\,\mathrm{GHz/nm}, 41\,\mathrm{kHz}, 51.8\,\mathrm{MHz}, 15\,\mathrm{MHz})$, placing it well into the resolved sideband regime [125].

Modal splitting

Our ring cavity can support two counterpropagating modes which are frequency degenerate for symmetry reasons. The propagation direction of the light in the coupling region therefore determines which mode is excited. However, as noted in early work on microspheres [126], and in theoretical as well as experimental work [127, 46, 128], due to residual scattering of light at the surface or in the bulk glass, the counterpropagating mode can also be significantly populated.

The essence of the phenomenon can be described by a coupled mode theory: if the two modes a_{cw} and a_{ccw} (see figure 4.4) are coupled by a coupling rate γ, the

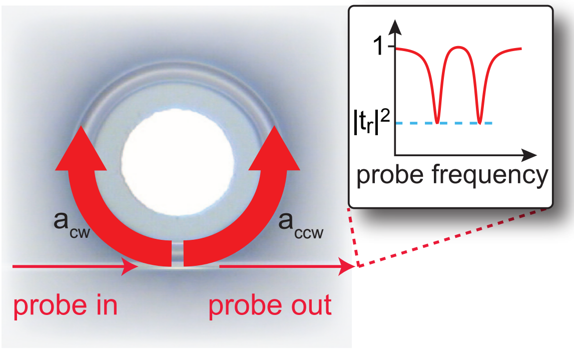

Figure 4.4: **Modal splitting.** In a ring cavity, two counterpropagating modes a_{cw} and a_{ccw} coexist. Only a_{ccw} is coupled to the waveguide, however, because of scattering into the counterpropagating mode, a_{cw} and a_{ccw} are coupled at a rate γ. For $\gamma \gg \kappa$, the frequency degeneracy of the new eigenmodes $a_+ = (a_{\mathrm{ccw}} + a_{\mathrm{cw}})/\sqrt{2}$ and $a_- = (a_{\mathrm{ccw}} - a_{\mathrm{cw}})/\sqrt{2}$ is lifted and the optical resonance splits up.

equations of motion become:

$$\dot{a}_{\mathrm{ccw}}(t) = (i(\Delta - Gx) - \kappa/2)a_{\mathrm{ccw}}(t) + i\frac{\gamma}{2}a_{\mathrm{cw}}(t) + \sqrt{\eta_c\kappa}\,s_{\mathrm{in}}(t) \tag{4.57}$$

$$\dot{a}_{\mathrm{cw}}(t) = (i(\Delta - Gx) - \kappa/2)a_{\mathrm{cw}}(t) + i\frac{\gamma}{2}a_{\mathrm{ccw}}(t), \tag{4.58}$$

and the radiation pressure force is now described by the equation:

$$\frac{d^2}{dt^2}x(t) + \Gamma_m\frac{d}{dt}x(t) + \Omega_m^2 x(t) + = -\frac{\hbar G}{m_{\mathrm{eff}}}(|a_{\mathrm{ccw}}|^2 + |a_{\mathrm{cw}}|^2). \tag{4.59}$$

Indeed, because of the symmetry of the radial breathing mode, the oscillator is not driven by the cross term $2\mathrm{Re}(a^*_{\mathrm{ccw}}a_{\mathrm{cw}})$. We can then easily rewrite these equations in terms of the two stationary modes $a_+ = (a_{\mathrm{ccw}} + a_{\mathrm{cw}})/\sqrt{2}$ and $a_- = (a_{\mathrm{ccw}} - a_{\mathrm{cw}})/\sqrt{2}$:

$$\dot{a}_+(t) = \left[i(\Delta - Gx + \frac{\gamma}{2}) - \kappa/2\right]a_+(t) + \sqrt{\frac{\eta_c\kappa}{2}}\,s_{\mathrm{in}}(t) \tag{4.60}$$

$$\dot{a}_-(t) = \left[i(\Delta - Gx - \frac{\gamma}{2}) - \kappa/2\right]a_-(t) + \sqrt{\frac{\eta_c\kappa}{2}}\,s_{\mathrm{in}}(t) \tag{4.61}$$

$$\frac{d^2}{dt^2}x(t) + \Gamma_m\frac{d}{dt}x(t) + \Omega_m^2 x(t) = -\frac{\hbar G}{m_{\mathrm{eff}}}(|a_+|^2 + |a_-|^2). \tag{4.62}$$

The two stationary modes are the eigenmodes of the evolution and the degeneracy is lifted by the coupling rate γ. In the limit $\gamma \gg \kappa$, the two modes are well resolved and only one of them (here: a_-) needs to be considered since the other one is non resonant and hence not populated. In this limit, the optomechanical system reads:

$$\dot{a}_-(t) = \left[i(\Delta - Gx - \frac{\gamma}{2}) - \kappa/2 \right] a_-(t) + \sqrt{\frac{\eta_c \kappa}{2}} s_{\text{in}}(t) \tag{4.63}$$

$$\frac{d^2}{dt^2} x(t) + \Gamma_m \frac{d}{dt} x(t) + \Omega_m^2 x(t) = -\frac{\hbar G}{m_{\text{eff}}} |a_-|^2. \tag{4.64}$$

The system is equivalent to (4.13) and (4.14) after formally replacing the coupling parameter η_c by $\bar{\eta}_c \equiv \eta_c/2$, and Δ by $\bar{\Delta} \equiv \Delta - \gamma/2$. This equivalence also holds for the transmitted fields

$$s_{\text{out}}(t) = s_{\text{in}}(t) - \sqrt{\eta_c \kappa} a_{\text{ccw}}(t) = s_{\text{in}}(t) - \sqrt{\eta_c \kappa/2} (a_-(t) + a_+(t) \tag{4.65}$$

$$\approx s_{\text{in}}(t) - \sqrt{\eta_c \kappa/2} a_-(t) \tag{4.66}$$

as illustrated in figure 4.4. The reduced effective coupling parameter arises from the scattering of half of the intracavity power to the uncoupled mode. Note that in this case part of the intracavity light can be dissipated to a reflected field

$$s_{\text{ref}}(t) = -\sqrt{\eta_c \kappa} a_{\text{cw}}(t) = -\sqrt{\eta_c \kappa/2} (-a_-(t) + a_+(t)) \tag{4.67}$$

$$\approx \sqrt{\eta_c \kappa/2} a_-(t), \tag{4.68}$$

which can constitute another channel of optical dissipation. In the regime we consider, an optical beam resonant with the a_- cavity eigenmode dissipates a fraction of $2\eta_c(1-\eta_c)$ of the launched power due to the intrinsic losses of the cavity, a fraction of $(1-\eta_c)^2$ is transmitted and a fraction of η_c^2 is reflected.

With our present settings, we measured a residual transmission of $|t_r|^2 \approx 0.5$ (note however that $|t_r|^2 < 0.01$ can be achieved with silica toroids [60]), we can hence infer the effective coupling parameter $\bar{\eta}_c$ by solving

$$|t_r|^2 = 1/2 = (1 - 2\bar{\eta}_c)^2, \tag{4.69}$$

leading to

$$\bar{\eta}_c = \frac{2 - \sqrt{2}}{4} \approx 0.15. \tag{4.70}$$

The intracavity power is hence smaller than the one calculated in the "standard" situation $\eta_c = 1/2$ and $\gamma = 0$. In the calculation of the coupling rate Ω_c, we took this factor into account; an additional reduction factor of 1.9 is also to be introduced in the analysis of the data to account for taper losses in this experiment.

Sideband Sweeps

To probe the cavity transmission spectrum in the presence of a control beam, the Ti:sapphire control laser is phase modulated at frequency Ω using a broadband phase modulator, creating two sidebands at $\omega_l + \Omega$ and $\omega_l - \Omega$. Keeping the laser detuned to the lower motional sideband of the cavity ($\bar{\Delta} \approx -\Omega_\mathrm{m}$), a sweep of the modulation frequency Ω scans the probe field through the cavity resonance. In the resolved sideband regime, only the upper sideband, being close to resonance, interacts with the cavity, acting as a weak probe beam. The lower one and carrier are transmitted unchanged through the tapered fiber. However, one has to take them into account in order to understand quantitatively the obtained results. As shown in the following, demodulation of the total homodyne signal at the modulation frequency Ω using a network analyzer (NA, c.f. Fig. 4.3) allows extracting a 'transmission' homodyne signal t_hom, which, in the RSB regime, is related to the probe transmission by the simple relation $t_\mathrm{hom} \approx 1 - t_\mathrm{p}$.

The incident fields at the homodyne beamsplitter are a carrier and two sidebands of the local oscillator, and the carrier and two sidebands of the beam entering the cavity. We note t_c, t_us and t_ls the complex transmission coefficient across the cavity for the carrier, upper sideband and lower sideband respectively. The phase of the local oscillator Φ is actively adjusted so that it matches the phase of the control beam emerging from the cavity.

At one exit of the beamsplitter the optical power is proportional to

$$\begin{aligned}\Bigg| & E_\mathrm{cav} e^{-i\omega_l t}\left(t_\mathrm{c} + i\frac{\beta}{2}e^{-i\Omega t}t_\mathrm{us} + i\frac{\beta}{2}e^{+i\Omega t}t_\mathrm{ls}\right) \\ & \qquad + iE_\mathrm{LO}e^{-i\omega_l t}e^{i\Phi}\left(1 + i\frac{\beta}{2}e^{-i\Omega t} + i\frac{\beta}{2}e^{+i\Omega t}\right)\Bigg|^2,\end{aligned} \tag{4.71}$$

where β is the depth of the modulation induced by the EOM, E_LO and E_cav are the field amplitudes in the local oscillator and signal arms of the homodyne setup. The interesting terms are the modulated cross-terms, they are given by

$$\begin{aligned} & 2\,\mathrm{Re}\left[\left(E_\mathrm{cav}e^{-i\omega_l t}t_\mathrm{c}\right)\cdot\left(iE_\mathrm{LO}e^{-i\omega_l t}e^{i\Phi}\left(i\frac{\beta}{2}e^{-i\Omega t} + i\frac{\beta}{2}e^{+i\Omega t}\right)\right)^*\right. \\ & \qquad \left. + \left(E_\mathrm{cav}e^{-i\omega_l t}\left(i\frac{\beta}{2}e^{-i\Omega t}t_\mathrm{us} + i\frac{\beta}{2}e^{+i\Omega t}t_\mathrm{ls}\right)\right)\cdot\left(iE_\mathrm{LO}e^{-i\omega_l t}e^{i\Phi}\right)^*\right] \\ & = \beta E_\mathrm{cav}E_\mathrm{LO}\,\mathrm{Re}\left[t_\mathrm{c}\cdot\left(-e^{-i\Phi}\left(e^{+i\Omega t} + e^{-i\Omega t}\right)\right) + \left(e^{-i\Omega t}t_\mathrm{us} + e^{+i\Omega t}t_\mathrm{ls}\right)\cdot\left(e^{-i\Phi}\right)\right] \\ & = \beta E_\mathrm{cav}E_\mathrm{LO}\,\mathrm{Re}\left[\left(e^{-i\Phi}\right)\left(-t_\mathrm{c}2\cos(\Omega t) + \left(e^{-i\Omega t}t_\mathrm{us} + e^{+i\Omega t}t_\mathrm{ls}\right)\right)\right]\end{aligned} \tag{4.72}$$

Now writing real and imaginary parts of the used functions as

$$e^{-i\Phi} \equiv \Phi' + i\Phi'' \tag{4.73}$$

$$t_\mathrm{c} \equiv t_c' + i t_c'' \tag{4.74}$$

$$t_\mathrm{us} \equiv t_\mathrm{us}' + i t_\mathrm{us}'' \tag{4.75}$$

$$t_\mathrm{ls} \equiv t_\mathrm{ls}' + i t_\mathrm{ls}'' \tag{4.76}$$

we get (omitting the prefactor $\beta E_\mathrm{cav} E_\mathrm{LO}$)

$$\begin{aligned} &\cos(\Omega t) \underbrace{\left(-2\Phi' t_\mathrm{c}' + 2\Phi'' t_c'' + (t_\mathrm{us}' + t_\mathrm{ls}')\Phi' - (t_\mathrm{us}'' + t_\mathrm{ls}'')\Phi''\right)}_{A} \\ &+ \sin(\Omega t) \underbrace{\left((t_\mathrm{us}'' - t_\mathrm{ls}'')\Phi' + (t_\mathrm{us}' - t_\mathrm{ls}')\Phi''\right)}_{B} \end{aligned} \tag{4.77}$$

A and B represent the in-phase and quadrature response of the system to the input modulation. In the resolved sideband regime, only the upper sideband is affected by the cavity. In this case $\Phi' = t_c' = t_\mathrm{ls}' = 1$ and $\Phi'' = t_\mathrm{c}'' = t_\mathrm{ls}'' = 0$. Moreover, the upper sideband, close to resonance, is probing the OMIT signal $t_\mathrm{us} = t_p$. The quadratures measured by the network analyzer are then:

$$|A| \approx 1 - t_\mathrm{us}' = 1 - \mathrm{Re}(t_p) \tag{4.78}$$

$$|B| \approx -t_\mathrm{us}'' = -\mathrm{Im}(t_p). \tag{4.79}$$

The complex amplitude response $t_\mathrm{hom} = A + iB$ as measured on the network analyzer is hence given in good approximation by:

$$t_\mathrm{hom} \approx 1 - t_p. \tag{4.80}$$

The normalized response t_hom' is directly related to the normalized transmission $t_p{}'$:

$$t_\mathrm{hom}' = \frac{t_\mathrm{hom}}{1 - t_r} \tag{4.81}$$

$$= 1 - t_p{}'. \tag{4.82}$$

In particular, if we consider the form (4.37) for the probe beam transmission, the measured signal is then given by:

$$t_\mathrm{hom}' = \frac{\Gamma_m \kappa - 2i\Delta' \kappa}{\Omega_c^2 + \Gamma_m \kappa - 2i\Delta' \kappa}. \tag{4.83}$$

We can easily calculate the normalized transmitted power:

$$|t'_{\text{hom}}|^2 = 1 - \frac{\Omega_c^2/\kappa\left(\Omega_c^2/\kappa + 2\Gamma_m\right)}{\left(\Gamma_m + \Omega_c^2/\kappa\right)^2 + (2\Delta')^2} \tag{4.84}$$

The measured signal is hence an inverted Lorentzian peak with width Γ_{OMIT} (same width as $|t_p|^2$). The minimum value of the dip $|t'_{\text{hom}}(\Delta' = 0)|^2$ can be linked very easily to the maximum value of the transmission window $|t'_p(\Delta' = 0)|^2$ by remarking that for $\Delta' = 0$ the transmission coefficients t_p and t_{hom} are real. The relation (4.80) gives then:

$$|t'_{\text{hom}}(\Delta' = 0)|^2 = \left(1 - \sqrt{|t'_p(\Delta' = 0)|^2}\right)^2 \tag{4.85}$$

4.1.4 Results

Figure 4.5A shows the theoretically expected response of the optomechanical system and the detected signals. Clearly, the OMIT window is apparent in the intracavity probe power as described by Eq. (4.31), occurring simultaneously with the onset of radiation-pressure-driven mechanical oscillations. The excitation of the intracavity probe field therefore is suppressed, and the transmitted field nearly equals the probe field sent to the cavity. The lowest panel shows the corresponding homodyne signal, and the five panels in Fig. 4.5B show experimentally measured homodyne traces for detunings $\bar{\Delta}/2\pi$ varying from −69.1 MHz to −35.4 MHz, and a control laser power of 0.5 mW. The center of the probe extinction (maximum of the homodyne signal) always occurs for $\Omega \approx -\bar{\Delta}$, as the probe laser then matches the cavity resonance ($\omega_{\text{p}} \approx \omega'_{\text{c}}(\bar{x})$). Importantly however, the sharp OMIT window occurs only when the two-photon resonance condition $\Omega = \Omega_{\text{m}}$ (with $\Omega = \omega_{\text{p}} - \omega_{\text{l}}$) is met, independent of the detuning $\bar{\Delta}$ of the control beam—giving clear evidence to the theoretically suggested underlying mechanism.

To analyze the effect of the control beam more systematically, its detuning was fixed to the lower motional sideband. Varying its power from 0.125 to 6.5 mW, traces of the homodyne signal are taken in the vicinity of the two-photon resonance (Fig. 4.6). Dips of increasing depth and width are observed, which can be modeled by a simple Lorentzian function (see (4.84)). The minimum homodyne signal is obtained under the condition of the two-photon resonance $\Delta' = 0$. In this case, the homodyne signal power and the probe power transmission are simply interrelated by $|t'_{\text{p}}|^2 = \left(1 - |t'_{\text{hom}}|\right)^2$, where $t'_{\text{hom}} = t_{\text{hom}}/(1 - t_{\text{r}})$ (see (4.81) and (4.82))is the normalized homodyne signal. The width of the measured dip in the normalized homodyne signal is equal to that of the coupling-induced transmission window $\Gamma_{\text{OMIT}} \approx \Gamma_{\text{m}}(1 + C)$, where $C \equiv \Omega_{\text{c}}^2/\Gamma_{\text{m}}\kappa$ (4.42)is an equivalent optomechanical cooperativity parameter [114]. From the model (4.31), the expected probe transmission on resonance is simply given by $t'_{\text{p}}(\Delta' = 0) =$

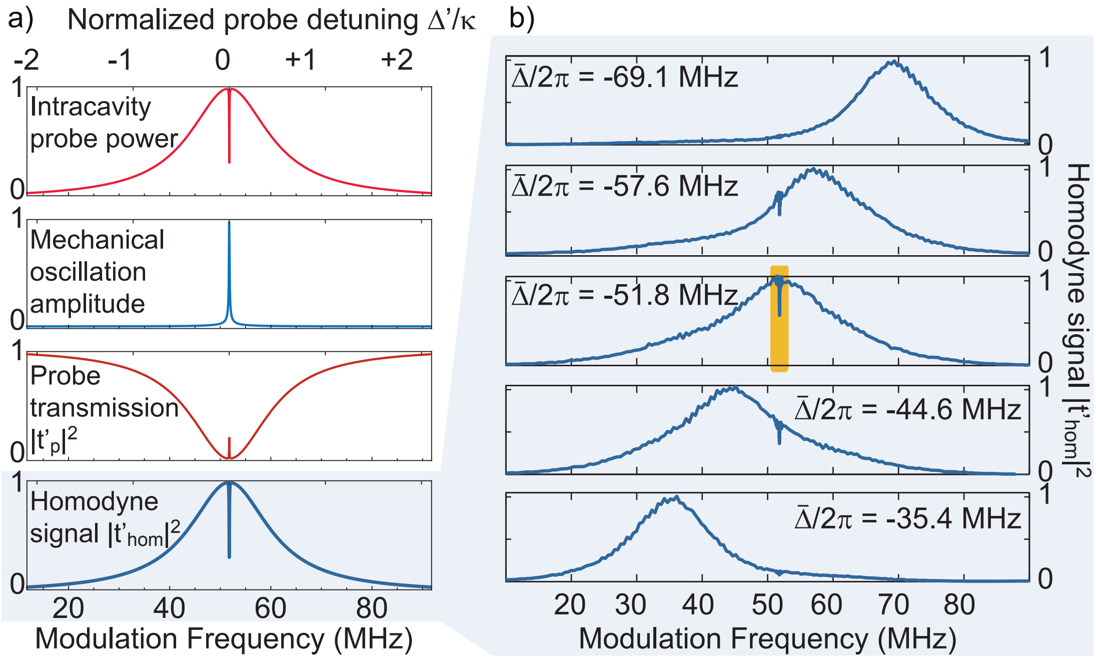

Figure 4.5: **Observation of OMIT.** A) Theoretically expected intracavity probe power $|A^-|^2$, oscillation amplitude X, normalized probe power transmission $|t'_\mathrm{p}|^2$ and the normalized homodyne signal $|t'_\mathrm{hom}|^2$ as a function of the modulation frequency $\Omega/2\pi$ (top to bottom panels). The first two panels have additionally been normalized to unity. When the two-photon resonance condition $\Delta' = 0$ is met, the mechanical oscillator is excited, giving rise to destructive interference of excitation pathways for an intracavity probe field. The probe transmission therefore exhibits an inverted dip, which can be easily identified in the homodyne signal. B) Experimentally observed normalized homodyne traces when the probe frequency is scanned by sweeping the phase modulator frequency Ω for different values of control beam detuning $\bar{\Delta}$. While the center of the response of the bare optical cavity shifts correspondingly, the sharp dip characteristic of OMIT occurs always for $\Delta' = 0$. The power of the control beam sent to the cavity is 0.5 mW in these measurements. The middle panel shows the operating conditions where the control beam is tuned to the lower motional sideband $\bar{\Delta} \approx -\Omega_\mathrm{m} = -2\pi \cdot 51.8\,\mathrm{MHz}$. The region around the central dip (orange background) is studied in more detail in a dedicated experimental series (cf. Fig. 4).

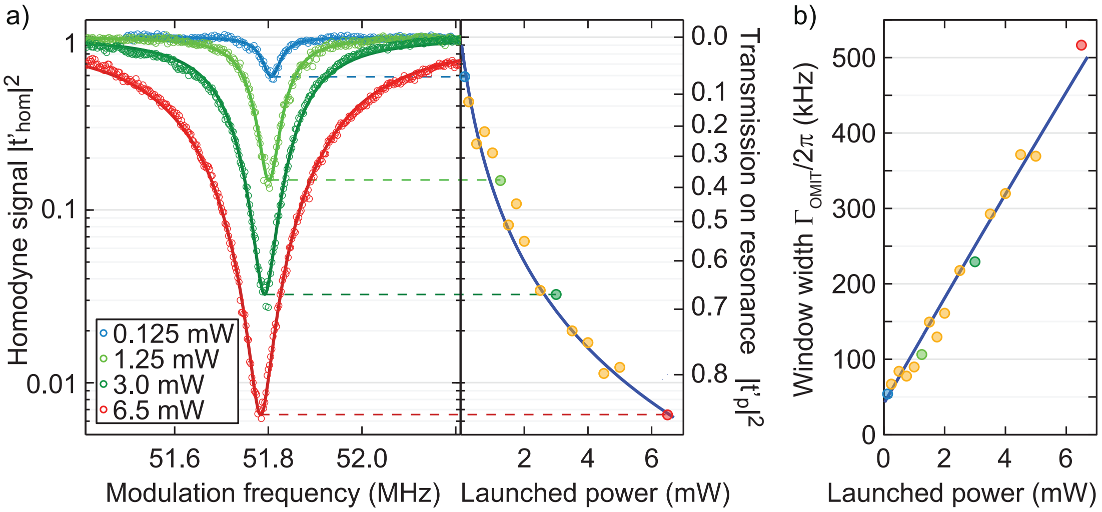

Figure 4.6: **Controlling optomechanically induced transparency.** A) Experimental normalized homodyne traces in the presence of a control beam (circles) for four different powers in the control beam from 0.125 mW up to 6.5 mW, and Lorentzian models. The minimum homodyne signal (measured at $\Delta' = 0$) directly indicates the maximum probe power transmission achieved in this case. These values are given in the right panel for a larger set of probe scans, together with the theoretical model developed in this work. See text for more information. B) Width of the transparency window extracted from the same set of probe scans. Good agreement with the theoretical prediction is found over the entire power range.

$C/(C+1)$ (4.43). Our data match these expectations extremely well if we allow for a linear correction factor in the optomechanical coupling frequency Ω_c due to the modal coupling explained earlier and losses in the fiber taper. We have reached probe power transmission $|t_p'|^2$ up to 81%, indicating the high contrast achievable in OMIT.

In fact, any optomechanical system reaching $C \gtrsim 1$ can realize an appreciable control-induced probe transmission, as desired, for example, in all-optical switches. Interestingly, the systems available already today, reach $C \approx 1$ with only thousands [44] or even hundreds [129] of control photons in the cavity, and recently emerging integrated nano-optomechanical structures [130] may be able to further reduce this number.

4.1.5 Conclusion

The resulting extreme optical non-linearities could be of interest for both fundamental and applied studies.

The tunable probe transmission window also modifies the propagation of a probe pulse due to the variation of the complex phase picked by its different frequency components. EIT is the underlying phenomenon allowing for slowing down of light pulses. Indeed, the sharp transparency window in the medium is accompanied by a very abrupt change of its refractive index leading to slow group velocities (see [123] for a detailed analysis of the phenomenon). In the case of a single optically active element like an optomechanical device, the rapid phase dispersion $\phi(\omega) = \arg(t_p(\omega))$ leads to a 'group delay' τ_g given by:

$$\tau_g = -\frac{d\phi}{d\omega}. \tag{4.86}$$

A full calculation based on the expression (4.31) shows that the group delay diverges for small values of the transparency. However, in the regime $C \gtrsim 1$, where the medium is not completely opaque, a simple calculation based on expression (4.37) is perfectly valid:

$$\phi(\Delta') = \arctan\left(\frac{2\Delta'\kappa}{\Omega_c + \Gamma_m\kappa}\right). \tag{4.87}$$

This gives for the middle of the transparency window ($\Delta' = 0$):

$$\tau_g(\Delta' = 0) = \frac{2\kappa}{\Omega_c^2 + \Gamma_m\kappa} = \frac{1}{\Gamma_m}\left(\frac{2}{C+1}\right) = \frac{2}{\Gamma_{\mathrm{OMIT}}}. \tag{4.88}$$

As a consequence a resonant probe pulse experiences a group delay of $\tau_{\mathrm{g}} \approx 2/\Gamma_{\mathrm{OMIT}}$ in the regime $C \gtrsim 1$ of interest, a value exceeding several seconds in some available optomechanical systems [41, 131]. However, undistorted pulse propagation only occurs if the full probe pulse spectrum is contained within the transparency window of the system. This restricts the effectiveness of such a delay due to the fixed delay-bandwidth product of $\tau_{\mathrm{g}}\Gamma_{\mathrm{OMIT}} \approx 2$. A cascade of systems may alleviate this shortcoming—the most interesting scenario being a large array of concatenated optomechanical systems, as suggested in the context of OMIT [52, 93, 132], and RF/microwave photonics [115]. The group delay could then be dynamically tuned while the probe pulse is propagating through the array. Such systems could be practically implemented in lithographically designed optomechanical systems both in the microwave [129] and optical [133, 134] domain.

4.2 Optomechanical Sideband Cooling of a Micromechanical Oscillator Close to the Quantum Ground State

This section is based on Rivière *et al.* [2] published in the journal *Physical Review A* in June 2011 and summarizes the experiments performed at MPQ aiming at ground state cooling in a helium-3 cryostat.

4.2.1 Introduction

The quantum regime of macroscopic mechanical systems has received significant interest over the past decade [135, 136, 137, 138]. Mechanical systems cooled to the quantum ground state may allow probing quantum-mechanical phenomena on an unprecedentedly large scale, could enable quantum-state preparation of mechanical systems, and have been proposed as an interface between photons and stationary qubits [139]. To achieve ground state cooling, two challenges have to be met: first, most mechanical oscillators have vibrational frequencies $\Omega_\mathrm{m}/2\pi < 100\,\mathrm{MHz}$, such that low mode temperatures T_eff are required to achieve $\hbar\Omega_\mathrm{m} > k_\mathrm{B}T_\mathrm{eff}$ ($\hbar$ is the reduced Planck constant and k_B Boltzmann's constant). Second, quantum-limited measurements of mechanical motion must be performed at the level of the zero point motion, $x_\mathrm{zpf} = \sqrt{\hbar/2m_\mathrm{eff}\Omega_\mathrm{m}}$ in order to probe the state of the oscillator of mass m_eff.

A few months prior to this work a piezomechanical oscillator has been cooled to the quantum regime [29]. Due to its GHz resonance frequency, conventional cryogenics could be employed for cooling, while it was probed using its piezoelectrical coupling to a superconducting qubit. In contrast, cooling schemes based on dynamical backaction [140, 141] can be applied to a much wider class of nano- and micromechanical oscillators. Following the observation of optical cooling based on a photothermal effect [142], dynamical backaction cooling by radiation pressure [26, 27, 28, 143], as predicted more than forty years ago [140], was demonstrated. This scheme is based on parametric coupling of an optical and mechanical resonance and simultaneously allows sensitive detection of mechanical motion. In analogy to the case of trapped ions, in which sideband cooling has led to the preparation of the vibrational ground state [144], dynamical backaction sideband cooling has been theoretically shown to allow reaching the quantum ground state of a mechanical mode [55, 145, 56].

Despite major progress, ground state cooling using this approach has remained challenging, owing to insufficiently low starting temperatures and/or excess heating by the electromagnetic field used for cooling [125, 43, 146]. Here we demonstrate an experimental optomechanical setting that successfully addresses these challenges and achieve cooling to only 9 ± 1 quanta, implying that the oscillator resides $(10 \pm 1)\%$ of its time in the quantum ground state. Our experiment operates in the temperature

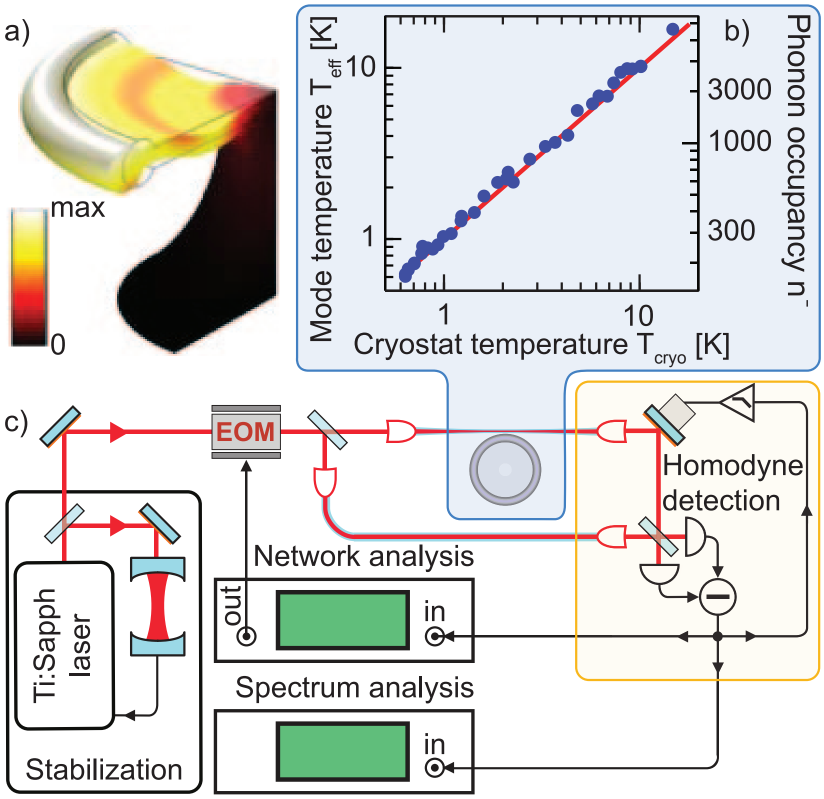
a)
max
0
b)
Mode temperature T_{eff} [K]
10
1
1
10
Cryostat temperature T_{cryo} [K]
3000
1000
300
Phonon occupancy n
c)
EOM
Homodyne detection
Network analysis
out
in
Spectrum analysis
in
Ti:Sapph laser
Stabilization

Figure 4.7: **Cooling a micromechanical oscillator.** (a) High Q mechanical and optical modes are co-located in a silica microtoroid. The simulated displacement pattern of the mechanical radial breathing mode (RBM) is shown, with the color code illustrating the strain. The optical whispering gallery mode (WGM) is confined to the rim. (b) Thermalization of the RBM to the temperature of the ^{3}He gas, with the lowest achieved temperature corresponding to a mean occupancy of the RBM below 200 quanta. (c) Optical setup used for displacement monitoring of the mechanical mode, based on homodyne analysis of the light re-emerging from the toroid's WGM (see text for detailed description).

regime below 1 K, where the coupling of the mechanical mode to two level systems (TLS) induces significant mechanical dissipation. The temperature-dependent effects of TLS in glass can be harnessed for a novel and independent thermometry method, in addition to conventional noise thermometry of the mechanical modes. Using two independent methods for the determination of the mechanical oscillator's temperature, we are able to reliably quantify resonant and off-resonant heating by the cooling laser. Our measurements demonstrate that resonant heating is negligible for the chosen experimental system, enabling a wide range of future experiments in quantum optomechanics.

4.2.2 Experiment

We use silica toroidal resonators, which support whispering gallery modes (WGM) of ultrahigh finesse co-located with a low loss mechanical radial breathing mode (RBM) [113, 93] and large mutual optomechanical coupling. The devices used here have been optimized for narrow optical linewidths κ, and moderately high mechanical frequencies Ω_{m}, thereby operating deeply in the resolved sideband (RSB) regime ($\Omega_{\mathrm{m}} \approx 2\pi \times 70\ \mathrm{MHz} \gtrsim 10\kappa$), while at the same time the pillar geometry was engineered for low mechanical dissipation [74, 92] (Fig. 4.7).

For the cryogenic laser cooling experiments, we subject these samples directly to a ^{3}He gas evaporated from a reservoir of liquid ^{3}He. At a pressure of ~ 0.7 mbar, the gas provides a thermal bath at a temperature of about 600 mK. However, it is essential to verify thermalization of the toroid to the exchange gas. To this end, a low-noise fiber laser is coupled to a WGM through a fiber taper positioned in the near field of the mode via piezoelectric actuators. The displacement fluctuations of the RBM can be extracted and used to infer its noise temperature [66, 48]. As shown in Fig. 4.7b, it follows the temperature of the helium gas down to temperatures of 600 mK for weak probing (i.e. $< 1\ \mu$W input laser power).

For optomechanical sideband cooling, we employed a frequency-stabilized Ti:sapph laser and a homodyne detection scheme [125] for quantum-limited detection of mechanical displacement fluctuations (Fig. 4.7c). Spectral analysis of the homodyne signal provides direct access to the mechanical displacement spectrum, from which the mechanical damping and resonance frequency can be extracted. The spectra are calibrated in absolute terms by applying a known frequency modulation to the laser using an electro-optic modulator (EOM) as detailed in Refs. [125, 48]. After the acquisition of each spectrum, the precise detuning of the laser from the cavity resonance is determined by sweeping the modulation frequency of the EOM and recording the demodulated homodyne signal with a network analyzer (see 4.1.3 in paragraph "Sideband Sweeps" and [1]).

The independent thermometry method we are presenting is based on the strong temperature dependence of the material's mechanical properties caused by the presence of structural defects modeled as two-level-systems (TLS) [66, 81]. Relaxation of the TLS under excitation from an acoustic wave modifies the mechanical susceptibility as described earlier (3.2), leading to a change in mechanical resonance frequency Ω_{m} and a change of the damping rate $\Gamma_{\mathrm{m}} = \Omega_{\mathrm{m}}/Q_{\mathrm{m}}$ (with the mechanical quality factor Q_{m}).

Two different relaxation regimes have to be considered for sample temperatures T between 0.6 K to 3 K: tunneling-assisted relaxation [147, 82], and single phonon

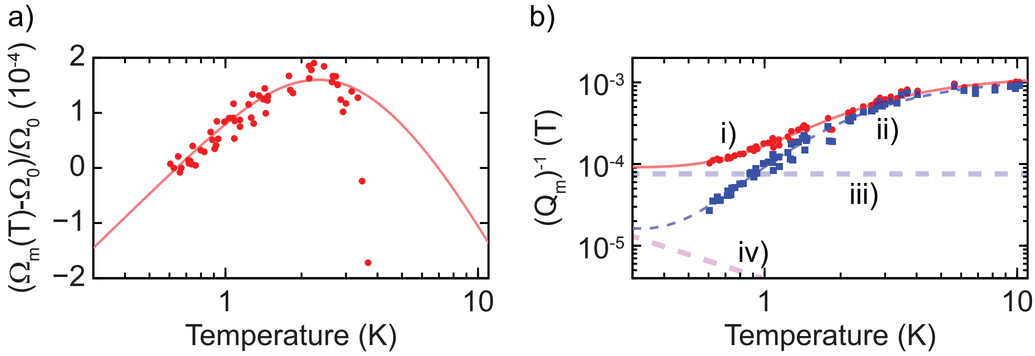

Figure 4.8: **Contribution from TLS.** TLS-induced change of the resonance frequency ($\Omega_\mathrm{m}(T)$) (a) and inverse mechanical quality factor ($Q_\mathrm{m}^{-1}(T)$) (b) of the radial breathing mode. Measured data (red points) agree well with the models (red solid lines) described in eqs. (4.89) and (4.90). Subtraction of the temperature-independent clamping damping (line iii) yields the theoretically possible material-limited damping values (blue squares and line ii). At very low temperatures, damping by resonant interaction with TLS (line iv) would be dominant. Ω_0 is the mechanical angular frequency Ω_m measured at the arbitrary temperature $T = 620$ mK. The model parameters are given in 3.2.3

resonant interaction [82]. Thermally activated relaxation [84] dominates the frequency shift at temperatures above 3 K, but is negligible in the temperature range at which the laser cooling experiments are performed. In the presence of tunneling relaxation ("tun") and resonant interactions ("res") the mechanical oscillator properties can be expressed as

$$\Omega_\mathrm{m}(T) = \Omega_\mathrm{upt} + \delta\Omega_\mathrm{tun}(T) + \delta\Omega_\mathrm{res}(T), \tag{4.89}$$

$$Q_\mathrm{m}^{-1}(T) = Q_\mathrm{cla}^{-1} + Q_\mathrm{tun}^{-1}(T) + Q_\mathrm{res}^{-1}(T), \tag{4.90}$$

where Ω_upt is the unperturbed angular frequency in the absence of TLS-induced effects and $\Omega_\mathrm{m} Q_\mathrm{cla}^{-1}$ is the damping rate due to the clamping of the resonator to the substrate, dominating Γ_m at room temperature. For readability we simply take $\Omega_\mathrm{m} \equiv \Omega_\mathrm{m}(T_\mathrm{cryo})$ with T_cryo being the independently measured temperature of the cryostat, when the TLS-induced thermal dependence of the frequency is quantitatively neglected over the temperature range of interest (relative shift of the order of 10^{-4}). For the damping however, since the TLS significantly alter its value, the short notation $Q_\mathrm{m} \equiv Q_\mathrm{m}(T)$ and $\Gamma_\mathrm{m} \equiv \Gamma_\mathrm{m}(T)$ still signifies that the thermal dependence is taken into account. The respective temperature dependencies in the relevant regimes of TLS damping are also detailed in 3.2. In contrast to previous experiments using ^{4}He [125, 43], where Q_m was limited to ~ 3000 at $T \approx 3$ K due to TLS damping, Q_m reaches values exceeding 10^4 with significant contributions from clamping losses for the lowest temperatures of 600 mK. Such values are sufficient to enable ground state cooling since $Q_\mathrm{m}/\bar{n}_\mathrm{i} \gg 1$ and $\bar{n}_\mathrm{i}\Omega_\mathrm{m}/Q_\mathrm{m} \ll \kappa$ ($\bar{n}_\mathrm{i}$ is the initial occupancy) [121]. The temperature dependence of the mechanical Q is in excellent quantitative agreement with the one caused by TLS defects (Fig. 4.8). This well-understood temperature dependence of the TLS-induced effects [Eqs. (4.89)-(4.90)] enables its use as a "thermometer" of the sample temperature T after a calibration measurement as shown in Fig. 4.8 has been performed once. Importantly, this method can reveal excess heating by the cooling laser.

4.2.3 Results

We studied optomechanical cooling [26, 27, 28] by performing a series of experiments in which mechanical displacement noise spectra were recorded while varying the laser detuning $\bar{\Delta} \equiv \omega_\mathrm{l} - \bar{\omega}_\mathrm{c}$. Here, ω_l is the laser's (angular) frequency and $\bar{\omega}_\mathrm{c}$ the WGM frequency. To model radiation-pressure induced dynamical backaction [140] for the present microresonators, we take into account that backscattering of light couples modes a_ccw and a_cw with opposite circulation sense [126, 46]. As a consequence the degeneracy between the system's eigenmodes $a_\pm = (a_\mathrm{ccw} \pm a_\mathrm{cw})/\sqrt{2}$ is lifted and the resonance frequencies are split by the scattering coupling rate γ. During a detuning series as reported here, both modes are populated with a mean field $\bar{a}_\pm = \sqrt{\kappa_\mathrm{ex}/2}\, L_\pm(\bar{\Delta}) s_\mathrm{in}$, where $P_\mathrm{in} = |s_\mathrm{in}|^2 \hbar\omega_\mathrm{l}$ is the driving laser power, κ_ex the coupling rate to the fiber taper, $|\bar{a}_\pm|^2$ the mean photon population in the new eigenmodes, and $L_\pm(\bar{\Delta}) \equiv \left(-i(\bar{\Delta} \pm \gamma/2) + \kappa/2\right)^{-1}$ the modes' Lorentzian response. In the following section the effects caused by modal splitting will be derived in more detail.

Model for split modes

As in equations (4.60) - (4.62) the coupled optomechanical equations of motion can be derived as

$$\dot{a}_+(t) = \left(i\left(\Delta - Gx(t) + \frac{\gamma}{2}\right) - \frac{\kappa}{2}\right) a_+(t) + \sqrt{\frac{\eta_\mathrm{c}\kappa}{2}} s_\mathrm{in}(t) \tag{4.91}$$

$$\dot{a}_-(t) = \left(i\left(\Delta - Gx(t) - \frac{\gamma}{2}\right) - \frac{\kappa}{2}\right) a_-(t) + \sqrt{\frac{\eta_\mathrm{c}\kappa}{2}} s_\mathrm{in}(t) \tag{4.92}$$

$$m_\mathrm{eff}\left(\ddot{x}(t) + \Gamma_\mathrm{m}\dot{x}(t) + \Omega_\mathrm{m}^2 x(t)\right) = -\hbar G\left(|a_+(t)|^2 + |a_-(t)|^2\right) + \delta F(t), \tag{4.93}$$

where $\delta F(t)$ is an additional external force, e. g. the thermal Langevin force. We then apply the usual linearization

$$a_\pm(t) = \bar{a}_\pm + \delta a_\pm(t) \tag{4.94}$$

$$x(t) = \bar{x} + \delta x(t) \tag{4.95}$$

assuming $|\bar{a}_\pm| \gg |\delta a_\pm(t)|$ and $|\bar{x}| \gg |\delta x(t)|$. For the large mean occupancy of the modes and the mean mechanical displacement, we then obtain

$$\bar{a}_+ = \frac{\sqrt{\eta_\mathrm{c}\kappa/2}\,\bar{s}_\mathrm{in}}{-i(\bar{\Delta}+\gamma/2)+\kappa/2} =: \sqrt{\eta_\mathrm{c}\kappa/2}\,L_+(\bar{\Delta})\,\bar{s}_\mathrm{in} \tag{4.96}$$

$$\bar{a}_- = \frac{\sqrt{\eta_\mathrm{c}\kappa/2}\,\bar{s}_\mathrm{in}}{-i(\bar{\Delta}-\gamma/2)+\kappa/2} =: \sqrt{\eta_\mathrm{c}\kappa/2}\,L_-(\bar{\Delta})\,\bar{s}_\mathrm{in} \tag{4.97}$$

$$\bar{x} = -\frac{\hbar G}{m_\mathrm{eff}\Omega_\mathrm{m}^2}\left(|\bar{a}_+|^2 + |\bar{a}_-|^2\right). \tag{4.98}$$

The average displacement $\bar{x}$ induces a small static frequency shift, as does the (usually dominant) static shift due to absorption-induced heating [148], which are both absorbed into the mean detuning $\bar{\Delta} = \omega_\mathrm{l} - (\omega_\mathrm{c}(T) + G\bar{x})$. One then obtains the equations of motion for small fluctuations,

$$\delta\dot{a}_+(t) = \left(i\left(\bar{\Delta}+\frac{\gamma}{2}\right)-\frac{\kappa}{2}\right)\delta a_+(t) - iG\bar{a}_+\delta x(t) \tag{4.99}$$

$$\delta\dot{a}_-(t) = \left(i\left(\bar{\Delta}-\frac{\gamma}{2}\right)-\frac{\kappa}{2}\right)\delta a_-(t) - iG\bar{a}_-\delta x(t) \tag{4.100}$$

$$m_\mathrm{eff}\left(\delta\ddot{x}(t) + \Gamma_\mathrm{m}\delta\dot{x}(t) + \Omega_\mathrm{m}^2\delta x(t)\right) = -\hbar G\left(\bar{a}_+^*\delta a_+(t) + \bar{a}_-^*\delta a_-(t) + \text{c.c.}\right) + \delta F(t). \tag{4.101}$$

Fourier transformation gives

$$\delta a_+(\Omega) = \frac{-iG\bar{a}_+\delta x(\Omega)}{-i\left(\bar{\Delta}+\gamma/2+\Omega\right)+\kappa/2} = -iG\bar{a}_+\,L_+(\bar{\Delta}+\Omega)\,\delta x(\Omega) \tag{4.102}$$

$$\delta a_-(\Omega) = \frac{-iG\bar{a}_-\delta x(\Omega)}{-i\left(\bar{\Delta}-\gamma/2+\Omega\right)+\kappa/2} = -iG\bar{a}_-\,L_-(\bar{\Delta}+\Omega)\,\delta x(\Omega) \tag{4.103}$$

$$\delta x(\Omega)/\chi_\mathrm{m}(\Omega) = -\hbar G\left(\bar{a}_+^*\delta a_+(+\Omega) + \bar{a}_-^*\delta a_-(+\Omega) + \text{c.c.}\right) + \delta F(\Omega). \tag{4.104}$$

With

$$\chi_\mathrm{m}(\Omega) = \frac{1}{m_\mathrm{eff}\left(-\Omega^2 - i\Omega\Gamma_\mathrm{m} + \Omega_\mathrm{m}^2\right)} \tag{4.105}$$

Solving equations (4.102) to (4.104) for δx yields

$$\begin{aligned}\delta x(\Omega)^{-1} = &\frac{1/\chi_\mathrm{m}(\Omega) - i\hbar G^2|\bar{a}_+|^2\left(L_+(\bar{\Delta}+\Omega) - \left(L_+(\bar{\Delta}-\Omega)\right)^*\right)}{\delta F(\Omega)} \\ &- \frac{i\hbar G^2|\bar{a}_-|^2\left(L_-(\bar{\Delta}+\Omega) - \left(L_-(\bar{\Delta}-\Omega)\right)^*\right)}{\delta F(\Omega)}\end{aligned} \tag{4.106}$$

so that we can write

$$\begin{aligned}\frac{1}{\chi_{\mathrm{eff}}(\Omega)} = &\frac{1}{\chi_{\mathrm{m}}(\Omega)} - i\hbar G^2 \left[|\bar{a}_+|^2 \left(L_+(\bar{\Delta}+\Omega) - \left(L_+(\bar{\Delta}-\Omega)\right)^*\right)\right.\\ &\left. +|\bar{a}_-|^2 \left(L_-(\bar{\Delta}+\Omega) - \left(L_-(\bar{\Delta}-\Omega)\right)^*\right)\right]\end{aligned} \tag{4.107}$$

and, in the regime of weak optomechanical coupling [121], the effective susceptibility is still approximately Lorentzian with a damping rate and resonance frequency given by

$$\begin{aligned}\Gamma_{\mathrm{eff}} \approx \Gamma_{\mathrm{m}} + 2x_{\mathrm{zpf}}^2 G^2 \mathrm{Re}&\left[|\bar{a}_+|^2 \left(L_+(\bar{\Delta}+\Omega) - \left(L_+(\bar{\Delta}-\Omega)\right)^*\right)\right.\\ &\left. +|\bar{a}_-|^2 \left(L_-(\bar{\Delta}+\Omega) - \left(L_-(\bar{\Delta}-\Omega)\right)^*\right)\right]\end{aligned} \tag{4.108}$$

$$\begin{aligned}\Omega_{\mathrm{eff}} \approx \Omega_{\mathrm{m}} + x_{\mathrm{zpf}}^2 G^2 \mathrm{Im}&\left[|\bar{a}_+|^2 \left(L_+(\bar{\Delta}+\Omega) - \left(L_+(\bar{\Delta}-\Omega)\right)^*\right)\right.\\ &\left. +|\bar{a}_-|^2 \left(L_-(\bar{\Delta}+\Omega) - \left(L_-(\bar{\Delta}-\Omega)\right)^*\right)\right].\end{aligned} \tag{4.109}$$

In the context of cavity optomechanics, it is important to realize that three-mode interactions [149] can be neglected in the present configuration. The radiation pressure forces induced by the light in these modes can therefore simply be added. The usual linearization procedure [32, 33] then yields an inverse effective mechanical susceptibility

$$\left[\chi_{\mathrm{eff}}(\Omega)\right]^{-1} = \left[\chi_{\mathrm{m}}(\Omega)\right]^{-1} - i\Omega_{\mathrm{m}} m_{\mathrm{eff}} f(\Omega), \tag{4.110}$$

in which the bare mechanical susceptibility $\chi_{\mathrm{m}}(\Omega)$ is modified by the dynamical backaction term

$$f(\Omega) = 2g_0^2 \sum_{\sigma=\pm} |\bar{a}_\sigma|^2 \left(L_\sigma(\bar{\Delta}+\Omega) - (L_\sigma(\bar{\Delta}-\Omega))^*\right) \tag{4.111}$$

with the vacuum optomechanical coupling rate [48] $g_0 \equiv G x_{\mathrm{zpf}}$ and $G = \mathrm{d}\omega_{\mathrm{c}}/\mathrm{d}x$. For moderate driving powers [121], the susceptibility of the mechanical mode is the one of a harmonic oscillator with effective damping rate and resonance frequency of

$$\Gamma_{\mathrm{eff}} \approx \Gamma_{\mathrm{m}}(T) + \mathrm{Re}\left[f(\Omega_{\mathrm{m}})\right], \tag{4.112}$$

$$\Omega_{\mathrm{eff}} \approx \Omega_{\mathrm{m}}(T) + \mathrm{Im}\left[f(\Omega_{\mathrm{m}})\right]/2. \tag{4.113}$$

Data and Data analysis

For the sample of radius $R \approx 25\ \mu$m studied in the following, a coupling rate of $|g_0| \approx 2\pi \times (1.2 \pm 0.2)$ kHz is determined from the coupling parameter $|G| = \omega_{\mathrm{c}}/R \approx 2\pi \times 16$ GHz/nm and effective masse $m_{\mathrm{eff}} = 20\pm5$ ng. Fig. 4.9 shows the results of a detuning series, which was taken with an input laser power of 2 mW, with the temperature of the

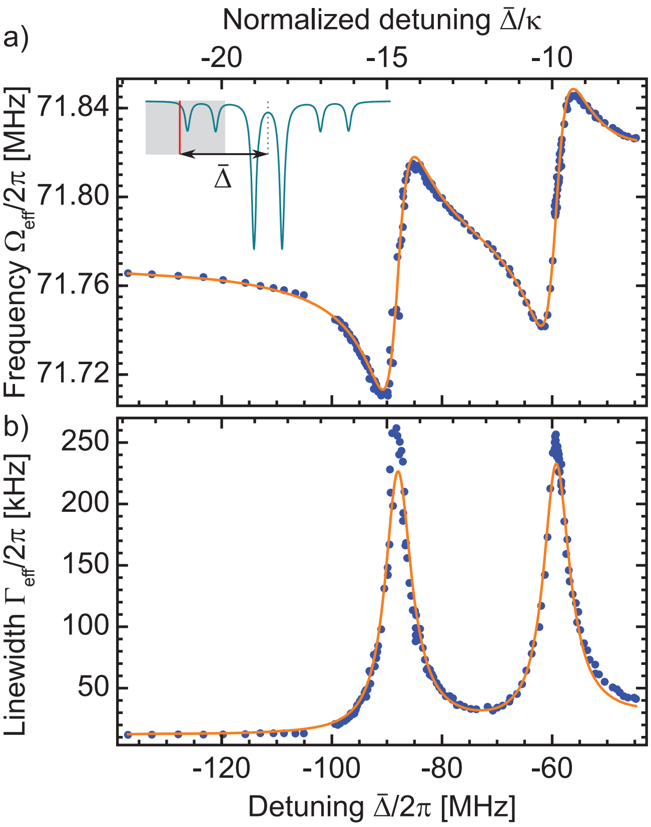

Figure 4.9: **Detuning series.** Effective resonance frequency (a) and linewidth (b) of the RBM when a 2 mW-power laser is tuned through the lower mechanical sideband of the split optical mode (inset). Blue points are measured data extracted from the recorded spectra of thermally induced mechanical displacement fluctuations, solid lines are a coupled fit using the model of eqs.(4.112)-(4.113), taking into account resonant and off-resonant (stray light) heating, modifying temperature-dependent damping and frequency shift caused by the TLS.

^{3}He gas stabilized to $T_{\mathrm{cryo}} = 850$ mK at a pressure of 2.8 mbar. We found it necessary to give more weight in the coupled fit to the optical spring effect (relative weight 0.9) than the damping rate, since the mechanical resonance frequency can be extracted from the spectra with higher accuracy than the damping rate. The obtained fit parameters κ, γ, and s_{in} are found to be in good agreement with independent results deduced from the frequency modulation measurement ($\kappa \approx 2\pi \times 6$ MHz, $\gamma \approx 2\pi \times 30$ MHz) and the measured laser power. The excellent quality of the fit, together with the measured temperature dependence of the TLS effects on the mechanical mode, furthermore allows us to extract the temperature T of the sample. Importantly, for large detunings $|\bar{\Delta}| \gg \kappa$, the TLS thermometer reveals (via a decrease of the mechanical quality factor to $Q_{\mathrm{m}} = 5970$) an increase of the sample temperature by $\delta T_{\mathrm{stray}} \approx 220$ mK, which we attribute to heating induced by absorbed stray light scattered from defects on the taper fiber, which were observed to aggregate upon its production. As the laser is tuned closer to resonance, more light is coupled into the WGM leading to the appearance of an additional (detuning dependent) temperature increase

$$T \approx T_{\mathrm{cryo}} + \delta T_{\mathrm{stray}} + \delta T_{\mathrm{WGM}}. \tag{4.114}$$

Here, $\delta T_{\mathrm{WGM}} = \beta\kappa_{\mathrm{abs}}(|a_+|^2 + |a_-|^2)\hbar\omega_{\mathrm{l}}$ denotes the increase in temperature following the cavity's double-Lorentzian absorption profile, $\kappa_{\mathrm{abs}} \lesssim \kappa - \kappa_{\mathrm{ex}}$ is the photon absorption rate and β the temperature increase per absorbed power. This heating term will lead via the TLS dependent mechanical susceptibility (cf. Fig. 4.8) to additional changes in Γ_{eff} and Ω_{eff} in the detuning series (cf. Fig. 4.9), from which the amount of additional resonant heating (δT_{WGM}) can be extracted. Applying this procedure to the data yields a temperature increase of $\delta T_{\mathrm{WGM}} \approx 70$ mK on the lower sideband (i.e. for $\bar{\Delta} = -\Omega_{\mathrm{m}} - \gamma/2$ corresponding to the optimum detuning $\bar{\Delta}_{\mathrm{opt}}$ in the deep RSB regime). This modest increase can be explained by the large sideband factor [74], which implies that only little optical power ($\sim \kappa_{\mathrm{abs}}|a_+|^2\hbar\omega_{\mathrm{l}} \lesssim P_{\mathrm{in}}/1300$) can be absorbed in the cavity when $\bar{\Delta} = \bar{\Delta}_{\mathrm{opt}}$.

Importantly, we can test the consistency of the derived detuning-dependent quantities T, $\Gamma_{\mathrm{m}}(T)$ and Γ_{eff} by comparing the expected effective temperature of the RBM due to optomechanical cooling, i.e. $T_{\mathrm{eff}} = T \cdot \Gamma_{\mathrm{m}}(T)/\Gamma_{\mathrm{eff}}$, with the effective temperature derived from noise thermometry via integration of the calibrated noise spectra [125]. Fig. 4.10a shows this comparison for the detuning series discussed above. Using the model of eqs. (4.112)-(4.113) adjusted to the data of Fig. 4.9, we obtain good agreement for the effective temperatures obtained in both ways. To achieve this level of agreement, it is necessary to take into account the optomechanical deamplification [53] of the laser phase modulation used for calibrating the mechanical fluctuation spectra in absolute terms, which is just the same effect as described in 4.1, where a probe tone falls into the OMIT window. Fig. 4.10b shows the same comparison for a cooling run at a high laser power (4 mW), for which we observe slightly increased heating by $\delta T_{\mathrm{stray}} \approx 400$ mK, while additional heating by δT_{WGM} could not be discerned in this measurement. In spite of the reduced mechanical quality factor $Q_{\mathrm{m}}(T_{\mathrm{cryo}} + \delta T_{\mathrm{stray}}) = 4880$, the lowest extracted occupancy is $\bar{n} = 10$ according to the detuning series fit. The lowest inferred *noise* temperature of a single measurement is even slightly lower, corresponding to $\bar{n} = 9 \pm 1$, where the uncertainty is dominated by systematic errors, which we estimate from the deviations of the effective temperature derived in the two independent ways described above. Note that this occupancy implies already a probability of $P(n = 0) = (1 + \bar{n})^{-1} = (10 \pm 1)\%$ to find the oscillator in its quantum ground state.

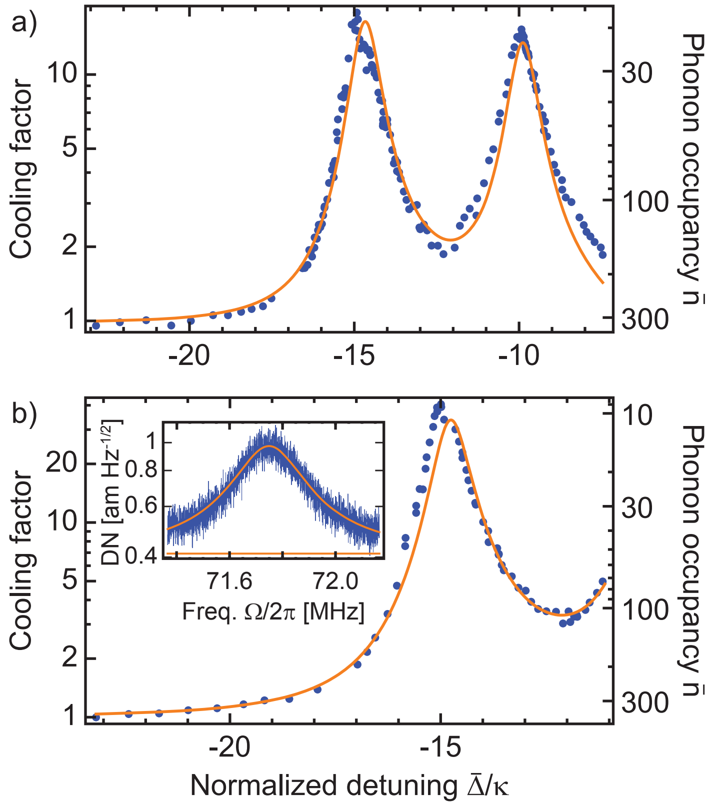

Figure 4.10: **Cooling factor** $(T_{\text{cryo}} + \delta T_{\text{stray}}) / T_{\text{eff}}$ **and phonon occupancy of the RBM versus laser detuning** $\bar{\Delta}$ **for (a)** $P_{\text{in}} = 2$ mW **and (b)** $P_{\text{in}} = 4$ mW**.** Points are phonon occupancies derived from the measured noise temperature, while solid lines correspond to the occupancies expected from the dependency of sample temperature and (intrinsic and effective) damping extracted from the detuning series as shown in Fig. 4.9. A minimum phonon number of $\bar{n} = 9 \pm 1$ is obtained. The inset shows a mechanical displacement noise (DN) spectrum at the optimum detuning ($\bar{\Delta} = \bar{\Delta}_{\text{opt}}$), illustrating the high signal-to-noise ratio achieved despite the low occupancy for $P_{\text{in}} = 2$ mW.

Imprecision-Backaction Product

In the context of quantum measurements [150], it is interesting to characterize the sources of noise responsible for the mechanical displacement measurement uncertainty. For a given mechanical spectra, the measured (double-sided, symmetrized) spectral density of displacement fluctuations is given by

$$S_{xx}^{\text{meas}}(\Omega) = S_{xx}^{\text{imp}}(\Omega) + |\chi_{\text{eff}}(\Omega)|^2 S_{FF}(\Omega) \tag{4.115}$$

where $S_{xx}^{\text{imp}}(\Omega)$ describes the measurement imprecision due to apparent displacement fluctuations, which are actually caused by noise in the displacement transducer itself. $S_{FF}(\Omega)$ is the force noise acting on the mechanical oscillator, and $\chi_{\text{eff}}(\Omega)$ its effective mechanical susceptibility. It is particularly interesting to evaluate these quantities for the lowest occupancy obtained at the optimum detuning of $\bar{\Delta} = -\Omega_\mathrm{m} - \frac{\gamma}{2}$ and at the Fourier frequency $\Omega = \Omega_\mathrm{m}$.

In our experiment, the *measurement imprecision* is dominated by shot noise, and we extract a value of

$$S_{xx}^\mathrm{imp} \equiv S_{xx}^\mathrm{imp}(\Omega_\mathrm{m}) = (3.2 \times 10^{-19}\ \mathrm{m}/\sqrt{\mathrm{Hz}})^2$$

from the fit to the background of the recorded mechanical spectrum as shown in Fig. 4.10. Its measured linear dependence on the laser input power P_in shows that it is strongly dominated by the quantum noise of the input laser. This behavior is indeed expected at the frequencies of interest in our work, where classical quadrature fluctuations are negligible in Ti:sapphire lasers.

The thermal force noise (for $\frac{k_\mathrm{B} T}{\hbar \Omega_\mathrm{m}} \gg 1$) driving the mechanical oscillator is given by

$$S_{FF}^\mathrm{the} \equiv S_{FF}^\mathrm{the}(\Omega_\mathrm{m}) = 2 m_\mathrm{eff} k_\mathrm{B} T \Gamma_\mathrm{m}(T) \tag{4.116}$$

given by the fluctuation-dissipation theorem [124]. In the presence of dynamical backaction, we can estimate this force noise from the more directly measured linewidth Γ_eff and noise temperature T_eff using $T_\mathrm{eff} \approx T \cdot \Gamma_\mathrm{m}(T)/\Gamma_\mathrm{eff}$, and

$$S_{FF}^\mathrm{the} \approx 2 m_\mathrm{eff} k_\mathrm{B} T_\mathrm{eff} \Gamma_\mathrm{eff} \tag{4.117}$$

It evaluates to

$$S_{FF}^\mathrm{the} = ((8 \pm 2) \times 10^{-15}\ \mathrm{N}/\sqrt{\mathrm{Hz}})^2$$

where Γ_eff and T_eff are extracted from the fits to the detuning series, evaluated at the detuning $\bar{\Delta} = -\Omega_\mathrm{m} - \frac{\gamma}{2}$ as described in the main manuscript. This value gives a conservative estimate of the *classical measurement backaction*, considering effectively *all force noise* present in the system (including thermal noise due to the non-zero cryostat temperature) as a classical backaction of the measurement.

A less conservative estimate on the backaction of the actual displacement measurement using the laser coupled to the WGM can be made by separating two different contributions in the force noise,

$$S_{FF}^\mathrm{the} = S_{FF}^\mathrm{cryo} + S_{FF}^\mathrm{ba}, \tag{4.118}$$

where S_{FF}^cryo is the Langevin force noise due to the finite cryostat temperature T_cryo and S_{FF}^ba the thermal backaction in the form of excess Langevin force noise due to the heating of the cavity by laser light. S_{FF}^ba gives an estimate of the classical perturbation of the system by the measurement, the *classical excess backaction*, which is technically avoidable.

The thermal force noise originating from the bath

$$S_{FF}^{\mathrm{cryo}} = 2m_{\mathrm{eff}}k_{\mathrm{B}}T_{\mathrm{cryo}}\Gamma_{\mathrm{m}}(T_{\mathrm{cryo}}) \tag{4.119}$$

is estimated to

$$S_{FF}^{\mathrm{cryo}} = ((5 \pm 1) \times 10^{-15}\,\mathrm{N}/\sqrt{\mathrm{Hz}})^2.$$

T_{cryo} and $\Gamma_{\mathrm{m}}(T_{\mathrm{cryo}})$ are extracted from independent low input power measurements where the RBM is thermalized to the cryostat temperature.

Consequently, the excess classical backaction evaluates to

$$S_{FF}^{\mathrm{ba}} = ((6 \pm 2) \times 10^{-15}\,\mathrm{N}/\sqrt{\mathrm{Hz}})^2$$

and accounts for 60 % of the thermal force fluctuations driving the mechanical oscillator.

In addition to classical backaction, the quantum fluctuations of the intracavity photon number give rise to a *quantum measurement backaction* for which the force noise is given by

$$S_{\mathrm{FF}}^{\mathrm{qba}} \equiv S_{\mathrm{FF}}^{\mathrm{qba}}(\Omega_{\mathrm{m}}) \approx \frac{2\hbar G^2 P_{\mathrm{in}}\eta_{\mathrm{c}}}{\bar{\omega}_{\mathrm{c}}\Omega_{\mathrm{m}}^2} = \frac{4g_0^2 m_{\mathrm{eff}}P_{\mathrm{in}}\eta_{\mathrm{c}}}{\bar{\omega}_{\mathrm{c}}\Omega_{\mathrm{m}}} \tag{4.120}$$

in the case of high resolved sideband factor $\frac{\Omega_{\mathrm{m}}}{\kappa} \gg 1$ [125] and at the detuning of interest. It is of the order of $(1 \times 10^{-15}\,\mathrm{N}/\sqrt{\mathrm{Hz}})^2$ in our case, negligible compared to the classical backaction.

Therefore, a conservative estimate of the *imprecision-backaction product* is given by (for $\frac{k_{\mathrm{B}}T}{\hbar\Omega_{\mathrm{m}}} \gg 1$)

$$\sqrt{S_{xx}^{\mathrm{imp}}(S_{FF}^{\mathrm{the}} + S_{FF}^{\mathrm{qba}})} \approx \sqrt{S_{xx}^{\mathrm{imp}}S_{FF}^{\mathrm{the}}} = (49 \pm 8)\frac{\hbar}{2}.$$

In an ideal quantum measurement [150], this product is equal to $\frac{\hbar}{2}$, corresponding to the optimal compromise between quantum imprecision and quantum backaction, both arising from the quantum fluctuations of the optical field quadratures.

As shown in the last paragraph, laser absorption heating, responsible for the classical excess backaction $S_{\mathrm{FF}}^{\mathrm{ba}}$, is mainly caused by scattered light off the tapered fiber being absorbed by the toroid (in our case by dust particles on the tapered fiber originating from particles in the air of our laboratory). It is thus within technical reach to strongly reduce this effect and perform measurements for which light-induced backaction would be dominated by quantum fluctuations.

Due to the resolved-sideband operation, force noise coming from quantum backaction (as yet only observed on cold atomic gases [151]) is expected to be nearly two orders of magnitude weaker and therefore negligible.

4.2.4 Conclusion

We have cooled a mechanical oscillator using a combination of cryogenic ^{3}He exchange gas pre-cooling and optomechanical sideband cooling to 9 ± 1 quanta, implying that the mechanical oscillator occupies the ground state $10 \pm 1\%$ of the time. This is the lowest phonon occupancy that has been achieved with optomechanical sideband cooling so far. It is possible to populate the quantum ground state with higher probability by avoiding excess heating due to fiber contamination, by using higher cooling powers and by improving g_0^2/Γ_m, which can be achieved by engineering mechanical modes [92] for lower mass and clamping losses. Simultaneously, such a system bears promise to give access to the regime of strong optomechanical coupling [121, 114] in which the coherent coupling rate $\sqrt{\bar{n}_\mathrm{p}}g_0$ exceeds the cavity decay rate κ and the thermal decoherence rate $k_\mathrm{B}T/\hbar Q_\mathrm{m}$ of $2\pi \times 2.6\,\mathrm{MHz}$ in the present experiment ($\bar{n}_\mathrm{p}$ is the average cavity photon number). For occupancies $\bar{n} \lesssim 1$, individually resolved anti-Stokes and Stokes sidebands [55, 74] of an independent resonant readout laser will display a measurable asymmetry of $\bar{n}/(\bar{n}+1)$ arising from the non-zero commutator of the ladder operators describing the mechanical harmonic oscillator in quantum terms. In addition, the described system may give experimental access to the regime where quantum backaction becomes comparable or exceeds thermal noise, allowing pondermotive squeezing [32] or QND photon measurements.

4.3 Quantum-Coherent Coupling

This section is based on Verhagen *et al.* [3] published in the journal *Nature* in February 2012 and contains the first results entirely obtained at EPFL. It involves major advances in sample properties (especially coupling rates), in the setup as well as the understanding of the measured traces. Here the regime of quantum coherent coupling is achieved enabling quantum control of the motional state of a mechanical oscillator.

4.3.1 Introduction

Mechanical oscillators are at the heart of many precision experiments and can exhibit exceptionally low dissipation. The possibility to control the quantum states of engineered micro- or nano-mechanical oscillators has been a subject of longstanding interest [152, 135]. Recent experiments have successfully prepared such devices in their quantum ground state, either using standard cryogenic techniques [29] or via dynamical backaction cooling [30, 31]. Full control over the quantum state of a mechanical oscillator can be achieved by coupling it to an auxiliary system—whose quantum state can be controlled and measured—under the condition that the coherent coupling rate exceeds the decoherence rate of each of the subsystems. Such quantum-coherent coupling and control at the single-phonon level has been recently demonstrated in the microwave domain, by achieving strong coupling of a GHz piezoelectrical dilatation oscillator to a (frequency-degenerate) superconducting qubit [29]. Moreover, an electromechanical system has reached the quantum-coherent regime using parametric coupling of a MHz micromechanical oscillator to a GHz microwave resonator [39, 30]. Achieving quantum-coherent coupling in the optical domain would provide an interface between mechanical quantum states and optical fields, whose low thermal occupancy at room temperatures allows decoherence-free propagation of quantum states out of a cryogenic environment and which can be coupled to a variety of quantum systems. Additionally, optical techniques benefit from the wide availability of quantum limited detection techniques. In fact, simultaneous achievement of quantum-coherent coupling in the optical and microwave domain provides the possibility of realizing optical-to-microwave conversion of quantum states [153].

Parametric optomechanical coupling occurs in an optical microcavity that simultaneously exhibits a mechanical resonator mode, whose displacement alters the optical resonance frequency. The coupling can be described by the interaction Hamiltonian $H = \hbar g_0 \hat{a}^\dagger \hat{a} \left(\hat{b}^\dagger + \hat{b}\right)$, where $\hat{a}$ ($\hat{a}^\dagger$) and $\hat{b}$ ($\hat{b}^\dagger$) are the photon and phonon annihilation (creation) operators, respectively, $\hbar$ is the reduced Planck constant and g_0 is the vacuum optomechanical coupling rate. In the resolved sideband regime (where the mechanical resonance frequency Ω_m exceeds the cavity energy decay rate κ), with an intense laser tuned close to the lower optomechanical sideband, one obtains in the rotating wave approximation the effective Hamiltonian

$$H = \hbar g \left(\hat{a}\hat{b}^{\dagger} + \hat{a}^{\dagger}\hat{b} \right) \tag{4.121}$$

for the operators $\hat{a}$ and $\hat{b}$ now displaced by their steady state values. We have introduced here the field-enhanced coupling rate [55, 56, 121] $g = \sqrt{\bar{n}_{\mathrm{c}}} g_0$, where $\bar{n}_{\mathrm{c}}$ denotes the average number of photons in the cavity. In the absence of decoherence, the unitary evolution (4.121) corresponds to swapping of the (displaced) optical and mechanical quantum states with a period of $2\pi/\Omega_{\mathrm{c}}$, where $\Omega_{\mathrm{c}} = 2g$ is the coherent coupling rate, i.e., the rate at which the two systems exchange energy. This state swapping is at the heart of most quantum control protocols [117, 154, 155, 156, 157, 22]. In practice, however, this unitary evolution is compromised by the coupling of both degrees of freedom to their respective environments. Hence, it is important for Ω_{c} to exceed both the optical decoherence rate κ and the relevant mechanical decoherence rate γ. If the mechanical linewidth is limited by dissipation (as is the case in our system [66]), the mechanical decoherence is caused by energy relaxation to the hot environment. Thus, both decoherence rates are defined here as the inverse of the time needed for a single excitation to be lost into the environment. Importantly, the mechanical mode is coupled to an environment that generally has a large thermal occupancy $\bar{n}_{\mathrm{m}} \approx k_{\mathrm{B}} T/\hbar\Omega_{\mathrm{m}}$ due to the relatively small mechanical frequency. Therefore, the mechanical *decoherence* rate $\gamma = \Gamma_{\mathrm{m}}(\bar{n}_{\mathrm{m}} + 1) \approx k_{\mathrm{B}} T/\hbar Q_{\mathrm{m}}$ (where $Q_{\mathrm{m}} = \Omega_{\mathrm{m}}/\Gamma_{\mathrm{m}}$) [158, 156] is much larger than the *dissipation* rate Γ_{m}. This means that the strong coupling regime $\Omega_{\mathrm{c}} > (\kappa, \Gamma_{\mathrm{m}})$ [114] does not suffice to enable quantum control, in contrast to the situation in atomic cavity QED [159] or in resonant coupling to superconducting qubits of sufficiently high frequency [29]. Instead, for parametrically coupled systems the more stringent condition $\Omega_{\mathrm{c}} > (\kappa, \gamma)$ signals the relevant regime, which we denote as quantum-coherent coupling.

Here, we realize quantum-coherent coupling of an optical cavity field to a micromechanical oscillator. In this regime, the system is appropriately described as an optomechanical polariton whose decoherence time exceeds the period of the Rabi oscillations between light and mechanics. Although the ground state has recently been prepared with optical cooling [31], in that work Ω_{c} was much smaller than κ. In contrast, the present system achieves a coupling rate exceeding both the optical and mechanical decoherence rates, thereby satisfying the necessary conditions for full control of the quantum state of a mechanical oscillator with optical fields [154, 155, 156, 157, 22, 114]. The experimental setting is a micro-optomechanical system in the form of a spoke-anchored toroidal optical microcavity [92]. Such devices exhibit high quality factor whispering gallery mode resonances (with a typical cavity decay rate $\kappa/2\pi < 10\,\mathrm{MHz}$) coupled to mechanical radial breathing modes via

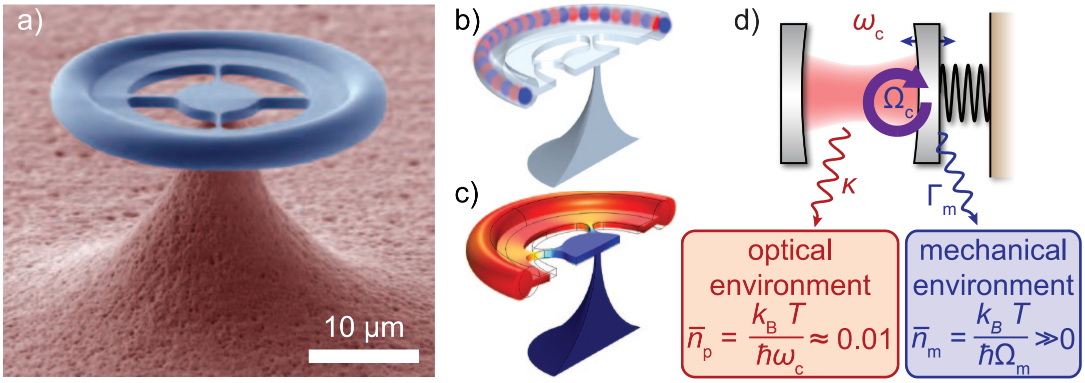
a)
10 µm
b)
c)
d)
ω_c
Ω_c
κ
Γ_m
optical environment
$\bar{n}_p = \frac{k_B T}{\hbar\omega_c} \approx 0.01$
mechanical environment
$\bar{n}_m = \frac{k_B T}{\hbar\Omega_m} \gg 0$

Figure 4.11: **Optomechanical microresonators. a**, False-color scanning electron micrograph of a spoke-anchored toroidal resonator 31 μm in diameter used for the optomechanical experiments reported in this work. **b**, Sketch of an optical whispering gallery mode in the microresonator (colors indicating optical phase). **c**, Simulated displacement (exaggerated for clarity) of the fundamental radial breathing mode of the structure. **d**, Equivalent optomechanical Fabry-Pérot cavity: Quantum-coherent coupling is achieved when the enhanced coupling rate Ω_c is comparable to or exceeds the optical and mechanical decoherence rates (κ, $\Gamma_m \bar{n}_m$). Owing to the large asymmetry between mechanical and optical frequencies, the occupancies of the two environments are widely different.

radiation pressure [113]. The vacuum optomechanical coupling rate $g_0 = \frac{\omega_c}{R} x_{ZPM}$ can be increased by reducing the radius R of the cavity (here ω_c is the optical cavity resonance frequency and x_{ZPM} is the zero point motion). However, the larger per photon force $\hbar\omega_c/R$ is then usually partially compensated by the increase in the mechanical resonance frequency Ω_m—and correspondingly smaller zero point motion $x_{ZPM} = \sqrt{\hbar/(2m_{eff}\Omega_m)}$ (where m_{eff} is the effective oscillator mass). Moreover, small structures also generally feature larger dissipation through clamping losses. To compensate these opposing effects we use an optimized spoke anchor design (cf. Fig. 4.11 and 3.3) that maintains low clamping losses and a moderate mechanical resonance frequency while reducing the dimensions of the structure. Devices fabricated in this manner (with $R = 15\,\mu$m) exhibited coupling rates as high as $g_0 = 2\pi \times 3.4$ kHz at 780nm for a resonance frequency of 78 MHz and a critically coupled sideband factor $\Omega_m/\kappa = 11$. The quoted value of g_0 is determined independently at room temperature via a calibrated phase modulation technique.

4.3.2 Theoretical model

This section summarizes the theoretical model which was used to extract all entities of interest from our data. Figure 4.12 shows the parameters and variables of the model, and their mutual connections.

Conservative dynamics

The conservative dynamics of an optomechanical system are described by the Hamiltonian [119]

$$H = \frac{1}{4}\hbar\Omega_\mathrm{m}\left(q^2+p^2\right)+\hbar\omega_\mathrm{c}\left(a^\dagger a+\frac{1}{2}\right)+\hbar g_0\, q\, a^\dagger a, \tag{4.122}$$

where mechanical quadrature operators q and p are related to the corresponding mechanical ladder operators b and $b^\dagger$ via

$$q = b+b^\dagger \tag{4.123}$$

$$p = (b-b^\dagger)/i. \tag{4.124}$$

With these definitions $[q,p]=2i$, and the actual mechanical displacement and momentum are given by $x' = x_\mathrm{zpm} q$ and $p' = \hbar p/2x_\mathrm{zpm}$ with the amplitude of the zero-point motion

$$x_\mathrm{zpm} = \sqrt{\frac{\hbar}{2m_\mathrm{eff}\Omega_\mathrm{m}}}. \tag{4.125}$$

The vacuum optomechanical coupling rate g_0 quantifies the strength of the optomechanical interaction and is given by $g_0 = Gx_\mathrm{zpm}$ with $G = \partial\omega_\mathrm{c}/\partial x$.

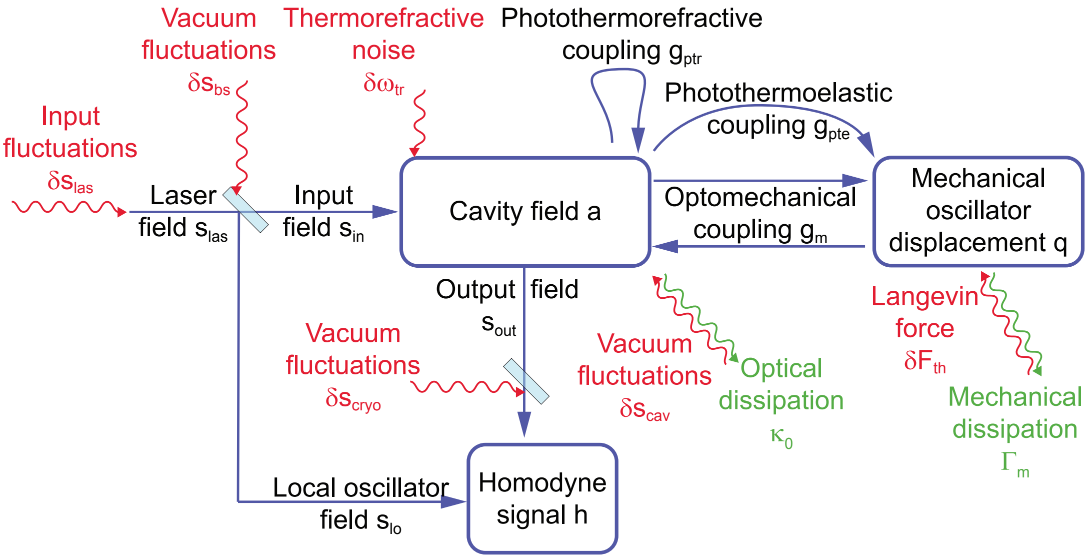
Vacuum fluctuations δs_bs
Thermorefractive noise $\delta\omega_\mathrm{tr}$
Photothermorefractive coupling g_ptr
Input fluctuations δs_las
Photothermoelastic coupling g_pte
Laser field s_las
Input field s_in
Cavity field a
Optomechanical coupling g_m
Mechanical oscillator displacement q
Output field s_out
Vacuum fluctuations δs_cryo
Vacuum fluctuations δs_cav
Optical dissipation κ_0
Langevin force δF_th
Mechanical dissipation Γ_m
Local oscillator field s_lo
Homodyne signal h

Figure 4.12: **Theoretical model used.** See text for details.

Quantum Langevin equations

The Hamiltonian (4.122) determines the conservative evolution of the optomechanical degrees of freedom. Optical and mechanical dissipation, and the corresponding fluctuations, can be taken into account by introducing the mechanical dissipation rate Γ_m and the optical dissipation rate $\kappa = \kappa_0 + \kappa_\mathrm{ex}$ (where κ_ex represents losses to the coupling waveguide and κ_0 all other optical losses) as well as the optical noise terms δs_in, δs_cav and the thermal Langevin force, which we express as a rate δf_th by writing the physical force in momentum units of $\hbar/2x_\mathrm{zpm}$. This leads to the well-known Langevin equations of cavity optomechanics [32, 33, 34]:

$$\dot{a}(t) = \left(i\Delta - \frac{\kappa}{2}\right) a(t) - i g_0\, q(t) a(t) + \sqrt{\kappa_\mathrm{ex}}(\bar{s}_\mathrm{in} + \delta s_\mathrm{in}(t)) + \sqrt{\kappa_0}\delta s_\mathrm{cav}(t) \tag{4.126}$$

$$\dot{q}(t) = \Omega_\mathrm{m} p(t) \tag{4.127}$$

$$\dot{p}(t) = -\Omega_\mathrm{m} q(t) - 2g_0\, a^\dagger(t) a(t) - \Gamma_\mathrm{m} p(t) + \delta f_\mathrm{th}(t), \tag{4.128}$$

where the convention $\Delta = \omega_\mathrm{l} - \omega_\mathrm{c}$ was used to denote the detuning of the laser (angular) frequency ω_l from the bare cavity resonance frequency ω_c, and a is expressed in a frame rotating at ω_l.

In order to accurately model the response of the optomechanical system over a wide range of parameters (detuning, Fourier frequency, optical and mechanical excitation) for a single set of parameters, we have refined this generic model (that was also used in the previous sections 4.1 and 4.2) by including other effects which are known to be inherent to most optical microcavities, and are discussed in the following.

Photothermoelastic backaction. Thermoelastic forces driven by temperature gradients induced by light absorption can induce mechanical displacements. The starting point to model these displacements are the coupled equations of motion known from the standard theory of thermoelasticity [95]

$$\mu \vec{\nabla}^2 \vec{u} + (\lambda + \mu)\vec{\nabla}(\vec{\nabla}\cdot\vec{u}) + \vec{f} = (3\lambda + 2\mu)\alpha\vec{\nabla}\theta + \rho\ddot{\vec{u}} \tag{4.129}$$

$$k_\mathrm{t}\vec{\nabla}^2\theta - c_\mathrm{t}\rho\dot{\theta} = (3\lambda + 2\mu)\alpha T_0(\vec{\nabla}\cdot\dot{\vec{u}}) - \upsilon\kappa_\mathrm{abs} a^\dagger a. \tag{4.130}$$

These equations connect the displacement field $\vec{u}(\vec{r}, t)$ and the temperature elevation $\theta(\vec{r}, t)$ above the mean temperature T_0. Here, λ and μ are the Lamé parameters, α the thermal expansion coefficient, ρ the mass density, $\vec{f}$ a body force (e.g. due to radiation pressure), k_t the thermal conductivity, κ_abs the photon absorption rate, c_t the heat capacity, and the function $\upsilon(\vec{r})$ describes the spatial distribution of the light absorption. Evidently, a thermoelastic body force

$$\vec{f}_\mathrm{te}(\vec{r}, t) = -(3\lambda + 2\mu)\alpha\vec{\nabla}\theta(\vec{r}, t) \tag{4.131}$$

acts on the mechanical modes of the structure when a temperature gradient $\vec{\nabla}\theta(\vec{r},t)$ is present. In the scalar representation of the mechanical dynamics, we therefore have to add a thermoelastic force $f_{\mathrm{te}}(t)$ proportional to the material parameters λ, μ and α, as well as an overlap integral of the mechanical mode's displacement pattern and the temperature gradient $\vec{\nabla}\theta(\vec{r},t)$. Assuming that the temperature gradients are predominantly driven by the absorption of laser light in the resonator, one can express the scalar photothermoelastic force as

$$f_{\mathrm{pte}}(t) = \chi_{\mathrm{pte}}(t) * \kappa_{\mathrm{abs}} a^{\dagger}(t)a(t), \tag{4.132}$$

where we have absorbed the spatial overlap integrals between the mechanical and (the gradient of) the thermal modes, as well as the thermal modes and the spatial pattern of light absorption into the magnitude of the function $\chi_{\mathrm{pte}}(t)$. The temporal dynamics of the adjustment of the relevant temperature gradients to a changing amount of light absorption is represented by the time-dependence of $\chi_{\mathrm{pte}}(t)$ ("$*$" denotes a convolution). Note that while this formulation accounts for the quantum fluctuations of the intracavity field $a(t)$, the statistical nature of photon absorption events is neglected. This is justified considering that the quantum fluctuations of optical heat deposition ("photothermoelastic shot noise") have a much smaller effect on the mechanical mode than the direct fluctuations of the radiation pressure term $2g_0\, a^{\dagger}a$.

Dynamic photothermorefractive frequency shift. A temperature elevation $\theta(\vec{r},t)$ within the optical mode volume furthermore changes the refractive index, and therefore the optical resonance frequency. In analogy to the description in the previous section, we are using a simple scalar description of the form

$$\Delta\omega_{\mathrm{ptr}}(t) = \chi_{\mathrm{ptr}}(t) * \kappa_{\mathrm{abs}} a^{\dagger}(t)a(t) \tag{4.133}$$

for this frequency shift, where the response function $\chi_{\mathrm{ptr}}(t)$ accommodates spatial overlap integrals of the light absorption pattern $v(\vec{r})$ and the thermal modes as well as the temporal dynamics of the latter, and, in addition, the spatial sampling of the induced refractive index changes

$$\Delta n(\vec{r},t) = \frac{\mathrm{d}n}{\mathrm{d}T}\theta(\vec{r},t) \tag{4.134}$$

by the optical mode.

Thermorefractive noise. The local temperature elevation $\theta(\vec{r},t)$ also undergoes thermal fluctuations—independent of the presence of light. Within a volume V, they amount to squared fluctuations of [160]

$$\langle \theta(\vec{r},t)^2 \rangle_V = \frac{k_B T_0^2}{c_p \rho V}. \tag{4.135}$$

The spatial distribution of these fluctuations can be calculated using a Langevin ansatz [161], by adding a fluctuational source term to the heat diffusion equation (4.130). Predominantly via the thermorefractive effect ($\mathrm{d}n/\mathrm{d}T \neq 0$), the resulting temperature fluctuations again induce resonance frequency fluctuations $\delta\omega_{\mathrm{tr}}(t)$. Its temporal correlation function (or equivalently, power spectral density) have been estimated for simple whispering-gallery mode resonator geometries [162, 54, 25].

Taking these additional three effects into account, the equations of motion can be written as

$$\begin{aligned}
\dot{a}(t) &= \left(i(\Delta - \Delta\omega_{\mathrm{ptr}}(t) - \delta\omega_{\mathrm{tr}}(t)) - \frac{\kappa}{2}\right) a(t) - i g_0\, q(t) a(t) + \\
&\quad + \sqrt{\kappa_{\mathrm{ex}}}(\bar{s}_{\mathrm{in}} + \delta s_{\mathrm{in}}(t)) + \sqrt{\kappa_0}\delta s_{\mathrm{cav}}(t) && (4.136)\\
\dot{q}(t) &= \Omega_{\mathrm{m}} p(t) && (4.137)\\
\dot{p}(t) &= -\Omega_{\mathrm{m}} q(t) - 2g_0\, a^\dagger(t) a(t) - \Gamma_{\mathrm{m}} p(t) + \delta f_{\mathrm{th}}(t) + f_{\mathrm{pte}}(t). && (4.138)
\end{aligned}$$

Linearized model

A large coherent field sent to the optomechanical system induces a relatively large classical intracavity field $\bar{a}$, and induces a displacement of the mechanical mode by $\bar{q}$. If the system is stable around this steady-state, the dynamics of the small fluctuations around this equilibrium are described by a set of equations obtained via the substitution $a(t) = \bar{a} + \delta a(t)$ and $q(t) = \bar{q} + \delta q(t)$, and retaining only first-order terms in the fluctuations. This yields

$$\begin{aligned}
\delta\dot{a}(t) &= \left(+i\bar{\Delta} - \frac{\kappa}{2}\right)\delta a(t) - i\kappa_{\mathrm{abs}}\bar{a}\chi_{\mathrm{ptr}}(t) * (2\bar{a}^*\delta a(t) + \bar{a}\delta a^\dagger(t)) - i g_0\, \bar{a}\delta q(t) - \\
&\quad - i\bar{a}\delta\omega_{\mathrm{tr}}(t) + \sqrt{\kappa_{\mathrm{ex}}}\delta s_{\mathrm{in}}(t) + \sqrt{\kappa_0}\delta s_{\mathrm{cav}}(t) && (4.139)
\end{aligned}$$

$$\begin{aligned}
\Omega_{\mathrm{m}}^{-1}\left[\delta\ddot{q}(t) + \Gamma_{\mathrm{m}}\delta\dot{q}(t) + \Omega_{\mathrm{m}}^2\delta q(t)\right] &= -2g_0\,(\bar{a}\delta a^\dagger(t) + \bar{a}^*\delta a(t)) + \\
&\quad + \delta f_{\mathrm{th}}(t) + \chi_{\mathrm{pte}}(t) * (\bar{a}\delta a^\dagger(t) + \bar{a}^*\delta a(t))
\end{aligned} \tag{4.140}$$

with $\bar{\Delta} = \omega_\mathrm{l} - \big(\omega_\mathrm{c} + g_0\, \bar{q} + \kappa_\mathrm{abs}|\bar{a}|^2(\chi_\mathrm{ptr}(t) * 1)\big)$. This set of equations is best solved in the Fourier domain, yielding

$$\begin{aligned}\big(-i(\bar{\Delta}+\Omega)+\kappa/2\big)\,\delta a(\Omega) &= -i\kappa_\mathrm{abs}\bar{a}\chi_\mathrm{ptr}(\Omega)(2\bar{a}^*\delta a(\Omega)+\bar{a}\delta a^\dagger(\Omega)) - i g_0\, \bar{a}\delta q(\Omega)\\ &\quad - i\bar{a}\delta\omega_\mathrm{tr}(\Omega)+\sqrt{\kappa_\mathrm{ex}}\delta s_\mathrm{in}(\Omega)+\sqrt{\kappa_0}\delta s_\mathrm{cav}(\Omega)\end{aligned} \tag{4.141}$$

$$\frac{-\Omega^2 - i\Omega\Gamma_\mathrm{m}+\Omega_\mathrm{m}^2}{\Omega_\mathrm{m}}\delta q(\Omega) = \big(-2g_0\, + \chi_\mathrm{pte}(\Omega)\big)\,(\bar{a}\delta a^\dagger(\Omega)+\bar{a}^*\delta a(\Omega)) + \delta f_\mathrm{th}(\Omega). \tag{4.142}$$

For simplicity, we refer to the Fourier transform of the respective functions by simply writing them with a frequency (Ω) argument. Note that $\delta a^\dagger(\Omega)$ denotes the Fourier transform of $\delta a^\dagger(t)$, equal to $[\delta a(-\Omega)]^\dagger$; and that $[\delta q(-\Omega)]^\dagger = \delta q(\Omega)$ for the Hermitian operator $\delta q(t)$.

To further simplify the problem, we approximate the response functions of the photothermal effects by a single-pole, low-pass response, assuming implicitly that the relevant temperature (gradient) distributions adjust themselves only with a certain delay to a change in the absorbed optical power. Assuming that this delay is larger than the relevant oscillation periods considered here, one can approximate

$$\chi_\mathrm{ptr}(\Omega) \approx \frac{g_\mathrm{ptr}}{\kappa_\mathrm{abs}}\frac{\Omega_\mathrm{m}}{-i\Omega} \tag{4.143}$$

$$\chi_\mathrm{pte}(\Omega) \approx 2g_\mathrm{pte}\frac{\Omega_\mathrm{m}}{-i\Omega} \tag{4.144}$$

and finally obtains

$$\begin{aligned}\big(-i(\bar{\Delta}+\Omega)+\kappa/2\big)\,\delta a(\Omega) &= \bar{a}g_\mathrm{ptr}\frac{\Omega_\mathrm{m}}{\Omega}(2\bar{a}^*\delta a(\Omega)+\bar{a}\delta a^\dagger(\Omega)) - i g_0\, \bar{a}\delta q(\Omega)\\ &\quad - i\bar{a}\delta\omega_\mathrm{tr}(\Omega)+\sqrt{\kappa_\mathrm{ex}}\delta s_\mathrm{in}(\Omega)+\sqrt{\kappa_0}\delta s_\mathrm{cav}(\Omega)\end{aligned} \tag{4.145}$$

$$\frac{-\Omega^2 - i\Omega\Gamma_\mathrm{m}+\Omega_\mathrm{m}^2}{\Omega_\mathrm{m}}\delta q(\Omega) = -2\left(g_0\, - i g_\mathrm{pte}\frac{\Omega_\mathrm{m}}{\Omega}\right)(\bar{a}\delta a^\dagger(\Omega)+\bar{a}^*\delta a(\Omega)) + \delta f_\mathrm{th}(\Omega). \tag{4.146}$$

These equations are used to calculate the coherent response and fluctuation spectra in the following sections.

Homodyne detection

The optomechanical experiment is embedded into one arm of a balanced homodyne interferometer. At the initial beamsplitter, the laser field (and fluctuations in the fiber mode) are split up into a ‘local oscillator’ arm, and the arm that serves as input to the cavity:

$$s_{\mathrm{in}} = \sqrt{1-r}\, s_{\mathrm{las}} - \sqrt{r}\, s_{\mathrm{bs}} \tag{4.147}$$

$$s_{\mathrm{lo}} = \sqrt{r}\, s_{\mathrm{las}} + \sqrt{1-r}\, s_{\mathrm{bs}}, \tag{4.148}$$

evidently valid both in time and frequency domain. Here, we also take into account the vacuum fluctuations δs_{bs} entering the beamsplitter at the unoccupied port,

$$s_{\mathrm{las}} = \bar{s}_{\mathrm{las}} + \delta s_{\mathrm{las}} \tag{4.149}$$

$$s_{\mathrm{bs}} = \delta s_{\mathrm{bs}}. \tag{4.150}$$

The field s_{in} drives both the mean field $\bar{a}$ and the field fluctuations within the cavity, as described in the previous section. The intracavity field a, in turn, couples back into the single-mode fiber taper, and the usual input-output formalism gives the field s_{out} at the output of the cavity via the relation

$$s_{\mathrm{in}} - s_{\mathrm{out}} = \sqrt{\kappa_{\mathrm{ex}}}\, a \tag{4.151}$$

We furthermore take into account that only a fraction η_{cryo} of the light power at the output of the cavity is measured as 'signal' in the homodyne detector due to optical losses, e.g. in the cryostat. For $\eta_{\mathrm{cryo}} < 1$, we again have to account for quantum vacuum δs_{cryo} that enters the optical mode,

$$s_{\mathrm{sig}} = \sqrt{\eta_{\mathrm{cryo}}}\, s_{\mathrm{out}} + \sqrt{1-\eta_{\mathrm{cryo}}}\, s_{\mathrm{cryo}} \tag{4.152}$$

$$s_{\mathrm{cryo}} = \delta s_{\mathrm{cryo}}. \tag{4.153}$$

Finally, in the homodyne receiver, the differential signal

$$\delta h = \bar{s}_{\mathrm{lo}} e^{+i\phi_{\mathrm{lo}}} \delta s_{\mathrm{sig}}^{\dagger} + \bar{s}_{\mathrm{lo}}^{*} e^{-i\phi_{\mathrm{lo}}} \delta s_{\mathrm{sig}} + \bar{s}_{\mathrm{sig}} e^{-i\phi_{\mathrm{lo}}} \delta s_{\mathrm{lo}}^{\dagger} + \bar{s}_{\mathrm{sig}}^{*} e^{+i\phi_{\mathrm{lo}}} \delta s_{\mathrm{lo}} \tag{4.154}$$

is measured. The fluctuational terms δh and δq of interest can then be expressed as a linear function of the fluctuations driving the system,

$$\begin{pmatrix} \delta h \\ \delta q \end{pmatrix} = M \cdot \begin{pmatrix} \delta s_{\mathrm{las}} & \delta s_{\mathrm{las}}^{\dagger} & \delta s_{\mathrm{bs}} & \delta s_{\mathrm{bs}}^{\dagger} & \delta s_{\mathrm{cav}} & \delta s_{\mathrm{cav}}^{\dagger} & \delta s_{\mathrm{cryo}} & \delta s_{\mathrm{cryo}}^{\dagger} & \delta \omega_{\mathrm{tr}} & \delta f_{\mathrm{th}} \end{pmatrix}^{T}. \tag{4.155}$$

Here, the coefficients of the matrix M follow directly from the relations (4.145)-(4.154).

Calculation of noise covariances

We assume that all input noise terms of eq. (4.155) can be described by zero-mean Gaussian noise operators whose variances are known. Representing the covariances between two noise operators x and y as a symmetrized spectrum $\bar{S}_{xy}(\Omega)$ defined according to

$$\frac{1}{2}\left\langle\left\{x(\Omega), y(\Omega')\right\}\right\rangle = 2\pi \bar{S}_{xy}(\Omega)\,\delta(\Omega+\Omega'), \tag{4.156}$$

the only non-zero covariances are characterized by the spectra

$$\bar{S}_{\delta s^\dagger_{\mathrm{las}}\delta s_{\mathrm{las}}}(\Omega) = \bar{S}_{\delta s^\dagger_{\mathrm{cav}}\delta s_{\mathrm{cav}}}(\Omega) = \bar{S}_{\delta s^\dagger_{\mathrm{bs}}\delta s_{\mathrm{bs}}}(\Omega) = \bar{S}_{\delta s^\dagger_{\mathrm{cryo}}\delta s_{\mathrm{cryo}}}(\Omega) = \frac{1}{2} \tag{4.157}$$

for the optical quantum noise entering the system,

$$\bar{S}_{\delta f_{\mathrm{th}}\delta f_{\mathrm{th}}}(\Omega) \approx 4\bar{n}_{\mathrm{m}}\Gamma_{\mathrm{m}} \tag{4.158}$$

for the thermal Langevin force, where we have assumed $\bar{n}_{\mathrm{m}} \approx k_{\mathrm{B}}T/\hbar\Omega_{\mathrm{m}} \gg 1$, and

$$\bar{S}_{\delta\omega_{\mathrm{tr}}\delta\omega_{\mathrm{tr}}}(\Omega) = \bar{S}_{\mathrm{trn}}(\Omega), \tag{4.159}$$

for the thermorefractive noise [162], whose contribution we found to be negligible in the data presented in the following. By the linearity of equation (4.155), it follows that the covariance matrix N_{out} of the output noise operators is then related to the input covariance matrix N_{in} by the simple expression

$$N_{\mathrm{out}} = M(+\Omega)\cdot N_{\mathrm{in}}\cdot M(-\Omega)^T. \tag{4.160}$$

Coherent dynamics of the system

In order to calculate the coherent response of the system to the probing by a phase-modulated input as already shown in 4.1, eq. (4.155) can be used. By assuming a sufficiently narrow detection bandwidth and/or sufficiently large phase modulation of depth $\delta\varphi$, one can set

$$\delta s^\dagger_{\mathrm{cav}} \approx \delta s_{\mathrm{cav}} \approx \delta s^\dagger_{\mathrm{bs}} \approx \delta s_{\mathrm{bs}} \approx \delta s^\dagger_{\mathrm{cryo}} \approx \delta s_{\mathrm{cryo}} \approx \delta f_{\mathrm{th}} \approx \delta\omega_{tr} \approx 0 \tag{4.161}$$

$$\delta s_{\mathrm{las}} = i\bar{s}_{\mathrm{las}}\delta\varphi, \tag{4.162}$$

and calculate the frequency-dependent transfer function from a phase modulation $\delta\varphi$ to the homodyne signal δh.

This coherent response is obviously directly measured in the sideband sweeps that we routinely perform. Moreover, by multiplication of the (complex) spectrum of the excitation pulse with this transfer function, the response of the homodyne signal in the time domain can be numerically determined via the inverse Fourier transform.

Analysis of the coherent response

The coherent response spectra are important to accurately extract the different parameters of the optomechanical interaction as well as to calibrate the mechanical noise spectra. A typical coherent response is shown in Fig. 4.13a. The Lorentzian peak centered around $\Omega_{\mathrm{mod}} = 140$ MHz results from the absorption of the upper modulation sideband by the cavity and reflects the optical response of the system. The maximum of the homodyne signal is obtained when the modulation sideband is resonant with the cavity. Hence, the center frequency and width of this peak correspond to the detuning $|\Delta|$ and the linewidth κ of the cavity, respectively. The sharp feature at $\Omega_{\mathrm{mod}} = \Omega_{\mathrm{m}}$ is the manifestation of Optomechanically Induced Transparency [1]; an interference effect due to the resonant excitation of the mechanical mode. For weak coupling power and/or large detuning, the dynamics of the mechanical mode is hardly affected by the optomechanical interaction and the width of the dispersive feature is given by the mechanical linewidth Γ_{m}.

For larger laser power, the width of the OMIT window increases, reflecting the width of the damped mode $\Gamma_{\mathrm{m}} + \Omega_c^2\kappa / \left(\kappa^2 + 4(\Delta + \Omega_{\mathrm{m}})^2\right)$. Hence, the fit of the coherent response allows to extract the coupling rate Ω_c and the corresponding intracavity field $\bar{a}$. We introduce $\bar{a}_0 \equiv \bar{a} / \frac{\kappa/2}{-i\bar{\Delta}+\kappa/2}$ to obtain a parameter independent of detuning. The model of eq. (4.155), assuming pure radiation pressure backaction, fits the measurements well (cf. Fig. 4.13a). However, as can be seen in Fig. 4.13b, a small systematic deviation appears for high coupling power. This systematic effect is very well reproduced by the model including the photothermoelastic effect.

Finally, Figure 4.13c shows a series of coherent response spectra taken for decreasing laser detunings, and a laser power of 0.6 mW. The observed increase of the amplitudes for small detuning can be fitted accurately by introducing the photothermorefractive effect in the model (red lines). This is justified also by the observation of a non-negligible contribution of thermal effects as found in the response measurement described in section 3.6. The parameter g_{ptr} introduced here is dependent on detuning since the thermorefractive coefficient $\frac{\mathrm{d}n}{\mathrm{d}T}$ depends on temperature.

For example, we have extracted from the fits to the full detuning series of Fig. 4.16 shown in the following results section. $\Omega_{\mathrm{m}}/2\pi = 78.2\,\mathrm{MHz}$, $\kappa/2\pi = 6.0\,\mathrm{MHz}$, $\bar{a}_0 = 14.2 \cdot 10^3$ (with $g_0/2\pi = 3.4\,\mathrm{kHz}$), $g_{\mathrm{pte}}/2\pi = -122\,\mathrm{Hz}$ and $g_{\mathrm{ptr}}/2\pi = 0.32\,\mathrm{Hz}$ (at the lower mechanical sideband).

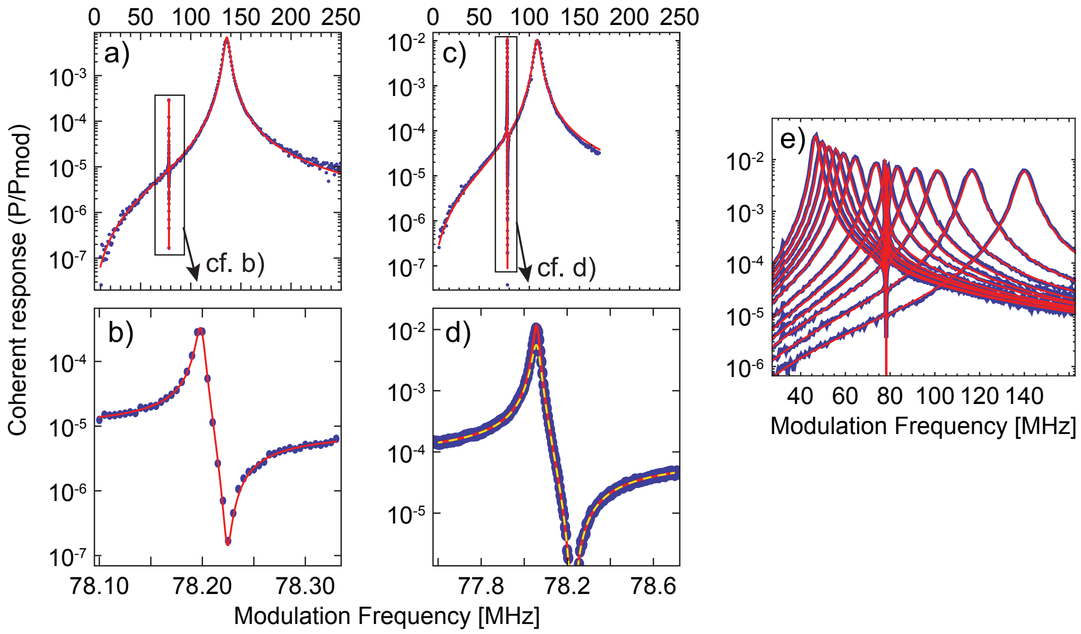

Figure 4.13: **Fitting the model to the coherent response.** *(a+b)* A coherent response spectrum taken with a power of 0.56 mW, at T=0.65 K. *(c+d)* Spectrum for 1.4 mW, at T=0.8 K with fits including the photothermoelastic effect (red line) and without (yellow dashed). (e) Spectra for 0.6 mW at T=0.75 K, for various detunings. The photothermorefractive effect is included in the fitted model and accounts for the increased amplitude for small detuning.

Extraction of the decoherence rate

The fits of the coherent response spectra determine all parameters characterizing the optomechanical interaction, and therefore the transduction of mechanical displacement fluctuations to optical fluctuations. The spectral shape of the noise originating from the Langevin force is thus fixed, so that the amplitude of this contribution can be fitted using the model of eq. (4.160). As we fit the spectral density of the actually measured *voltage* signal, these extracted amplitudes depend on the gain of the subsequent detection chain, which is not precisely known.

This ambiguity is removed by a calibration technique [2] based on a reference phase modulation, which allows to relate noise spectra taken under arbitrarily different acquisition conditions. In this manner, we link the low-temperature noise spectra to a measurement at a higher cryostat temperature (4 K), in which a high helium gas pressure, and low optical power (~ 100 nW) ensure the thermalization of the sample, so that the Langevin force is known to an estimated accuracy of 3%. In this high-temperature measurement, a known phase modulation is applied, whose amplitude can be compared with the coherent response spectra acquired with every low-temperature measurement. Assuming that no drift occurs in the phase mod-

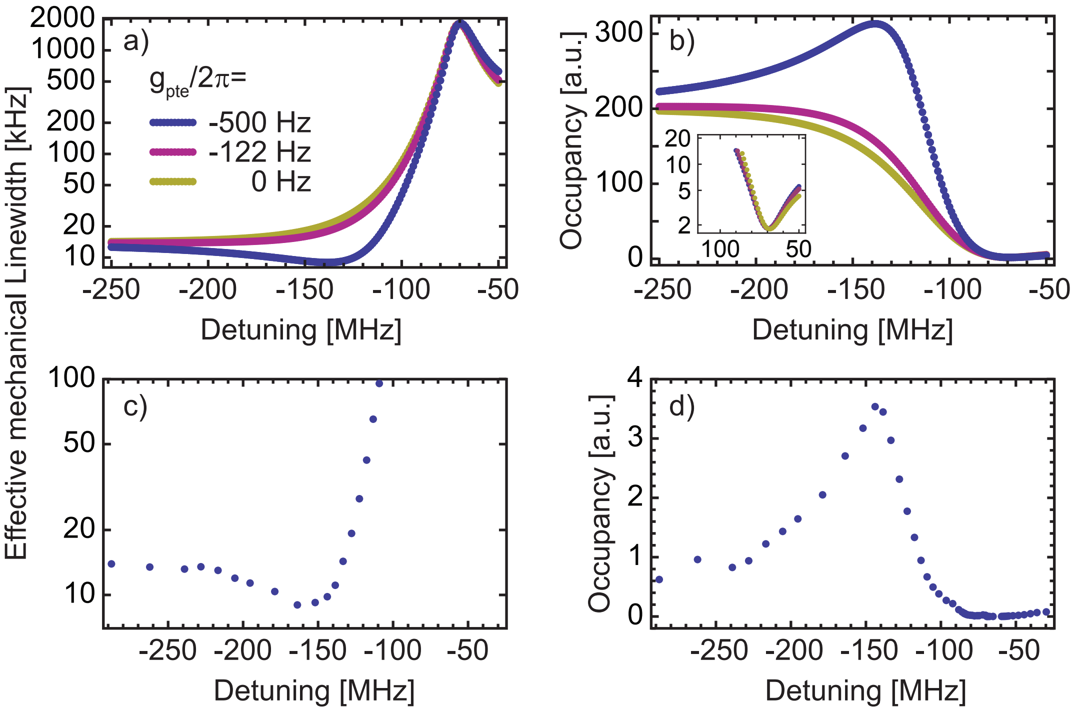

Figure 4.14: **Influence of the photothermoelastic effect on noise spectra.** *a+b)* Theoretical curves showing the influence of a non-zero photothermoelastic coupling g_{pte} on the effective mechanical linewidth and apparent occupancy (extracted from the integrated noise spectral density) as a function of the laser's detuning. The three chosen values correspond to a vanishing photothermoelastic coupling (0 Hz), a value as typically found (−122 Hz, only a slight deviation is found) and finally an order of magnitude compatible with the traces in *c)* and *d)* (−500 Hz). The latter clearly shows a reduced mechanical linewidth and increased occupancy for a detuning of around $\Delta \approx 2\Omega_{\mathrm{m}}$. Note that the final occupancy that can be reached on the red mechanical sideband is not significantly affected (see inset). Resonant heating is not included into the model. *c+d)* Experimental data showing qualitatively similar features.

ulation chain, this method allows to absolutely calibrate the Langevin force—and therefore the mechanical decoherence rate—in the low-temperature measurements. Importantly, this derivation reveals possible changes of the decoherence rate both due to a changed temperature (bath occupation $\bar{n}_{\mathrm{m}}$) and mechanical dissipation rate Γ_{m}.

Influence of the photothermoelastic effect on noise spectra

The photothermoelastic effect described earlier can potentially influence the mechanical line-width and occupancy, as it changes the relative phase between the optical ($\delta a(t)$) and mechanical ($\delta q(t)$) fluctuations relevant for radiation pressure cooling (cf. equation (4.140)). As the relevant Fourier frequencies are much larger than the cutoff frequency of the thermal response (refer to section 3.6) the thermal response reacts with a phase shift of π relative to an optical fluctuation $\delta a(t)$. For sufficiently large photothermoelastic coupling g_{pte} this can even give rise to a significant driving of the mechanical mode for a laser detuned below the red mechanical sideband, resulting in an increased occupation of the mechanical mode and a reduced mechanical linewidth. Fig. 4.14 illustrates this phenomenon for a microresonator that exhibited an unusually strong photothermoeleastic effect (most probably due to increased optical absorption within the fused silica or to a larger thermal cutoff frequency). Theory curves in panels a) and b) reproduce the observed effects of decreased linewidth and increased occupations for detunings $\Delta < -\Omega_{\mathrm{m}}$. Importantly, the influence of the photothermal effect on the minimum occupation at $\Delta \approx -\Omega_{\mathrm{m}}$ is very small (see inset of panel b)). Note however, that most of the samples do not show this prominent driving feature (cf. Figs. 4.9,4.10,4.16).

4.3.3 Experiment

Experimental setup

Figure 4.15 shows a schematic of the employed experimental setup. At the heart of the optical setup is a Ti:Sapphire laser (Sirah Matisse TX) operating at a wavelength around 780 nm. The laser exhibits quantum limited amplitude and phase noise at Fourier frequencies relevant for this experiment. During the experiments the laser is locked to an external reference cavity such that drifts of the laser detuning Δ can be neglected during the acquisition time.

To reduce the mechanical decoherence rate $\gamma \approx \Gamma_{\mathrm{m}} \bar{n}_{\mathrm{m}}$ and to pre-cool the mechanical mode to low temperatures a helium-3 exchange gas cryostat (Oxford Instruments Heliox TL) is used. Since the toroids are situated directly above the surface of the liquefied helium-3, the achievable temperature is directly linked to the vapor pressure curve of helium-3. As the toroidal microstructures are thermally very well isolated from the substrate, one relies on cooling via the helium-3 exchange gas. As a consequence, cryostat temperature setpoints of at least 650 mK (corresponding to pressures larger than ≈ 0.15 mbar) are favorable. Coupling of light into the toroid is achieved via a tapered optical fiber that is approached using piezo positioners, which are compatible with low temperature operation. The fiber ends are guided through and out of the cryostat and constitute one arm of the interferometer that is part of the balanced homodyne detection scheme. The length of one of the ca. 8 m long arms is servo-locked using a movable mirror to cancel the DC-component of the interferometer's signal. This setting allows a shot-noise limited read-out of the phase noise imprinted onto the transmitted laser field. Care is taken to avoid excess noise in the coupling beam, as this would cause an effective increase of $\bar{n}_{\mathrm{min}}$ and precludes any quantum state manipulation. The laser passes an electro-optical modulator that allows to create sidebands around the laser frequency. Last, the laser power is stabilized actively in absolute terms at the input of the experiment to ensure operation at a constant light intensity.

The three colored building blocks highlighted in Figure 4.15 depict the three different measurements that are routinely performed one after the other.

- *Coherent response.*
  A network analyzer sweeps the upper modulation sideband over the optical resonance and demodulates the corresponding (coherent) signal (cf. sections 1.5 and 2.4).
- *Noise spectrum.*
  Connecting only an electronic spectrum analyzer gives access to the incoherent noise spectrum (cf. sections 1.3 and 2.2).
- *Time domain response.*
  Sending a pulsed stimulus from an arbitrary waveform generator to the EOM which modulates the coupling laser gives access to the dynamic time domain

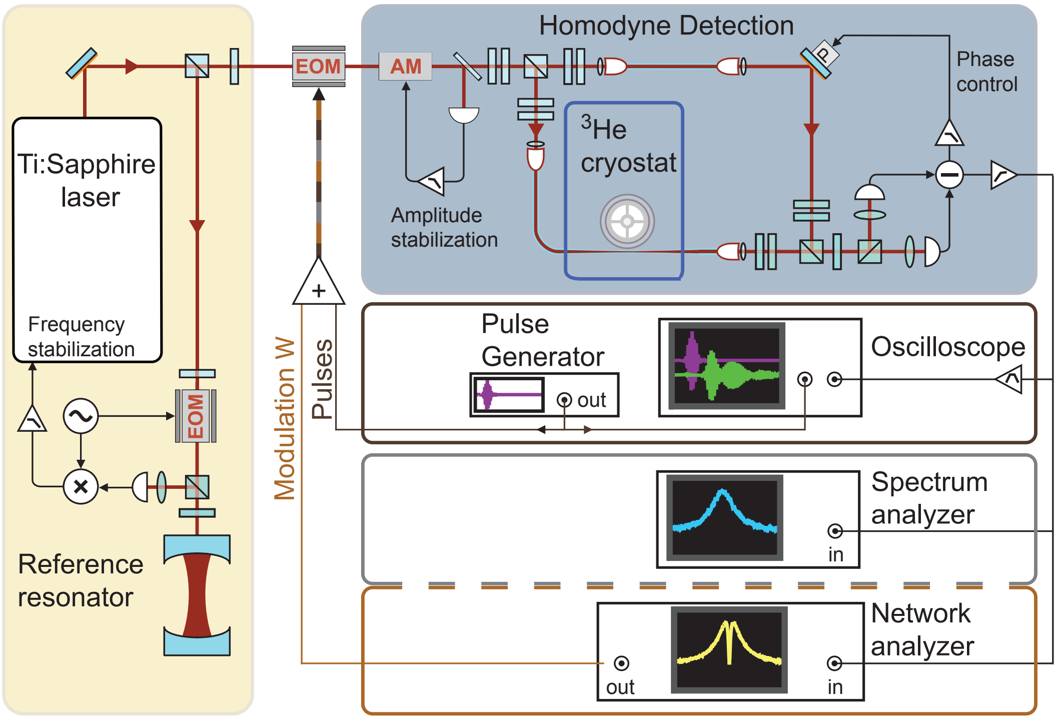
Homodyne Detection
EOM
AM
P
Phase control
Ti:Sapphire laser
^{3}He cryostat
Amplitude stabilization
Frequency stabilization
+
Modulation W
Pulses
EOM
Pulse Generator
out
Oscilloscope
Spectrum analyzer
in
Reference resonator
Network analyzer
out
in

Figure 4.15: **Setup.** See text for details.

response of the optomechanical system (cf. section 4.3.3).

While the coherent coupling rate Ω_c can be determined unambiguously by probing the coherent response of the system, as discussed in the previous section, the mechanical decoherence rate is affected in a non-trivial way by the light-absorption-dependent sample temperature and the mechanical mode's coupling to its environment, which is dominated by two-level fluctuators at cryogenic temperatures [66, 2]. In order to systematically assess the aforementioned effects on the decoherence rate, the coupling laser's frequency $\omega_\mathrm{l} = \omega_\mathrm{c} + \Delta$ (where Δ denotes the laser detuning) is varied in the vicinity of the lower mechanical sideband, while keeping the launched power constant. This allows to bring the displaced cavity mode $\hat{a}$ (of frequency $|\Delta|$) in and out of resonance with the mechanical mode $\hat{b}$ (of frequency Ω_m). For each detuning point, we acquire the coherent response of the system to an optical excitation of swept frequency $\omega_\mathrm{l} + \Omega_\mathrm{mod}$ in a first step (Ω_mod is the frequency difference to the coupling laser). These spectra (Fig. 4.16a allow to determine all parameters of the model characterizing the optomechanical interaction (4.3.2). For large detunings $|\Delta| > \Omega_\mathrm{m}$, they essentially feature a Lorentzian response of width κ and center frequency $|\Delta|$. The sharp dip at $\Omega_\mathrm{mod} \approx \Omega_\mathrm{m}$ originating from Optomechanically Induced Transparency (OMIT) [1], and for $\Omega_\mathrm{m} = -\Delta$, its width is approximately $\Omega_\mathrm{c}^2/\kappa$. The coupling rate, as derived from a fit of the coherent response for a laser power of 0.56 mW, is $\Omega_\mathrm{c} = 2\pi \times (3.7 \pm 0.05)$ MHz (corresponding to an intracavity photon number of $\bar{n}_\mathrm{c} = 3 \cdot 10^5$).

Additionally, for each value of the detuning the noise spectrum of the homodyne signal is recorded in the absence of any external excitation (Fig. 4.16b). The observed peak represents the phase fluctuations imprinted on the transmitted light by the mechanical mode's thermal motion. The constant noise background on these spectra is the shot-noise level for the (constant) laser power used throughout the laser sweep. Importantly, the amplitude of the peak is determined by the coupling to and the temperature of the environment, and therefore allows to extract the mechanical decoherence rate. All parameters now having been measured, it is moreover possible to retrieve the mechanical displacement spectrum (cf. Fig. 4.16c)). As can be seen, for detunings close to the sideband, when the (displaced) optical and mechanical modes are degenerate, the fluctuations are strongly reduced. This effect of optomechanical resolved sideband cooling [74] can be understood in a simple picture: In the regime $\Omega_\mathrm{c} \ll \kappa$, the optical decay is faster than the swapping between the vacuum in the displaced optical field and the thermal state in the mechanical oscillator. In this case, the mechanical oscillator is coupled to an effective optical bath at near-zero thermal occupancy $\bar{n}_\mathrm{min}$ with the rate $\Gamma_\mathrm{cool} = \Omega_\mathrm{c}^2/\kappa$. Ideally, $\bar{n}_\mathrm{min} = \kappa^2/16\Omega_\mathrm{m}^2 \ll 1$ is governed by non-resonant Stokes terms $\hat{a}^\dagger \hat{b}^\dagger + \hat{a}\hat{b}$ neglected in the Hamiltonian (4.121) [55, 56].

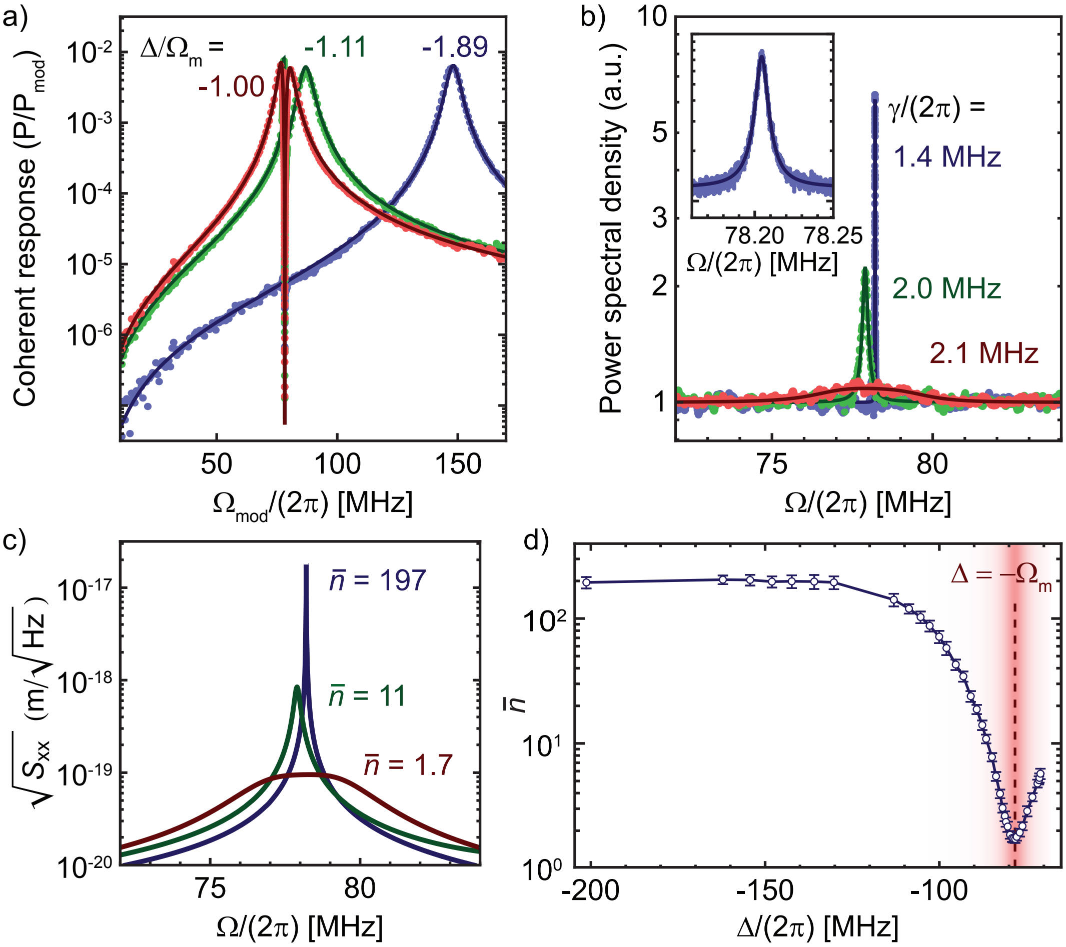

Figure 4.16: **Optomechanical interaction in the weak coupling regime** ($\Omega_c \lesssim \kappa/2$). *a)*, The coherent response of the system is obtained by sweeping a weak probe beam (at frequency $\omega_l + \Omega_{mod}$) over the cavity resonance and recording the homodyne signal P (normalized to the power P_{mod} used to create the probe beam). The fitted detuning is indicated for each of the traces. The fit provides accurate estimation of the coupling rate Ω_c via the OMIT window (4.3.2). *b)*, The measured Brownian noise spectrum in the absence of a coherent probe for each of the detunings in *a)*. The spectra are corrected for the detector response and a small contribution of Guided Acoustic Wave Brillouin scattering in the fibers (see 3.5). The inset shows a close-up of the spectrum obtained for $\Delta/\Omega_m = -1.89$. The indicated decoherence rates γ are deduced from the amplitude of each noise spectrum (curves show the result of the model with fitted γ). *d)*, Retrieved occupancy as a function of detuning. The minimum occupancy is 1.7±0.1, meaning that the oscillator has a 37±4% probability to occupy its ground state. *c)* shows the inferred mechanical displacement spectral density S_{xx} for detunings used in *a)* and *b)* calculated using the extracted parameters. Error bars, estimated s.d. (see 4.3.3).

Measurements

Evaluating the mechanical decoherence rate for $\Delta = -\Omega_m$ at a cryostat setpoint of 0.65 K, we find $\gamma = 2\pi \times (2.2 \pm 0.2)$ MHz—significantly smaller than Ω_c. Simultaneously, the average occupancy of the mechanical mode is reduced to $\bar{n} = 1.7 \pm 0.1$ (corresponding to $37 \pm 4\%$ ground state occupation), which is limited by the onset of normal mode splitting. Indeed, as Ω_c approaches κ, the thermal fluctuations are only partially dissipated into the optical bath, and partially written back onto the mechanics after one Rabi cycle.

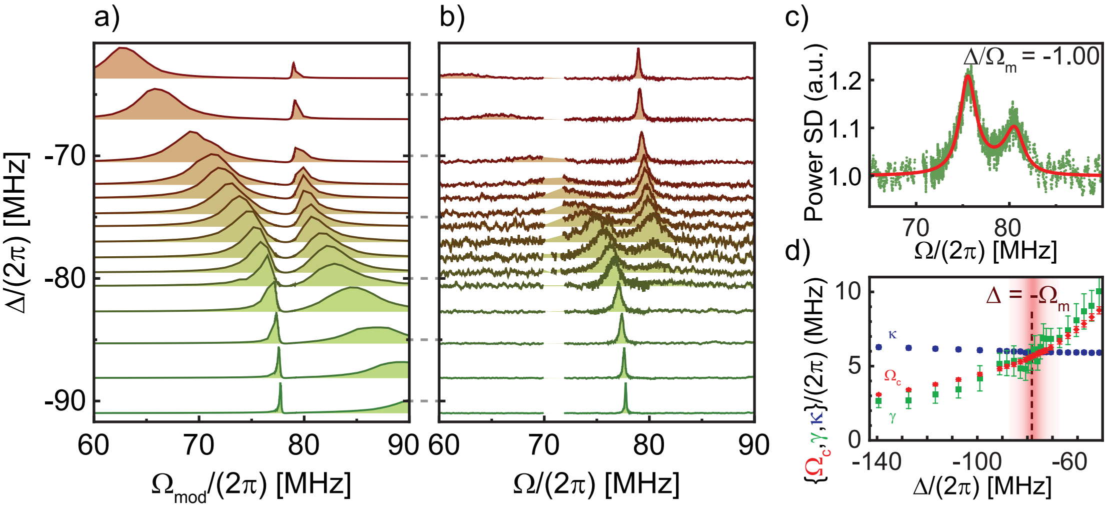

Figure 4.17: **Quantum-coherent coupling.** The coherent optical response (**a**) and the incoherent mechanical noise spectrum (**b**) for various detunings of the coupling laser (with constant power P = 1.4 mW). All curves are normalized, and vertically displaced by the detuning. Evident in both panels is the avoided crossing which originates from optomechanical normal mode splitting. A second much more weakly coupled mechanical mode at 71 MHz is omitted and the curves are shaded for clarity. **c**, Homodyne noise spectrum obtained for $\Delta = -\Omega_m$. The red line is a fit of the model. Only the decoherence rate (determining the amplitude) is fitted, while the shape is fixed through the parameters determined from the coherent response. **d**, Comparison of the mechanical (green) and optical (blue) decoherence rates with the coherent coupling rate (red) as a function of detuning. The increase of γ close to resonance reflects heating of the cavity due to the larger amount of absorbed light. On the lower mechanical sideband, where the interaction is resonant, the decoherence rates are comparable to the coupling rate, achieving quantum-coherent coupling. Error bars indicate estimated s.d. (see 4.3.3).

We subsequently increase the strength of the coupling field to reach $\Omega_c \approx \kappa$. The signature of normal mode splitting [121, 56, 114, 39] can be seen from both the coherent response and the fluctuation spectra as shown in Fig. 4.17. Both detuning series exhibit a clear anti-crossing, the splitting frequency Ω_c being 5.7 MHz. Note that, in contrast to microwave experiments [30], no squashing is observed in the normal mode splitting data. The decoherence rate (see Fig. 4.17d) is slightly raised compared to Fig. 4.16 due to laser heating and a higher buffer gas temperature of 0.8 K, amounting to $\gamma = 2\pi \times (5.6 \pm 0.9)$ MHz at the lower mechanical sideband. We hence demonstrate

$\Omega_c/\gamma = 1.0$, which constitutes a four-orders of magnitude improvement over the only previous work demonstrating strong coupling in the optical domain [114], and brings the system into the regime of quantum-coherent coupling. Even though all observed signatures are consistent with classical behavior, entering this regime opens the door to preparation and control of nonclassical states of mechanical motion with light.

Error analysis

We use the large number of traces acquired during a detuning sweep to estimate an error on each of the four parameters assumed to be independent of the detuning (Ω_m, κ, $\bar{a}_0$, g_{pte}). This is achieved by successively letting each of these parameters vary with the detuning, while the three others are still fitted globally. The error on each parameter X is obtained by calculating the standard deviation $\Delta X = \sqrt{\langle (X - X_0)^2 \rangle}$, where X_0 is the value obtained when all four parameters are kept constant over the whole detuning range. Advantageously, this procedure reflects also systematic errors due to drifts of the experimental settings over the detuning series, and physical effects that are not captured by the model. The following uncertainties were obtained with this method for the presented run: $\Omega_m/2\pi = (78.2260 \pm 0.0007)\,\mathrm{MHz}$, $\kappa/2\pi = (6.04 \pm 0.08)\,\mathrm{MHz}$, $\bar{a}_0 = (14.2 \pm 0.2) \times 10^3$, $g_{pte}/2\pi = (122 \pm 52)\,\mathrm{Hz}$. These errors, by affecting the shape of the expected noise spectra, also translate in an error on the fitted decoherence rate and occupation. A Monte-Carlo approach is used to assess the final error on γ and $\bar{n}$. The fit of the noise spectrum is repeated with a set of randomly drawn parameters, assuming an independent normal distribution for each of the previous parameters. Importantly, the resulting uncertainty depends on the particular detuning point. On the lower optomechanical sideband, the standard deviation of the results is given by $\left(\Delta\gamma/\gamma\right)_{\mathrm{model}} = 6\,\%$ and $(\Delta\bar{n}/\bar{n})_{\mathrm{model}} = 4\,\%$. Another source of uncertainty for these two parameters is the independent calibration of the optomechanical transduction that we estimate to be on the order of $\Delta_{\mathrm{calib}} = 3\%$ from the scatter between calibration measurements taken at different probing power. Finally, as discussed in section 3.5.1, an uncertainty Δ_{GAWBS} is quadratically added to account for the possible presence of GAWBS in the optical fibers before the cavity.

The data shown in Fig. 3.18b have been taken under the same conditions as the lowest occupation run shown in Fig. 4.16. The residual noise at 78 MHz (due to small portions of fibers that have not been etched) is approximately a factor seven smaller than the initial peaks, corresponding to a noise level of approximately 2 % of the shot-noise. This noise is generated along the fibers, both before and after the cavity. Special care was taken to minimize the length of unetched fiber before the cavity. The fact that an influence of the cavity detuning and coupling parameters on the transduction of these classical noise peaks into a measured signal is not discernible indicates that indeed most remaining noise originates from fiber after the cavity. Under this assumption, the independent noise of the GAWBS can be subtracted from the signal in order to estimate the decoherence rate and occupation. Figure 4.17c shows that the shape of the spectra, as predicted from independently measured parameters, is in excellent agreement with the data after subtraction, in which no signs of squashing are observed. Nonetheless, we have performed an additional analysis for the lowest-occupancy data under the assumption that half of the noise is generated before the cavity, which leads to deviations of the decoherence rate and occupation of 7 % and 5 %, respectively. This upper bound of the influence of GAWBS corresponds to an uncertainty of 0.08 phonons. The total error for this example is then given by

$$\frac{\Delta\gamma}{\gamma} = \sqrt{\left(\frac{\Delta\gamma}{\gamma}\right)^2_{\text{model}} + {\Delta_{\text{calib}}}^2 + \Delta^2_{\text{GAWBS}}} = 10\,\%$$

$$\frac{\Delta\bar{n}}{\bar{n}} = \sqrt{\left(\frac{\Delta n}{n}\right)^2_{\text{model}} + {\Delta_{\text{calib}}}^2 + \Delta^2_{\text{GAWBS}}} = 7\,\%.$$

Time-domain response

As a proof of principle and as a first classical illustration of the potential of time-domain experiments, we finally demonstrate the dynamical exchange of a pulsed coherent excitation between the optical and mechanical degrees of freedom. By measuring the homodyne signal upon launching a weak pulse resonant with the cavity in the presence of the detuned coupling field (Fig. 4.18a) it is possible to directly observe the coherent exchange of energy on an oscilloscope. This pulse is generated by modulating the coupling laser's phase at the mechanical resonance frequency, creating a pair of sidebands—one of which is resonant with the optical cavity.

An arbitrary signal generator (Agilent 33250A) is used to generate the RF pulses. The time dependent voltage $U(t)$ is a sine wave modulated by a Gaussian envelope:

$$U(t) = E(t)\sin(\Omega_{\text{mod}}t + \phi_0) \tag{4.163}$$

$$E(t) = U_0 e^{-\left(\frac{t-t_0}{\tau}\right)^2} \tag{4.164}$$

with a carrier frequency $\Omega_{\text{mod}} = 2\pi\cdot 77\,\text{MHz}$ and an envelope duration $\tau = 32\,\text{ns}$ (FWHM = 54 ns). A digital oscilloscope, synchronously triggered with the signal generator is used to record and average the homodyne response. The very small signal originating from the balanced detectors is amplified and filtered, around a frequency of 75 MHz, with a bandwidth of 100 MHz. For low excitation amplitude, averaging is necessary to extract the coherent response out of the incoherent thermal and quantum noises from the optomechanical system.

The modulation depth $\beta(t)$ corresponding to the instantaneous value of the slowly varying envelope is given by:

$$\beta(t) = \pi \frac{E(t)}{V_\pi}, \tag{4.165}$$

where $V_\pi = 154$ V is the voltage corresponding to a π phase shift of the beam in the EOM (NewFocus 4002). For a weak modulation depth ($\beta \ll 1$), a fraction $\left(\beta/2\right)^2$ of the optical carrier power P_c is scattered into each of the two first modulation sidebands. The total optical power in the upper sideband can hence be simply approximated by

$$P(t) \approx P_c \left(\pi \frac{E(t)}{2V_\pi}\right)^2 \tag{4.166}$$

The total energy in the pulse can then be obtained by integrating the instantaneous power over the duration of the pulse. The average number of photons in one pulse is hence given by:

$$n \approx \frac{1}{\hbar\omega} \int_{-\infty}^{+\infty} P_c \left(\frac{\pi E(t)}{2V_\pi}\right)^2 \mathrm{d}t = \frac{\pi^{5/2}}{4\sqrt{2}} \frac{\tau P_c}{\hbar\omega} \left(\frac{U_0}{V_\pi}\right)^2 \tag{4.167}$$

Although the employed detection is far from optimized for time-domain experiments, a signal-to-noise ratio of 40 is achieved in Fig. 4.18b by averaging 250,000 traces within two minutes for $\bar{n} = 10$.

In the regime of weak coupling, the optical pulse excites the mechanical mode to a finite oscillation amplitude, which decays slowly at the optically damped mechanical dissipation rate. This in turn only imprints a weak signature on the homodyne signal (Fig. 4.18b). Increasing the laser power, we reach $\Omega_\mathrm{c}/2\pi = 11.4$ MHz $> \kappa/2\pi = 7.1$ MHz, and the envelope of the homodyne signal—corresponding to the amplitude of the measured sideband field—undergoes several cycles of energy exchange with the mechanical oscillator, before it decays with a modified rate of $(\kappa + \Gamma_\mathrm{m})/2 \approx \kappa/2$, corresponding to the decay rate of the optomechanical polariton excited. Using our model (which has been matched to separately taken coherent response measurements), we can derive not only the homodyne signature—which reproduces our data very well—but also the expected mechanical oscillations resulting from this pulsed excitation. These reveal how the excitation cycles continuously between the optical and mechanical modes. Reducing the excitation further so that one pulse contains less than one photon on average, a clear signature of several swapping cycles can still be observed (Fig. 4.18c). Although the average evolution observed here follows classical dynamics and is not affected by decoherence, replacing the weak coherent state in this experiment by a single photon [155, 22] is expected to result in Rabi-like oscillation of the Fock state from optics to mechanics. This is possible because the

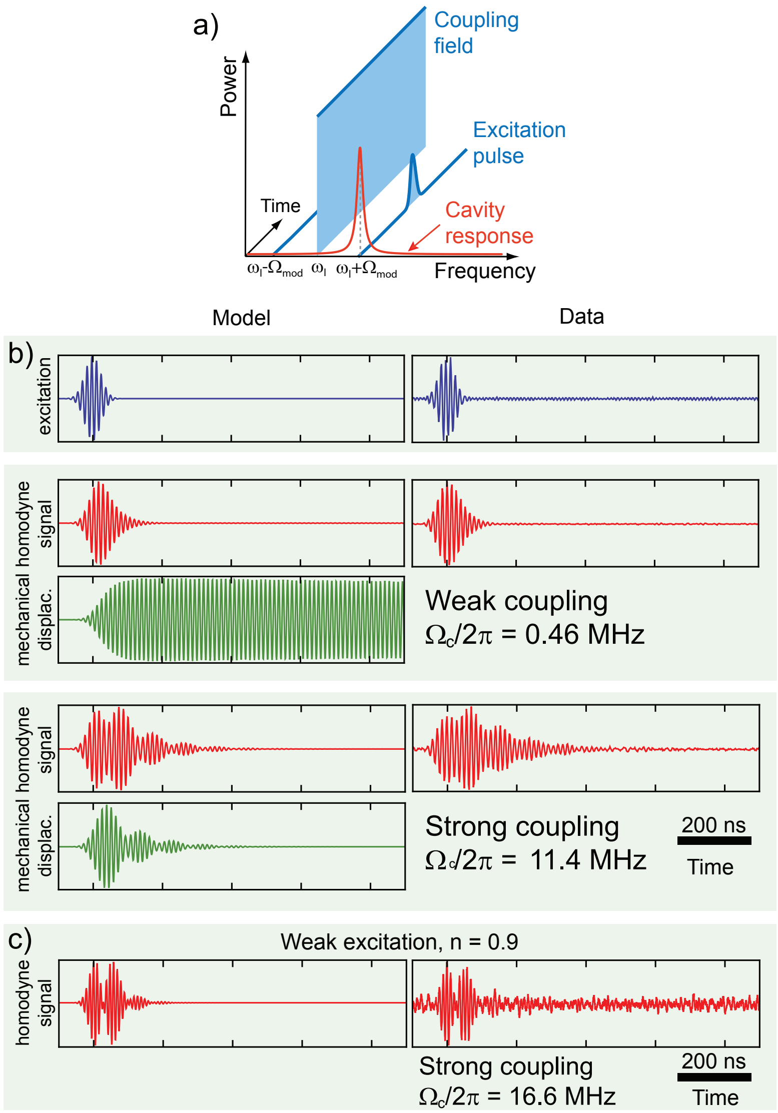

Figure 4.18: **Coherent exchange between the optical field and the micromechanical oscillator** probed in the time domain as measured (“Data”) and calculated numerically (“Model”). A modulation pulse (blue traces) applied to the phase modulator creates an excitation pulse probing the dynamics of the optomechanical system in the presence of the coupling field. The response of the system is encoded into the homodyne output signal (red traces). Using the full model of the system, the mechanical displacement can be simulated in addition (green traces). **a**, Schematic of the excitation scheme, with the cavity frequency response sketched as the red curve. **b**, In the regime of weak coupling (upper panels), the optical output pulse exhibits only a weak signature of the mechanical ringdown excited by the short burst of radiation pressure. In the case of strong coupling (lower panels) the modulated envelopes of the time-domain response indicate several cycles of oscillation between coherent optical and mechanical excitations of the system. **c**, Results for weak excitation ($\bar{n} = 0.9$) and strong coupling, (**c**)) coherent optical and mechanical excitations of the system.

system resides in the quantum-coherent regime, which we have proved above on the basis of measurements of classical signatures. A repeated quadrature measurement yielding a bimodal distribution would then provide an unambiguous signature of the quantum nature of the state after the full swap [163].

Summary and Outlook

Obtaining quantum-coherent coupling $\Omega_c \gtrsim (\gamma, \kappa)$ has several interesting consequences. It allows the mapping of elemental quantum states of the optical field onto the mechanical mode via the use of a time-dependent coupling field. For example, preparation of the mode in the ground state or the Fock state $|1\rangle$ can be efficiently achieved in this regime using a π-pulse which swaps the thermal state of the oscillator and the quantum state of the displaced optical field. Note that the manipulation of large quantum states becomes increasingly challenging since the lifetime of the number state $|n\rangle$ scales with $1/n$. In this context, it will be beneficial to reduce spurious laser heating and employ materials with low intrinsic loss, as well as to increase the optomechanical coupling rate by further miniaturization. The regime of quantum-coherent coupling demonstrated here has been proposed as a general quantum link between electromagnetic fields of vastly different frequencies, e.g., different wavelengths in the optical spectrum or microwave and optical photons [154, 153]. Electrical actuation of whispering gallery mode resonators has recently been demonstrated at an elementary level [164]. In this context, the efficient coupling of the demonstrated system to a low-loss single mode optical fiber is beneficial. Moreover, quantum-coherent coupling enables the use of the mechanical oscillator as a transducer to link otherwise incompatible elements in hybrid quantum systems, such as solid-state spin, charge, or superconducting qubits and propagating optical fields [156].

In conclusion, the reported experiments—which achieve quantum-coherent coupling between a micromechanical oscillator and an optical mode—represent a crucial step into the experimental investigation and optical quantum control of the most tangible harmonic oscillator: a mechanical vibration.

5 Outlook

The primary goal defined in the beginning of this thesis was "to enter the quantum-regime" by ground-state cooling. A few groups have now achieved comparable or slightly smaller phonon occupations in different systems [29, 101, 30, 31]. Each of these systems poses different advantages and disadvantages. Although not boasting extremely large mechanical quality factors, silica microtoroids offer several favorable properties that will be beneficial in future quantum optomechanics experiments. For example, the ready availability of very high Q optical modes (yielding sideband factors exceeding 10) have enabled to reach quantum-coherent coupling as described in this thesis, which paves the way for transferring quantum states of the optical field to the mechanical mode. Moreover, the fact that these cavities can be easily tuned to overcoupled conditions is very favorable for quantum optical experiments where a high quantum efficiency is required. Moreover, the mechanical resonance frequencies are in the range where quantum limited homodyne detection can be performed at moderate light levels. However, on the road to such experiments, several technical advances can be readily implemented that allow to venture deeper into the quantum regime and simplify future experiments.

5.1 Locking of the cooling laser

One major inconvenience until now was the inability to reliably lock the laser to the mechanical sideband, or to implement a computer controlled continuous adjustment of the laser's detuning, as already a minor change in power or coupling affects the toroid's optical resonance frequency severely and thus changes the detuning. While for (typically) rather large Fabry-Pérot-cavities, locking to the next longitudinal optical mode can be performed easily by using a frequency shifter, this is obviously no longer possible for devices such as microtoroids with free-spectral ranges in the THz range. Locking of the laser is required whenever experiments are to be done at a fixed detun-

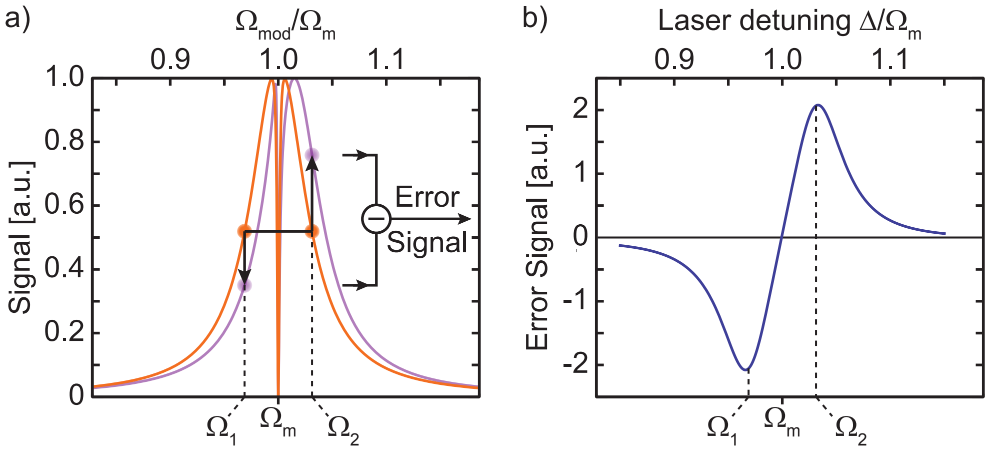

Figure 5.1: **Dual tone locking scheme.** Refer to text for details.

ing while experimental conditions are varying (e.g. swept input power, swept cryostat temperature), or if a second laser is to be used. So far, experiments with two lasers have always been performed using overcoupled and sufficiently broad resonances in combination with small laser power levels, such that some drift or jitter could be tolerated. Alternatively, a simple PDH or offset lock was used.

However, while pump-probe experiments can be realized easily in this way, once it is necessary to keep a laser detuned to the mechanical sideband of a critically coupled (i.e. narrow) resonance this approach is no longer suitable. As emphasized on multiple occasions, a driving tone (as required for a PDH lock) that coincides with the mechanical resonance frequency cannot be tolerated as it gives rise to a driving of the mechanics when the drive falls into the OMIT window, which can become rather wide in the case of strong coupling.

A possible alternative locking scheme is shown in Fig. 5.1. In Fig. 5.1a two traces are shown as obtained in a sideband sweep with $\Delta_{\mathrm{set}} = -\Omega_{\mathrm{m}}$ (orange), where the laser is supposed to be locked, and slightly detuned with $\Delta = -(\Omega_{\mathrm{m}} + \kappa/5)$ (violet). The idea is to select two points of this response that lie on the flanks of the optical resonance and that are symmetric around the locking frequency (here: $\Omega_{1,2} = \Omega_{\mathrm{m}} \pm \kappa/2$), as indicated by the dashed lines and circles. Taking the difference between these two (amplitude) signals gives a useful error signal centered at the desired detuning of $-\Omega_{\mathrm{m}}$. As long as the difference $\left|\Omega_{1,2} - \Omega_{\mathrm{m}}\right|$ is larger than the OMIT window, no influence on the mechanics is expected. They should not be too far off, though, in order to obtain a sufficiently strong signal.

To implement this, two RF tones at $\Delta_{\mathrm{set}} \pm \Omega$ are combined and the resulting signal is split into two. One is sent to a phase modulator in the cooling laser beam path, then passes the entire homodyne setup. The RF signal captured by the balanced detector is subsequently mixed with the second part of the signal serving as LO. One can show, that by balancing the armlengths of signal and LO armlengths of the RF paths, and adding a constant phase shift onto the LO signals, an error signal as depicted in 5.1b can be generated. A first promising test at room-temperature has been done, which showed a stable locking. In combination with automated data acquisition and fitting of a sideband sweep, one can also correct minor deviations from the ideal behavior due to the detector cutoff or additional contributions from the photothermoelastic and -refractive effect (4.3.2) that lead to a deformation of the response and thus a shift of the zero of the error signal.

5.2 Real-time spectrum analysis

In the experiments reported in this thesis a conventional electronic spectrum analyzer (Agilent N9020A MXA) was used, which sweeps a filter of a certain configurable bandwidth (“Resolution Band Width”, RBW) across the chosen span. Typically the ratio of span and RBW is of order 100 or larger, which allows to acquire about 100 completely independent spectral points within the chosen frequency span. However, this means, that most of the information contained in a time-domain signal is lost, since during the acquisition time (approximately the inverse of the RBW) of an individual point, all spectral components are filtered out and lost. Since recently, so-called real-time spectrum analyzers have become available that acquire real-time time-domain traces with high voltage (14bit) and temporal (1/300MHz) sampling resolution, allowing an analysis bandwidth of several tens of MHz. These traces are undergoing a real-time FFT in parallel to the acquisition of new data and the spectra are output immediately. This concept avoids loss of information and can speed up the process of data acquisition and averaging by the aforementioned factor of span/RBW.

Such a device (Tektronix RSA 5106A, 40 MHz bandwidth) has been recently included into the setup, where a 40 MHz frequency band between DC and 6 GHz can be chosen that is mixed to low frequency and analyzed in real-time.

Using this device, not only measurement times are greatly reduced, but one can also hope to acquire spectra of the dynamics of optomechanical experiments. An additional idea is to replace the cw cooling laser by a “pulsed” beam that needs to be long enough to cool, while keeping the mean power in the cavity small enough to reduce resonant and off-resonant heating.

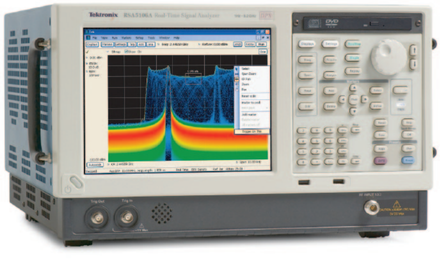

Figure 5.2: **Real-time spectrum analyzer Tektronix RSA5106A.**

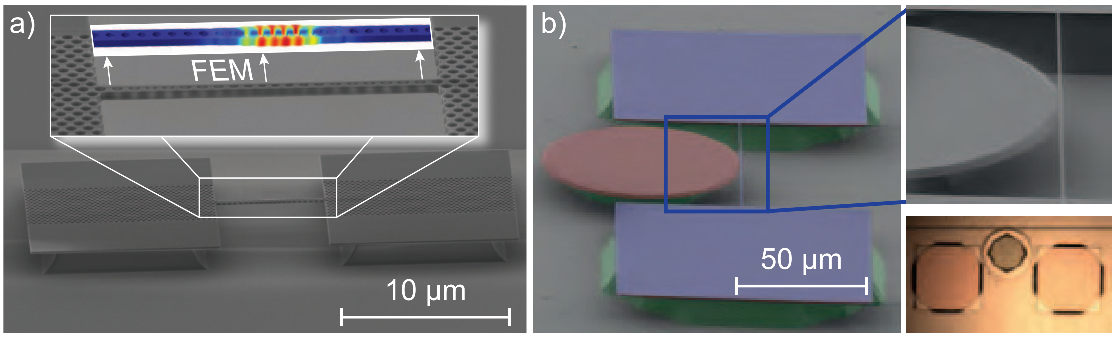

Figure 5.3: **Future optomechanical systems.** *a)* Photonic crystal cavities as currently developed within our group. The inset shows a zoom and a finite-element simulation of a localized mechanical mode. The optical mode extends over a very similar volume, yielding very high coupling rates. *(Courtesy to Simon Müller) b)* Integrated mechanical beam resonator, evanescently coupled to a WGM microdisc resonator. The optical image shows the device being coupled to a tapered fiber. *(Courtesy to Emanuel Gavartin [45], see also [44])*

5.3 Samples

Improvement of the toroidal silica microresonators has enabled major progress in the past two years, especially by increasing the vacuum optomechanical coupling rate. However, significant improvements can probably not be expected on this side. The mechanical linewidth is fixed by TLS, a decrease in initial cooling-temperature goes along with a reduced vapor pressure, i.e. inferior thermalization, and in terms of sample dimensions also a hard boundary is approaching. Here, fabrication sets a limit, as the laser reflow process does not allow arbitrarily small distances between spokes and rim. Also, the inner pad needs to be sufficiently large, such that it is not completely undercut before releasing the rest of the structure by means of XeF_2 etching. Besides that, also coupling in the cryostat becomes a more and more challenging task. Assuming, that most of the observed off-resonant heating is due to absorption of light on the silicon chip, a reflective layer on the substrate close to the toroids could help to reduce this source of heating.

A promising long-term evolution for optomechanical experiments at He-3 temperatures is to develop different optomechanical systems. Two different systems are currently pursued. The first is to use photonic crystal cavities as depicted in Fig. 5.3a which exhibit very high frequency ($\sim 6\,\mathrm{GHz}$) localized mechanical modes [133] such that already a cryogenic precooling to 600 mK is sufficient to reduce the occupancy of the mechanical oscillator below ten quanta. However, tapered fiber coupling to these structures is not as simple and efficient (10% incoupling efficiency has been measured in [40]) as for toroidal microresonators, reducing the achievable cooling rate and also the detection efficiency. On the detection side, the very high mechanical frequencies require very fast detectors, which come with substantially higher noise backgrounds but reduced optical damage powers, such that a direct shot-noise limited detection without further mixing to lower frequencies in the optical domain is out of reach. Only very small signal-to-noise ratios can be expected [31]. Moreover, also thermalization behavior, off-resonant and resonant heating, as well as coupling to TLS needs to be carefully investigated.

The second system is a high stress silicon nitride nanobeam that is evanescently coupled to a microdisk [45]. These feature mechanical frequencies of $\Omega_\mathrm{m} \approx 2\pi\,3\,\mathrm{MHz}$ with quality factors $Q_\mathrm{m} \approx 5\times10^5$ and small masses $m_\mathrm{eff} = 9\,\mathrm{pg}$ have been demonstrated. First experiments have been done at low temperature and pressure ($T = 4\,\mathrm{K}$ and $p = 10^{-3}\,\mathrm{mbar}$), showing that quality factors and the vacuum optomechanical coupling rate even slightly improved to $Q_\mathrm{m} = 7\times10^5$ and $g_0 = 2\pi\,33\,\mathrm{MHz/nm}$. Due to fabrication related defects the optical linewidths are in the current generation of samples rather large ($\kappa = 2\pi\,3\,\mathrm{GHz}$) and sideband cooling is not efficient. Instead, feedback cooling was applied and cooling to a mean occupancy of around 100 phonons could be demonstrated [165], which is an improvement by more than two orders of magnitude over previous experiments at room temperature [164]. These preliminary results also show that resonant heating seems to have a small influence, probably because the optical and mechanical degrees of freedom are not connected thermally. Drastic improvements on the optical linewidths ($\Gamma_\mathrm{m} < 2\pi\,5\,\mathrm{MHz}$ have already been shown [166]) and potentially a factor of three larger coupling rates can be envisaged for the future. Therefore, however, new fabricational methods need to be developed.

5.4 Experiments

We have recently acquired a second Ti:Sapphire laser to be used within the cryogenic optomechanics experiment, which allows a variety of quantum optomechanics experiments.

Sideband spectroscopy

In order to see the first real “quantum” signatures of macroscopic mechanical motion in our systems, it is envisioned to perform experiments to spectroscopically measure the relative heights of the two individual mechanical sidebands, in a similar fashion to the recent work by Safavi-Naeini *et al.* [167]. The Stokes and anti-Stokes sidebands scale with the phonon occupancy $\bar{n}+1$ and $\bar{n}$, respectively, and thus allow to measure the occupancy accurately close to the quantum groundstate. This quantum signature has been used in cold atom experiments for a long time [11, 168, 12]. In [167] a weak read-out laser was consecutively tuned to the red and blue mechanical sideband of an optical resonance, while the cooling laser resided on the red mechanical sideband of another optical mode. Under the assumption that backaction caused by the read-out laser is much weaker than caused by the cooling laser, they could directly compare the integrated noise spectral densities of the mechanical peaks obtained from the transmitted read-out laser for the two measurements. Alternatively it would be interesting to put the read-out laser on resonance of a second optical mode in order to *simultaneously* assess the two mechanical sidebands in a single measurement. As the beating frequencies of the two sidebands with the local oscillator of a homodyne setup are degenerate, we are planning on using heterodyne detection, where the local oscillator is shifted in such a way that the two sidebands are well separated. One inconvenience is the strong modulation caused by the beating between the carrier frequency and the shifted local oscillator. The expected ratio of power scattered into the mechanical sidebands close to the mechanical groundstate is of order 10^{-8}, which means that the dynamic range of the detection circuitry must exceed 80 dB. In particular the absolute power of the strong beating might just saturate the low-noise preamplifier within the balanced photodetector. If this is the case, it is envisaged to partically cancel this beating signal by a laser beam, which is amplitude modulated at the beating frequency by means of a phase shifted feed forward, and directly—without passing the interferometer—sent onto the detectors.

Quantum backaction evasion

If laser tones are tuned to both mechanical sidebands simultaneously, a time-varying interaction strength results that only couples to one quadrature of the mechanical motion. This allows a measurement of one quadrature of the oscillator that is not affected by backaction with an imprecision below the standard quantum limit and at the same time leads to squeezing of the mechanical motional state [169, 170].

This scheme has been implemented experimentally in the microwave domain, where it was shown that the measurement imprecision could be decreased by almost an order of magnitude below the (in this case: classical) noise floor [171].

The combination of large sideband factors and quantum-limited laser sources and detection schemes should allow to evade *quantum* backaction and to show measurement induced squeezing of mechanical motion.

Bibliography

[1] S. Weis, R. Rivière, S. Deléglise, E. Gavartin, O. Arcizet, A. Schliesser, and T. J. Kippenberg. Optomechanically induced transparency. *Science*, 330:1520–1523, 2010.

[2] R. Rivière, S. Deléglise, S. Weis, E. Gavartin, O. Arcizet, A. Schliesser, and T. J. Kippenberg. Optomechanical sideband cooling of a micromechanical oscillator close to the quantum ground state. *Physical Review A*, 83(6):063835, 2011. PRA.

[3] E. Verhagen, S. Deléglise, S. Weis, A. Schliesser, and T. J. Kippenberg. Quantum-coherent coupling of a mechanical oscillator to an optical cavity mode. *Nature*, 482:63–67, 2012.

[4] E. Schrödinger. Die gegenwärtige Situation in der Quantenmechanik. *Naturwissenschaften*, 23:807–812, November 1935.

[5] T. H. Maiman. Stimulated Optical Radiation in Ruby. *Nature*, 187:493–494, August 1960.

[6] T. W. Hänsch and A. L. Schawlow. Cooling of gases by laser radiation. *Optics Communications*, 13:68–69, 1975.

[7] J. Dalibard and C. Cohen-Tannoudji. Laser cooling below the doppler limit by polarization gradients: simple theoretical models. *J. Opt. Soc. Am. B*, 6(11):2023–2045, Nov 1989.

[8] D. J. Wineland and H. Dehmelt. Proposed $10^{14}\delta\nu < \nu$ laser fluorescence spectroscopy on Tl^{+} ion mono-oscillator. *Bulletin of the American Physical Society*, 20:637, 1975.

[9] W. Neuhauser, M. Hohenstatt, P. Toschek, and H. Dehmelt. Optical-sideband cooling of visible atom cloud confined in parabolic well. *Phys. Rev. Lett.*, 41(4):233–236, 1978.

[10] D. J. Wineland, R. E. Drullinger, and F. L. Walls. Radiation-pressure cooling of bound resonant absorbers. *Phys. Rev. Lett.*, 40(25):1639–1642, 1978.

[11] F. Diedrich, J. C. Bergquist, Wayne M. Itano, and D. J. Wineland. Laser cooling to the zero-point energy of motion. *Physical Review Letters*, 62(4):403–406, 1989.

[12] C. Monroe, D. M. Meekhof, B. E. King, S. R. Jefferts, W. M. Itano, D. J. Wineland, and P. Gould. Resolved-sideband raman cooling of a bound atom to the 3D zero point energy. *Physical Review Letters*, 75(22):4011–4014, 1995.

[13] K. B. Davis, M. O. Mewes, M. R. Andrews, N. J. van Druten, D. S. Durfee, D. M. Kurn, and W. Ketterle. Bose-einstein condensation in a gas of sodium atoms. *Phys. Rev. Lett.*, 75:3969–3973, Nov 1995.

[14] M. H. Anderson, J. R. Ensher, M. R. Matthews, C. E. Wieman, and E. A. Cornell. Observation of bose-einstein condensation in a dilute atomic vapor. *Science*, 269(5221):198–201, 1995.

[15] A. Kubanek, M. Koch, C. Sames, A. Ourjoumtsev, P. W. H. Pinkse, K. Murr, and G. Rempe. Photon-by-photon feedback control of a single-atom trajectory. *Nature*, 462:898–901, 2009.

[16] D. L. Moehring, P. Maunz, S. Olmschenk, K. C. Younge, D. N. Matsukevich, L.-M. Duan, and C. Monroe. Entanglement of single-atom quantum bits at a distance. *Nature*, pages 68–71, 2007.

[17] A. Friedenauer, H. Schmitz, J. T. Glueckert, D. Porras, and T. Schaetz. Simulating a quantum magnet with trapped ions. *Nature Physics*, pages 757–761, 2008.

[18] J. Esteve, C. Gross, A. Weller, S. Giovanazzi, and M. K. Oberthaler. Squeezing and entanglement in a bose-einstein condensate. *Nature*, 455(7217):1216, 2008.

[19] W. S. Bakr, J. I. Gillen, A. Peng, S. Folling, and M. Greiner. A quantum gas microscope for detecting single atoms in a Hubbard-regime optical lattice. *Nature*, 462:74–77, November 2009.

[20] M. Köhl, H. Moritz, T. Stöferle, K. Günter, and T. Esslinger. Fermionic atoms in a three dimensional optical lattice: Observing fermi surfaces, dynamics, and interactions. *Phys. Rev. Lett.*, 94:080403, Mar 2005.

[21] B. Zimmermann, Müller T., Meineke J., Esslinger T., and H. Moritz. High-resolution imaging of ultracold fermions in microscopically tailored optical potentials. *New Journal of Physics*, 13(4):043007, 2011.

[22] O. Romero-Isart, A. C. Pflanzer, M. L. Juan, R. Quidant, N. Kiesel, M. Aspelmeyer, and J. I. Cirac. Optically levitating dielectrics in the quantum regime: Theory and protocols. *Physical Review Astroparticle Physics*, 83(1):013803, 2011.

[23] T. J. Kippenberg and K. Vahala. Cavity opto-mechanics. *Optics Express*, 15:17172–17205, 2007.

[24] J. D. Teufel, R. Donner, M. A. Castellanos-Beltran, J. W. Harlow, and K. W. Lehnert. Nanomechanical motion measured with precision beyond the standard quantum limit. *Nature Nanotechnology*, 4:820–823, 2009.

[25] G. Anetsberger, E. Gavartin, O. Arcizet, Q. P. Unterreithmeier, E. M. Weig, M. L. Gorodetsky, J. P. Kotthaus, and T. J. Kippenberg. Measuring nanomechanical motion with an imprecision far below the standard quantum limit. *Physical Review A*, 82:061804, 2010.

[26] A. Schliesser, P. Del'Haye, N. Nooshi, K. J. Vahala, and T. J. Kippenberg. Radiation pressure cooling of a micromechanical oscillator using dynamical backaction. *Phys. Rev. Lett.*, 97(24):243905–, 2006.

[27] O. Arcizet, P.-F. Cohadon, T. Briant, M. Pinard, and A. Heidmann. Radiation-pressure cooling and optomechanical instability of a micromirror. *Nature*, 444:71–74, 2006.

[28] S. Gigan, H. R. Böhm, M. Paternosto, F. Blaser, G. Langer, J. B. Hertzberg, K. C. Schwab, D. Bäuerle, M. Aspelmeyer, and A. Zeilinger. Self-cooling of a micromirror by radiation pressure. *Nature*, 444:67–70, 2006.

[29] A. D. O'Connell, M. Hofheinz, M. Ansmann, Radoslaw C Bialczak, M. Lenander, E. Lucero, M. Neeley, D. Sank, H. Wang, M. Weides, J. Wenner, J. M. Martinis, and A. N. Cleland. Quantum ground state and single-phonon control of a mechanical resonator. *Nature*, 464:697–703, 2010.

[30] J. D. Teufel, T. Donner, Dale Li, J. W. Harlow, M. S. Allman, K. Cicak, A. J. Sirois, J. D. Whittaker, K. W. Lehnert, and R. W. Simmonds. Sideband cooling of micromechanical motion to the quantum ground state. *Nature*, 475:359–363, 2011.

[31] J. Chan, T. P. M. Alegre, A. H. Safavi-Naeini, J. T. Hill, A. Krause, S. Groeblacher, M. Aspelmeyer, and O. Painter. Laser cooling of a nanomechanical oscillator into its quantum ground state. *Nature*, 478:89–92, 2011.

[32] C. Fabre, M. Pinard, S. Bourzeix, A. Heidmann, E. Giacobino, and S. Reynaud. Quantum-noise reduction using a cavity with a movable mirror. *Physical Review A*, 49:1337–1343, 1994.

[33] S. Mancini and P. Tombesi. Quantum noise reduction by radiation pressure. *Physical Review A*, 49:4055–4065, 1994.

[34] C. W. Gardiner and P. Zoller. *Quantum Noise*. Springer, 2004.

[35] V. Giovannetti and D. Vitali. Phase-noise measurement in a cavity with a movable mirror undergoing quantum brownian motion. *Physical Review A*, 63:023812, 2001.

[36] G. D. Cole, I. Wilson-Rae, K. Werbach, M. R. Vanner, and M. Aspelmeyer. Phonon-tunnelling dissipation in mechanical resonators. *Nature communications*, 2:231, 2011.

[37] A. G. Kuhn, M. Bahriz, O. Ducloux, C. Chartier, O. Le Traon, T. Briant, P.-F. Cohadon, A. Heidmann, C. Michel, L. Pinard, and R. Flaminio. A micropillar for cavity optomechanics. *Applied Physics Letters*, 99(12):121103, 2011.

[38] GEO 600 collaboration. The geo 600 gravitational wave detector. *Classical and Quantum Gravity*, 19(7):1377, 2002.

[39] J. D. Teufel, D. Li, M. S. Allman, K. Cicak, A. J. Sirois, J. D. Whittaker, and R. W. Simmonds. Circuit cavity electromechanics in the strong coupling regime. *Nature*, 471:204–208, 2011.

[40] E. Gavartin, R. Braive, I. Sagnes, O. Arcizet, A. Beveratos, T. J. Kippenberg, and I. Robert-Philip. Optomechanical coupling in a two-dimensional photonic crystal defect cavity. *Physical Review Letters*, 106:203902, 2011.

[41] J. D. Thompson, B. M. Zwickl, A. M. Jayich, F. Marquardt, S. M. Girvin, and J. G. E. Harris. Strong dispersive coupling of a high finesse cavity to a micromechanical membrane. *Nature*, 452:72–75, 2008.

[42] K. Yamamoto, D. Friedrich, T. Westphal, S. Goßler, K. Danzmann, K. Somiya, S. L. Danilishin, and R. Schnabel. Quantum noise of a michelson-sagnac interferometer with a translucent mechanical oscillator. *Physical Review A*, 81(3):033849, 2010.

[43] Y.-S. Park and H. Wang. Resolved-sideband and cryogenic cooling of an optomechanical resonator. *Nature Physics*, 5:489–493, 2009.

[44] G. Anetsberger, O. Arcizet, Q. P. Unterreithmeier, R. Rivière, A. Schliesser, E. M. Weig, J. P. Kotthaus, and T. J. Kippenberg. Near-field cavity optomechanics with nanomechanical oscillators. *Nature Physics*, 5:909–914, 2009.

[45] E. Gavartin, P. Verlot, and T. J. Kippenberg. A hybrid on-chip opto-nano-mechanical transducer for ultra-sensitive force measurements. *arXiv:1112.0797*, 2011.

[46] T. J. Kippenberg, S. M. Spillane, and K. J. Vahala. Modal coupling in traveling-wave resonators. *Optics Letters*, 27(19):1669–1671, 2002.

[47] J. Zhu, S. K. Ozdemir, Y.-F. Xiao, L. Li, L. He, D. R. Chen, and L. Yang. On-chip single nanoparticle detection and sizing by mode splitting in an ultrahigh-Q microresonator. *Nature Photonics*, 4:46–49, 2010.

[48] M. Gorodetsky, A. Schliesser, G. Anetsberger, S. Deléglise, and T. J. Kippenberg. Determination of the vacuum optomechanical coupling rate using frequency noise calibration. *Optics Express*, 18:23236–23246, 2010.

[49] A. Gillespie and F. Raab. Thermally excited vibrations of the mirrors of laser interferometer gravitational wave detectors. *Physical Review D*, 52:577–585, 1995.

[50] H. B. Callen and T. A. Welton. Irreversibility and generalized noise. *Physical Review*, 83:34–40, 1951.

[51] P. R. Saulson. Thermal noise in mechanical experiments. *Physical Review D*, 42:2437–2445, 1990.

[52] A. Schliesser. *Cavity Optomechanics and Optical Frequency Comb Generation with Silica Whispering-Gallery-Mode Microresonators*. PhD thesis, Ludwigs-Maximilians-Universität München, 2009.

[53] P. Verlot, A. Tavernarakis, T. Briant, P.-F. Cohadon, and A. Heidmann. Backaction amplification and quantum limits in optomechanical measurements. *Physical Review Letters*, 104:133602, 2010.

[54] A. Schliesser, G. Anetsberger, R. Rivière, O. Arcizet, and T. J. Kippenberg. High-sensitivity monitoring of micromechanical vibration using optical whispering gallery mode resonators. *New Journal of Physics*, 10:095015, 2008.

[55] I. Wilson-Rae, N. Nooshi, W. Zwerger, and T. J. Kippenberg. Theory of ground state cooling of a mechanical oscillator using dynamical backaction. *Phys. Rev. Lett.*, 99(9):093901–, 2007.

[56] F. Marquardt, J. P. Chen, A. A. Clerk, and S. M. Girvin. Quantum theory of cavity-assisted sideband cooling of mechanical motion. *Physical Review Letters*, 99:093902, 2007.

[57] C. Genes, D. Vitali, P. Tombesi, S. Gigan, and M. Aspelmeyer. Ground-state cooling of a micromechanical oscillator: Comparing cold-damping and cavity-assisted cooling schemes. *Physical Review A*, 77:033804, 2008.

[58] T. J. Kippenberg, A. Schliesser, and M. Gorodetsky. Phase noise measurement of external cavity diode lasers and implications for optomechanical sideband cooling of GHz mechanical modes. *arXiv:1112.6277*, December 2011.

[59] B. E. Little, J. P. Laine, and H. A. Haus. Analytic theory of coupling from tapered fibers and half-blocks into microsphere resonators. *Journal of Lightwave Technology*, 17(4):704–715, 1999.

[60] M. Cai, O. Painter, and K. J. Vahala. Observation of critical coupling in a fiber taper to a silica-microsphere whispering-gallery mode system. *Physical Review Letters*, 85(1):74–77, 2000.

[61] M. Cai and K. Vahala. Highly efficient hybrid fiber taper coupled microsphere laser. *Optics Letters*, 26(12):884–886, 2001.

[62] R. Rivière. *Cavity Optomechanics with Silica Toroidal Microresonators down to Low Phonon Occupancy*. PhD thesis, Ludwigs-Maximilians-Universität München, 2011.

[63] H. A. Haus. *Waves and fields in optoelectronics*. Prentice-Hall, 1984.

[64] S. M. Spillane, T. J. Kippenberg, O. J. Painter, and K. J. Vahala. Ideality in a fiber-taper-coupled microresonator system for application to cavity quantum electrodynamics. *Physical Review Letters*, 91(4):043902, 2003.

[65] V. S. Ilchenko and M. L. Gorodetskii. Thermal nonlinear effects in optical whispering gallery microresonators. *Laser Physics*, 2(2):1004–1009, 1992.

[66] O. Arcizet, R. Rivière, A. Schliesser, G. Anetsberger, and T. J. Kippenberg. Cryogenic properties of optomechanical silica microcavities. *Physical Review A*, 80:021803(R), 2009.

[67] V. B. Braginsky and Yu. I. Vorontsov. Quantum-mechanical limitations in macroscopic experiments and modern experimental technique. *Soviet Physics Uspekhi*, 17:644–650, 1975.

[68] A. A. Clerk, M. H. Devoret, S. M. Girvin, Florian Marquardt, and R. J. Schoelkopf. Introduction to quantum noise, measurement, and amplification. *Rev. Mod. Phys.*, 82(2):1155–1208, 2010.

[69] C. M. Caves. Quantum-mechanical noise in an interferometer. *Physical Review D*, 23:1693, 1981.

[70] R. W. P. Drever, J. L. Hall, F. V. Kowalski, J. Hough, G. M. Ford, A. J. Munley, and H. Ward. Laser phase and frequency stabilization using an optical resonator. *Applied Physics B*, 31:97–105, 1983.

[71] E. D. Black. An introduction to pound-drever-hall laser frequency stabilization. *American Journal of Physics*, 69:79–87, 2001.

[72] T. W. Hänsch and B. Couillaud. Laser frequency stabilization by polarization spectroscopy of a reflecting reference cavity. *Optics Communications*, 35(3):441–444, 1980.

[73] P. Verlot, A. Tavernarakis, T. Briant, P.-F. Cohadon, and A. Heidmann. Scheme to probe optomechanical correlations between two optical beams down to the quantum level. *Physical Review Letters*, 102:103601, 2009.

[74] A. Schliesser, R. Rivière, G. Anetsberger, O. Arcizet, and T. Kippenberg. Resolved-sideband cooling of a micromechanical oscillator. *Nature Physics*, 4:415–419, 2008.

[75] R. O. Pohl, X. Liu, and E. Thompson. Low-temperature thermal conductivity and acoustic attenuation in amorphous solids. *Review of Modern Physics*, 74:991–1013, 2002.

[76] J. S. Butterworth, C. R. Brome, P. R. Huffman, C. E. H. Mattoni, D. N. McKinsey, and J. M. Doyle. A demountable cryogenic feedthrough for plastic optical fibers. *REVIEW OF SCIENTIFIC INSTRUMENTS*, 69(10):3697–3698, OCT 1998.

[77] M. L. Gorodetsky, A. A. Savchenkov, and V. S. Ilchenko. Ultimate q of optical microsphere resonators. *Optics Letters*, 21(7):453–455, 1996.

[78] H. Rokhsari, S. M. Spillane, and K. J. Vahala. Loss characterization in microcavities using the thermal bistability effect. *Applied Physics Letters*, 85(15):3029–3031, 2004.

[79] Minoru Tomozawa and Kenneth M Davis. Time dependent diffusion coefficient of water into silica glass at low temperatures. *Materials Science and Engineering: A*, 272(1):114 – 119, 1999.

[80] O. Humbach, H. Fabian, U. Grzesik, U. Haken, and W. Heitmann. Analysis of oh absorption bands in synthetic silica. *Journal of Non-Crystalline Solids*, 203(0):19 – 26, 1996.

[81] C. Enss and S. Hunklinger. *Low Temperature Physics*. Springer, 2005.

[82] J. Jäckle. On the ultrasonic attenuation in glasses at low temperature. *Zeitschrift für Physik*, 257:212–223, 1972.

[83] L. Pauling. The rotational motion of molecules in crystals. *Physical Review*, 36(3):430–443, 1930. PR.

[84] R. Vacher, E. Courtens, and M. Foret. Anharmonic versus relaxational sound damping in glasses. ii. vitreous silica. *Physical Review B*, 72:214205, 2005.

[85] S. Hunklinger, W. Arnold, St Stein, R. Nava, and K. Dransfeld. Saturation of the ultrasonic absorption in vitreous silica at low temperatures. *Physics Letters A*, 42(3):253–255, 1972.

[86] C. Laermans, W. Arnold, and S. Hunklinger. Influence of an electromagnetic wave on the acoustic absorption of borosilicate glass at low temperatures. *Journal of Physics C: Solid State Physics*, 10(8):L161, 1977.

[87] O. Arcizet, V. Jacques, A. Siria, P. Poncharal, P. Vincent, and S. Seidelin. A single nitrogen-vacancy defect coupled to a nanomechanical oscillator. *Nature Physics*, 7:879–883, 2011.

[88] L. Tian. Cavity cooling of a mechanical resonator in the presence of a two-level-system defect. *Phys. Rev. B*, 84:035417, Jul 2011.

[89] G. J. Grabovskij, T. Peichl, J. Lisenfeld, G. Weiss, and A. V. Ustinov. Strain tuning of individual atomic tunneling systems detected by a superconducting qubit. to be published, 2012.

[90] T. J. Kippenberg, S. M. Spillane, and K. J. Vahala. Kerr-nonlinearity optical parametric oscillation in an ultrahigh-Q toroid microcavity. *Physical Review Letters*, 93(8):083904, 2004.

[91] P. Del'Haye, A. Schliesser, O. Arcizet, T. Wilken, R. Holzwarth, and T. Kippenberg. Optical frequency comb generation from a monolithic microresonator. *Nature*, 450:1214–1217, 2007.

[92] G. Anetsberger, R. Rivière, A. Schliesser, O. Arcizet, and T. J. Kippenberg. Ultralow-dissipation optomechanical resonators on a chip. *Nature Photonics*, 2:627–633, 2008.

[93] A. Schliesser and T. J. Kippenberg. Cavity optomechanics with whispering-gallery mode optical micro-resonators, 2010.

[94] J. M. Dobrindt, B. Schröter, S. Krysiak, E. Gavartin, B. Nickel, J. Rädler, and T. J. Kippenberg. Dispersive, label-free bio-sensing with high time resolution and high sensitivity using optical microresonators. in preparation, 2012.

[95] W. Nowacki. *Dynamic problems of thermoelasticity*. Springer, 1975.

[96] M. A. Green and M. J. Keevers. Optical properties of intrinsic silicon at 300 k. *Progress in Photovoltaics: Research and Applications*, 3(3):189–192, 1995.

[97] M. A. Green, M. J. Keevers, and on PVeducation.org. Optical properties of silicon. http://pveducation.org/pvcdrom/appendicies/optical-properties-of-silicon#ref1.

[98] P. Rabl, C. Genes, K. Hammerer, and M. Aspelmeyer. Phase-noise induced limitations in resolved-sideband cavity cooling of mechanical resonators. *Physical Review A*, 80:063819, 2009.

[99] L. Diósi. Laser linewidth hazard in optomechanical cooling. *Physical Review A*, 78:021801, 2008.

[100] T. J. Kippenberg, R. Holzwarth, and S. A. Diddams. Microresonator-based optical frequency combs. *Science*, 332:555, 2011.

[101] T. Rocheleau, T. Ndukum, C. Macklin, J. B. Hertzberg, A. A. Clerk, and K. C. Schwab. Preparation and detection of a mechanical resonator near the ground state of motion. *Nature*, 463(7277):72–75, 2010.

[102] R. M. Shelby, M. D. Levenson, and P. W. Bayer. Guided acoustic-wave brillouin scattering. *Phys. Rev. B*, 31(8):5244–5252, 1985.

[103] C. R. Kurkjian, M. J. Matthewson, and J. M. Rooney. Effects of heat treatment and hf etching on the strength of silica lightguides. In H. G. Limberger and M. J. Matthewson, editors, *Reliability of Optical Fiber Components, Devices, Systems, and Networks II*, volume 5465, pages 223–229, 2004.

[104] M. Fleischhauer, A. Imamoglu, and J. P. Marangos. Electromagnetically induced transparency: Optics in coherent media. *Review of Modern Physics*, 77:633–673, 2005.

[105] K.-J. Boller, A. Imamoglu, and S. E. Harris. Observation of electromagnetically induced transparency. *Physical Review Letters*, 66(20):2593–2596, 1991.

[106] A. Kasapi, M. Jain, G. E. Yin, and S. E. Harris. Electromagnetically induced transparency: Propagation dynamics. *Physical Review Letters*, 74(13):2447–2450, 1995.

[107] L. V. Hau, S. E. Harris, Z. Dutton, and C. H. Behroozi. Light speed reduction to 17 metres per second in an ultracold atomic gas. *Nature*, 397:594–598, 1999.

[108] D. F. Phillips, A. Fleischhauer, A. Mair, R. L. Walsworth, and M. D. Lukin. Storage of light in atomic vapor. *Physical Review Letters*, 86:783–786, 2001.

[109] C. Liu, Z. Dutton, C.H. Behroozi, and L.V. Hau. Observation of coherent optical information storage in an atomic medium using halted light pulses. *Nature*, 409:490–493, 2001.

[110] M. D. Lukin and A. Imamoglu. Controlling photons using electromagnetically induced transparency. *Nature*, 413(6853):273–276, 2001.

[111] A. V. Turukhin, V. S. Sudarshanam, M. S. Shahriar, J. A. Musser, B. S. Ham, and P. R. Hemmer. Observation of ultraslow and stored light pulses in a solid. *Physical Review Letters*, 88(2):023602, 2002.

[112] D. Brunner, B. D. Gerardot, P. A. Dalgarno, G. Wüst, K. Karrai, N. G. Stoltz, P. M. Petroff, and R. J. Warburton. A coherent single-hole spin in a semiconductor. *Science*, 325(5936):70–72, 2009.

[113] T. J. Kippenberg, H. Rokhsari, T. Carmon, A. Scherer, and K. J. Vahala. Analysis of radiation-pressure induced mechanical oscillation of an optical microcavity. *Physical Review Letters*, 95:033901, 2005.

[114] S. Gröblacher, K. Hammerer, M. R. Vanner, and M. Aspelmeyer. Observation of strong coupling between a micromechanical resonator and an optical cavity field. *Nature*, 460:724–727, 2009.

[115] Q. Lin, J. Rosenberg, D. Chang, R. Camacho, M. Eichenfield, K. J. Vahala, and O. Painter. Coherent mixing of mechanical excitations in nano-optomechanical structures. *Nature Photonics*, 4:236–242, 2010.

[116] G. S. Agarwal and S. Huang. Electromagnetically induced transparency in mechanical effects of light. *Physical Review A*, 81:041803, 2010.

[117] J. Zhang, K. Peng, and S. L. Braunstein. Quantum-state transfer from light to macroscopic oscillators. *Physical Review A*, 68:013808, 2003.

[118] M. Mücke, E. Figueroa, J. Bochmann, C. Hahn, K. Murr, S. Ritter, C. J. Villas-Boas, and G. Rempe. Electromagnetically induced transparency with single atoms in a cavity. *Nature*, 465:755–758, 2010.

[119] C. K. Law. Interaction between a moving mirror and radiation pressure: A hamiltonian formulation. *Physical Review A*, 51:2537–2541, 1995.

[120] A. Dorsel, J. D. McCullen, P. Meystre, E. Vignes, and H. Walther. Optical bistability and mirror confinement induced by radiation pressure. *Physical Review Letters*, 51(17):1550–1553, 1983.

[121] J. M. Dobrindt, I. Wilson-Rae, and T. J. Kippenberg. Parametric normal-mode splitting in cavity optomechanics. *Physical Review Letters*, 101:263602, 2008.

[122] H. J. Kimble. Structure and dynamics in cavity quantum electrodynamics, 1994.

[123] P. W. Milonni. *Fast light, slow light and left-handed light.* Taylor and Francis, 2005.

[124] M. O. Scully and M. S. Zubairy. *Quantum Optics.* Cambridge University Press, 1997.

[125] A. Schliesser, O. Arcizet, R. Rivière, G. Anetsberger, and T. Kippenberg. Resolved-sideband cooling and position measurement of a micromechanical oscillator close to the heisenberg uncertainty limit. *Nature Physics*, 5:509–514, 2009.

[126] D. S. Weiss, V. Sandoghdar, J. Hare, V. Lefévre-Seguin, J. M. Raimond, and S. Haroche. Splitting of high-Q mie modes induced by light backscattering in silica microspheres. *Optics Letters*, 20(18):1835–1837, 1995.

[127] M. L. Gorodetsky, A. D. Pryamikov, and V. S. Ilchenko. Rayleigh scattering in high-Q microspheres. *Journal of the optical society of America B - Optical physics*, 17(6):1051–1057, 2000.

[128] A. Mazzei, S. Götzinger, L. de S. Menezes, G. Zumofen, O. Benson, and V. Sandoghdar. Controlled coupling of counterpropagating whispering-gallery modes by a single rayleigh scatterer: a classical problem in a quantum optical light. *Physical Review Letters*, 99:173603, 2007.

[129] C. A. Regal, J. D. Teufel, and K. W. Lehnert. Measuring nanomechanical motion with a microwave cavity interferometer. *Nature Physics*, 4:555–560, 2008.

[130] M. Eichenfield, R. Camacho, J. Chan, K. Vahala, and O. Painter. A picogram and nanometer scale photonic crystal opto-mechanical cavity. *Nature*, 459:550–555, 2009.

[131] A. H. Safavi-Naeini, T. P. Mayer, I. Alegre, J. Chan, M. Eichenfield, M. Winger, J. Q. Lin, J. T. Hill, D. E. Chang, and O. Painter. Electromagnetically induced transparency and slow light with optomechanics. *Nature*, 472:69–73, 2011.

[132] D. E. Chang, A. H. Safavi-Naeini, M. Hafezi, and O. Painter. Slowing and stopping light using an optomechanical crystal array. *New Journal of Physics*, 13:023003, 2011.

[133] M. Eichenfield, J. Chan, R. M. Camacho, K. J. Vahala, and O. Painter. Optomechanical crystals. *Nature*, 462:78–82, 2009.

[134] M. Winger, T. D. Blasius, T. P. Mayer Alegre, A. H. Safavi-Naeini, S. Meenehan, J. Cohen, S. Stobbe, and O. Painter. A chip-scale integrated cavity-electro-optomechanics platform. *Opt. Express*, 19(25):24905–24921, Dec 2011.

[135] K. C. Schwab and M. L. Roukes. Putting mechanics into quantum mechanics. *Physics Today*, 58(7):36–42, 2005.

[136] T. J. Kippenberg and K. J. Vahala. Cavity optomechanics: Back-action at the mesoscale. *Science*, 321:1172–1176, 2008.

[137] F. Marquardt and S. M. Girvin. Optomechanics. *Physics*, 2:40, 2009.

[138] I. Favero and K. Karrai. Optomechanics of deformable optical cavities. *Nature Photonics*, 3:201–205, 2009.

[139] P. Rabl, S. J. Kolkowitz, F. H. L. Koppens, J. G. E. Harris, P. Zoller, and M. D. Lukin. A quantum spin transducer based on nanoelectromechanical resonator arrays. *Nature Physics*, 6:602–608, 2010.

[140] V. B. Braginskii and A. B. Manukin. Ponderomotive effects of electromagnetic radiation. *Soviet Physics JETP Letters*, 25(4):653–655, 1967.

[141] M. I. Dykman. Heating and cooling of local and quasilocal vibrations by a nonresonance field. *Soviet Physics - Solid State*, 20:1306–1311, 1978.

[142] C. Höhberger Metzger and K. Karrai. Cavity cooling of a microlever. *Nature*, 432:1002–1005, 2004.

[143] T. Corbitt, Y. Chen, E. Innerhofer, H. Muller-Ebhardt, D. Ottaway, H. Rehbein, D. Sigg, S. Whitcomb, Ch. Wipf, and N. Mavalvala. An all-optical trap for a gram-scale mirror. *Physical Review Letters*, 98(15):150802, 2007.

[144] D. Leibfried, R. Blatt, C. Monroe, and D. Wineland. Quantum dynamics of single trapped ions. *Review of Modern Physics*, 75(1):281–324, 2003.

[145] M. Bhattacharya and P. Meystre. Trapping and cooling a mirror to its quantum mechanical ground state. *Physical Review Letters*, 99(7):073601, 2007.

[146] S. Gröblacher, J. B. Hertzberg, M. R. Vanner, S. Gigan, K. C. Schwab, and M. Aspelmeyer. Demonstration of an ultracold micro-optomechanical oscillator in a cryogenic cavity. *Nature Physics*, 5:485–488, 2009.

[147] W. A. Phillips. Two-level states in glasses. *Reports on Progress in Physics*, 50(12):1657, 1987.

[148] T. Carmon, L. Yang, and K. J. Vahala. Dynamical thermal behavior and thermal selfstability of microcavities. *Optics Express*, 12:4742–4750, 2004.

[149] V. B. Braginsky, S. E. Strigin, and V. P. Vyatchanin. Parametric oscillatory instability in fabry-perot interferometer. *Physics Letters A*, 287(5-6):331–338, 2001.

[150] V. B. Braginsky and F. Y. Khalili. *Quantum Measurement.* Cambridge University Press, 1992.

[151] K. W. Murch, K. L. Moore, S. Gupta, and D. M. Stamper-Kurn. Observation of quantum-measurement backaction with an ultracold atomic gas. *Nature Physics*, 4:561–564, 2008.

[152] V. B. Braginsky and A. B. Manukin. *Measurement of Weak Forces in Physics Experiments.* University of Chicago Press, 1977.

[153] C. A. Regal and K. W. Lehnert. From cavity electromechanics to cavity optomechanics. *Journal of Physics: Conference Series*, 264(1):012025, 2011.

[154] L. Tian and H. Wang. Optical wavelength conversion of quantum states with optomechanics. *Physical Review A*, 82(5):053806, 2010.

[155] U. Akram, N. Kiesel, M. Aspelmeyer, and G. J. Milburn. Single-photon optomechanics in the strong coupling regime. *New Journal of Physics*, 12:083030, 2010.

[156] K. Stannigel, P. Rabl, A. S. Sorensen, P. Zoller, and M. D Lukin. Optomechanical transducers for long-distance quantum communication. *Physical Review Letters*, 105:220501, 2010.

[157] F. Khalili, S. Danilishin, H. Miao, H. Müller-Ebhardt, H. Yang, and Y. Chen. Preparing a mechanical oscillator in non-Gaussian quantum states. *Phys. Rev. Lett.*, 105:070403, Aug 2010.

[158] D. J. Wineland, C. Monroe, W. M. Itano, D. Leibfried, B. W. King, and D. M. Meekhof. Experimental issues in coherent quantum-state manipulation of trapped atomic ions. *Journal of Research of the National Institute of Standards and Technology*, 103(3):259–328, 1998.

[159] H. J. Kimble. Strong interactions of single atoms and photons in cavity qed. *Physica Scripta*, 1998(T76):127, 1998.

[160] L. D. Landau and E. M. Lifshitz. *Statistical Physics*, volume 5. Pergamon Press, 1980.

[161] V. B. Braginsky, M. L. Gorodetsky, and S. P. Vyatchanin. Thermodynamical fluctuations and photo-thermal shot noise in gravitational wave antennae. *Physics Letters A*, 264:1–10, 1999.

[162] M. L. Gorodetsky and I. S. Grudinin. Fundamental thermal fluctuations in microspheres. *Journal of the Optical Society of America B*, 21:697–705, 2004.

[163] A. I. Lvovsky, H. Hansen, T. Aichele, O. Benson, J. Mlynek, and S. Schiller. Quantum state reconstruction of the single-photon fock state. *Phys. Rev. Lett.*, 87(5):050402, 2001.

[164] K. H. Lee, T. G. McRae, G. I. Harris, J. Knittel, and W. P. B. Cooling and control of a cavity optoelectromechanical system. *Phys. Rev. Lett.*, 104:123604, Mar 2010.

[165] E. Gavartin. in preparation, 2012.

[166] T. Kippenberg, J. Kalkman, A. Polman, and K. J. Vahala. Demonstration of an erbium-doped microdisk laser on a silicon chip. *Physical Review A*, 74:051802(R), 2006.

[167] A. H. Safavi-Naeini, J. Chan, J. T. Hill, T. P. Mayer Alegre, A. Krause, and O. Painter. Observation of quantum motion of a nanomechanical resonator. *Phys. Rev. Lett.*, 108:033602, Jan 2012.

[168] P. S. Jessen, C. Gerz, P. D. Lett, W. D. Phillips, S. L. Rolston, R. J. C. Spreeuw, and C. I. Westbrook. Observation of quantized motion of rb atoms in an optical field. *Phys. Rev. Lett.*, 69:49–51, 1992.

[169] V. B. Braginsky, Y. I. Vorontsov, and K. Thorne. Quantum nondemolition measurements. *Science*, 209:547–557, 1980.

[170] A. A. Clerk, F. Marquardt, and K. Jacobs. Back-action evasion and squeezing of a mechanical resonator using a cavity detector. *New Journal of Physics*, 10:095010, 2008.

[171] J. B. Hertzberg, T. Rocheleau, T. Ndukum, M. Savva, A. A. Clerk, and K. C. Schwab. Back-action-evading measurements of nanomechanical motion. *Nature Physics*, 6:213–217, 2010.

Optomechanically Induced Transparency

S. Weis, R. Rivière, S. Deléglise, E. Gavartin, O. Arcizet, A. Schliesser, T. J. Kippenberg

Science **330,** 1520 (2010)

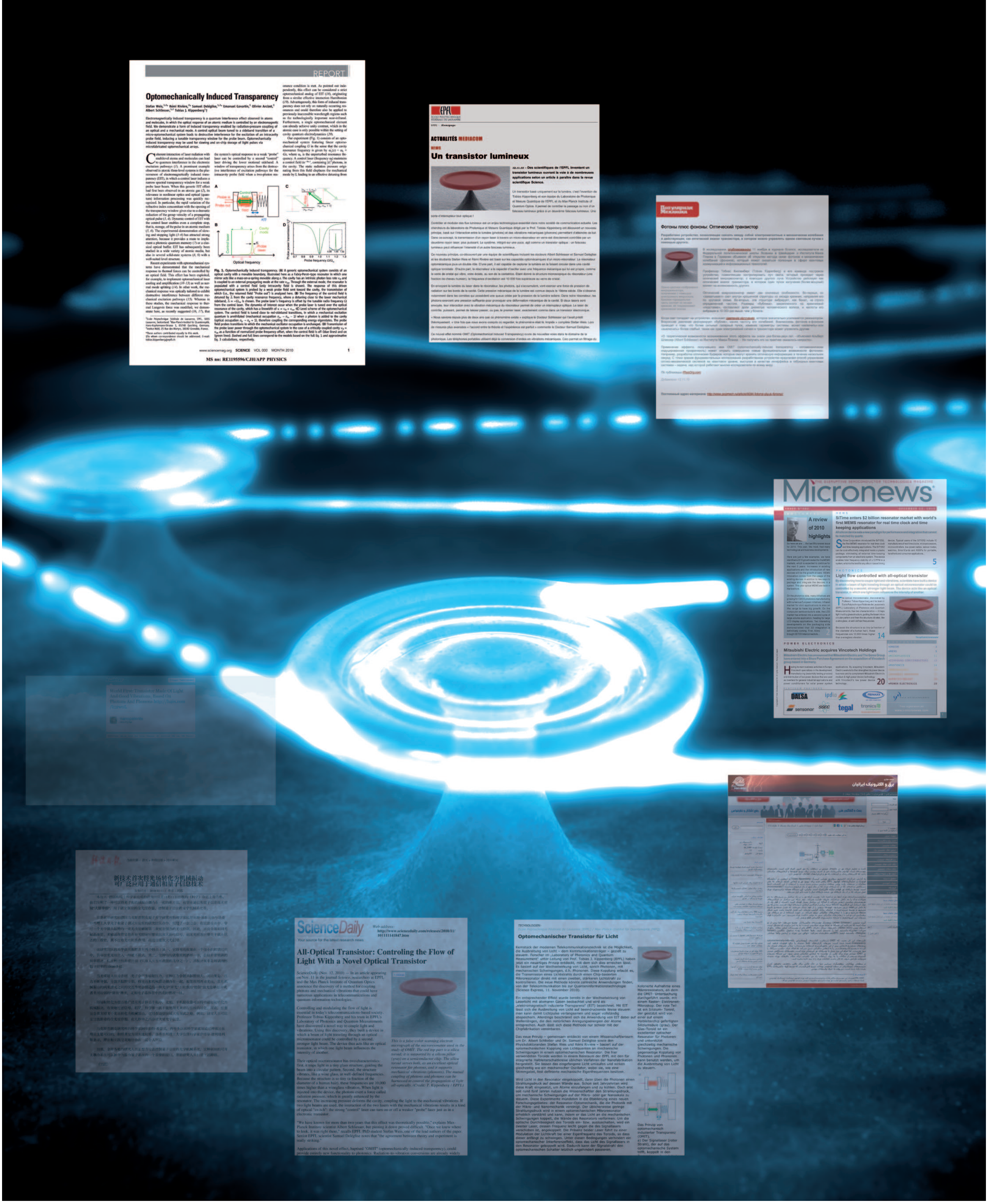

REPORT

Optomechanically Induced Transparency

Stefan Weis,[1,2]* Rémi Rivière,[2]* Samuel Deléglise,[1,2]* Emanuel Gavartin,[1] Olivier Arcizet,[3] Albert Schliesser,[1,2] Tobias J. Kippenberg[1]†

Electromagnetically induced transparency is a quantum interference effect observed in atoms and molecules, in which the optical response of an atomic medium is controlled by an electromagnetic field. We demonstrate a form of induced transparency enabled by radiation-pressure coupling of an optical and a mechanical mode. A control optical beam tuned to a sideband transition of a micro-optomechanical system leads to destructive interference for the excitation of an intracavity probe field, inducing a tunable transparency window for the probe beam. Optomechanically induced transparency may be used for slowing and on-chip storage of light pulses via microfabricated optomechanical arrays.

Coherent interaction of laser radiation with multilevel atoms and molecules can lead to quantum interference in the electronic excitation pathways (1). A prominent example observed in atomic three-level systems is the phenomenon of electromagnetically induced transparency (EIT), in which a control laser induces a narrow spectral transparency window for a weak probe laser beam. When this generic EIT effect had first been observed in an atomic gas (2), its relevance in nonlinear optics and optical (quantum) information processing was quickly recognized. In particular, the rapid variation of the refractive index concomitant with the opening of the transparency window gives rise to a dramatic reduction of the group velocity of a propagating optical pulse (3, 4). Dynamic control of EIT with the control laser enables even a complete stop, that is, storage, of the pulse in an atomic medium (5, 6). The experimental demonstration of slowing and stopping light (3–6) has attracted strong attention, because it provides a route to implement a photonic quantum memory (7) or a classical optical buffer. EIT has subsequently been studied in a wide variety of atomic media, but also in several solid-state systems (8, 9) with a well-suited level structure.

Recent experiments with optomechanical systems have demonstrated that the mechanical response to thermal forces can be controlled by an optical field. This effect has been exploited, for example, to implement optomechanical laser cooling and amplification (10–13) as well as normal mode splitting (14). In other work, the mechanical response was optically tailored to exhibit destructive interference between different mechanical excitation pathways (15). Whereas in these studies, the mechanical response to thermal Langevin force was modified, we demonstrate here, as recently suggested (16, 17), that the system's optical response to a weak "probe" laser can be controlled by a second "control" laser driving the lower motional sideband. A window of transparency arises from the destructive interference of excitation pathways for the intracavity probe field when a two-photon resonance condition is met. As pointed out independently, this effect can be considered a strict optomechanical analog of EIT (18), originating from a similar effective interaction Hamiltonian (19). Advantageously, this form of induced transparency does not rely on naturally occurring resonances and could therefore also be applied to previously inaccessible wavelength regions such as the technologically important near-infrared. Furthermore, a single optomechanical element can already achieve unity contrast, which in the atomic case is only possible within the setting of cavity quantum electrodynamics (20).

Our experiment (Fig. 1) consists of an optomechanical system featuring linear optomechanical coupling G in the sense that the cavity resonance frequency is given by $\omega_c(x) = \omega_c + Gx$, where ω_c is the unperturbed resonance frequency. A control laser (frequency ω_l) maintains a control field $\bar{a}e^{-i\omega_l t}$, containing $|\bar{a}|^2$ photons, in the cavity. The static radiation pressure originating from this field displaces the mechanical mode by $\bar{x}$, leading to an effective detuning from

Fig. 1. Optomechanically induced transparency. (A) A generic optomechanical system consists of an optical cavity with a movable boundary, illustrated here as a Fabry-Perot–type resonator in which one mirror acts like a mass-on-a-spring movable along x. The cavity has an intrinsic photon loss rate κ_0 and is coupled to an external propagating mode at the rate κ_{ex}. Through the external mode, the resonator is populated with a control field (only intracavity field is shown). The response of this driven optomechanical system is probed by a weak probe field sent toward the cavity, the transmission of which (i.e., the returned field "Probe out") is analyzed here. **(B)** The frequency of the control field is detuned by $\bar{\Delta}$ from the cavity resonance frequency, where a detuning close to the lower mechanical sideband, $\bar{\Delta} \approx -\Omega_m$, is chosen. The probe laser's frequency is offset by the tunable radio frequency Ω from the control laser. The dynamics of interest occur when the probe laser is tuned over the optical resonance of the cavity, which has a linewidth of $\kappa = \kappa_0 + \kappa_{ex}$. **(C)** Level scheme of the optomechanical system. The control field is tuned close to red-sideband transitions, in which a mechanical excitation quantum is annihilated (mechanical occupation $n_m \to n_m - 1$) when a photon is added to the cavity (optical occupation $n_p \to n_p + 1$), therefore coupling the corresponding energy eigenstates. The probe field probes transitions in which the mechanical oscillator occupation is unchanged. **(D)** Transmission of the probe laser power through the optomechanical system in the case of a critically coupled cavity $\kappa_0 = \kappa_{ex}$ as a function of normalized probe frequency offset, when the control field is off (blue lines) and on (green lines). Dashed and full lines correspond to the models based on the full Eq. 1 and approximative Eq. 3 calculations, respectively.

---

[1]École Polytechnique Fédérale de Lausanne, EPFL, 1015 Lausanne, Switzerland. [2]Max-Planck-Institut für Quantenoptik, Hans-Kopfermann-Strasse 1, 85748 Garching, Germany. [3]Institut Néel, 25 Rue des Martyrs, 38042 Grenoble, France.

*These authors contributed equally to this work.

†To whom correspondence should be addressed. E-mail: tobias.kippenberg@epfl.ch

www.sciencemag.org SCIENCE VOL 000 MONTH 2010 1

MS no: RE1195596/CJH/APP PHYSICS

EPFL
ÉCOLE POLYTECHNIQUE FÉDÉRALE DE LAUSANNE

EPFL > Homepage

ACTUALITÉS MEDIACOM

NEWS

Un transistor lumineux

12.11.10 - Des scientifiques de l'EPFL inventent un transistor lumineux ouvrant la voie à de nombreuses applications selon un article à paraître dans la revue scientifique Science.

Un transistor basé uniquement sur la lumière, c'est l'invention de Tobias Kippenberg et son équipe du Laboratoire de Photonique et Mesure Quantique de l'EPFL et du Max Planck Institute of Quantum Optics. Il permet de contrôler le passage ou non d'un faisceau lumineux grâce à un deuxième faisceau lumineux. Une sorte d'interrupteur tout optique !

Contrôler et moduler des flux lumineux est un enjeu technologique essentiel dans notre société de communication actuelle. Les chercheurs du laboratoire de Photonique et Mesure Quantique dirigé par le Prof. Tobias Kippenberg ont découvert un nouveau principe, basé sur l'interaction entre la lumière (photons) et des vibrations mécaniques (phonons) permettant d'atteindre ce but. Dans ce concept, la transmission d'un rayon laser à travers un micro-résonateur en verre est directement contrôlée par un deuxième rayon laser, plus puissant. Le système, intégré sur une puce, agit comme un transistor optique : un faisceau lumineux peut influencer l'intensité d'un autre faisceau lumineux.

Ce nouveau principe, co-découvert par une équipe de scientifiques incluant les docteurs Albert Schliesser et Samuel Deléglise et les étudiants Stefan Weis et Rémi Rivière est basé sur les capacités optomécaniques d'un micro-résonateur. Le résonateur optomécanique joue un double rôle. D'une part, il est capable de capturer la lumière en la faisant circuler dans une cavité optique toroïdale. D'autre part, le résonateur a la capacité d'osciller avec une fréquence mécanique qui lui est propre, comme le verre de cristal qui vibre, voire éclate, au son de la cantatrice. Etant donné la structure microscopique du résonateur (une fraction de cheveu humain), la fréquence d'oscillation est 10 000 fois supérieure au verre de cristal.

En envoyant la lumière du laser dans le résonateur, les photons, qui s'accumulent, vont exercer une force de pression de radiation sur les bords de la cavité. Cette pression mécanique de la lumière est connue depuis le 19ème siècle. Elle s'observe notamment dans les comètes qui possèdent une queue créée par la pression de la lumière solaire. Dans notre résonateur, les photons exercent une pression suffisante pour provoquer une déformation mécanique de la cavité. Si deux lasers sont envoyés, leur interaction avec la vibration mécanique du résonateur permet de créer un interrupteur optique. Le laser de contrôle, puissant, permet de laisser passer, ou pas, le premier laser, exactement comme dans un transistor électronique.

« Nous savions depuis plus de deux ans que ce phénomène existe » explique le Docteur Schliesser qui l'avait prédit théoriquement. « Une fois que nous avons compris où regarder, le phénomène était là, limpide » complète Stefan Weis. Lors de mesures plus avancées « l'accord entre la théorie et l'expérience est parfait » commente le Docteur Samuel Deléglise.

Ce nouvel effet nommé OMIT (Optomechanical Induced Transparency) ouvre de nouvelles voies dans le domaine de la photonique. Les téléphones portables utilisent déjà la conversion d'ondes en vibrations mécaniques. Ceci permet un filtrage du

---

Популярная Механика

Фотоны плюс фононы: Оптический транзистор

Разработано устройство, позволяющее связать между собой электромагнитные и механические колебания и действующее, как оптический аналог транзистора, в котором можно управлять одним световым лучом с помощью другого.

Ложно-цветное изображение микрорезонатора, полученное с помощью электронного микроскопа. Красная тороидальная часть состоит из оксида кремния, ее поддерживает кремниевая основа

В исследовании, опубликованном 11 ноября в журнале Science, исследователи из Федеральной политехнической школы Лозанны в Швейцарии и Института Макса Планка в Германии объявили об открытии метода связи фотонов и механических колебаний (фононов), который может оказаться полезным в сфере квантовых коммуникаций и информационных технологий.

Профессор Тобиас Киппенберг (Tobias Kippenberg) и его команда построили устройство, позволяющее контролировать луч света, который проходит через оптический микрорезонатор, с помощью другого луча. Устройство действует как оптический аналог транзистора, в котором один пучок излучения (более мощный) влияет на интенсивность другого.

Оптический микрорезонатор имеет две ключевых особенности. Во-первых, он «захватывает» свет внутри крошечной структуры из оксида кремния, направляя его по круговой схеме. Во-вторых, эта структура вибрирует, как бокал, на строго определенной частоте. Размеры «бублика», закрепленного на кремниевой «подставке», составляют доли диаметра человеческого волоса, и частоты его вибрации в 10 000 раз выше, чем у бокала.

Когда свет попадает на устройство, возникает давление излучения, которое значительно усиливается резонатором. Возросшее давление деформирует «бублик», меняя частоту его колебаний. Взаимосвязь фотонов и фононов приводит к тому, что более сильный лазерный пучок, изменяя параметры системы, может «включить» или «выключить» более слабый, также как один электрический сигнал в транзисторе может управлять другим.

«О теоретической возможности возникновения этого эффекта мы знали уже более двух лет, - объясняет Альберт Шлиссер (Albert Schliesser) из Института Макса Планка. – Но получить его на практике оказалось непросто».

Применение эффекта, получившего имя OMIT (optomechanically-induced transparency – оптомеханически индуцированная прозрачность) может открыть совершенно новые функциональные возможности фотоники. Например, разработка оптических буферов, которые смогут хранить оптическую информацию в течение нескольких секунд. С точки зрения фундаментальных исследований разработанное устройство предлагает способ управления оптико-механической системой на квантовом уровне, выступая в качестве интерфейса в гибридных квантовых системах – задача, над которой работают многие исследователи по всему миру.

По публикации PhysOrg.com

Добавлено: 12.11.10

Постоянный адрес материала: http://www.popmech.ru/article/8094-fotonyi-plyus-fononyi/

THE DISRUPTIVE SEMICONDUCTOR TECHNOLOGIES MAGAZINE

Micronews®

EDITORIAL

A review of 2010 highlights

So here we are ... the last Micronews issue for 2010. This year, like most, had many technological and business developments.

Here are just a few examples, we have identified a 2010 growth restart for the MEMS markets, which is expected to continue for the next 5 years. Increases in existing applications and the introduction of new devices will be the growth drivers. MEMS innovation comes from the usage of the existing devices, in addition to new ways to package and integrate the devices in a system. This year optical MEMS are back in the forefront.

On the photonics side, many initiatives are growing for CMOS photonics manufacturing with numerous European initiatives. Infrared market for civil applications is also on the verge to have big growth. On the compound semiconductors side, the LED market has entered into a second cycle of large volume application, heading for large LCD display applications. Two interesting developments on the packaging side demonstrated that 3D integration is definitively coming. First, Xilinx brought 3D TSV interconnects to... 2

MEMS

SiTime enters $2 billion resonator market with world's first MEMS resonator for real time clock and time keeping applications

All silicon device sets a new paradigm for performance and integration that cannot be matched by quartz.

SiTime Corporation introduced the SiT1052, the first MEMS resonator for real time clock and time keeping applications. The SiT1052 can be cost-effectively integrated inside a plastic package, eliminating all external time-keeping components from an electronic system. The device enables total frequency stability of ± 5 PPM in a system, which is the best for any silicon-based timing device. Typical users of the SiT1052 include IC manufacturers of real time clocks, microprocessors, microcontrollers, low power radios, sensor nodes, watches, SmartCards and ASSPs for portable, handheld and consumer applications... 5

PHOTONICS

Light flow controlled with all-optical transistor

By discovering how to couple light and vibrations, scientists have built a device in which a beam of light traveling through an optical microresonator could be controlled by a second, stronger light beam. The device acts like an optical transistor, in which one light beam influences the intensity of another.

The optical microresonator, discovered by Professor Tobias Kippenberg and his team in Ecole Polytechnique Fédérale de Lausanne's (EPFL) Laboratory of Photonics and Quantum Measurements, has two characteristics — it traps light in a tiny glass structure, guiding the beam into a circular pattern and then the structure vibrates, like a wine glass, at well-defined frequencies.

Because the structure is so tiny (a fraction of the diameter of a human hair), these frequencies are 10,000 times higher than a wineglass vibration. 14

The optical microresonator

POWER ELECTRONICS

Mitsubishi Electric acquires Vincotech Holdings

Mitsubishi Electric has announced that Mitsubishi Electric and The Gores Group have entered into a Share Purchase Agreement on the acquisition of Vincotech group based in Germany.

Having its main business activities in Europe, Vincotech specializes in the development, manufacturing (assembly testing process) and distribution of low power devices that are used as inverters for general industrial applications and power conditioners for solar power system applications. By acquiring Vincotech, Mitsubishi Electric seeks to further strengthen its power device business and to complement Mitsubishi Electric's medium & high power device technology with Vincotech's low power device technology... 20

- INSIDE 3
- MEMS 5
- MICROFLUIDICS 11
- COMPOUND SEMICONDUCTORS 12
- PHOTONICS 14
- POWER ELECTRONICS 20

PLATINUM PARTNERS

DALSA ipdia PRIMAXX sensonor SSEC tegal tronics microsystems

برق و الکترونیک ایرانیان

新技术首次将光场转化为机械振动 可广泛应用于通信和量子信息技术

ScienceDaily
Your source for the latest research news

Web address:
http://www.sciencedaily.com/releases/2010/11/101111141847.htm

All-Optical Transistor: Controling the Flow of Light With a Novel Optical Transistor

ScienceDaily (Nov. 12, 2010) — In an article appearing on Nov. 11 in the journal *Science*, researchers at EPFL and the Max Planck Institute of Quantum Optics announce the discovery of a method for coupling photons and mechanical vibrations that could have numerous applications in telecommunications and quantum information technologies.

This is a false-color scanning electron micrograph of the microresonator used in the study of OMIT. The red top part is a silica toroid; it is supported by a silicon pillar (gray) on a semiconductor chip. The silica toroid serves both, as an excellent optical resonator for photons, and it supports mechanical vibrations (phonons). The mutual coupling of photons and phonons can be harnessed to control the propagation of light all-optically. (Credit: T. Kippenberg / EPFL)

Controlling and modulating the flow of light is essential in today's telecommunications-based society. Professor Tobias Kippenberg and his team in EPFL's Laboratory of Photonics and Quantum Measurements have discovered a novel way to couple light and vibrations. Using this discovery, they built a device in which a beam of light traveling through an optical microresonator could be controlled by a second, stronger light beam. The device thus acts like an optical transistor, in which one light beam influences the intensity of another.

Their optical microresonator has two characteristics. first, it traps light in a tiny glass structure, guiding the beam into a circular pattern. Second, the structure vibrates, like a wine glass, at well-defined frequencies. Because the structure is so tiny (a fraction of the diameter of a human hair), these frequencies are 10,000 times higher than a wineglass vibration. When light is injected into the device, the photons exert a force called radiation pressure, which is greatly enhanced by the resonator. The increasing pressure deforms the cavity, coupling the light to the mechanical vibrations. If two light beams are used, the interaction of the two lasers with the mechanical vibrations results in a kind of optical "switch": the strong "control" laser can turn on or off a weaker "probe" laser just as in a electronic transistor.

"We have known for more than two years that this effect was theoretically possible," explains Max-Planck Institute scientist Albert Schliesser, but pinning it down proved difficult. "Once we knew where to look, it was right there," recalls EPFL PhD student Stefan Weis, one of the lead authors of the paper. Senior EPFL scientist Samuel Deléglise notes that "the agreement between theory and experiment is really striking."

Applications of this novel effect, baptised "OMIT" (optomechanically-induced transparency), could provide entirely new functionality to photonics. Radiation-to-vibration conversions are already widely

---

TECHNOLOGIEN-
Ecole Polytechnique Fédérale de Lausanne (EPFL) / Max-Planck-Institut für Quantenoptik (MPQ)

Optomechanischer Transistor für Licht

Kernstück der modernen Telekommunikationstechnik ist die Möglichkeit, die Ausbreitung von Licht – dem Kommunikationsträger – gezielt zu steuern. Forscher im „Laboratory of Photonics and Quantum Measurement" unter Leitung von Prof. Tobias J. Kippenberg (EPFL) haben jetzt ein neuartiges Prinzip entdeckt, mit dem sich dies erreichen lässt. Es basiert auf der Wechselwirkung von Licht, sprich Photonen, mit mechanischen Schwingungen, d.h. Phononen. Diese Kopplung erlaubt es, die Transmission eines Lichtstrahls durch einen Chip-basierten Mikroresonator direkt mit einen zweiten, stärkeren Lichtstrahl zu kontrollieren. Die neue Methode könnte zahlreiche Anwendungen finden, von der Telekommunikation bis zur Quanteninformationstechnologie (Science Express, 11. November 2010).

Kolorierte Aufnahme eines Mikroresonators, an dem die OMIT- Untersuchung durchgeführt wurde, mit einem Raster- Elektronen-Mikroskop. Der rote Teil ist ein Silizium- Toroid, der gestützt wird von einer auf einem Halbleiterchip gefertigten Siliziumsäule (grau). Der Glas-Toroid ist ein exzellenter optischer Resonator für Photonen und unterstützt gleichzeitig mechanische Schwingungen. Die gegenseitige Kopplung von Photonen und Phononen kann benutzt werden, um die Ausbreitung von Licht zu steuern.

Ein entsprechender Effekt wurde bereits in der Wechselwirkung von Laserlicht mit atomaren Gasen beobachtet und wird als „elektromagnetisch induzierte Transparenz" (EIT) bezeichnet. Mit EIT lässt sich die Ausbreitung von Licht auf beeindruckende Weise steuern: man kann damit Lichtpulse verlangsamen und sogar vollständig abspeichern. Allerdings beschränkt sich die Anwendung von EIT dabei auf Wellenlängen, die den natürlichen Anregungsenergien der Atome entsprechen. Auch lässt sich diese Methode nur schwer mit der Chipfabrikation vereinbaren.

Das neue Prinzip – gemeinsam entdeckt von einem Wissenschaftlerteam um Dr. Albert Schließer und Dr. Samuel Deléglise sowie den Physikdoktoranden Stefan Weis und Rémi Rivière – basiert auf der optomechanischen Kopplung von Lichtquanten an mechanische Schwingungen in einem optomechanischen Resonator. Die hier verwendeten Toroide werden in einem Reinraum der EPFL mit den für integrierte Halbleiterschaltkreise üblichen Verfahren der Nanofabrikation hergestellt. Sie lassen das eingefangene Licht umlaufen und wirken gleichzeitig wie ein mechanischer Oszillator, wobei sie, wie eine Stimmgabel, fest definierte mechanische Eigenfrequenzen besitzen.

Wird Licht in den Resonator eingekoppelt, dann üben die Photonen einen Strahlungsdruck auf dessen Wände aus. Schon seit Jahrzehnten wird diese Kraft eingesetzt, um Atome einzufangen und zu kühlen. Doch erst seit rund fünf Jahren nutzen die Wissenschaftler den Strahlungsdruck, um mechanische Schwingungen auf der Mikro- oder gar Nanoskala zu steuern. Diese Experimente mündeten in die Etablierung eines neuen Forschungsgebietes: der Resonator-Optomechanik, die die Photonik mit der Mikro- und Nanomechanik vereinigt. Der üblicherweise geringe Strahlungsdruck wird in einem optomechanischen Mikroresonator erheblich verstärkt und kann, indem er das Licht an die mechanischen Schwingungen koppelt, die Wände des Resonators verformen. Um die optische Durchlässigkeit des Toroids ein- bzw. auszuschalten, wird ein zweiter Laser, dessen Frequenz leicht gegen die des Signallasers verschoben ist, angekoppelt. Die Präsenz beider Laser führt zu einer Modulation der Lichtkraft bei einer Eigenfrequenz des Toroids, so dass dieser anfängt zu schwingen. Unter diesen Bedingungen verhindert ein optomechanischer Interferenzeffekt, dass das Licht des Signallasers in den Resonator gekoppelt wird. Dadurch kann der Signalstrahl den optomechanischen Schalter letztlich ungehindert passieren.

Das Prinzip von optomechanisch induzierter Transparenz (OMIT).
a) Der Signallaser (roter Strahl), der auf das optomechanische System trifft, koppelt in den

Quantum-Coherent Coupling of a Mechanical Oscillator to an optical cavity mode

E. Verhagen*, S. Deléglise*, S. Weis*, A. Schliesser* and T. J. Kippenberg

Nature **482**, 63-67 (2012)

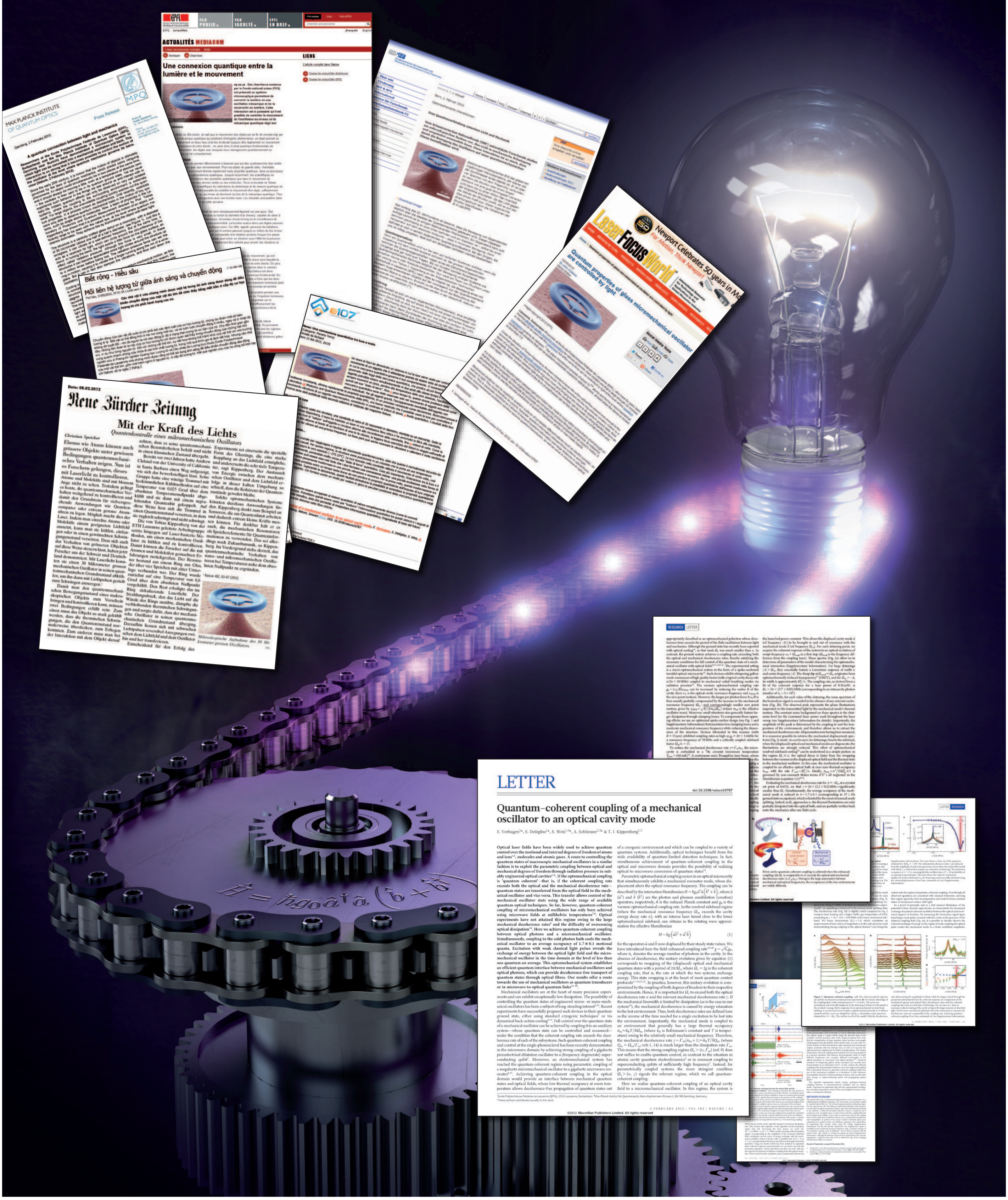

MAX PLANCK INSTITUTE OF QUANTUM OPTICS

Press Release

Garching, 2 February 2012

A quantum connection between light and mechanics

Researchers at the Ecole Polytechnique Fédérale de Lausanne (EPFL, Switzerland) and the Max Planck Institute of Quantum Optics (MPQ, Garching near Munich) have demonstrated a microscopic system in which light can be converted into a mechanical oscillation and back. This interaction is so strong that it becomes possible to control the motion of the oscillator at the level where quantum mechanics governs its behaviour (Nature, 2 February 2012).

ACTUALITÉS MEDIACOM

Une connexion quantique entre la lumière et le mouvement

02.02.12 - Des chercheurs soutenus par le Fonds national suisse (FNS) ont présenté un système microscopique permettant de convertir la lumière en une oscillation mécanique et de la reconvertir en lumière. Cette interaction est si puissante qu'il est possible de contrôler le mouvement de l'oscillateur au niveau où la mécanique quantique régit son comportement.

Optomechanische Interaktionen

Eine Quantenverbindung zwischen Licht und Mechanik

Vom Schweizerischen Nationalfonds (SNF) unterstützte Forschende stellen ein mikroskopisches System vor, das Licht in mechanische Schwingung und umgekehrt umwandeln kann. Diese Interaktion ist so stark, dass damit die Bewegung des Oszillators auf einer quantenmechanischen Ebene beeinflussbar wird.

Quantum properties of glass micromechanical oscillator are controlled by light

By John Wallace, Senior Editor

Biết rộng - Hiểu sâu

Mối liên hệ lượng tử giữa ánh sáng và chuyển động

Các nhà vật lí vừa chứng minh được một hệ trong đó ánh sáng được dùng để điều khiển chuyển động của một vật đủ lớn để nhìn thấy bằng mắt trần ở cấp độ cơ học lượng tử chi phối hành trạng của nó.

News: Una connessione quantistica tra luce e moto

Date: 08.02.2012

Neue Zürcher Zeitung

Mit der Kraft des Lichts

Quantenkontrolle eines mikromechanischen Oszillators

Christian Speicher

Ebenso wie Atome können auch grössere Objekte unter gewissen Bedingungen quantenmechanisches Verhalten zeigen. Nun ist es Forschern gelungen, dieses mit Laserlicht zu kontrollieren.

Atome und Moleküle sind mit blossem Auge nicht zu sehen. Trotzdem gelingt es heute, ihr quantenmechanisches Verhalten weitgehend zu kontrollieren und damit den Grundstein für vielversprechende Anwendungen wie Quantencomputer oder extrem genaue Atomuhren zu legen. Möglich macht dies der Laser. Indem man einzelne Atome oder Moleküle einem geeigneten Lichtfeld aussetzt, kann man sie kühlen, einfangen oder in einen gewünschten Schwingungszustand versetzen. Dass sich auch das Verhalten von grösseren Objekten auf diese Weise steuern lässt, haben jetzt Forscher aus der Schweiz und Deutschland demonstriert. Mit Laserlicht konnten sie einen 30 Mikrometer grossen mechanischen Oszillator in seinen quantenmechanischen Grundzustand abkühlen, um ihn dann mit Lichtpulsen gezielt zum Schwingen anzuregen.[1]

Damit man den quantenmechanischen Bewegungszustand eines makroskopischen Objekts zum Vorschein bringen und kontrollieren kann, müssen zwei Bedingungen erfüllt sein: Zum einen muss das Objekt so stark gekühlt werden, dass die thermischen Schwingungen, die den Quantenzustand normalerweise überdecken, zum Erliegen kommen. Zum anderen muss man bei der Interaktion mit dem Objekt darauf achten, dass es seine quantenmechanischen Besonderheiten behält und nicht in einen klassischen Zustand übergeht.

Bereits vor zwei Jahren hatte Andrew Cleland von der University of California in Santa Barbara einen Weg aufgezeigt, wie sich das bewerkstelligen lässt. Seine Gruppe hatte eine winzige Trommel mit herkömmlichen Kühlmethoden auf eine Temperatur von 0,025 Grad über dem absoluten Temperaturnullpunkt abgekühlt und sie dann mit einem supraleitenden Quantenbit gekoppelt. Auf diese Weise liess sich die Trommel in einen Quantenzustand versetzen, in dem sie zugleich schwingt und nicht schwingt.

Die von Tobias Kippenberg von der ETH Lausanne geleitete Arbeitsgruppe setzte hingegen auf Laser-basierte Methoden, um einen mechanischen Oszillator zu kühlen und zu kontrollieren. Damit können die Forscher auf die mit Atomen und Molekülen gemachten Erfahrungen zurückgreifen. Der Resonator bestand aus einem Ring aus Glas, der über vier Speichen mit einer Unterlage verbunden war. Der Ring wurde zunächst auf eine Temperatur von 0,6 Grad über dem absoluten Nullpunkt vorgekühlt. Den Rest erledigte das im Ring zirkulierende Laserlicht. Der Strahlungsdruck, den das Licht auf die Wände des Rings ausübte, dämpfte die verbleibenden thermischen Schwingungen und sorgte dafür, dass der mechanische Oszillator in seinen quantenmechanischen Grundzustand überging. Daraufhin liessen sich mit schwachen Lichtpulsen reversibel Anregungen zwischen dem Lichtfeld und dem Oszillator hin und her transferieren.

Entscheidend für den Erfolg des Experiments sei einerseits die spezielle Form des Glasrings, die eine starke Kopplung an das Lichtfeld ermögliche, und andererseits die sehr tiefe Temperatur, sagt Kippenberg. Der Austausch von Energie zwischen dem mechanischen Oszillator und dem Lichtfeld erfolge in dieser kalten Umgebung so schnell, dass die Kohärenz der Quantenzustände gewahrt bleibe.

Solche optomechanischen Systeme könnten durchaus Anwendungen finden. Kippenberg denkt zum Beispiel an Sensoren, die am Quantenlimit arbeiten und dadurch extrem kleine Kräfte messen können. Für denkbar hält er es auch, die mechanischen Resonatoren als Speicherelemente für Quanteninformationen zu verwenden. Das sei allerdings noch Zukunftsmusik, so Kippenberg. Im Vordergrund stehe derzeit, das quantenmechanische Verhalten von nano- und mikromechanischen Oszillatoren bei Temperaturen nahe dem absoluten Nullpunkt zu ergründen.

Mikroskopische Aufnahme des 30 Mikrometer grossen Oszillators. EPFL

[1] Nature 482, 63–67 (2012).

LETTER

doi:10.1038/nature10787

Quantum–coherent coupling of a mechanical oscillator to an optical cavity mode

E. Verhagen[1]*, S. Deléglise[1]*, S. Weis[1,2]*, A. Schliesser[1,2]* & T. J. Kippenberg[1,2]

Optical laser fields have been widely used to achieve quantum control over the motional and internal degrees of freedom of atoms and ions[1,2], molecules and atomic gases. A route to controlling the quantum states of macroscopic mechanical oscillators in a similar fashion is to exploit the parametric coupling between optical and mechanical degrees of freedom through radiation pressure in suitably engineered optical cavities[3–6]. If the optomechanical coupling is 'quantum coherent'—that is, if the coherent coupling rate exceeds both the optical and the mechanical decoherence rate—quantum states are transferred from the optical field to the mechanical oscillator and vice versa. This transfer allows control of the mechanical oscillator state using the wide range of available quantum optical techniques. So far, however, quantum-coherent coupling of micromechanical oscillators has only been achieved using microwave fields at millikelvin temperatures[7,8]. Optical experiments have not attained this regime owing to the large mechanical decoherence rates[9] and the difficulty of overcoming optical dissipation[10]. Here we achieve quantum-coherent coupling between optical photons and a micromechanical oscillator. Simultaneously, coupling to the cold photon bath cools the mech-

of a cryogenic environment and which can be coupled to a variety of quantum systems. Additionally, optical techniques benefit from the wide availability of quantum-limited detection techniques. In fact, simultaneous achievement of quantum-coherent coupling in the optical and microwave domain provides the possibility of realizing optical-to-microwave conversion of quantum states[15].

Parametric optomechanical coupling occurs in an optical microcavity that simultaneously exhibits a mechanical resonator mode, whose displacement alters the optical resonance frequency. The coupling can be described by the interaction Hamiltonian $H=\hbar g_0\hat{a}^\dagger\hat{a}\left(\hat{b}^\dagger+\hat{b}\right)$, where $\hat{a}$ ($\hat{a}^\dagger$) and $\hat{b}$ ($\hat{b}^\dagger$) are the photon and phonon annihilation (creation) operators, respectively, $\hbar$ is the reduced Planck constant and g_0 is the vacuum optomechanical coupling rate. In the resolved sideband regime (where the mechanical resonance frequency Ω_m exceeds the cavity energy decay rate κ), with an intense laser tuned close to the lower optomechanical sideband, one obtains in the rotating wave approximation the effective Hamiltonian

$$H=\hbar g\left(\hat{a}\hat{b}^\dagger+\hat{a}^\dagger\hat{b}\right) \quad (1)$$

Curriculum Vitae

Stefan WEIS
Route Cantonale 33, C. 22
1025 St-Sulpice
Switzerland

Phone: +41 (0)7 67 99 33 25
Email: stefan.weis@epfl.ch

Nationality: German
Birthday: February 1st, 1983 in Heilbronn, Germany

PROFESSIONAL EDUCATION

05/2010 — 05/2012	Doctoral thesis in the field of cavity optomechanics in the group of Prof. Tobias J. Kippenberg, Laboratory of Photonics and Quantum Measurements (LPQM) at the Ecole Polytechnique Fédérale de Lausanne (EPFL), Switzerland ...
AND	
03/2008 — 05/2010	... and at the Max Planck Institute of Quantum Optics, Garching, Germany
10/2002 — 11/2007	Physics studies at Ruprecht-Karls-University, Heidelberg, Germany
11/2006 — 11/2007	Diploma thesis in the group of Prof. Markus Oberthaler, Kirchhoff-Institute for Physics, entitled "Setup of a Laser System for Ultracold Sodium - Towards a Degenerate Gas of Ultracold Fermions"
08/2005 — 08/2006	Two semesters at the Université Paris-Sud XI within the Erasmus-Program
04/2004	Intermediate diploma in Physics from the University of Heidelberg Germany
08/1993 — 05/2002	Secondary School, Heilbronn

PROFESSIONAL EXPERIENCE

05/2007 — 11/2007	Teaching assistant for the advanced lab course on basic electronics
05/2005 — 07/2005	Internship at the Institut d'Electronique Fondamentale, Université Paris-Sud, Orsay, France

1999 —2001	Internship at Vishay Semiconductor GmbH, Heilbronn, followed by a two years part-time employment in the ion implantation department

HARD SKILLS

Computing:	Matlab, LabView, Python, C++, LaTeX, SolidWorks, MS Office
Technical skills:	Lasers and optics, electronics, cryogenics, vacuum technology, metal working

LANGUAGES German (mother tongue), English (fluent), French (fluent)

HOBBIES

Sports, e.g. volleyball, badminton, sailing, skiing, hiking; electronics